Spin- and Angle-Resolved Photoelectron Spectroscopy on Topological Insulators and Bulk Rashba Systems

---

Dissertation
zur
Erlangung der naturwissenschaftlichen Doktorwürde
(Dr. sc. nat.)
vorgelegt der
Mathematisch-naturwissenschaftlichen Fakultät
der
Universität Zürich

von

Gabriel Landolt
aus Glarus Nord GL

Promotionskomitee
Prof. Dr. Jürg Osterwalder (Vorsitz)
Prof. Dr. Jan Hugo Dil
Prof. Dr. Hartmut Buhmann

Zürich, 2014

Die vorliegende Arbeit wurde von der mathematisch-naturwissenschaftlichen Fakultät der Universität Zürich im Herbstsemester 2014 als Dissertation angenommen.

Promotionskomitee:

Prof. Dr. Jürg Osterwalder (Vorsitz)
Prof. Dr. Jan Hugo Dil
Prof. Dr. Hartmut Buhmann

῾Ο μὲν βίος βραχύς, ἡ δὲ τέχνη μακρά.

— ῾Ιπποκράτης ὁ Κῷος

Abstract

In this dissertation the electronic structures of semiconducting crystals with strong spin–orbit interactions are investigated by means of spin- and angle-resolved photoelectron spectroscopy. The first part of this thesis deals with the electronic properties of three-dimensional topological insulators, which are crystals with a band gap of a semiconductor in the bulk and two-dimensional metallic states at the crystal boundaries. Intriguingly, the existence of surface states is guaranteed by a topological property of the bulk band structure. In first order approximation, topological surface states resemble a gas of helical, massless Dirac fermions which disperse linearly with the momentum and possess a finite spin polarization which is locked perpendicular to the momentum and the crystal surface. By the example of the topological insulator $PbBi_4Te_7$ it is shown, that the surface state dispersion may experience a strong hexagonal warping in the reduced symmetry of the crystal potential of a C_{3v} surface. This warping is accompanied by a finite spin polarization component along the crystal surface normal showing a three-fold oscillation along a constant energy contour of the dispersion. Another remarkable feature of the surface states in this material is that they can be buried deep beneath the crystal surface as their wave function is derived from states of primarily certain atoms in the large unit cell.

Topological surface states are robust against small perturbations. In particular, they can not be gapped out by implanting non-magnetic impurities as long as the topology of the bulk remains unchanged. In this thesis it will be illustrated that in films of the bulk topological insulator Bi_2Se_3 the surface states on either side of the films exhibit a resolvable gap for film thicknesses below six so-called quintuple layers. Related to their relatively large spatial extension, the surface states hybridize in sufficiently thin films resulting is a mass acquisition of the Dirac fermions. By means of spin-resolved measurements it could be demonstrated that the massive Dirac states show a Rashba-like spin splitting arising from the substrate-induced structural inversion asymmetry. In contrast to a classical Rashba system, here the branches of the spin-split dispersion are localized in the topmost and bottommost quintuple layer of the film and turn into the topological surface states for large film thicknesses.

Spin splittings occur in almost all trivial and topological surface states as long as a sufficiently large spin–orbit interaction is present. Whereas the spin degeneracy of electronic bulk states can only be lifted by spin–orbit interaction in crystals without inversion symmetry in the unit cell. Recently, the class of noncentrosymmetric semiconductors BiTeX with X = Cl, Br, I was discovered to feature an unusually large bulk spin splitting because of their stacked structure of charged atomic layers. Within this work, the three-dimensional dispersion of the bulk states of BiTeI and BiTeCl could directly be mapped out by means of angle-resolved photoelectron spectroscopy in the soft X-ray range. Depending on the position of the chemical

potential, the toroidal Fermi surfaces of these materials change their topology. Spin-resolved measurements show a spin texture of the Fermi torus that in first order approximation is in agreement with a three-dimensional Rashba system. Due to the absence of inversion symmetry these crystals have two different surface terminations. At these surfaces, the crystal potential evokes a staircase-like surface band bending and two-dimensional states split off from the bulk states in the potential steps. The surface states are characteristic for the different surface terminations and show a strong Rashba-type spin splitting similar to the bulk states.

In a further part of this Thesis, the photoemission-induced effects on the measured spin polarizations of photoelectrons excited from the topological surface state of Bi_2Se_3 are investigated. Recent studies demonstrated a dependence of spin texture on the orbitals admixed to the surface state by exploiting the orbital selectivity of the photoemission process. On the other hand, strong photon-energy-dependent spin interference effect were predicted for certain photoemission geometries. Within the scope of this work, similar effect were indeed observed, but they turned out to be smaller and with different characteristics than predicted.

Zusammenfassung

In dieser Dissertation wird die elektronische Struktur von Halbleiterkristallen mit starker Spin–Bahn-Kopplung vermittels spin- und winkelaufgelöster Photoelektronenspektroskopie untersucht. Der erste Teil der Arbeit befasst sich mit den elektronischen Eigenschaften von dreidimensionalen topologischen Isolatoren. Dies sind Kristalle, die in ihrem Volumen eine halbleitende Bandlücke und an den Kristallbegrenzungen metallische Oberflächenzustände aufweisen. Diese Zustände zeichnen sich dadurch aus, dass ihre Spin-Entartung aufgehoben ist und ihre Existenz von einer topologischen Eigenschaft der Volumenbandstruktur geschützt ist. In erster Näherung werden diese topologischen Oberflächenzustände durch die Dispersion helikaler, masseloser Dirac-Fermionen beschrieben. Anhand des topologischen Isolators $PbBi_4Te_7$ wird gezeigt, dass durch die reduzierte Symmetrie des Oberflächenpotentials die Dispersion der Oberflächenzustände eine starke hexagonale Deformation erfahren kann. Damit einhergehend neigt sich der Spinpolarisationsvektor aus der Ebene der Kristalloberfläche heraus und vollführt im Impulsraum entlang einer Kontur konstanter Energie eine dreifach symmetrische Oszillationsbewegung. Eine weitere bemerkenswerte Eigenschaft dieser Oberflächenzustände ist, dass sie von Zuständen bestimmter Atome in der grossen Einheitszelle abgeleitet sind und deshalb tief unterhalb der Oberfläche lokalisiert sein können.

Topologische Oberflächenzustände sind robust gegenüber kleineren Störungen; im Speziellen kann durch nicht-magnetische Fremdstoffe keine Energielücke erzeugt werden. Dies kann nur erreicht werden, wenn die Topologie der Volumenbänder verändert wird. Am Beispiel dünner Schichten des Materials Bi_2Se_3, welches als Volumenkristall ebenfalls ein topologischer Isolator ist, wird gezeigt, dass für Schichtdicken unterhalb sechs sogenannter Quintupellagen die Oberflächenzustände auf beiden Begrenzungsflächen des Schichtkristalls eine messbare Lücke aufweisen. Bedingt durch ihre relativ grosse räumliche Ausdehnung können die Zustände in genügend dünnen Schichten miteinander hybridisieren und haben in der Folge die Dispersion massiver Dirac-Teilchen. Durch spin-aufgelöste Messungen konnte eine Rashba-ähnliche Auspaltung der Oberflächenzustände nachgewiesen werden, welche durch eine vom Substrat herrührende strukturelle Inversionsasymmetrie induziert wird. Im Gegensatz zu einem Rashba-System sind in diesem Falle die Äste der spin-aufgespaltenen Dispersion aber in verschiedenen Quintupellagen lokalisiert und entwickeln sich mit zunehmender Schichtdicke zu den topologischen Oberflächenzuständen an der Ober- und Unterseite des Schichtkristalls.

Spin-Aufspaltung tritt in beinahe allen Oberflächenzuständen auf, auch in topologisch trivialen, solange eine genügend starke Spin–Bahn-Kopplung vorhanden ist. Die Spin-Entartung von elektronischen Volumenzustände hingegen kann durch Spin–Bahn-Kopplung nur in Kris-

tallen ohne Inversionsymmetrie aufgehoben werden. Unlängst wurde die Klasse von nichtzentrosymmetrischen Halbleitern BiTeX mit X = Cl, Br, I entdeckt, in denen die Spin-Aufspaltung der Volumenzustände ausserordentlich gross ist aufgrund einer aus geschichteten Lagen unterschiedlicher elektrischer Ladung aufgebauten Kristallstruktur. Durch winkelaufgelöste Photoelektronenspektroskopie mit Photonen im Bereich weicher Röntgenstrahlen konnte die dreidimensionale Dispersion der Volumenzustände von BiTeI und BiTeCl direkt abgebildet werden. Abhängig von der energetischen Lage des chemischen Potetials ändern die toroidalen Fermi-Flächen dieser Materialien ihre Topologie. Spin-augelöste Messungen zeigen eine Spin-Struktur, die der eines dreidimensionalen Rashba-Systems entspricht. Aufgrund der abwesenden Inversionsymmetrie dieser Kristalle existieren für jede Verbindung zwei mögliche Oberflächenterminierungen. Die Kristallpotentiale erfahren an den Oberflächen treppenartige Verbiegungen in deren Stufen sich zweidimensionale Zustände von den Volumenzuständen abspalten. Diese Oberflächenzustände sind charakteristisch für die jeweilige Oberfläche und zeigen ähnlich den Volumenzuständen eine starke Rashba-artige Spin-Aufspaltung.

In einem weiteren Teil dieser Arbeit wurden photoemission-induzierte Effekte auf die gemessene Spin-Polarisation von Photoelektronen aus dem topologischen Oberflächenzustand von Bi_2Se_3 untersucht. Neuere Studien zeigten, dass die Spin-Strukturen für die dem Zustand beigemischten Orbitalen verschieden sind und durch Orbitalselektion im Photoemissionprozess unterschieden werden können. Andererseits sind in bestimmten Photoemissionsgeometrien starke Spin-Interferenzeffekte in Abhängigkeit von der Photonenergie vorausgesagt worden. Im Rahmen dieser Arbeit wurden ähnliche Effekte tatsächlich beobachtet, allerdings in schwächeren Ausmass als vorausgesagt und in anderer Ausprägung.

List of acronyms

5L	quintuple layer
7L	septuple layer
ARPES	angle-resolved photoelectron spectroscopy
CD	circular dichroism
DFT	density functional theory
EDC	energy distribution curve
GGA	generalized gradient approximation
GMR	giant magneto-resistance
HRPES	high-resolution photoemission spectroscopy
IQH	integer quantum Hall
LDA	local density approximation
LDOS	local density of states
MDC	momentum distribution curve
MRAM	magnetic random access memory
PAW	projector augmented-wave
QL	quintuple layer
QSH	quantum spin Hall
SIS	Surface and Interface Spectroscopy
SLS	Swiss Light Source
STS	scanning tunneling spectroscopy
STM	scanning tunneling microscopy
SX-ARPES	soft X-ray angle-resolved photoelectron spectroscopy

TMR	tunneling magneto-resistance
TRIM	time-reversal invariant momentum
UV-ARPES	ultra-violet angle-resolved photoelectron spectroscopy
VASP	Vienna Ab-initio Simulation Package
XPD	X-ray photoelectron diffraction
XPS	X-ray photoelectron spectroscopy

Contents

1 Introduction **1**

2 Experimental and theoretical methods **5**

2.1 Angle-resolved photoelectron spectroscopy 5

2.1.1 High-resolution ultra-violet photoelectron spectroscopy 8

2.1.2 Soft X-ray angle-resolved photoelectron spectroscopy 9

2.2 Spin- and angle-resolved photoelectron spectroscopy 12

2.2.1 Spin polarization in the photoemission process 12

2.2.2 COPHEE endstation 13

2.3 Density functional theory 15

3 Spin–orbit interaction in solids **19**

3.1 Relativistic corrections to the atomic energy levels 19

3.2 Spin–orbit coupling in bulk crystals 21

3.3 Principles of the Rashba-Bychkov effect in two-dimensional electron gases . . . 24

3.4 Topological insulators 30

3.4.1 Three-dimensional topological insulators 31

3.4.2 Topologically protected surface states 34

3.4.3 Experimental studies on three-dimensional topological insulators 36

4 Spin texture of the topological surface states in $PbBi_4Te_7$ **43**

4.1 Higher order corrections in the Dirac equation 43

4.2 Effects of the elemental contribution to the topological surface state 45

4.2.1 Bulk electronic structures of Pb-based Bismuth tellurides 46

4.2.2 Surface electronic structure of $PbBi_4Te_7$ 47

4.3 Fermi surface mapping of the $PbBi_4Te_7$ topological surface state 49
4.3.1 Spin structure of the $PbBi_4Te_7$ topological surface state 53
4.4 Conclusion 55

5 Topological transition in ultra-thin Bi_2Se_3 films **57**
5.1 Bulk properties of Bi_2Se_3 58
5.2 Bi_2Se_3 at the dimensional crossover 59
5.3 Bi_2Se_3 growth on InP(111)B 61
5.4 Topological transition of ultra-thin Bi_2Se_3 films 61
5.5 Evolution of the surface state spin texture 63
5.6 Ab-initio calculation of a model system 66
5.7 Discussion 68
5.8 Conclusion 70

6 Photoemission effects in spin-resolved ARPES on Bi_2Se_3 **71**
6.1 Spin–orbital texture 71
6.2 Orbital selectivity of ARPES 72
6.3 Polarization-dependent spin-resolved ARPES 73
6.4 Photon-energy-dependent spin-resolved ARPES 74
6.5 Discussion 78

7 Bulk Rashba effect in non-centrosymmetric crystals **81**
7.1 Fermi surface mapping of BiTeI 82
7.1.1 Bulk Fermi surface 83
7.1.2 Fermi surface of the surface spectrum 87
7.1.3 Discussion 90
7.1.4 Conclusion 93
7.2 Bulk band mapping of BiTeCl 94
7.2.1 BiTeCl crystal structure 94
7.2.2 Crystal growth 95
7.2.3 Energy spectrum of the two terminations of BiTeCl(0001) 95
7.2.4 Discussion 103
7.2.5 Conclusion 104

7.3 Spin structure of BiTeCl . . . 105
7.3.1 Spin structure of the valence band of Cl-terminated BiTeCl(0001) . . . 105
7.3.2 Discussion . . . 110
7.3.3 Conclusion . . . 111
7.4 Summary . . . 112

8 Conclusions and outlook **115**

Appendices **119**

A Tight binding model of a spin–orbit coupled system **121**

B Effects of magnetism on a Rashba gas **125**

Chapter 1

Introduction

In the year 1922 Gerlach and Stern discovered that a beam of Ag atoms separates into two branches when subject to an inhomogeneous magnetic field (Fig. 1.1) [1]. Their experiment confirmed the perception of the Bohr model that the magnetic moment of an atom is directionally quantized in units of the Bohr magneton. At the time, however, it remained unrealized that the total orbital angular momentum of a Ag atom is 0 and that the experiment actually proved the existence of a magnetic moment intrinsic to the *electron*. Concealed at first by the electron spin g-factor of about 2, the observed magnetic moment was only later attributed by the works of Pauli and Dirac to a $\hbar/2$ angular momentum of the electron – the spin. [2]

Today the importance of the spin in the field of solid state physics is not only its influence on the magnetic properties of materials but in general on their electronic structure. With the aid of the relativistic and quantum-mechanical Dirac equation the spin–orbit interaction was discovered which could finally explain the electronic fine structure of the H spectrum and later was found to have an essential effect on the formation of electronic band structures in crystals. Without the presence of spin–orbit interaction, the electronic spectrum of a crystal is divided into two independent sets of states for both spin species with the same energies. Under the influence of the spin–orbit interaction, however, this degeneracy can be lifted and bands with finite spin polarizations arise. In contrast to magnetic order which results in a net spin polarization in real space, the spin–orbit interaction induces spin polarization only in the momentum space while retaining a zero magnetic moment in real space.

Spin-polarized states originated from spin–orbit interaction or ferromagnetism play an important role in the research field of spintronics which has the aim of replacing the charge with the spin as a carrier of information. Probably the first spintronic device in commercial application makes use of the fact that the resistance between two ferromagnetic layers separated by a metallic interlayer strongly depends on the relative orientation of the two layers' magnetizations – the so-called giant magneto-resistance (GMR) effect [6]. Similar devices ex-

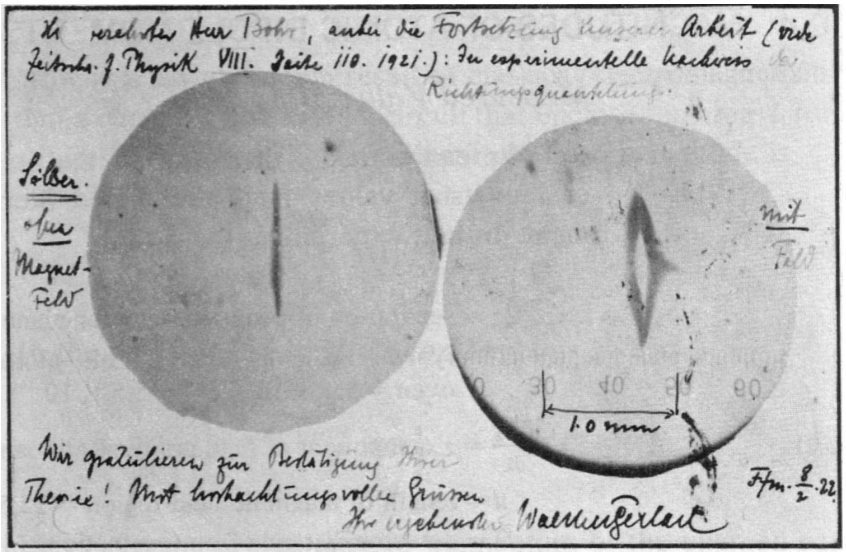

Figure 1.1: Walther Gerlach's postcard to Niels Bohr (8 February 1922): "We congratulate [you] on the confirmation of your theory." *Left photograph:* Deposited line of Ag evaporated from a collimated source. *Right photograph:* The Ag beam is split in two when passing through an inhomogeneous magnetic field. Figure adopted from Ref. [2].

ist based on the tunneling magneto-resistance (TMR) effect, where the metal in principle is replaced by an insulating layer and the tunneling probability is determined by the magnetization directions [7]. When one of the ferromagnetic layers is designed to easily switch in external magnetic fields, these devices can be employed as sensors and are in use as state-of-the-art read heads of hard discs and in novel magnetic random access memories (MRAMs) (Fig. 1.2a). While reading magnetic information is a well established technique, writing magnetic bits without external magnetic fields is a subject of ongoing research. It is known that by virtue of the spin-transfer torque exerted by spin-polarized currents, local magnetizations or magnetic domain walls can be manipulated [8]. This bears the potential for realizing novel types of shift-register-type MRAMs (Fig. 1.2b). Further, ideas exist to replace the transistor-based logic devices of today's computers with spin-based devices. The most famous concept by Datta and Das [5] describes a spin field-effect transistor (Fig. 1.2c). It exploits that spin-polarized currents injected into a material with bands of different spin polarization at the Fermi level, experience a precession of the spin polarization proportional to the traveled distance. By applying a gate voltage, the size of the spin splitting can in principle be controlled and in consequence also the precession length. By using ferromagnetic layers as spin valves before and after the gated channel, states of high and low resistance can be achieved by varying the gate voltage states.

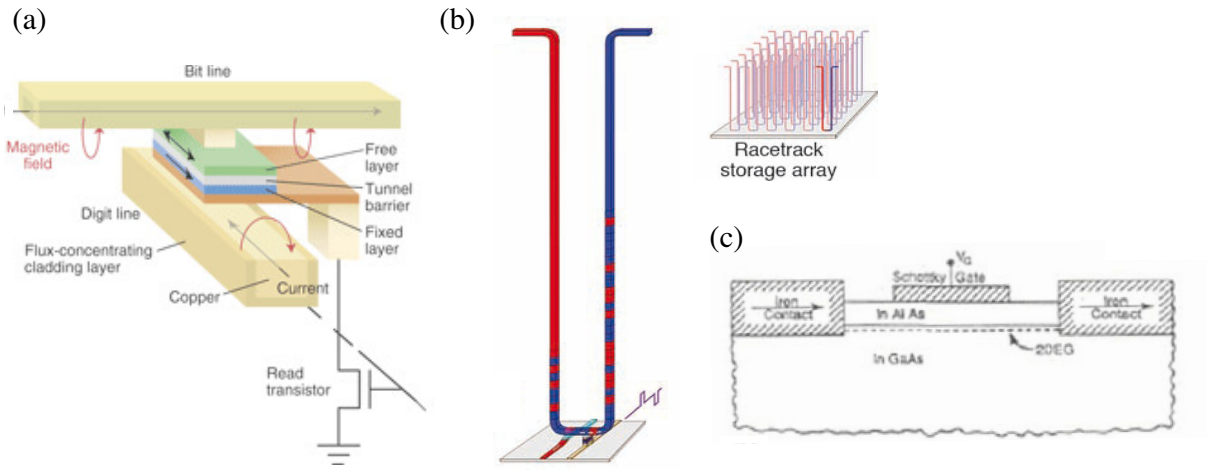

Figure 1.2: (a) Schematic of an MRAM bit. Writing is achieved by changing the magnetization of the ferromagnetic free layer by the magnetic field from currents applied through the Bit and the Digit lines. Reading is performed by measuring the TMR between the free and the fixed layer. [3] **(b)** Racetrack shift register. The process for writing and reading of the u-shaped ferromagnetic wire is conceptually the same as for the MRAM, but the magnetic domain walls of the bits can be shifted by spin-transfer torque from currents sent through the wire. [4] **(c)** Conceptual Datta-Das spin field-effect transistor based on a Rashba-split two-dimensional electron gas in a semiconductor heterostructure [5].

Spin-polarized states at the Fermi level also play an important role in the novel concepts for building quantum computers based on solid state qubits. If a material with a non-degenerate Fermi surface is brought into proximity of a superconductor, a so-called topological superconductor phase is predicted to be induced. From a theoretical point of view, in such systems excitations with the characteristics of localized Majorana fermions can engineered. A pair of separated Majorana bound states is said to form a degenerate two-level system which could serve as a non-local and thus fault-tolerant qubit. [9, 10]

In the prospect of realizing devices based on these novel concepts for spintronic and quantum computing, the hunt for materials with robust spin-polarized states was intensified. In general, spin splitting induced by spin–orbit interaction observed in the two-dimensional spectrum at the surfaces of crystals built from heavy atoms and is known as the Rashba effect [11]. Often such surface states, however, are sensitive to surface perturbations like defects or impurities and have a limited lifetime even in ultra-high vacuum conditions. Only recently it was discovered that the spin–orbit interaction can alter the band structure of semiconductor such that the existence of spin-polarized surface states is guaranteed [12, 13]. These materials are called topological insulators. While the bulk of these materials is insulating, metallic

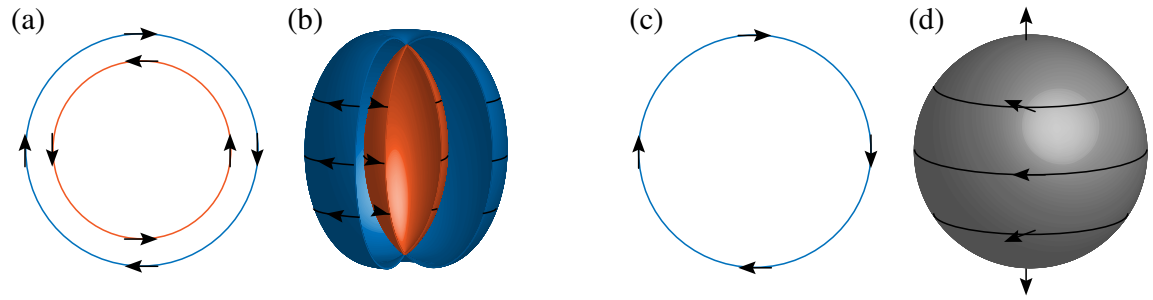

Figure 1.3: Schematic illustrations of the Fermi surfaces and spin structures of **(a)** a Rashba gas, **(b)** the three-dimensional analogon of a Rashba gas, **(c)** the surface state of a topological insulator, and **(d)** a three-dimensional Dirac state. The fundamental difference is that the topological trivial Rashba gases have an even number of spin-nondegenerate Fermi surface, in Dirac states there is only a single or an odd number of Fermi surfaces.

states at the surface cross the Fermi level and connect the valence with the conduction band. This property in principle allows for spin transport without shortcutting the currents through spin-degenerate bulk states. In this respect, semiconducting materials exhibiting the three-dimensional analogon of the Rashba effects offer an alternative approach. Here, the spin–orbit interaction splits all the bulk bands and especially the top of the valence band and the bottom of the conduction band due to an absence of inversion-symmetry in the unit cell of the crystal. Spin transport in these materials does not rely on surfaces states but is possible through the bulk of the material and is in this sense robust even though these materials are topologically trivial. Figure 1.3 illustrates the possible spin-polarized Fermi surfaces of Rashba systems and Dirac states in two and three dimensions.

In this Thesis the band and spin structure of such of bulk Rashba materials and of topological insulators are examined by various experimental techniques based on angle-resolved photoelectron spectroscopy (ARPES), introduced in Ch. 2, followed by a theoretical description of the spin–orbit interaction and its effects on the electronic structure of crystals in Ch. 3. Chapter 4 discusses the influence of the surface composition and symmetry on the electronic dispersion and spin structure of the surface state of a topological insulator. In Ch. 5 experimental data illuminates the fate of the topological surface state and its spin texture when the thickness of a topological insulator film is reduced to such a degree that it becomes an ordinary insulator. A more detailed discussion of the process of spin-resolved photoemission applied to topological insulators is given in Ch. 6. And finally, the last Chapter 7 is dedicated to the examination of the unusual Fermi surfaces and spin textures of two materials which belong to the second type of the above classes of materials and exhibit an extraordinarily large Rashba-type spin splitting in the bulk.

Chapter 2

Experimental and theoretical methods

This Chapter introduces the fundamentals of the experimental and theoretical techniques relevant for this thesis. The surface and bulk electronic structure of the examined materials were studied using ARPES in the ultra-violet and soft X-ray photon energy regime and the spin texture was measured with a spin-resolved ARPES setup based on Mott detectors. In order to compare the experimental findings with theoretical predictions, *ab-initio* band structure calculations were performed within the framework of the density functional theory (DFT).

2.1 Angle-resolved photoelectron spectroscopy

ARPES makes use of the photoelectric effect [14, 15] to experimentally study the band structures and the elementary excitation spectra of crystals, by measuring the intensity of photoemitted electrons as a function of kinetic energy and emission angle. The photoemission process is in principle an optical transition of an electronic N-body eigenstate of a finite crystal into an eigenstate of the ionized $(N-1)$-electron finite crystal, where the final state has a component propagating as a plane-wave in vacuum [16]. The description of the photoemission process based on this so-called *one-step* model is involved and subject of state-of-the-art photoemission calculations (e.g. [17]). Within the framework of the phenomenological *three-step* model of photoemission, the optical excitation of the electronic states in the bulk is considered separately from the subsequent travel of the excited electrons to the surface and the escape of the electrons into vacuum [18], as discussed in the following.

Optical excitation In this simplified model, the probability of an optical transition between an N electron initial state ψ_i^N and a final state ψ_f^N interacting with a photon field follows from

Fermi's golden rule

$$w_{fi} = \frac{2\pi}{\hbar} \, |\langle \psi_f^N | \mathcal{H}_{\text{int}} | \psi_i^N \rangle|^2 \, \delta(E_f^N - E_i^N - h\nu), \tag{2.1}$$

where E_i^N and E_f^N are the initial and final state energies of the N-particle system and $h\nu$ is the photon energy [16]. Within the so-called *dipole approximation*, the interaction with photons in the ultra-violet range is usually simplified by the Hamiltonian [16]

$$\mathcal{H}_{\text{int}} = \frac{e}{2mc} \, \boldsymbol{A} \cdot \boldsymbol{p}. \tag{2.2}$$

By applying the so-called *sudden approximation*, i.e. by assuming the sudden presence of a photo-hole, the final state can be factorized into an antisymmetric product of the one-particle photoelectron state ϕ_f and the Slater determinant of the remaining $(N-1)$-particle state, ψ_f^{N-1}. The initial state can always be written as an antisymmetric product of a one-particle state $\phi_i^{\boldsymbol{k}}$ and the antisymmetric state ψ_i^{N-1}. In this notation the experimentally accessible photoelectron intensity can be written as [16, 19]

$$\begin{aligned} I(\boldsymbol{k}, E) \sim \sum_{f,i} & f(E) \, |M_{f,i}^{\boldsymbol{k}}|^2 \, A(\boldsymbol{k}, E) \cdot \\ & \cdot \delta(\boldsymbol{k}_i - \boldsymbol{k}_f + \boldsymbol{G}) \, \delta(\varepsilon_f + E_f^{N-1} + E - E_i^N - h\nu), \end{aligned} \tag{2.3}$$

where $f(E)$ is the Fermi–Dirac distribution function. $M_{f,i}^{\boldsymbol{k}} \sim \langle \phi_f^{\boldsymbol{k}} | \boldsymbol{A} \cdot \boldsymbol{p} | \phi_i^{\boldsymbol{k}} \rangle$ are the one-electron transition matrix elements which are experimentally expressed by the dependence of the spectral intensities on the photon polarization and the scattering geometry (via $\boldsymbol{A} \cdot \boldsymbol{p}$), and the photon energy (determines the accessible final state $|\phi_f^k\rangle$) (see Ch. 6). The *one-particle spectral function* $A(\boldsymbol{k}, E)$ describes the excitation spectrum of the remaining $(N-1)$-system in non-equilibrium and it can be expressed as a Lorentzian of the electron *proper self energy* $\Sigma(\boldsymbol{k}, E) = \Sigma'(\boldsymbol{k}, E) + i\,\Sigma''(\boldsymbol{k}, E)$ [16]

$$A(\boldsymbol{k}, E) = -\frac{1}{\pi} \frac{\Sigma''(\boldsymbol{k}, E)}{[E - \varepsilon_i - \Sigma'(\boldsymbol{k}, E)]^2 + [\Sigma''(\boldsymbol{k}, E)]^2}. \tag{2.4}$$

In non-correlated systems ($|\Sigma(\boldsymbol{k}, E)| \to 0$) the spectral function becomes a δ function in energy and the observed quasiparticle energies reflect the energy of the initial one-electron ground state ε_i. Whereas in the case of correlated systems the quasiparticle energy is renormalized and the states experience an energy broadening (finite lifetime) due to interactions, such as electron–electron, electron–phonon or electron–magnon interactions [19].

Surface transmission After the transport to the surface, as a third step in the model, the photoelectron is transmitted through the surface. In an ARPES experiment, the intensity of the photoelectrons is measured as a function of the kinetic energy E_{kin} and the emission angle

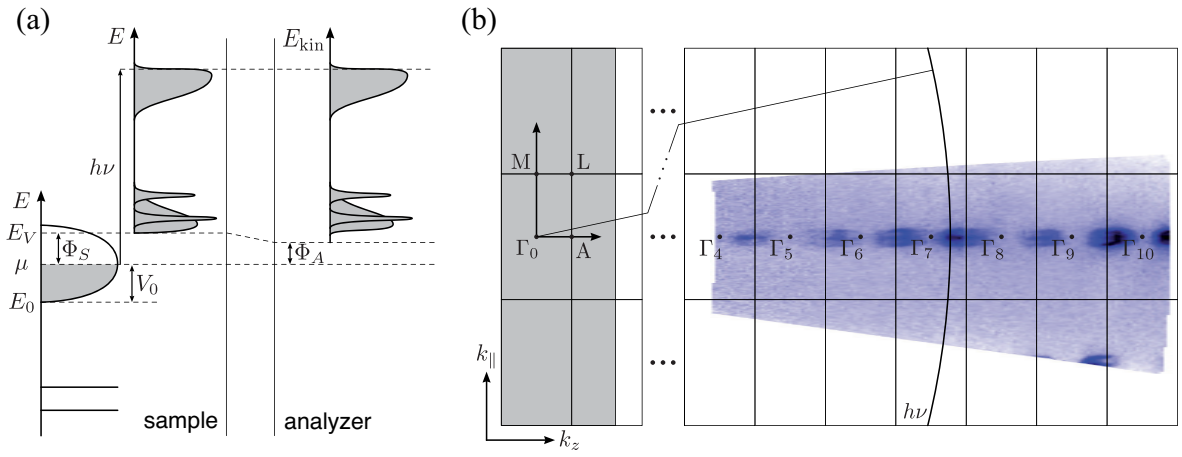

Figure 2.1: **(a)** Energy conservation in the photoemission process. Figure adapted from Refs. [16, 18]. **(b)** Momentum conservation in the free-electron final state approximation. An optical transition is allowed if the initial state (represented by the blue Fermi surface map) and the free-electron final state (circular arc) are separated by $h\nu$ in energy, and the momentum is conserved (i.e. initial and final state overlap in momentum space). Varying the photon energy (changing the arc radius) probes different k_z and allows to map the out-of-plane dispersion.

ϑ, from which the quasiparticle dispersion can be obtained. The binding energy ε measured with respect to the chemical potential μ is obtained from the photoelectron kinetic energy by [16, 18]

$$\varepsilon = h\nu - \Phi_A - E_{kin}. \tag{2.5}$$

As the chemical potential of the sample and the analyzer are at the same energy, the kinetic energy is measured with respect to the vacuum level E_V in the analyzer. Consequently, only the work function of the analyzer Φ_A is relevant in the above equation, while changes in sample work function do not affect the measured kinetic energy (Fig. 2.1a).

The momentum of the photoelectron can be obtained from its kinetic energy and the emission angles. As the photon wave vectors in the ultra-violet range are small compared to typical Brillouin zone extensions, the momentum transfer from the photons to the photoelectrons is usually negligible. Because of the translational symmetry along the surface, the Bloch wave functions and the photoelectron plane wave need to meet matching phase conditions. Analogously to Snell's law, it follows that the in-plane momentum is conserved and the Bloch momentum parallel to the surface is given by [16, 18]

$$k_{\parallel} = \sqrt{\frac{2m}{\hbar} E_{kin}}\ \sin\vartheta. \tag{2.6}$$

The momentum of a two-dimensional state at the surface of a crystal is is fully determined by the above equation, as the out-of-plane momentum k_z is not a good quantum number due to the state's finite extension along the surface normal. Three-dimensional states, on the other side, possess a well-defined k_z. For the determination of their out-of-plane momentum additional assumptions are necessary, due to the broken translational symmetry along the crystal surface normal. By presuming a free-electron final state with dispersion

$$E_f(\boldsymbol{k}) = \frac{\hbar^2(\boldsymbol{k}_\parallel^2 + k_z^2)}{2m} - E_0, \tag{2.7}$$

where E_0 correspond roughly to the bottom of the valence band (cf. Fig. 2.1a), one obtains

$$k_z = \sqrt{\frac{2m}{\hbar}(E_{kin}\cos\vartheta + V_0 + \Phi_A)}, \tag{2.8}$$

since $E_f = E_{kin} + \Phi_A$ [16]. V_0 is the *inner potential* acounting for the potential step along the surface normal. Figure 2.1b displays a bulk Fermi surface map of BiTeI (see Sect. 7.1) backcalculated into the $(k_\parallel, k_z)$ space using the free-electron final state approximation with $V_0 = 0\,\text{eV}$. The inner potential is obtained by fitting the experimentally measured k_z periodicity to the extension of the Brillouin zone along the z direction. Alternatively, the ARPES photon energy scan can be Fourier transformed along k_z for different values of the inner potential. At the correct inner potential the periodicity of the intensity variations matches the lattice parameter (Fig. 2.2).

2.1.1 High-resolution ultra-violet photoelectron spectroscopy

Most of the ultra-violet angle-resolved photoelectron spectroscopy (UV-ARPES) measurements shown in the course of this Thesis were performed at the high-resolution photoemission spectroscopy (HRPES) endstation of the Surface and Interface Spectroscopy (SIS) beamline at the Swiss Light Source (SLS) (geometry illustrated in Fig. 2.3a). At this endstation the energy and angular mapping of the photoelectron current is achieved by a VG SCIENTA R4000 analyzer with a total angular acceptance of 30 degrees. The alignment of the sample is performed by a six-axis CARVING manipulator equipped with a cryostat that allows for sample temperatures from 15 K to room temperature. The SIS beamline provides photons with energies ranging from 20 to 800 eV with linear s and p, and circular $C+$ and $C-$ polarization. In a typical ARPES experiment the overall energy and angle resolution is $\sim 15\,\text{meV}$ and $0.1\,^\circ$, respectively.

Mapping of the out-of-plane dispersion of three-dimensional initial states with UV-ARPES has proven to be problematic [20,21]. On the one hand, the photoelectron kinetic energies are close to the minimum of the universal curve for the inelastic mean free path λ of the electron

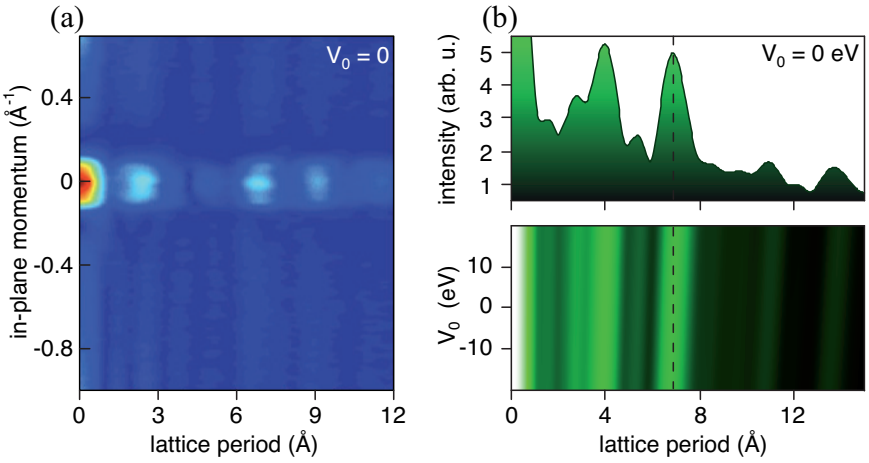

Figure 2.2: **(a)** Fourier transform of the BiTeI Fermi surface Fig. 2.1b for the inner potential $V_0 = 0\,\text{eV}$. **(b)** Absolute value of the Fourier transform along k_z of the BiTeI Fermi surface, summed up over the entire measured in-plane momentum and binding energy range. The dashed line indicates the out-of-plane lattice parameter of BiTeI $c = 6.854\,\text{Å}^{-1}$. **(c)** Same as (b) for various inner potentials. The peak corresponding to the lattice periodicity matches the lattice parameter c at $V_0 = 0\,\text{eV}$.

in solids (Fig. 2.4a). Meaning that the probing depth is low which results in a large uncertainty on the out-of-plane momentum $\Delta k_z \sim \lambda^{-1}$ (Fig. 2.4b). Together with the non-linear dispersion of the final state this can lead to a significant distortion of the photoemission intensity profile and in the worst case fully hide the initial state dispersion. On the other hand, the relatively low photon energies populate final states whose dispersions are still significantly affected by the crystal potential and can only be roughly approximated by free-electron dispersions. In general even more than one final state is accessible by the excitation. In consequence, the transition matrix elements can be complicated, leading to strong variations of the measured photoelectron intensity. Further, the above approximation (Eq. 2.8) for obtaining the k_z value is problematic, as the value for the inner potential may vary quickly depending on the final state energy and the in-plane momentum. [20]

The effects of the mentioned problems can be attenuated by increasing the photon energy to the soft X-ray or even hard X-ray regime, as will be discussed in the following section.

2.1.2 Soft X-ray angle-resolved photoelectron spectroscopy

The SX-ARPES endstation at the ADRESS beamline of the SLS is an ARPES endstation optimized for photon energies in the soft X-ray regime between 300–1600 eV equipped with a PHOIBOS-150 analyzer and a CARVING manipulator [23]. At these photon energies, the

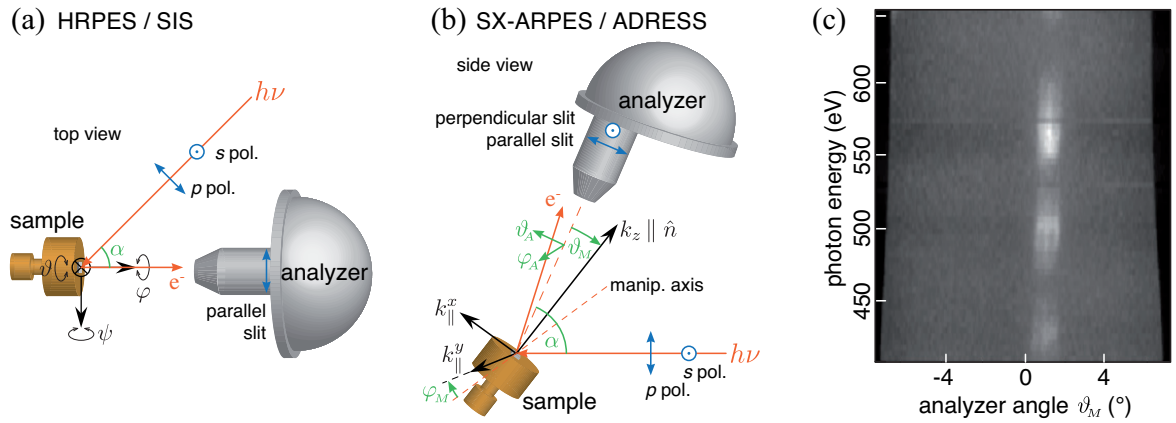

Figure 2.3: (a) UV-ARPES geometry at the SIS beamline ($\alpha = 45\,^\circ$). **(b)** SX-ARPES geometry at the ADRESS beamline with definitions of the manipulator angle ϑ_M, φ_M and the analyzer angles ϑ_A, φ_A ($\alpha = 70\,^\circ$) [22]. **(c)** Raw data of the BiTeI Fermi surface. The photon momentum transfer manifests itself in the shift towards higher analyzer angles with increasing photon energies.

photoexcitation cross sections of valence bands and core levels are reduced by several orders of magnitude with respect to the ultra-violet photon energies below 100 eV [22]. This drawback is compensated with a high photon flux of 10^{13} photons s^{-1} at 1 keV at a beam spot size of $10 \times 75\,\mu\text{m}^2$. The total cross section is further increased by a small incidence angle of the photon beam on the sample ($90\,^\circ - \alpha = 20\,^\circ$), such that the number of excited electrons within the escape depth from the surface is raised [22] (see Fig. 2.3b). Along with the increased flux, the energy resolution of the beamline is compromised and as the count rate is increased by a larger pass energy of the analyzer, the overall energy resolution in SX-ARPES is roughly one order of magnitude larger compared to typical high-resolution ARPES in the ultra-violet regime (energy and angular resolution ~ 100 meV, $0.07\,^\circ$). In addition, the photoelectrons experience an enhanced phonon scattering cross–section (increased Debye–Waller factor), which necessitates cooling of the sample to suppress the resulting incoherent background [22].

Apart from these handicaps, there are several fundamental advantages of SX-ARPES measurements when compared to conventional UV-ARPES (following Ref. [22]): *(i)* The higher kinetic energies of the photoelectrons result in larger escape depths λ (Fig. 2.4a), which in turn increases the sensitivity for bulk states and buried states. *(ii)* Along with the increased damping distance λ of the final state into the crystal, the k_z uncertainty, caused by finite probing depth, is reduced ($\Delta k_z = \lambda^{-1}$) (Fig. 2.4b) [20]. On top, due to its high energy, the final state becomes more free-electron-like. Together with the enhanced k_z resolution this simplifies the determination of the k_z value in the photoemission process (cf. Eq. 2.8) and

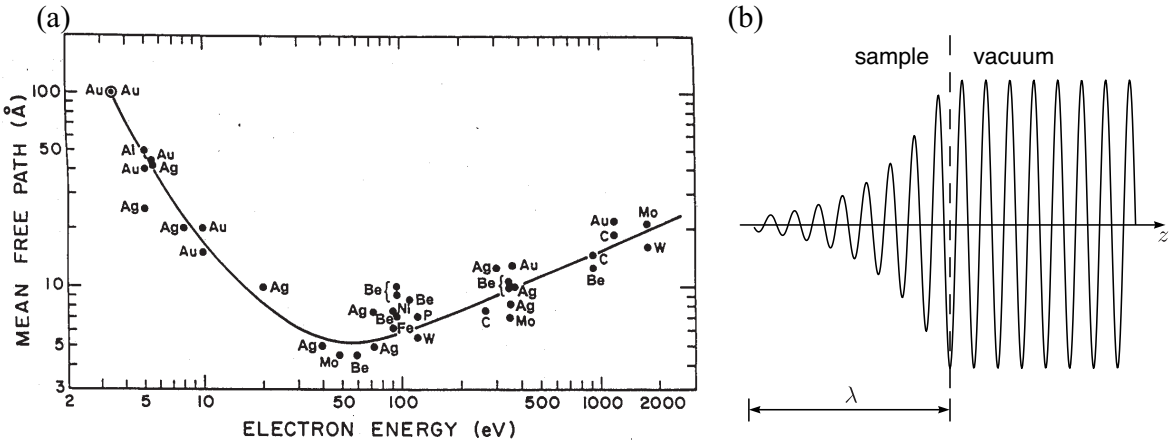

Figure 2.4: (a) Universal curve of the electron inelastic mean free path in solids (taken from Ref. [24]). **(b)** The photoemission final state decays into the sample bulk within a distance λ in the order of the inelastic mean free path

facilitates the study of three-dimensional states. *(iii)* The photoemission matrix elements are simplified and the angular dependence of the experimental intensity becomes similar to the X-ray photoelectron diffraction (XPD) pattern of core levels [25] while the energy dependence approaches the pure spectral function. *(iv)* Resonant photoemission allows element-specific enhancement of spectral features.

In sum, SX-ARPES is an ideal tool to study the electronic structure of three-dimensional materials, at cost of a slightly worse resolution and a higher measurement time when compared to state-of-the-art UV-ARPES stations.

Momentum correction Unlike in UV-ARPES, the photon momentum transferred to the photoelectron is not negligible for photons with energies between 300–1000 eV. The absolute value of the photon wave vector is 0.1–0.5 Å^{-1} and is thus comparable to typical Brillouin zone extensions. The photoelectron momentum is altered according to the exact geometry of the scattering process and depends on the photon energy. In the case of the SX-ARPES endstation at the ADRESS beamline, most of the photon momentum is transferred to the photoelectron's in-plane component in the scattering plane (along the analyzer slit) due to the grazing incidence angle (see Fig. 2.3b,c). Within the framework of the three-step model with free-electron

final states, the photoelectron momenta before leaving the crystal bulk are obtained by

$$\begin{aligned} k_{\parallel}^{x} &= +\sqrt{\frac{2m}{\hbar}E_{kin}}\ \sin(\vartheta_M+\vartheta_A) - \frac{h\nu}{\hbar c}\ \sin(\alpha-\vartheta_M) \\ k_{\parallel}^{y} &= -\sqrt{\frac{2m}{\hbar}E_{kin}}\ \sin(\varphi_M+\varphi_A) - \frac{h\nu}{\hbar c}\ \cos(\alpha-\vartheta_M)\ \sin(\varphi_M) \\ k_z &= \sqrt{\frac{2m}{\hbar}(E_{kin}+V_0+\Phi_A) - \boldsymbol{k}_{\parallel}^2} + \frac{h\nu}{\hbar c}\cos(\alpha-\vartheta_M), \end{aligned} \tag{2.9}$$

where ϑ_M is the angle between the true sample normal $\hat{n}$ and the optical axis of the analyzer lens, φ_M is the tilt angle, and ϑ_A, φ_A are the angles between the photoelectron momentum and the analyzer lens along the slit as defined in Fig. 2.3b. The analyzer slit orientation is selectable; for the measurements shown in this Thesis the slit orientation was parallel to the scattering plane ($\varphi_A = 0$).

2.2 Spin- and angle-resolved photoelectron spectroscopy

2.2.1 Spin polarization in the photoemission process

Since photons do not directly interact with the spin degree of freedom (cf. Hamiltonian 2.2), the spin is, in principle, conserved in the photoemission process and the photoelectron spin polarization reflects the spin polarization of the initial state [26]. However, a variety of effects is known to induce, reduce or reorient the spin polarization of the photoelectrons compared to the initial state [19, 27–34]. On the one hand, the spectral function $A(\boldsymbol{k}, E)$ in Eq. (2.3) can incorporate spin-dependent quasiparticle renormalization in materials with strong electron correlation [19]. In ferromagnetic materials, spin-filter effects can lead to a photoelectron transport to the surface different for the two spin species [19]. On the other hand, if spin–orbit interaction is present, the matrix elements $M_{f,i}^{\boldsymbol{k}}$ in Eq. (2.3) can lead to spin-dependent transition probabilities due to the optical selection rules regarding the total angular momentum. In particular, circularly polarized light is known to produce highly spin-polarized photoelectrons even from unpolarized initial states [35, 36]. But also linearly polarized or unpolarized light can induce spin polarization in the presence of spin–orbit interaction, caused by the scattering geometry, photoelectron phase shifts, finite probing depth and other [27, 37]. Even in the absence of the above mentioned photoemission final state effects, the spin polarization of photoelectrons originating from spin-polarized initial states depends on the photoemission matrix elements. Since the initial state is generally a superposition of different orbitals which are locked to different spin orientations via spin–orbit interaction, the orbital selectivity of an ARPES experiment directly affects the measured photoelectron spin polarization [28–31]. This kind of initial state photoemission effects on the photoelectron spin polarization will be discussed in more detail in Ch. 6.

2.2.2 COPHEE endstation

The spin-resolved ARPES measurements shown in this Thesis were performed at the COPHEE endstation of the SIS beamline [38,39]. Like in a conventional ARPES experiment, monochromatic photons impinge on a crystalline sample and excite a photocurrent characterized by emission angle, kinetic energy, and spin polarization. The spin polarization of an electronic state or an ensemble of states is a vector with the normalized spin expectation values along the spatial directions as components

$$\boldsymbol{P} = \frac{2}{\hbar}(\langle S_x \rangle, \langle S_y \rangle, \langle S_z \rangle). \tag{2.10}$$

While measuring the polarization with a Stern-Gerlach-type of spin separation [1] is in principle possible also for electron beams [40], an experimental realization is unfeasible, due to the Lorentz force acting on the charged electron [41]. Instead, the COPHEE endstation makes use of the spin sensitivity of *Mott scattering* [42].

Mott detectors In a spin-resolved ARPES measurement at COPHEE, the photoelectrons are angle-selected by a CARVING manipulator and energy-filtered by a hemispherical analyzer (Omicron EA125) and subsequently either directly counted by channeltrons for spin-integrated measurements or directed via a system of electrostatic lenses towards the spin detectors. In the so-called *Mott detectors* the electrons are accelerated to 40 keV and impinge on a gold foil. In the Coulomb potential of the gold nuclei the scattering electrons acquire an angular momentum which couples via spin–orbit interaction to the magnetic moment of the electron. As a consequence, the differential cross-section (spatial scattering probability) is dependent on the orientation of the spin polarization of the electrons. This phenomenon is known as Mott scattering. In the case of the COPHEE Mott detectors, for each spin channel two semiconductor-based detectors count the intensity of the elastically backscattered electrons N_R, N_L in a plane with the gold surface normal, at $\pm 60^\circ$ from the latter. The asymmetry $A_\perp$ of the measured intensities is proportional to the spatial component of the spin polarization $P_\perp$ perpendicular to the scattering plane

$$P_\perp = \frac{A_\perp}{S} = \frac{1}{S}\frac{N_L - \eta N_R}{N_L + \eta N_R}, \tag{2.11}$$

where S is the so called *Sherman function* which is equal to the asymmetry measured for fully spin-polarized electrons, i.e. for $P_\perp = 1$. The Sherman function depends on the details of the scattering process such as electron energy, scattering geometry and the integrated solid angle. The parameter η accounts for the naturally occuring differences in the detector sensitivities. This so-called sensfactor is specific to a pair of detectors and is used in practice to calibrate the

asymmetry to be zero at points of expectedly vanishing polarization, e.g. based on symmetry considerations (cf. Sect. 3.2).

The overall efficiency of a polarimeter can be judged from the figure of merit $f = (I/I_0)\,S^2$ where I/I_0 is the ratio of detected electrons to the total number of incoming electrons [39]. The statistical error on the asymmetry can be found as $\Delta A_\perp = 1/\sqrt{N_L + N_R}$. Thus, for a given number I_0 of incoming electrons the statistical error of the polarization is given by $\Delta P_\perp = 1/\sqrt{f\,I_0}$ [39]. Because of the low cross-section for elastic scattering of the electrons in the gold foil, the Mott detector's figure of merit is in the order of $f = 10^{-4}$. Therefore, in a typical spin-resolved ARPES measurement the number of counts is raised by increasing the pass energy and the analyzer aperture which results in an energy resolution and angular acceptance of 80 meV and $\pm 1\,^\circ$, respectively.

The COPHEE polarimeter is capable of measuring four components of the spin polarization vector with two orthogonal detector units into which the electrons are alternatingly deflected by an electrostatic lens. Each detector unit consists out of a gold foil and two orthogonally arranged pairs of detectors (Fig. 2.5a,c). The z component is determined redundantly and usually the statistical average is taken into account for further processing (Eq. 2.12).

For the transformation of the spin polarization vector measured in the coordinate frame of the Mott detectors (spanned by the normals of the scattering planes of the four detector pairs) into the sample frame, the orientation of the manipulator needs to be incorporated. The conversion consists of three rotations about Euler angles: *(i)* azimuthal rotation about the analyzer lens axis by $45\,^\circ$, *(ii)* rotation by ϑ ("polar" angle) about the primary axis of the manipulator, *(iii)* rotation by ψ (tilt angle) about the secondary axis of the manipulator (Fig. 2.5b). Thus, the polarization vector in the sample frame relates to the asymmetries in the Mott frame by an orthogonal matrix T

$$(P_x, P_y, P_z) = T\,(\tfrac{1}{S_R}\,A_x, \tfrac{1}{S_L}\,A_y, \tfrac{2}{S_R+S_L}\,A_z) \tag{2.12}$$

with

$$T = \frac{1}{\sqrt{2}} \begin{pmatrix} \cos\vartheta & -\cos\vartheta & \sqrt{2}\sin\vartheta \\ \cos\psi - \sin\vartheta\sin\psi & \cos\psi + \sin\vartheta\sin\psi & \sqrt{2}\cos\vartheta\sin\psi \\ -\sin\psi - \sin\vartheta\cos\psi & -\sin\psi + \sin\vartheta\cos\psi & \sqrt{2}\cos\vartheta\cos\psi \end{pmatrix}, \tag{2.13}$$

where S_L, S_R are the Sherman functions of the left and right Mott detector pairs[1].

Data analysis A spin-resolved ARPES measurement is typically performed as a line scan with a single sweep parameter; either the binding energy ε or the momentum $\boldsymbol{k}$ (corresponding to ϑ or ψ photoelectron emission angles). The data set consists of the total intensity $I(\varepsilon, \boldsymbol{k})$

[1] Throughout the work described in this Thesis the Sherman functions $S_L = S_R = 6.8\,\%$ were used.

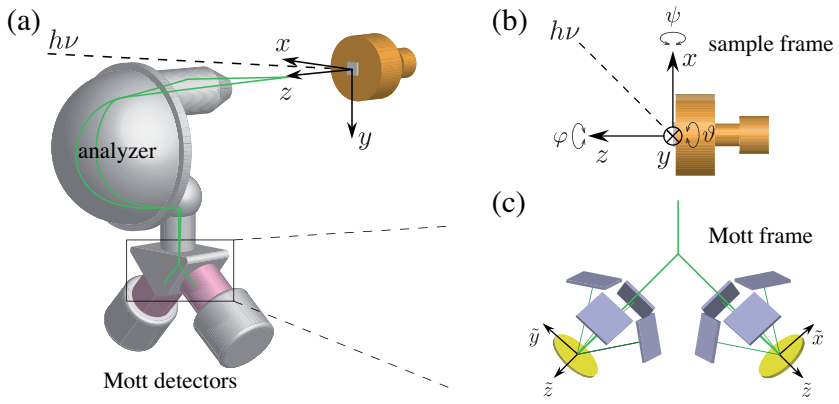

Figure 2.5: **(a)** Geometrical setup of COPHEE. **(b)** Coordinate system in the sample frame. **(c)** Schematic illustration of the Mott detector geometry and coordinate system defined in the Mott frame.

summing up the intensities of all channels of the Mott detectors, and the three components of the spin polarization vector $\boldsymbol{P}(\varepsilon, \boldsymbol{k})$.

Because of the intrinsic band broadening but mainly due the finite experimental resolution, the assignment of a spin polarization to individual bands contributing to the measured spectral intensity, demands a fitting procedure that simultaneously incorporates the total intensity and the spin polarization [44, 45]. The total intensity is modeled by the sum of a non-spin-polarized background $B(\varepsilon, \boldsymbol{k})$ and a set of peaks of Gaussian, Lorentzian or other shape $I^i(\varepsilon, \boldsymbol{k})$

$$I(\varepsilon, \boldsymbol{k}) = \sum_i I^i(\varepsilon, \boldsymbol{k}) + B(\varepsilon, \boldsymbol{k}). \tag{2.14}$$

To each band i a polarization vector $\boldsymbol{P}^i$ is assigned whose length and orientation are fit parameters. The measured polarization is then modeled by the sum of the $\boldsymbol{P}^i$ weighted by the peak shapes and normalized by the total intensity

$$\boldsymbol{P}(\varepsilon, \boldsymbol{k}) = \frac{\sum_i \boldsymbol{P}^i\, I^i(\varepsilon, \boldsymbol{k})}{I(\varepsilon, \boldsymbol{k})}. \tag{2.15}$$

An example of the result of a simultaneous fit of $I(\boldsymbol{k}_\parallel)$ and $\boldsymbol{P}(\boldsymbol{k}_\parallel)$ of a spin-resolved MDC at the Fermi level of Bi_2Se_3 is shown in Fig. 2.6. A more detailed description of the analysis process can be found in Refs. [44–46].

2.3 Density functional theory

Theoretical calculations of the physical properties of materials not only help in the understanding of experimental data, but are also a guidance in the hunt for materials with novel

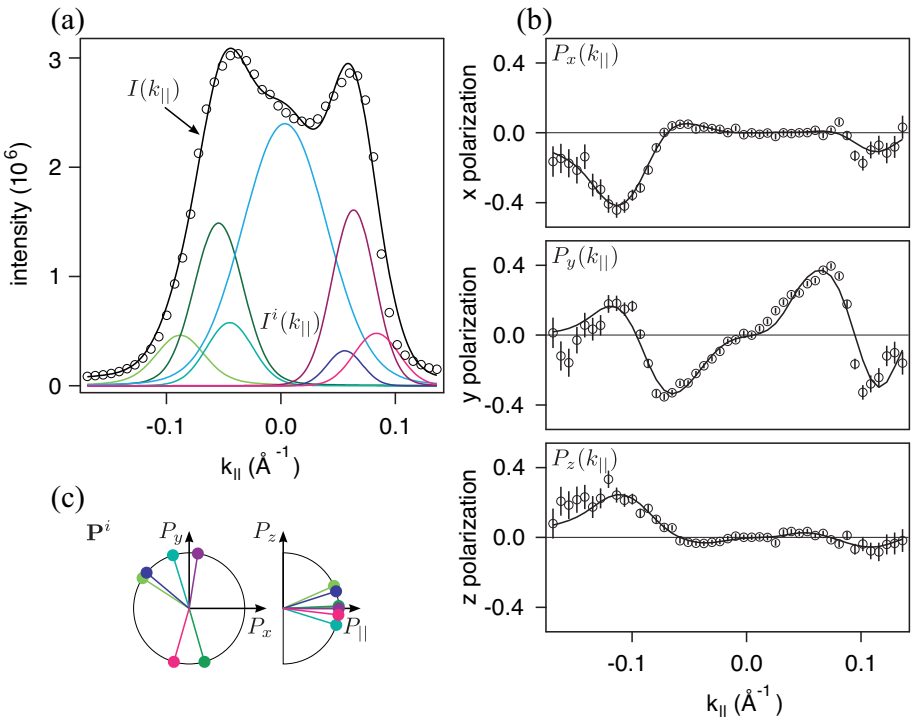

Figure 2.6: Spin-resolved MDC at the Fermi level of aged Bi_2Se_3 cutting through the topological surface state and the Rashba-split valence band quantum well states. **(a)** Measured ($\circ$) and fitted ($-$) total intensity and fitted peaks (colored). **(b)** Measured ($\circ$) and fitted ($-$) components of the polarization vector in the sample frame. **(c)** Spin polarization vectors of the individual peaks plotted; inplane (left) and out-of-plane (right) components are plotted separately. Figures adopted from data of Ref. [43].

physical properties. In this Thesis the band and spin structures were calculated within the framework of the so-called density functional theory (DFT) by the group of E. V. Chulkov. In the context of DFT, the intrinsic complexity of exactly solving the Schrödinger equation of an interacting many-body system can be effectively reduced. DFT is based on the *Hohenberg-Kohn* theorem [47] stating that *(i)* any observable of a many-electron system in the ground state is a unique functional of the ground state electron density $n(\boldsymbol{r})$ and *(ii)* the ground state energy is equal to the minimum of the energy functional. The energy functional of Coulomb-interacting electrons (second term in Eq. 2.16) in an external potential $v(\boldsymbol{r})$ (first term in Eq. 2.16) in the *Born-Oppenheimer approximation* can be written as (spin neglected)

$$E_v[n] = \int \mathrm{d}\boldsymbol{r}\, v(\boldsymbol{r})n(\boldsymbol{r}) + \frac{1}{2}\int \mathrm{d}\boldsymbol{r}\mathrm{d}\boldsymbol{r}'\, \frac{n(\boldsymbol{r})n(\boldsymbol{r}')}{|\boldsymbol{r}-\boldsymbol{r}'|} + (T_s[n] + E_{xc}[n]), \tag{2.16}$$

where $T_s[n]$ is the kinetic energy of a system of non-interacting electrons and $E_{xc}[n]$ is the exchange–correlation energy of the interacting system. For the latter, one can give no exact

expression for general $n(\boldsymbol{r})$. But it can be shown [48] that the *many-electron* density is equal to the *Kohn-Sham* density defined by

$$n(\boldsymbol{r}) = \sum_{i=1}^{N} |\psi_i(\boldsymbol{r})|^2 \tag{2.17}$$

where the Kohn-Sham functions ψ_i are the solutions of the *one-electron* Schrödinger equations (in atomic units)

$$\left(-\frac{1}{2}\nabla^2 + v(\boldsymbol{r}) + \int \mathrm{d}\boldsymbol{r}' \, \frac{n(\boldsymbol{r}')}{|\boldsymbol{r} - \boldsymbol{r}'|} + V_{xc}\right) \psi_i = \varepsilon_i \psi_i, \tag{2.18}$$

with the exchange–correlation potential $V_{xc}(n(\boldsymbol{r})) = \delta E_{xc}/\delta n$. The many-electron density can be much more efficiently calculated by self-consistently solving the one-electron Kohn-Sham equations (2.17) and (2.18). From the density then follow the properties of the many-electron system via the Hohenberg-Kohn theorem.

The general solution of V_{xc} is an unsolved problem and it is thus usually replaced with the local density approximation (LDA) where the electron density is assumed to be constant within infinitesimal volume elements [49]. In the DFT calculations included in this Thesis, the exchange–correlation potential additionally incorporates a gradient term according the generalized gradient approximation (GGA) [50] as implemented in the Vienna Ab-initio Simulation Package (VASP) [51]. The interaction between the ion cores and the valence electrons are described by the projector augmented-wave (PAW) method [52, 53]. The Hamiltonians include scalar relativistic corrections, and the spin–orbit coupling is taken into account by the second variation method [54].

The atom-resolved spin structures of the topological states shown in Ch. 4 were obtained by both VASP and fully relativistic multiple-scattering calculations (layer Korringa–Kohn–Rostoker method) [55,56]. In the latter case, the Dirac equation is solved from first principles. Experimental lattice parameters were used for the calculation of all the compounds discussed within the Thesis.

Chapter 3

Spin–orbit interaction in solids

This Chapter describes how the electronic states of crystals can be spin-polarized in the presence of spin–orbit interaction. Starting off at the *Dirac equation*, the relativistic corrections to electronic spectrum of the hydrogen atom will be discussed and linked to the band structures of crystals. It will be shown that the spin–orbit interaction is responsible for the lifting of the spin degeneracy of states lacking inversion symmetry. In addition, the effect of the spin–orbit coupling on the band structure may lead to a new phase of matter. In the context of these so-called topological insulators the Dirac equation once more becomes important.

3.1 Relativistic corrections to the atomic energy levels

The Dirac equation of a charged spin-half particle in a central Coulomb potential $\varphi(r)$ (with vector potential $\boldsymbol{A}(\boldsymbol{r},t)=0$) is given by

$$\left(i\hbar\,\frac{\partial}{\partial t}-c\,\boldsymbol{\alpha}\cdot\boldsymbol{p}-mc^2\,\beta-V\right)\boldsymbol{\psi}=0, \tag{3.1}$$

where $\boldsymbol{p}$ is the momentum operator, m the particle rest mass, $V=e\varphi(r)$ the potential energy operator, and β and $\boldsymbol{\alpha}$ are 4×4 matrices defined by $\beta=\begin{bmatrix}\mathbb{1} & 0\\ 0 & -\mathbb{1}\end{bmatrix}$ and $\boldsymbol{\alpha}=\begin{bmatrix}0 & \boldsymbol{\sigma}\\ \boldsymbol{\sigma} & 0\end{bmatrix}$, with $\mathbb{1}$ designating the unity matrix and the components of $\boldsymbol{\sigma}=(\sigma_x,\sigma_y,\sigma_z)$ being the Pauli matrices in standard definition [57]. The relevance of the Dirac equation originates from its compatibility with special relativity and quantum mechanics, the introduction of halfinteger spins, and the description of antiparticles. In the case of free particles ($V=0$), the energy eigenvalues of the time-independent Dirac equation are given by the well known relativistic energy–momentum relation for particles ($+$) and antiparticles ($-$)

$$E=\pm\sqrt{m^2c^4+p^2c^2}. \tag{3.2}$$

For electrons in the strong Coulomb potential of atomic nuclei in free atoms, molecules or in solid state materials, the Dirac equation explains the fine structure of the electronic spectrum, as it introduces sizeable relativistic corrections. By expressing the Dirac equation (3.1) in two-component wave functions $\boldsymbol{\psi} = (\boldsymbol{\psi}_1, \boldsymbol{\psi}_2)$ and solving for the positive energy part $\boldsymbol{\psi}_1$ with the replacement $E' = E - mc^2$, the Dirac equation for a hydrogen-like atom can be approximated with the following Schrödinger equation [57,58]:

$$E'\boldsymbol{\psi}_1 = \mathcal{H}\boldsymbol{\psi}_1 \tag{3.3}$$

$$\mathcal{H} = \underbrace{\frac{\boldsymbol{p}^2}{2m} + V}_{\text{non-relat.}} \quad \underbrace{-\frac{\boldsymbol{p}^4}{8m^3c^2}}_{\text{mass correction}} \quad \underbrace{-\frac{\hbar^2}{8m^2c^2}\frac{dV}{dr}\frac{\partial}{\partial r}}_{\text{Darwin term}} \underbrace{+\frac{1}{2m^2c^2}\frac{1}{r}\frac{dV}{dr}\boldsymbol{L}\cdot\boldsymbol{S}}_{\text{spin–orbit interaction}} \tag{3.4}$$

where $\boldsymbol{L} = \boldsymbol{x} \times \boldsymbol{p}$ and $\boldsymbol{S} = \frac{1}{2}\hbar\boldsymbol{\sigma}$ are the orbital momentum and the spin operator, respectively. The first two terms on the right side of Eq. (3.4) are the non-relativistic Schrödinger equation, followed by the relativistic mass correction. The fourth term is the so-called *Darwin term* which arises in the vicinity of the nucleus due to zitterbewegung of the electron. The last term finally describes the *spin–orbit interaction*. In a heuristic picture, the electron orbits in the central Coulomb field $\boldsymbol{E}$ which partly transforms into a magnetic field $\boldsymbol{B}$ in the rest frame of the electron $\boldsymbol{B} \sim \boldsymbol{E} \times \boldsymbol{v} \sim \boldsymbol{x} \times \boldsymbol{p} = \boldsymbol{L}$. The magnetic moment of the electron $\boldsymbol{\mu} \approx \frac{e\boldsymbol{S}}{m}$ couples to this magnetic field $\mathcal{H}_{LS} = -\boldsymbol{\mu}\cdot\boldsymbol{B} \sim \boldsymbol{L}\cdot\boldsymbol{S}$ giving rise to the mentioned spin–orbit term. [58]
Since $\boldsymbol{S}\cdot\boldsymbol{L} = \frac{1}{2}(\boldsymbol{J}^2 - \boldsymbol{L}^2 - \boldsymbol{S}^2)$ where $\boldsymbol{J} = \boldsymbol{L} + \boldsymbol{S}$ is the total angular momentum operator, the eigenfunctions of the Schrödinger equation can not be expressed as a product of eigenstates of the angular momentum and spin operator $|l, m_l\rangle|\uparrow\rangle$ and $|l, m_l\rangle|\downarrow\rangle$, respectively, as in the non-relativistic case, because L_z does no longer commute with the Hamiltonian. The new set of quantum numbers is $\boldsymbol{J}^2, \boldsymbol{L}^2, \boldsymbol{S}^2, J_z$; in particular the z component of the spin is no longer a good quantum number. In fact, the eigenstates of the Hamiltonian are superpositions of both spin states with the *Clebsch-Gordan-Coefficients* as mixing factors [58,59]:

$$|j = l \pm \tfrac{1}{2}, m_j, l\rangle = \pm\sqrt{\frac{l \pm m_j + \frac{1}{2}}{2l+1}}|l, m_j - \tfrac{1}{2}\rangle|\uparrow\rangle \tag{3.5}$$

$$+\sqrt{\frac{l \mp m_j + \frac{1}{2}}{2l+1}}|l, m_j + \tfrac{1}{2}\rangle|\downarrow\rangle. \tag{3.6}$$

In first order perturbation theory the mentioned relativistic corrections lead to a j-dependent energy shift of [58]

$$\Delta E_{n,j,l} = \frac{\mathrm{Ry}Z^2}{n^2}\frac{(Z\alpha)^2}{n^2}\left(\frac{3}{4} - \frac{n}{j+\frac{1}{2}}\right) \tag{3.7}$$

with respect to the non-relativistic Hamiltonian with hydrogen-like Coulomb potential $V_c(r) = -\frac{Ze}{r}$. All of the mentioned relativistic correction produce fine structure corrections in the

same order of magnitude, with the exception that the Darwin term is only non-zero for $l = 0$ (Fig. 3.1). Finally, it is important to note that the spin–orbit interaction does not lift the spin degeneracy, in fact the atomic levels are at least $2j + 1$-fold degenerate (neglecting hyperfine shifts). In the next Section will be shown that the spin–orbit interaction only produces spin-polarized eigenstates in Coulomb potentials lacking inversion symmetry.

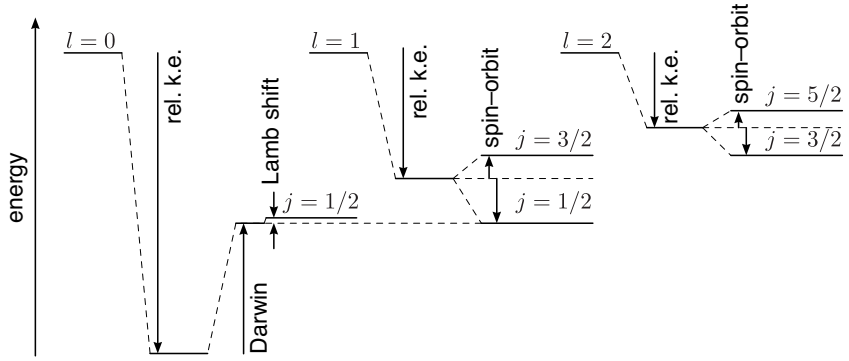

Figure 3.1: Relativistic energy corrections of the hydrogen atom including relativistic kinetic energy term (rel. k.e.), Darwin term, spin–orbit interaction, and Lamb shift (electron–vacuum interactions), excluding hyperfine shifts (electron–nucleus interactions). Figure adopted from [60].

3.2 Spin–orbit coupling in bulk crystals

The lower symmetry of the potential felt by a valence electron in a crystal as compared to a free atom, reduces the degeneracy with respect to the atomic eigenstates. In this respect, the crystal potential can be regarded as a perturbation of the free atom potential and the resulting energy splitting is called *crystal field splitting*. In consequence, the energy eigenstates are in general no longer eigenstates of the total angular momentum as discussed below (following Ref. [61]).

The single-particle Hamiltonian for an arbitrary potential $V(\boldsymbol{x})$ including spin–orbit coupling (and neglecting other relativistic corrections) has the form (cf. Eq. 3.4)

$$\mathcal{H} = \frac{1}{2m}\boldsymbol{p}^2 + V(\boldsymbol{x}) + \frac{\hbar}{4m^2c^2}\boldsymbol{\sigma}\cdot(\boldsymbol{\nabla}V(\boldsymbol{x})\times\boldsymbol{p}). \tag{3.8}$$

In the case of a periodic potential, the eigenfunctions of the Hamiltonian are Bloch waves. In agreement with the atomic case, the Hamiltonian eigenfunctions are not eigenstates of the spin but are a mixture of spin up and spin down states. Generally the Bloch functions can be

written as

$$\varphi_{\boldsymbol{k},\uparrow}(\boldsymbol{x}) = e^{i\boldsymbol{k}\cdot\boldsymbol{x}} u_{\boldsymbol{k}\uparrow}(\boldsymbol{x}) = \chi_{\boldsymbol{k},\uparrow}(\boldsymbol{x})|\uparrow\rangle + \gamma_{\boldsymbol{k},\uparrow}(\boldsymbol{x})|\downarrow\rangle, \tag{3.9}$$

where the first identity follows the Bloch theorem with $u_{\boldsymbol{k}\uparrow}$ being a crystal-periodic function and $\boldsymbol{k}$ a point in the reciprocal space. The $\uparrow$ in the index of the spatial part of the wave function only indicates that the spin *expectation value* along the quantization axis is positive $\langle\varphi_{\boldsymbol{k},\uparrow}|\sigma_z|\varphi_{\boldsymbol{k},\uparrow}\rangle > 0$, and accordingly $\langle\varphi_{\boldsymbol{k},\downarrow}|\sigma_z|\varphi_{\boldsymbol{k},\downarrow}\rangle < 0$.

In this framework it can be shown that if the Hamiltonian commutes with the time-reversal operator $\mathcal{K}$ (i.e. in the absence of magnetic fields), that $\mathcal{K}\varphi_{\boldsymbol{k},\uparrow} = \varphi_{-\boldsymbol{k},\downarrow}$ apart from a phase factor. In this case, the energy eigenvalues belonging to $\varphi_{\boldsymbol{k},\uparrow}$ and $\varphi_{-\boldsymbol{k},\downarrow}$ are equal $\varepsilon_{\boldsymbol{k},\uparrow} = \varepsilon_{-\boldsymbol{k},\downarrow}$, and the spin expectation values are the same with opposite sign $\langle\varphi_{\boldsymbol{k},\uparrow}|\sigma_z|\varphi_{\boldsymbol{k},\uparrow}\rangle = -\langle\varphi_{-\boldsymbol{k},\downarrow}|\sigma_z|\varphi_{-\boldsymbol{k},\downarrow}\rangle$. This means that the dispersion of an electronic state in a non-magnetic system is always point-symmetric around the Γ point of the reciprocal space. By using the translational symmetry $\mathcal{T}$, it can be shown that this holds for all $\boldsymbol{k}$ points with $\boldsymbol{k} = \frac{\boldsymbol{G}}{2}$, where $\boldsymbol{G}$ is a point of the reciprocal lattice

$$\varepsilon_{\frac{\boldsymbol{G}}{2}+\boldsymbol{k},\uparrow} \overset{\mathcal{K}}{=} \varepsilon_{-\frac{\boldsymbol{G}}{2}-\boldsymbol{k},\downarrow} \overset{\mathcal{T}}{=} \varepsilon_{\frac{\boldsymbol{G}}{2}-\boldsymbol{k},\downarrow}. \tag{3.10}$$

From this directly follows *Kramers theorem* which states that at these $\boldsymbol{k}$ values all the states are at least two-fold degenerate

$$\varepsilon_{\frac{\boldsymbol{G}}{2},\uparrow} = \varepsilon_{\frac{\boldsymbol{G}}{2},\downarrow}. \tag{3.11}$$

Because of this property, the points $\frac{\boldsymbol{G}}{2}$ are called time-reversal invariant momenta (TRIM).

Additional symmetries naturally increase the degree of degeneracy. In centrosymmetric crystals the electrostatic potential is invariant under space inversion $\mathcal{J}$. Since $\mathcal{J}$ changes the sign of the space and momentum operator but leaves the axial spin operator unchanged, the Hamiltonian (3.8) commutes with $\mathcal{J}$ if $\mathcal{J}V(\boldsymbol{x}) = V(\boldsymbol{x})$ and it follows that $\varphi_{\boldsymbol{k},\uparrow}(\boldsymbol{x}) = \varphi_{-\boldsymbol{k},\uparrow}(-\boldsymbol{x})$, apart from a phase factor. The states $\varphi_{\boldsymbol{k},\uparrow}$ and $\varphi_{-\boldsymbol{k},\uparrow}$ thus have the same energy eigenvalues $\varepsilon_{\boldsymbol{k},\uparrow} = \varepsilon_{-\boldsymbol{k},\uparrow}$. As $\mathcal{J}$ and σ_z commute, the spin expectation values are equal $\langle\varphi_{\boldsymbol{k},\uparrow}|\sigma_z|\varphi_{\boldsymbol{k},\uparrow}\rangle = \langle\varphi_{-\boldsymbol{k},\uparrow}|\sigma_z|\varphi_{-\boldsymbol{k},\uparrow}\rangle$.

In a crystal with both, time-reversal and spatial inversion symmetry present, every Bloch state is at least doubly degenerate

$$\varepsilon_{\boldsymbol{k},\uparrow} \overset{\mathcal{K}}{=} \varepsilon_{-\boldsymbol{k},\downarrow} \overset{\mathcal{J}}{=} \varepsilon_{\boldsymbol{k},\downarrow}, \tag{3.12}$$

where $\varphi_{\boldsymbol{k},\downarrow} = \mathcal{K}\mathcal{J}\varphi_{\boldsymbol{k},\uparrow}$, apart from a phase factor. In addition, the spin expectation values of the two states cancel out each other at every $\boldsymbol{k}$ point, such that the state are not spin-polarized.

Figure 3.2 illustrates the effect of spin–orbit interaction on the valence band structure of diamond, Ge, and GaAs for small k. While in diamond the spin–orbit coupling is weak, in

Ge, which also crystallizes in a diamond cubic crystal structure, the spin–orbit interaction induces a gap between the Γ_8^+ states and the split-off band Γ_7^+. The splitting of these p-derived states is directly related to the spin–orbit splitting in the free atom; consistently the s-derived Γ_6^+ state is not split. Away from the Γ point the $(2j+1)$-fold degeneracy is partly lifted into a heavy and a light hole band according the crystal symmetry [1]. But as the crystal structure is inversion-symmetric, all the bands remain doubly spin degenerate (Eq. 3.12). On the other hand, in GaAs, which has a noncentrosymmetric zincblende crystal structure, the spin degeneracy of the valence bands is lifted for every $\boldsymbol{k}$ apart from the TRIM. This splitting induced by the so-called *bulk inversion asymmetry* of the crystal and the accompanying spin-polarization of the bands is called *Dresselhaus effect* [62] in cubic crystals and Rashba effect [11] in hexagonal crystals. In contrast to magnetic materials, these types of spin splitting do not lead to a real space magnetic order, since time-reversal symmetry ensures that the spin polarization of all states $\varphi_{\boldsymbol{k},\uparrow}$ is compensated by the spin polarization of its partner state $\varphi_{-\boldsymbol{k},\downarrow}$ with the same energy.

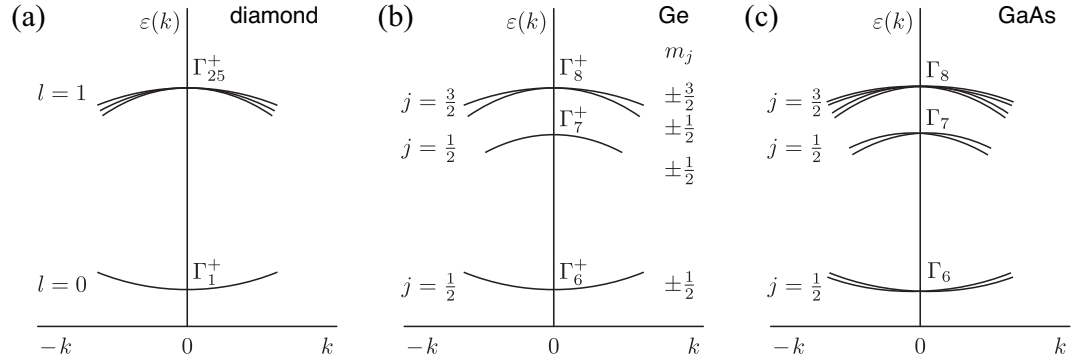

Figure 3.2: Schematic dispersion $\varepsilon(k)$ in diamond, Ge and GaAs for small k. **(a)** Without spin–orbit coupling, each band in diamond has a two-fold spin degeneracy. **(b)** Spin–orbit splitting of the p-derived bands in Ge, with each band remaining doubly degenerate. **(c)** Lifting of the valence band spin degeneracy by the spin–orbit interaction in noncentrosymmetric GaAs. Figure adopted from Refs. [63, 64]

[1] Note that j is not a good quantum number in a solid; if the crystal field is of the same order or bigger as the spin–orbit interaction, the orbital angular momentum is quenched.

3.3 Principles of the Rashba-Bychkov effect in two-dimensional electron gases

Even centrosymmetric crystals lack inversion symmetry at their surfaces or at interfaces to other materials, known as *structural inversion aysmmetry*. As long as a sizeable spin–orbit interaction is present, spin splitting is generally observed in the spectrum of two-dimensional electron gases localized at surfaces or interfaces where the confining potential is asymmetric. Band splitting in two-dimensional states arising due to structural inversion asymmetry is called *Rashba-Bychkov effect* [11]. While the mechanism is the same as for the Dresselhaus or Rashba effect in three-dimensional states, the spin splitting and spin texture can differ depending on the crystal and surface symmetry. Spin splitting induced by structural and bulk inversion asymmetry can also occur simultaneously in thin films of noncentrosymmetric materials, such as in GaAs/InGaAs quantum well states [65]. In this Section we will concentrate on the Rashba-Bychkov effect alone, i.e. neglecting the crystal symmetry.

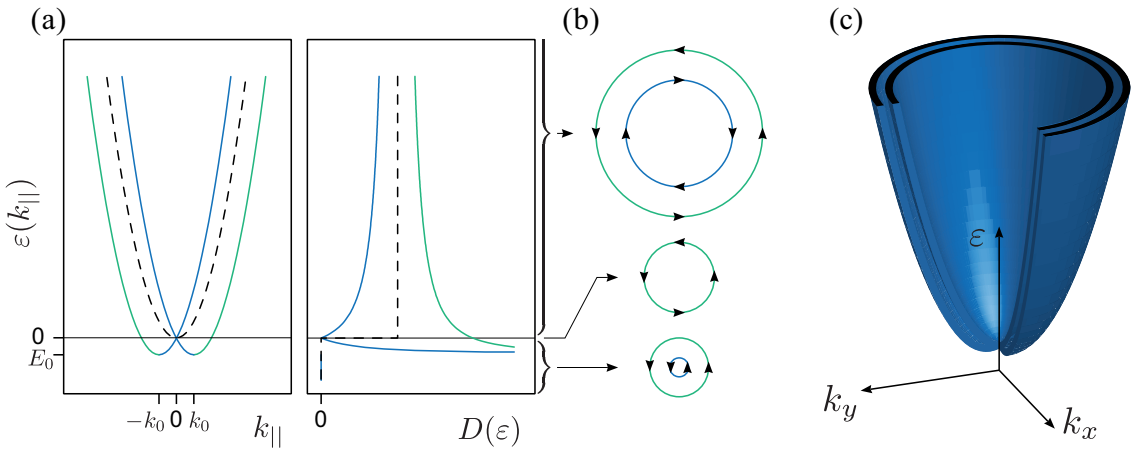

Figure 3.3: **(a)** *Left panel*: Schematic Rashba spectrum $\varepsilon(k_{||})$ with two constant-in-k-split parabola (solid) in comparison with the free electron dispersion (dashed). *Right panel*: Density of states $D(\varepsilon)$ of the inner (blue) and outer (green) branches of the Rashba dispersion, vanishing at the degeneracy point and featuring a van Hove singularity at the band apex energy; in comparison the density of states of a free two-dimensional electron gas (dashed). (Figure adopted from Ref. [45]) **(b)** Constant energy contours above, at, and below the degeneracy point; the arrows indicate the chirality of the in-plane, helical spin polarization. **(c)** Three-dimensional illustration of the Rashba spectrum.

Effective Hamiltonian Rashba and Bychkov rewrote the spin–orbit term of Eq. (3.8) for the strongly simplified case of a two-dimensional gas of free electrons in a constant electric

field [11]. After substituting the periodic crystal potential with $V(\boldsymbol{x}) = Ez$, by assuming an effective electric field E along the surface normal $\hat{z}$, the Hamiltonian reads

$$\begin{aligned}\mathcal{H} &= \frac{\boldsymbol{p}^2}{2m} + \alpha\, \boldsymbol{\sigma} \cdot (\hat{z} \times \boldsymbol{p}) \\ &= \frac{\boldsymbol{p}^2}{2m} + \alpha\, (\sigma_y p_x - \sigma_x p_y),\end{aligned} \tag{3.13}$$

where $\alpha = \frac{e\hbar^2}{4m^2c^2}E$ is called the Rashba parameter. The eigenfunctions are product states of a plane wave with quantum number $\boldsymbol{k}_\parallel = (k_x, k_y, 0)$ of the form $e^{i\,\boldsymbol{k}_\parallel \cdot \boldsymbol{x}}$ and a two-component spinor. Substitution of the momentum operator with its space representation $\boldsymbol{p} = -i\hbar\boldsymbol{\nabla}$ and subsequent diagonalization leads to the well known Rashba dispersion

$$\varepsilon^{\pm}(k_\parallel) = \frac{\hbar {k_\parallel}^2}{2m} \pm \alpha k_\parallel, \tag{3.14}$$

with the normalized eigenstates

$$\boldsymbol{\psi}^{\pm} = \frac{1}{\sqrt{2}}\, e^{i\,\boldsymbol{k}_\parallel \cdot \boldsymbol{x}} \begin{pmatrix} \pm i\, e^{i\,\varphi} \\ 1 \end{pmatrix}, \tag{3.15}$$

and φ being defined by the polar angle of $\boldsymbol{k}_\parallel = k_\parallel(\cos\varphi, \sin\varphi, 0)$.

The spin polarization vector is formed by the three spatial components of the spin expectation value $\boldsymbol{P} = \langle\boldsymbol{\sigma}\rangle$ normalized to 1

$$\langle\boldsymbol{\psi}^{\pm}|\sigma_x|\boldsymbol{\psi}^{\pm}\rangle = \pm\sin\varphi, \quad \langle\boldsymbol{\psi}^{\pm}|\sigma_y|\boldsymbol{\psi}^{\pm}\rangle = \mp\cos\varphi, \quad \langle\boldsymbol{\psi}^{\pm}|\sigma_y|\boldsymbol{\psi}^{\pm}\rangle = 0. \tag{3.16}$$

The left panel of Fig. 3.3a illustrates the dispersion of a Rashba-like split two-dimensional electron gas (solid lines). Away from the $\overline{\Gamma}$ point, the splitting increases linearly in $k_\parallel$ such that the minimal energy is lowered by $E_0 = -\alpha^2 m/2\hbar^2$ and is shifted towards $k_0 = \alpha m/\hbar^2$ with respect to the free electron paraboloid (dashed line). At the $\overline{\Gamma}$ point the Kramers theorem (Eq. 3.11) ensures two-fold degeneracy. The energy of the degeneracy point marks the transition point of the Fermi surface topology. Depending on the band filling the Fermi surface is formed by two concentric Fermi rings with helical spin structure of opposing (equal) chirality if the chemical potential is positive (negative) or by a single spin-polarized Fermi ring if the chemical potential matches the energy of the point of degeneracy ($\mu = 0$), as shown in Fig. 3.3b.

As a result of the shifting of the band minima in reciprocal space, the density of states is no longer a constant as a function of energy as in the case of a two-dimensional gas of free electrons. Generally, for a spherically symmetric dispersion the density of states $D(\varepsilon)$ is proportional to the surface of a constant energy surface (contour) in k space divided the absolute value of the derivative of the energy dispersion with respect to the momentum

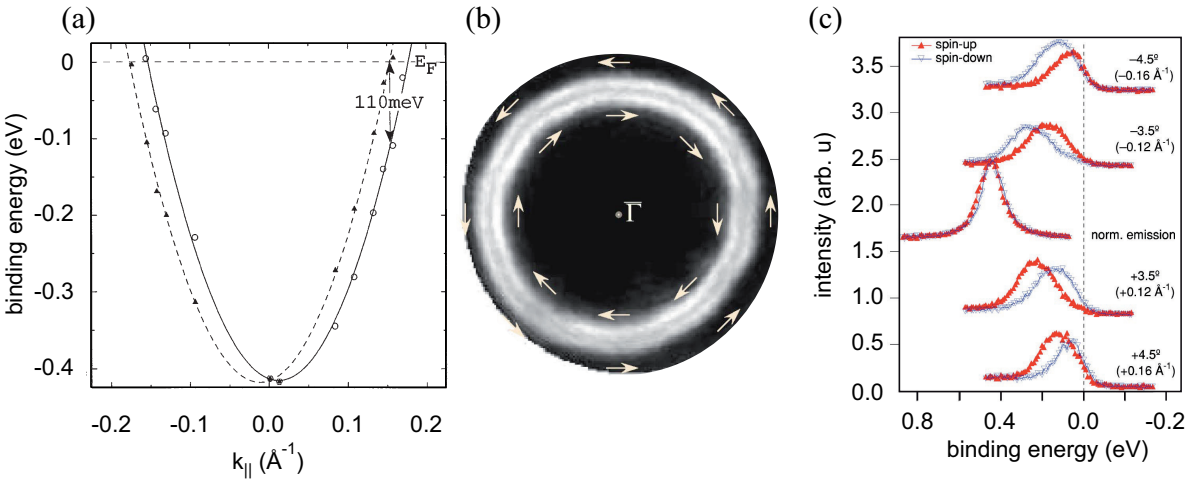

Figure 3.4: (a) Parabola fitted to the ARPES data of the Au(111) surface state (Figure taken from Ref. [66]). **(b)** ARPES Fermi surface map of the Au(111) surface state in the shape of two concentric rings (Ref. [67]). **(c)** Spin-resolved ARPES measurements at different $k_{||}$ confirm time-reversal symmetric spin texture of the Au(111) surface state (Ref. [67]).

$D(\varepsilon) \sim \int d\sigma / |\nabla_{\boldsymbol{k}}\, \varepsilon(\boldsymbol{k})|$ [68]. In other words, whenever at a given energy the group velocity is zero at an infinite amount of k points (for an infinitely large crystal), there is a singularity in the density of states. In the vicinity of the apex of the Rashba dispersion at k_0 this means $D(k_0 + k) \sim \frac{k_0+k}{|k|} \simeq \frac{k_0}{|k|}$, with $k \ll k_0$. Thus, when approaching the band apex ε_0, the inner and outer branches of the dispersion exhibit a so-called *van Hove* singularity in the density of states $D(\varepsilon) \sim \frac{1}{\sqrt{\varepsilon-\varepsilon_0}}$ [45], as in the case of a one-dimensional free electron gas. Further, the density of states of the inner branches of the Rashba dispersion drops to zero at the point of degeneracy since the circumference of its constant energy contour vanishes. The density of states of a two-dimensional Rashba gas is schematically shown in the right panel of Fig. 3.3a. The change of the Fermi surface topology and the singularity of the density of states is observable with scanning tunneling spectroscopy (STS) [69], and is related to alterations of the electronic many-body interactions such as changes in the Fermi liquid behavior [70], an enhanced electron–phonon coupling [71, 72], and a possible increase of the superconducting transition temperature [73]. [74]

Tight binding description The first ARPES measurements of a Rashba-split two-dimensional electron gas were performed on the surface state of the Au(111) surface by LaShell, *et al.* [66], Fig. 3.4a. In a later spin-resolved ARPES study, the splitting and the theoretically predicted in-plane helical spin texture were confirmed [67], (Fig. 3.4b–c). The two parabolae were found to be shifted by $0.023\,\text{Å}^{-1}$ in momentum which translated to a maximal energy splitting of

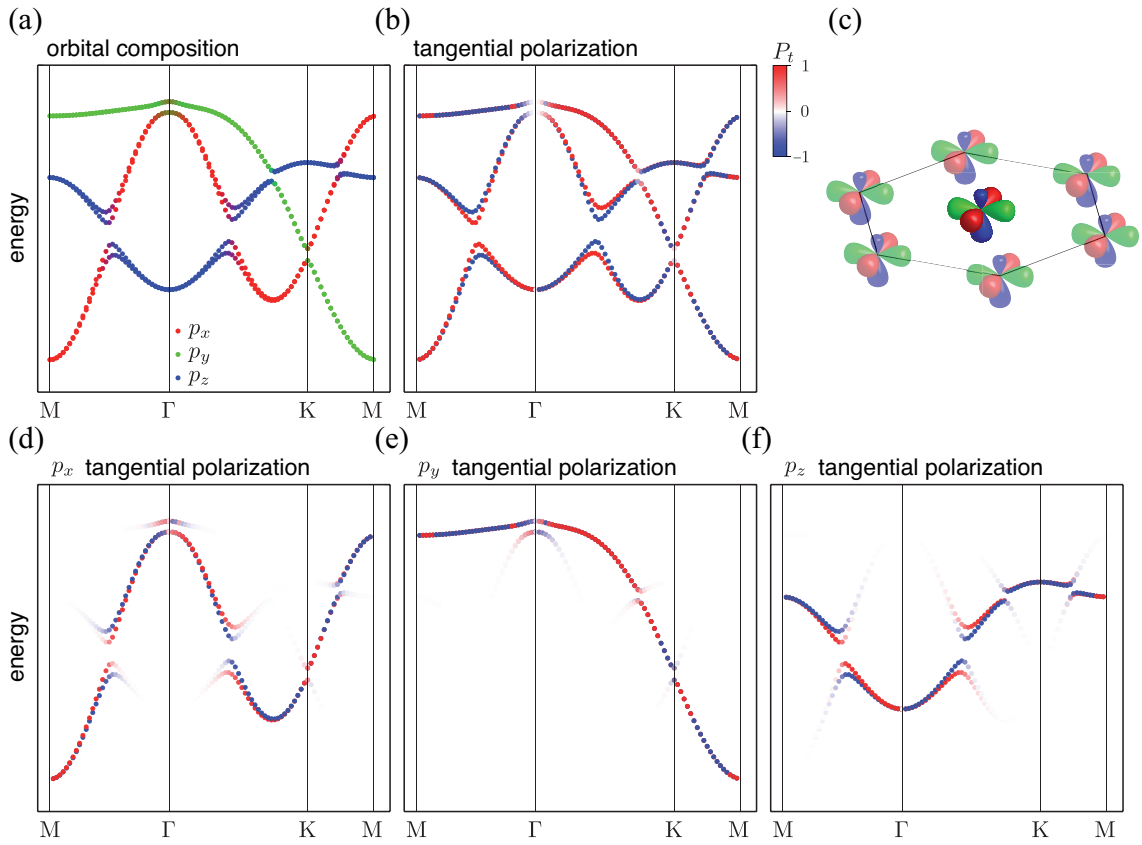

Figure 3.5: (a) Dispersion of a spin–orbit coupled tight binding model of p orbitals in a two-dimensional hexagonal lattice. For mimicking a broken structural inversion symmetry, the p_z orbitals are artificially made asymmetric. The colors of the data points indicate the orbital composition (see inset). **(b)** Same as (a), but with the colors indicating the degree of in-plane, tangential polarization (P_t). **(c)** Illustration of the orbitals relevant in the model. **(d)–(f)** Same as (b) but projected on the individual orbitals p_x, p_y and p_z.

110 meV at the Fermi momenta. This splitting is several orders of magnitude larger than expected from the simple Rashba model of a free electron gas in the surface potential gradient; the latter being typically in the order of 1 V/Å^{-1}, the model would lead to a splitting in the order of 10^{-6} eV [75]. It therefore can not directly be the surface electrostatic field that leads to the observed splitting. As realized by Petersen and Hedegård [75], the asymmetry of the potential confining the electronic state between the vacuum and the crystal bulk shifts the wave function with respect to the atomic cores in whose vicinity the potential gradient and thus the spin–orbit interaction is largest. In their *tight-binding* model the authors modeled the Au(111) surface state by a two-dimensional hexagonal lattice of p orbitals with nearest neighbour coupling. The structural inversion asymmetry is reflected by artificially introduc-

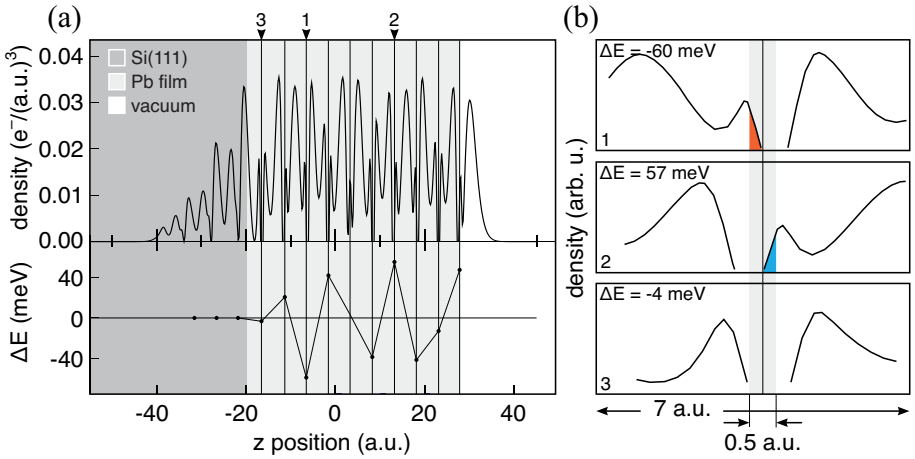

Figure 3.6: (a) *Upper panel:* Charge density perpendicular to the surface of a 10 monolayer Pb quantum well state ($n = 5$) calculated with DFT ($k_{\parallel} = 0.1\,\text{Å}^{-1}$). *Lower panel:* Layer-resolved energy splittings. **(b)** Magnifications into three specific regions of the slab. (Figures adopted from Ref. [77])

ing finite overlap integrals between p_z and p_x, p_y by making the p_z orbital aymmetric, which is equivalent to admixing s (and d) character to the orbitals [76].

The atomic spin–orbit interaction together with the orbital asymmetry naturally leads to a spin splitting in the correct order of magnitude. Figure 3.5a shows results from calculations based on [75], including corrections regarding the spin–orbit Hamiltonian as described in App. A. It is interesting to note that although S_z is not an eigenvalue of the Hamiltonian, whenever spin–orbit interaction is present, the eigenstates of the tight-binding Hamiltonian are almost eigenstates of S_z, i.e. show spin polarizations close to 1 or -1, respectively (Fig. 3.5b–f). A significant reduction of the spin polarization is observed when the orbital character of the state is mixed; in the present case when orbitals of different character hybridize. As will be discussed later in Ch. 6, the Bloch states in real crystals have always mixed orbital character to a certain extent and the intrinsic spin polarization is generally smaller than 100 %.

Ab-initio calculations By means of *ab-initio* calculations including relativistic corrections within the DFT framework, it was shown that the main contribution (90 %) to the Rashba splitting of the Au(111) surface state arises from within a sphere of 0.25 a.u. radius around the Au nuclei [76,78]. This is the reason why a tight-binding model manages to describe the size of the spin splitting reasonably well. In addition, the local origin of the Rashba splitting implies that the resulting spin splitting of a real Rashba gas experiences contributions from

several atomic layers, depending on the spatial localization of the electron gas. In the case of the quantum well states in Pb films on Si(111) for example, which unlike the Au(111) surface state are not localized within the first few atomic layers but spread throughout the entire Pb film, it was shown that every Pb layer contributes in an additive or subtractive manner to the final, relatively small Rashba splitting [77] (Fig. 3.6). The total spin splitting is found to be an integral of the electron densities $|\psi(\boldsymbol{x})|^2$, the gradient of the electrostatic potential along the surface normal $\frac{\partial V}{\partial z}$ and the in-plane crystal momentum $k_\parallel$: $\Delta\varepsilon \sim k_\parallel \int \mathrm{d}x^3 \frac{\partial V}{\partial z}|\psi(\boldsymbol{x})|^2$ [78]. From the formula it is again evident that the main contribution of the integral comes from the vicinity of the nuclei where the potential gradient is largest and it is only finite if the product of the potential gradient and the electron density is asymmetric. Depending on the slope of the envelope function in the vicinity of the contribution to the energy splitting is positive or negative (Fig. 3.6b).

Knowing the basic mechanism establishing the Rashba splitting, it is a natural question to ask how the spin splitting of a system can be tuned. First of all, the size of the spin splitting depends on the strength on the atomic spin–orbit interaction, due to the large near-nucleus contribution (Eq. 3.4). Therefore, the spin–orbit coupling directly scales with the atomic number Z. And secondly, for a finite spin splitting an asymmetric charge density distribution is necessary. The energy splitting is therefore crucially dependent on the localization of the state with respect to the nuclei which is highly sensitive to manipulations of the confining potential. For example it has been shown that the spin splitting in Pb/Si(111) quantum well states can be effectively tuned, by altering the semiconductor–metal interface, via substituting the interfacial atoms [77], or doping of the Si substrate [79]. Comparably, a change of the spin splitting of two-dimensional electron gases in semiconductor heterostructures could be obtained by applying a gate voltage [80–82]. Again, the crucial part of the splitting is not directly induced by the interface electric field, but indirectly via changing the asymmetry of the confinement and shifting the wave function envelope with respect to the atomic nuclei. In the same line of thought can be explained the exceptionally large spin splitting ($\alpha = 3.05\,\mathrm{eV\,Å}$) of the surface state in the surface alloys Bi/Ag(111) [83]. Here, the high Bi atoms ($Z = 83$) stick partly out of the Ag(111) surface and thus strongly enhance the asymmetric distribution around the Bi nuclei. In comparison, in the structurally similar surface alloy Pb/Ag(111) the surface state splitting is significantly reduced ($\alpha = 1.42\,\mathrm{eV\,Å}$) despite a comparable atomic number of the Pb atoms ($Z = 82$) [84]. But here, the surface corrugation is slightly smaller which corroborates the importance of the surface state localization on the Rashba effect [44, 85, 86].

Tuning of the spin texture away from the in-plane, tangential orientation of the confined free-electron case described by Eq. (3.13) is only possible by expanding the model to include effects of the crystal potential. In general terms, surfaces or interfaces lacking in-plane inver-

sion symmetry have noncentrosymmetric in-plane electric fields and introduce lateral wave function asymmetries. By imposing the spin quantization axes being perpendicular to the electric fields and the Bloch momenta, according Eq. (3.8), radial and out-of-plane polarizations become possible. In Ch. 4 the special case of spin–orbit-split surface states located on surfaces with odd-fold rotational symmetry will be discussed. On such surfaces, the in-plane structural inversion symmetry is broken, yielding a warping of the constant energy contours of the dispersion and an oscillating out-of-plane spin component.

In three-dimensional crystals, the spin texture is solely determined by the crystal symmetry. The simplest case is the three-dimensional analogon of the Rashba-Bychkov effect which occurs in the bulk states of inversion-asymmetric crystals with uniaxial electric fields. In Ch. 7 the example of noncentrosymmetric BiTeI and BiTeCl will be introduced, whose crystals are built up of charged layers stacked along their hexagonal crystal axis. Due to strong spin–orbit interaction, the bulk states of these materials exhibit a large spin splittings which for small k are described by the three-dimensional version of Eq. (3.13).

So far we have discussed Rasbha-split surface spectra, where eventually both branches of the dispersion connect either to the bulk valence or conduction band. There is however a class of semiconducting or insulating materials, where — in a naive picture — the inner Rashba branches merge with the bulk conduction band and the outer branches with the valence band. In contrast to Rashba surface states, the existence of these novel states and thus the surface metallicity is guaranteed by properties of the bulk band structure.

3.4 Topological insulators

Insulators, characterized by a Hamiltonian $\mathcal{H}(\boldsymbol{k})$ with Bloch waves $|u_m(\boldsymbol{k})\rangle$ as eigenfunctions and energy eigenvalues $\varepsilon(\boldsymbol{k})$, can be classified into topological equivalence classes of $\mathcal{H}(\boldsymbol{k})$, in which the members are connected by smooth tuning of the Hamiltonian without closing the energy band gap. The topology of a band structure can be distinguished by a topological invariant, an integer number that is a function of $|u_m(\boldsymbol{k})\rangle$ and characterizes the mapping from the crystal momentum ($\boldsymbol{k} \in$ Brillouin zone) into the space of Hamiltonians. [9]

It was first realized by Thouless *et al.* [87] that an integer quantum Hall (IQH) insulator [88] has a different band structure topology than an ordinary insulator, characterized by the so-called *Chern* invariant $n_m = \frac{i}{2\pi} \int \mathrm{d}^3\boldsymbol{k}\, \nabla \times \langle u_m|\nabla_k|u_m\rangle \in \mathbb{Z}$ (the total Berry flux [59] in the Brillouin zone). In fact, the authors could show that the filling factor N, describing the number of channels contributing to the quantized Hall conductivity

$$\sigma_{xy} = N\, e^2/h, \tag{3.17}$$

is identical to the total Chern number of the occupied bands $N = n = \sum n_m$. A more precise statement is expressed by the *bulk–boundary correspondence* principle which states that whenever the Chern number changes across an interface *(i)* there must be metallic boundary states and *(ii)* the difference of the number of states with positive (negative) N^+ (N^-) group velocity is equal to the change in the total Chern number across the interface $\Delta n = N^+ - N^-$ [9].

3.4.1 Three-dimensional topological insulators

In an IQH insulator the time-reversal symmetry is broken by the action of a magnetic field. Materials that are described by a Hamiltonian invariant under time reversal, therefore do not belong to the class of IQH insulators but form their own group of insulators classified by other topological invariants [89]. In two dimensions, the quantum spin Hall (QSH) insulators were found to be topologically distinct from a ordinary band insulators. These non-trivial insulators can be understood as two independent copies of the IQH for the two spin species, where the spin–orbit interaction takes the role of an intrinsic, time-reversal-symmetric magnetic field [12, 90]. In accordance with the bulk–boundary correspondence principle, spin-polarized chiral states are hosted at the boundaries to topologically trivial materials (including vacuum) [91,92]. This Chapter deals with a phase similar to the QSH phase, the so-called three-dimensional $\mathbb{Z}_2$ topological insulators.

Minimal model for Bi_2Se_3 It is instructive to start with a model for the bulk band structure of Bi_2Se_3, a well known member of this class of materials. As will be described in greater detail in Sect. 5.1, the electronic band defining the band gap of the bulk semiconductor Bi_2Se_3 are *p*-derived states with opposite parity (Fig. 5.1b). Of crucial importance is their peculiar property that the energetic order of the states at the gap is inverted at the Γ point with respect to the other TRIM by the action of a strong spin–orbit coupling. In the model, the basis of the states near the gap shall consist out of four bands defined as

$$|P1_z^+, \uparrow\rangle,\ |P1_z^+, \downarrow\rangle,\ |P2_z^-, \uparrow\rangle,\ |P2_z^-, \downarrow\rangle. \tag{3.18}$$

Where $\pm$ denote the parity eigenvalues and $\uparrow, \downarrow$ the spin. As the valence and the conduction band separated by a finite gap shall be described by a single Hamiltonian, the latter will be of the form of a Dirac equation. The time-independent version of the Dirac Hamiltonian (3.1)

expanded up to second order[2] in k (replaces p) with $V = 0$ reads [93, 94]

$$\begin{aligned}\mathcal{H} &= \varepsilon_0(\boldsymbol{k}) + \sum_{i=x,y,z} v_i \alpha_i k_i + (M - \sum_{i=x,y,z} B_i k_i^2)\beta \\ &= \varepsilon_0(\boldsymbol{k}) + \begin{pmatrix} \mathcal{M} & 0 & v_z k_z & v_\parallel k_- \\ 0 & \mathcal{M} & v_\parallel k_+ & -v_z k_z \\ v_z k_z & v_\parallel k_- & -\mathcal{M} & 0 \\ v_\parallel k_+ & -v_z k_z & 0 & -\mathcal{M} \end{pmatrix}.\end{aligned} \tag{3.19}$$

with $\boldsymbol{\alpha}$ and β as defined in Eq. (3.1), and $k_\pm = k_x \pm i k_y$. $\varepsilon_0(\boldsymbol{k}) = C - D_z k_z^2 - D_\parallel k_\parallel^2$ is the dispersion independent of the inter-band coupling, and $\mathcal{M} = M - B_z k_z^2 - B_\parallel k_\parallel^2$. The rest are material parameters with $v_\parallel = v_x = v_y$, $B_\parallel = B_x = B_y$. Note that the off-diagonal term must be linear in k, as they describe the coupling between states of opposite parity.

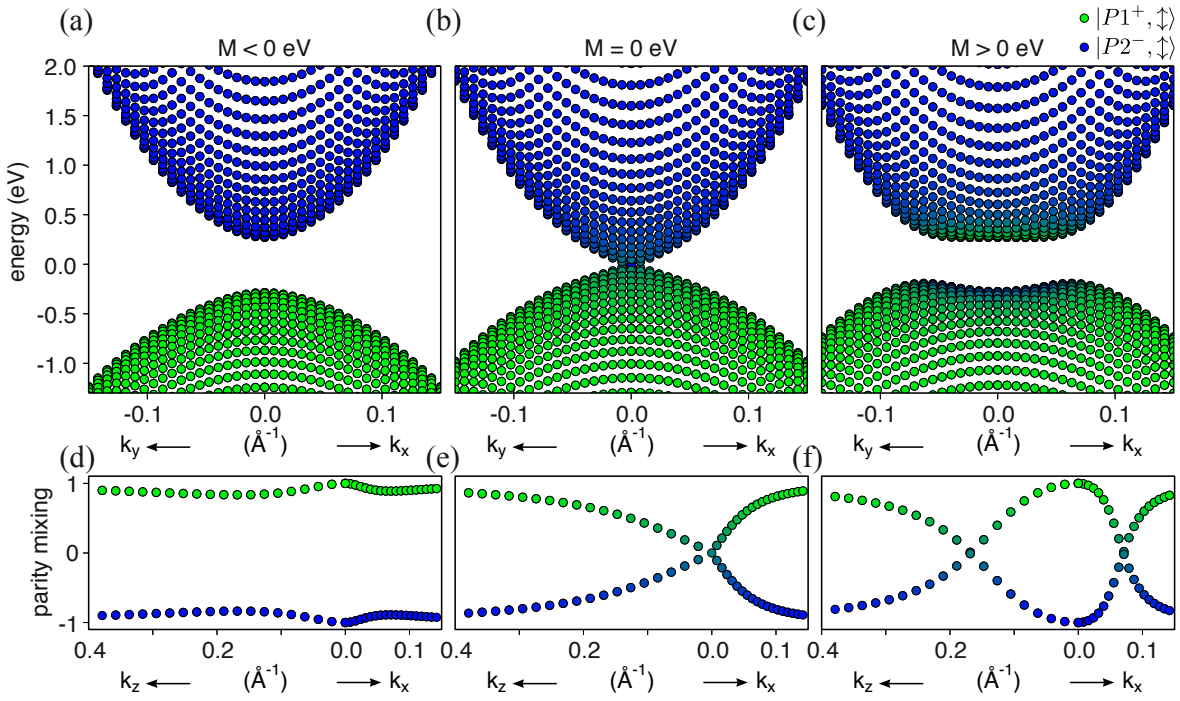

Figure 3.7: The spectrum of the modified Dirac Hamiltonian (3.19) shows a topological transition as a function of the mass parameter M: **(a)** trivial insulator ($M = -0.28\,\text{eV}$) **(b)** critical point ($M = 0\,\text{eV}$) **(c)** inverted regime ($M = 0.28\,\text{eV}$). **(d–f)** Parity inversion of the energy eigenstates for the respective M values.

Since under time-reversal $\boldsymbol{\alpha}$ and β transform as $\boldsymbol{\alpha} \to -\boldsymbol{\alpha}$ and $\beta \to \beta$, the products $\alpha_i k_i$ and βk_i^2 are time-reversal invariant and thus the Hamiltonian as a whole is time-reversal symmetric

[2]The inclusion of the second order term is needed, to break the particle–hole symmetry of the Dirac equation which makes the Hamiltonian topologically distinct from the original Dirac Hamiltonian [93].

[93]. It is further invariant under spatial inversion and (threefold) rotational symmetry of the crystal (111) surface [94]. The diagonal terms $\mathcal{M}$ are the mass terms and define the band order at the Γ point. It is evident that in the case where $M, B_1, B_{\|} > 0$ the order of the bands $P1_z$ and $P2_z$ at $\boldsymbol{k} = 0$ is inverted compared to large $\boldsymbol{k}$ [94], in this case the above Hamiltonian describes a topological non-trivial three-dimensional Dirac model with an uniaxial asymmetry in the z direction [93]. Figures 3.7a–c show the spectrum of the Hamiltonian (3.19) for the parameters obtained from DFT calculations for Bi_3Se_3, as given in Ref. [94] (ν_z, $\nu_{\|}$, B_z, $B_{\|}$, C, D_z, $D_{\|} = 2.2\,eV$, 4.1 eV Å, 10 eV Å^2, 56.6 eV Å^2, -0.0068 eV, 1.4 eV Å^2, 19.6 eV Å^2). The projection of the Hamiltonian eigenstates on the parity eigenstates $P1^+$ and $P2^-$ are shown in Figs. 3.7d–f. Note that only at the Γ point and for $|\boldsymbol{k}| \to \infty$ the eigenstates of the Hamiltonian are parity eigenstates.

Topological invariants Since the Hall conductivity Eq. (3.17) is odd under time reversal, the edge state of the IQH phase can not exist in time-reversal symmetric systems and the Chern number is 0 [9]. But there are additional topological invariants ν_0; $(\nu_1, \nu_2, \nu_3) \in \mathbb{Z}_2$ that distinguish between weak ($\nu_0 = 0$) and strong ($\nu_0 = 1$) topological insulators when time-reversal symmetry holds [9, 13]. In the following we will focus on strong topological insulators and the term "strong" is omitted. The topological invariant ν_0 is again a function of the occupied Bloch states and can be defined as

$$(-1)^{\nu_0} = \prod_{i=1}^{4} \delta_i \tag{3.20}$$

with $\delta_i = \mathrm{Pf}[w(\Gamma_i)] / \sqrt{\mathrm{Det}[w(\Gamma_i)]}$, where $w_{mn}(\boldsymbol{k}) = \langle u_m(\boldsymbol{k}) | \mathcal{K} | u_n(-\boldsymbol{k}) \rangle$ and Γ_i are the 8 TRIM of the bulk Brillouin zone (Pf is the Pfaffian and $\mathcal{K}$ the time-reversal operator) [9, 13, 95]. In crystals with inversion symmetry, the Bloch waves are eigenstates of the parity operator at all the TRIM (with parity $\xi_m(\Gamma_i)$). It can be shown that in this case the expression for the δ_i is simplified to [95]

$$\delta_i = \prod_m \xi_m(\Gamma_i). \tag{3.21}$$

For $M > 0$ the Hamiltonian (3.19) produces a single parity inversion at the Γ point, where the occupied band has negative parity $\xi(\Gamma) = -1$, whereas the parity is 1 for $|\boldsymbol{k}| \to \infty$. The $\mathbb{Z}_2$ topological number is evidently $\nu_0 = 1$ and the system is topologically non-trivial. In return, if the band order is not inverted at the Γ point ($M < 0$) the system describes an ordinary i.e. topologically trivial insulator ($\nu_0 = 0$).

Such topological phase transitions have been observed in real electronic systems, such as the HgTe quantum well states, which enter a quantum spin Hall phase above a citical HgTe film thickness $d_c = 6.3$ nm [91,92], or the $BiTl(S_{1-\delta}Se_\delta)_2$ series that undergo a topological transition with increasing Se doping at $\delta = 0.6$ [96, 97].

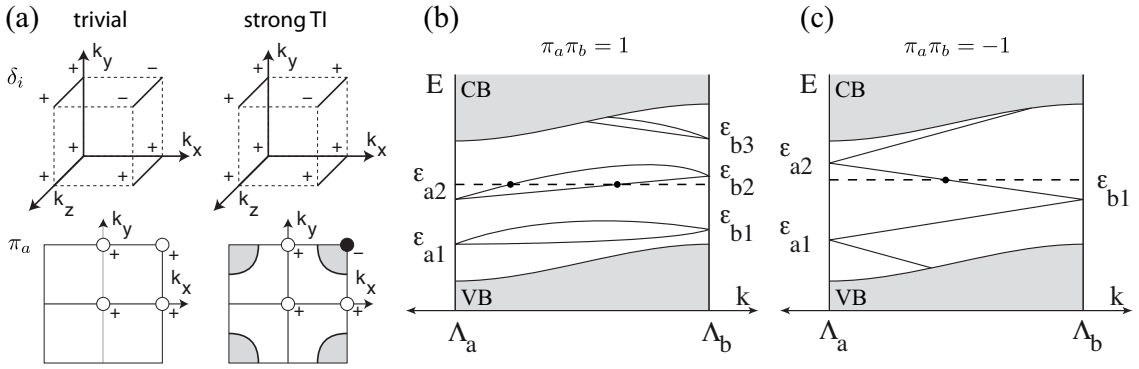

Figure 3.8: (a) *Top panels*: Possible δ_i at the bulk TRIM Γ_i (corners of a cubic Brillouin zone) for a trivial insulator and a strong topological insulator. *Bottom panels:* Corresponding π_a at the surface TRIM Λ_a. The solid lines indicate possible surface Fermi arcs. **(b)** Even number of Fermi level crossings of the spin-split surface spectrum between two surface TRIM ($\pi_a\pi_b = 1$). **(c)** Odd number of Fermi level crossings corresponding to *partner switching* of the Dirac points ($\pi_a\pi_b = -1$). Figure adapted from Ref. [13].

3.4.2 Topologically protected surface states

The importance of this topological classification is that, similar to the two-dimensional bulk–boundary correspondence principle, protected boundary states arise whenever the $\mathbb{Z}_2$ topology changes at a surface or across an interface, as could be shown by Fu *et al.* [13]: If an insulator is truncated perpendicular to a reciprocal lattice vector $\boldsymbol{G}$, the four TRIM of the surface Brillouin zone Λ_a are projections of two bulk TRIM Γ_{a1}, Γ_{a2} that are separated by $\boldsymbol{G}/2$. While the spin–orbit interaction splits every band of the surface spectrum away from the surface TRIM Λ_a, due to the Kramers theorem the states must have doubly degenerate Dirac points at the Λ_a. It is now the bulk topology that dictates how the Dirac points are connected. Along an arbitrary path between two TRIM Λ_a and Λ_b in the surface Brillouin zone, the surface spectrum crosses the Fermi level an odd (even) number of times, if $\pi_a\pi_b = -1\,(+1)$ where $\pi_a = \delta_{a1}\delta_{a2}$ [13,98] (Fig. 3.8). In a strong topological insulator one of the surface TRIM is such that on every path connecting to any of the other TRIM the number of Fermi level crossings of the surface spectrum is odd, i.e. $\pi_a\pi_b = -1$ (cf. Fig. 3.8c). This means that this TRIM is enclosed within a Fermi surface (cf. bottom right panel of Fig. 3.8a) dictated by a property of the bulk band structure. In other words, the existence of a surface state connecting the bulk valence and conduction band is guaranteed — or topologically protected. Small perturbation may only change the dispersion of the surface state but the metallicity of the surface is robust, while surface states on trivial insulators can be gapped out.

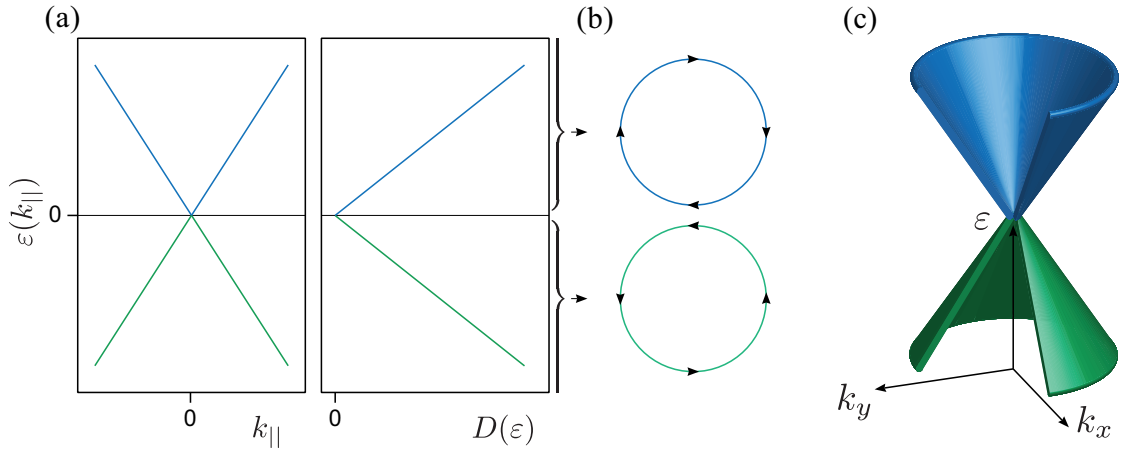

Figure 3.9: (a) *Left panel*: Massless Dirac spectrum with linear dispersion $\varepsilon(k_\parallel)$. *Right panel*: Linear density of states $D(\varepsilon)$ of a two-dimensional massless Dirac dispersion. **(b)** Constant energy cuts above and below the Dirac point with arrows indicating the chirality of the helical spin polarization. **(c)** Three-dimensional illustration of the positive and negative energy Dirac cones.

The dispersion of surface states is also described by the model Hamiltonian (3.19). In the presence of a surface perpendicular to the z direction, k_z is no longer a good quantum number and is to be replaced by $-i\partial_z$. Since the surface state must have finite norm, the surface solution of (3.19) is of the form $\psi = \psi_\lambda e^{\lambda z}$ with $\lambda \in \mathbb{C}$. Therefore $-i\partial_z \to -i\lambda z$ and the secular equation of the Schrödinger equation depends on the energy and λ. By applying semi-infinite boundary conditions $\psi(0) = 0$ and $\psi(z \to \infty) = 0$, one obtains $\pm\lambda_{1,2}$ and the energy eigenvalues of the surface states [99] The solution only exists if $\pm\lambda_{1,2}$ are real or complex conjugate partners, i.e. if $M/B_z > 0$ and $B_z^2 > D_z^2$ in the case of inverted band order. By projecting the Hamiltonian (3.19) into the space spanned by the eigenvectors of the surface energy eigenvalues, one obtains for small k the following effective Hamiltonian [93]

$$\mathcal{H}_{\text{eff}} = v_{\text{eff}} \left(k_x \sigma_y - k_y \sigma_x \right) \tag{3.22}$$

with $v_{\text{eff}} = \text{sgn}(B_z) v_\parallel \sqrt{1 - D_z^2/B_z^2}$. This is the Hamiltonian of a massless Dirac particle with broken particle–hole symmetry and a helical spin–momentum locking. In this small-k picture it has the same form as the Rashba Hamiltonian (Eq. 3.13). The positive and negative energy spectrum of the second term of Eq. (3.22) are depicted in Fig. 3.9a exhibiting a linear gapless dispersion with a linear density of states. The constant energy contours of the effective Hamiltonian are circles with a helical, i.e. in-plane and tangential spin polarization and opposite helicity above and below the degenerate Dirac point (Fig. 3.9b). Due to their linear-in-k dispersion for small k, the surface states of topological insulators are often referred to as

Dirac cones (Fig. 3.9c).

3.4.3 Experimental studies on three-dimensional topological insulators

The first experimentally verified three-dimensional topological insulator was the alloy $Bi_{1-x}Sb_x$. Bulk Sb is a semimetal with a parity inversion of the states defining the local gap at the L point, and topologically non-trivial surface states around the $\overline{\Gamma}$ point [9,100,101]. By replacing most of the Sb with Bi atoms, the band structure can be tuned such that for $0.07 < x < 0.22$ the bulk of $Bi_{1-x}Sb_x$ becomes insulating while the inverted band order at the L point is retained. In this range the alloy is a three-dimensional topological insulator with protected surface states. Figures 3.10a,b show the theoretically predicted odd number of Fermi level crossings of the (111) surface spectrum of $Bi_{0.91}Sb_{0.09}$ and the corresponding ARPES map, respectively. Ultimate proof of the non-trivial nature of the surface states was given later by showing the nondegeneracy of the surface states: by means of spin-resolved ARPES it could be shown that the surface states are spin-polarized and in the vicinity of the $\overline{M}$ point have the dispersion of a helical Dirac gas [102,103] (Fig. 3.10c).

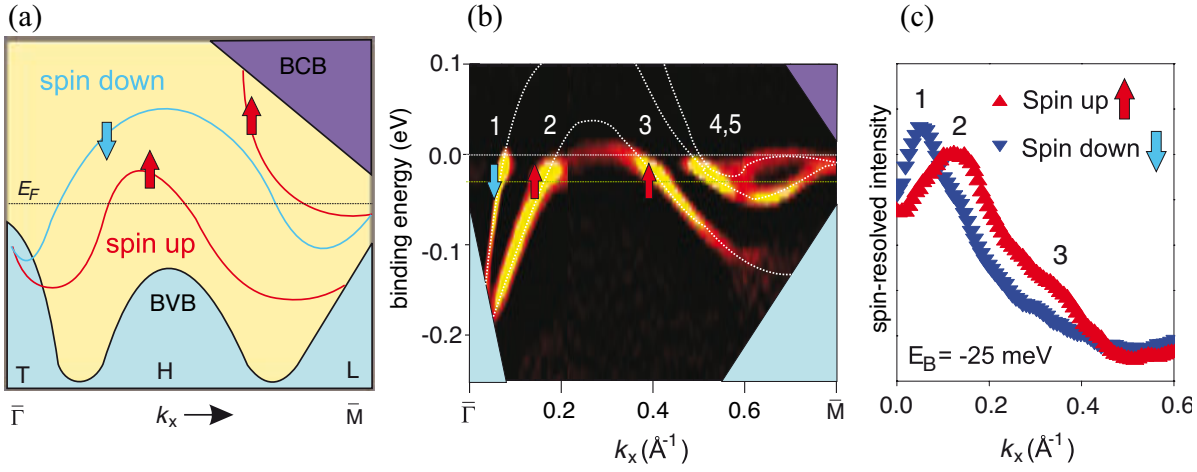

Figure 3.10: (a) Schematic of the dispersion of the spin-polarized surface states and the non-trivial connection of the valence and the conduction band between $\overline{\Gamma}$ and $\overline{M}$ due to the parity inversion at the L point of $Bi_{0.91}Sb_{0.09}$. **(b)** Spin-integrated ARPES intensity map of the surface state of $Bi_{0.91}Sb_{0.09}$ at the Fermi level. The arrows indicate the measured direction of the spin. **(c)** Spin-resolved MDCs taken at -25 meV binding energy showing single-spin degeneracy of the bands at 1, 2, and 3. The spin points in-plane and perpendicular to the momentum. Figure taken from Ref. [102].

Indirectly, the surface state spin structure could be observed by STS because of its effect on the real space interference patterns of the local density of states (LDOS) at the surface [104].

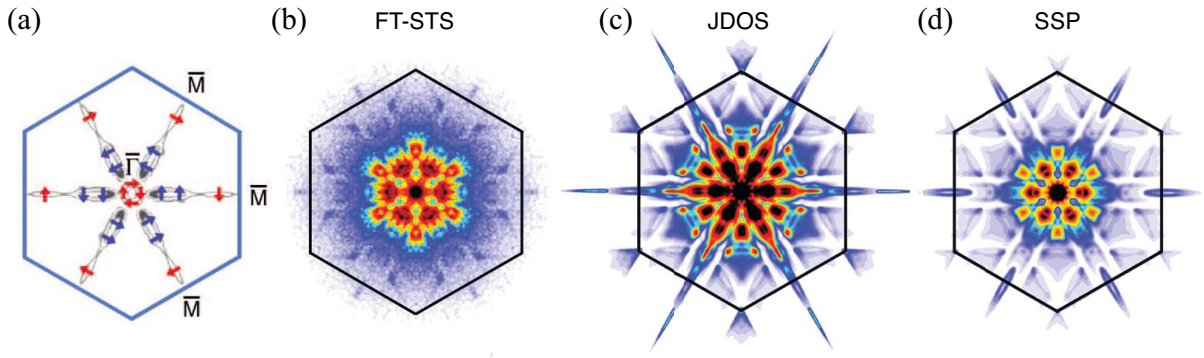

Figure 3.11: **(a)** $Bi_{0.91}Sb_{0.09}$ Fermi surface. **(b)** Joint density of states (JDOS) at E_F based on ARPES data. **(c)** Fourier transform of STS (FT-STS) measurements of the local density of states at E_F. **(d)** Spin-dependent scattering probability (SSP) at E_F based on ARPES data. Figure taken from Refs. [9, 104].

In the absence of magnetic impurities, scattering between states with opposite $\boldsymbol{k}$ is forbidden by time-reversal due to the opposite spin of the states (Fig. 3.11a). This suppressed backscattering could be directly observed in the Fourier transform of the interference pattern of the LDOS at the Fermi level measured by STS (Fig. 3.11b). For non-degenerate surface state the joint density of states of the Fermi surface models the conductance at a wavevector $\boldsymbol{q}$ due to elastic scattering of quasi-particles and their interference between different momentum states ($\boldsymbol{k}_1$ and $\boldsymbol{k}_2$, where $\boldsymbol{q} = \boldsymbol{k}_1 + \boldsymbol{k}_2$) (Fig. 3.11c) [104]. As shown in Ref. [105] in the case of spin-polarized states, however, the overlap of the spin states connected in the scattering process must be incorporated which results in a suppression of scattering certain channels (Fig. 3.11d). Indeed, Fig. 3.11b shares most features of the spin-dependent scattering probability Fig. 3.11d.

The surface state structure of $Bi_{1-x}Sb_x$ is complicated and the band gap rather small, this motivated a search for topological insulators with a larger gap and a simpler surface state dispersion [9]. A theoretical study predicted the stoichiometric compounds Bi_2Se_3, Bi_2Te_3, and Sb_2Te_3 to be three-dimensional topological insulators with a single cone-like surface state at the $\bar{\Gamma}$ point of the (111) surface [94]. At about the same time, ARPES maps on Bi_2Se_3 confirmed the simple dispersion of the surface state with almost circular constant energy contours and a sizeable bulk band gap of about 300 meV [106] (Fig. 3.12a). A similar Dirac cone is expected for Sb_2Te_3; experimentally it has not been verified because of the p doping of the crystal [107].

Later, an ARPES study [108] on Bi_2Te_3 (Fig. 3.12b) revealed a strong hexagonal warping of its surface state's constant energy contours (Fig. 3.12c) due to a combination of a smaller bulk

band gap and a strong trigonal potential, with implications for the spin structure [109] and the possibility for Fermi surface nesting [110]. In contrast to Bi_2Se_3 the Dirac point is not freestanding in the bulk band gap but surrounded by bulk states at higher momenta. Soon after, a variety of ternary compounds based on Bi_2Se_3, Bi_2Te_3, and Sb_2Te_3 with more complicated crystal structures and richer surface state physics were discovered to be topological insulators (see Ref. [111] for a list of experimentally verified topological insulators).

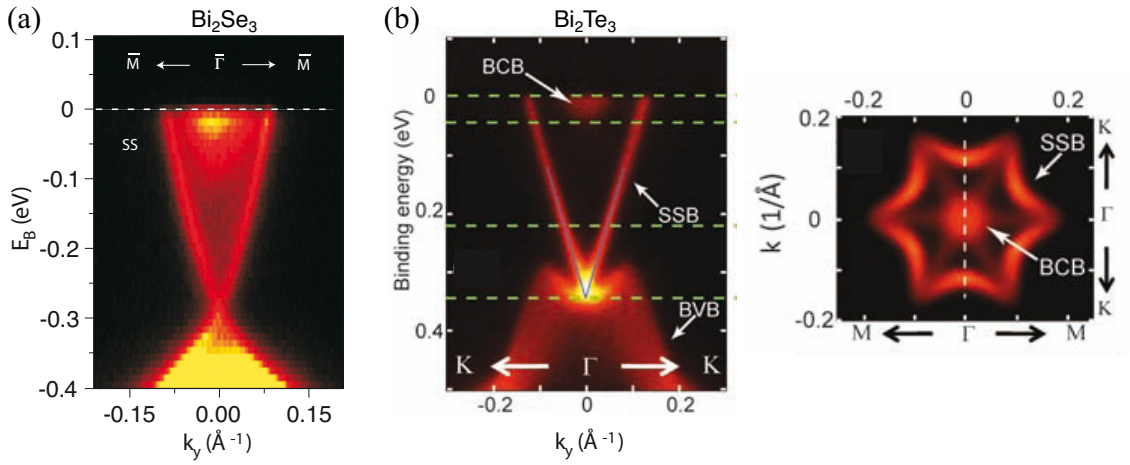

Figure 3.12: (a) ARPES band map of the surface state of Bi_2Se_3. Figure taken from [106]. **(b)** ARPES band map and Fermi surface of Bi_2Te_3 Figure taken from Ref. [108].

One of the most intriguing predicted property of the topological surface states is their guaranteed existence and insensitivity against perturbations. This triggered experimentalists to examine the influence of defects and impurities on the surface states. It was realized that Bi_2Se_3 undergoes a strong time-dependent downward band bending due to residual gases in the vacuum [112] which can be enhanced by e.g. CO or H_2O adsorption [113, 114]. In the emerging surface potential well the bulk conduction band is split into quantum well states with a Rashba-type spin splitting [43]. Due to the narrow band width of the top valence band, a quantization is simultaneously observed for these states [113]. Alternative interpretations based on DFT calculations explain the quantization with a liftoff of the top few layers due to intercalation of impurity atoms [115] which is corroborated by a combined scanning tunneling microscopy (STM) and ARPES study on Ag intercalated in the van der Waals gap of Bi_2Se_3 [116]. In all the mentioned studies the surface state was robust and only slight changes in its dispersion and line width were observed.

If magnetic order is introduced into a topological insulator, the time-reversal symmetry is broken and the protection of the surface state is lifted. For a magnetic field along the surface normal, in principle, a Zeeman gap is opened around the former Dirac point forming massive

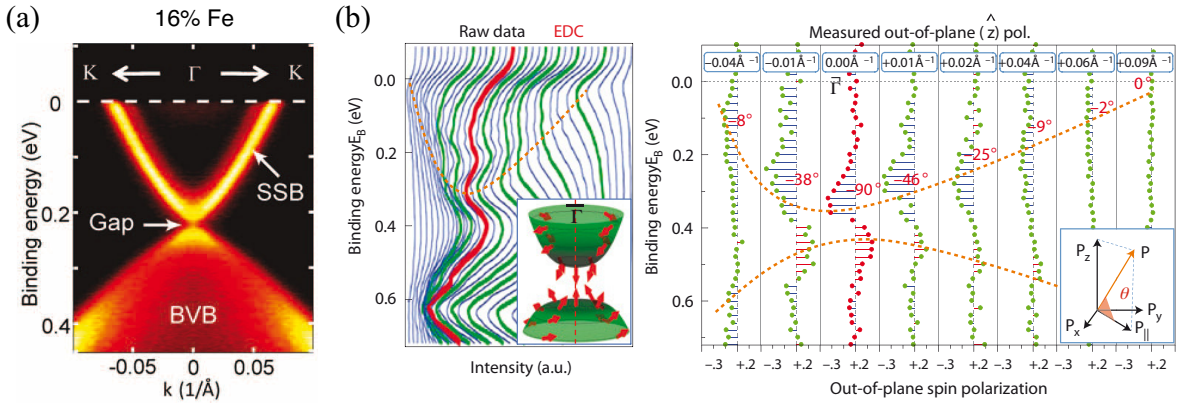

Figure 3.13: (a) ARPES band map of the surface state of Bi_2Se_3 with 16 % Fe doping featuring a gap at the former Dirac point. Figure taken from [117]. **(b)** Spin-integrated (left) and spin-resolved EDCs of the gapped surface state of Mn(2.5 %)-doped Bi_2Se_3 indicating out-of-plane polarization towards the $\overline{\Gamma}$ point. Figure taken from Ref. [118].

Dirac cones. In several ARPES studies, magnetic order was tried to achieve by magnetically doping the bulk crystal or by depositing magnetic atoms on the surface. In Ref. [117] a gap was indeed observed in Fe(12 %, 16 %)-doped Bi_2Se_3 crystal (Fig. 3.13a) which scaled with the doping concentration, whereas in the case of the non-magnetic dopant Tl (10 %) no gap was observed. Similar results were found for Mn($\leq$ 10 %)-doped crystals (Fig. 3.13b) [118]. In the latter study, spin-resolved ARPES measurements showed out-of-plane spin polarization, opposite for the upper and the lower massive Dirac cones, and increasing towards the $\overline{\Gamma}$ point (right panel of Fig. 3.13b), in accordance to what is expected from $k \cdot p$ models. Both studies lack measurements to show ferromagnetic ordering of the dilute dopants. The interpretation of a band gap opening due to ferromagnetic ordering has been called into question by more recent works. In Ref. [119] besides a slight doping effect, the gapless surface state proved to be robust against Fe deposition both at room temperature and $T = 8$ K. These findings are corroborated by a systematic ARPES study [120] for Cs, Gd, Rb as surface adsorbants, which showed similar results for nonmagnetic and magnetic dopants; in particular no gap opening was observed for the magnetic dopants but rather an immersing of the Dirac point into the bulk valence band. By means of X-ray magnetic circular dichroism measurements on a Fe-doped Bi_2Se_3(111) surfaces no hysteric behavior, i.e. no ferromagnetic order, was observed and an *in-plane* anisotropy for the Fe magnetic moments was found [121]. It remains an open question whether the previously observed gaps were induced by a remanent magnetization.

An interesting aspect of the topological surface states is their fate upon changing the bulk topology. As a fully tunable topological version of Bi_2Se_3 the compound $TlBi(S_{1-x}Se_x)_2$ was

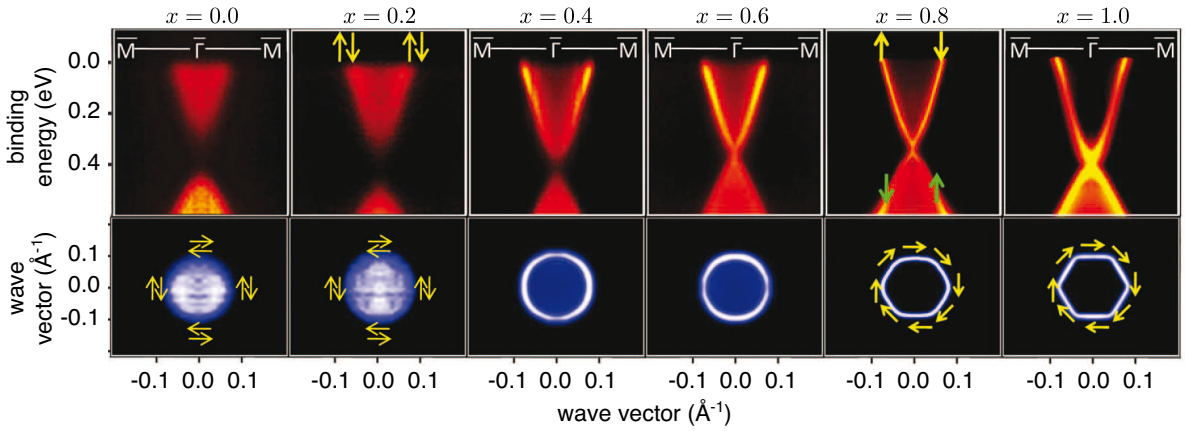

Figure 3.14: Topological transition of the system $TlBi(S_{1-x}Se_x)_2$ illustrated by ARPES band maps and Fermi surface map. For $x \geq 0.6$ the system is a three-dimensional topological insulator, for $x < 0.6$ a trivial insulator. On the trivial side of the transition spin-polarized precursor states exist at the surface. Figure taken from Ref. [96].

discovered [96, 122]. By effectively varying the S/Se ratio (x), both, the spin–orbit strength and the lattice parameters are effectively tuned [96]. As seen from Fig. 3.14, for large S concentrations the system is a trivial insulator with a direct band gap. Upon increasing the S content, the band gap decreases and two-dimensional surface states start to form at the rims of the bulk states. Around $x = 0.6$ the gap fully closes and the system enters the topological non-trivial phase with an in-direct band gap due to the slight dip in the top valence band (cf. the band map for $x = 1$ in Fig. 3.14). On the non-trivial side of the system, Dirac-cone-like surface states cross the band gap. Later spin-resolved ARPES experiments revealed that next to the topological surface state, which exhibit the typical helical spin texture, also the trivial precursor states on the trivial side of the transition have a finite spin polarization [97, 123].

In a wider context, the unique properties of the topological surface states are related to novel physical phenomena such as magnetic monopoles [124], Majorana fermions [125–127], and unconventional superconductivity [128]. After the discovery of topological insulators, other mechanism were found that can lead to new topologically distinct material classes, like topological crystalline insulators, where crystal symmetries take the role of the time reversal symmetry [129,130]. An other example is the class of topological Kondo insulators where a Kondo gap combined with a strong spin–orbit interaction results in a non-trivial phase [131, 132]. Both examples feature spin-polarized boundary states [133, 134].

It was also realized that certain band crossings in the bulk band structure of *metals* are topologically protected. Such as in the three-dimensional, magnetic Weyl semimetals [135] that are described by the Weyl equation $\mathcal{H} = \hbar v_F \, \boldsymbol{k} \cdot \boldsymbol{\sigma}$ around the Fermi level, and therefore can

not be gapped out. Their topological nature is expressed by the appearance of surface states in the form of Fermi arcs [135]. Related to this class of materials are the time-reversal invariant three-dimensional Dirac semimetals that also feature topological surface states with arcs as Fermi surfaces [136, 137].

Chapter 4

Spin texture of the topological surface states in $PbBi_4Te_7$

This Chapter describes the Dirac surface states of the topological insulator $PbBi_4Te_7$ which feature more complex physical properties than the simplest case of Dirac cones described by the effective Hamiltonian Eq. (3.22). On the one hand, the reduced symmetry of the crystal surface allows higher order corrections to the Dirac dispersion and results in a more complex spin texture (Sect. 4.1). On the other hand, the elemental contribution to the wave function of the topological surface state leads to a peculiar localization of the state, buried deep in a subsurface layer (Sect. 4.2). Parts of the text and the figures of this Chapter are published in Ref. [138].

4.1 Higher order corrections in the Dirac equation

The Dirac Hamiltonian Eq. (3.22) describes the dispersion of the topological surface state in full in-plane symmetry with circular constant energy contours and in-plane tangential spin polarization. In realistic crystal surfaces where the symmetry is reduced, the surface state dispersion can undergo a so-called warping and the spin structure deviates from the simple helical picture.

In general, the warped constant energy contours are restricted to have even-fold rotational symmetry around the TRIM, since the time-reversal symmetry guarantees the dispersion of any electronic state to be point-symmetric with respect to TRIM in the absence of magnetic fields (cf. Ch. 3). The spin texture, on the other hand, is antisymmetric with respect to the TRIM (Eq. 3.10), such that an out-of-plane polarization is only allowed in odd-fold rotational symmetric surfaces (Fig. 4.1a). If in addition, the crystal surface contains mirror planes, the

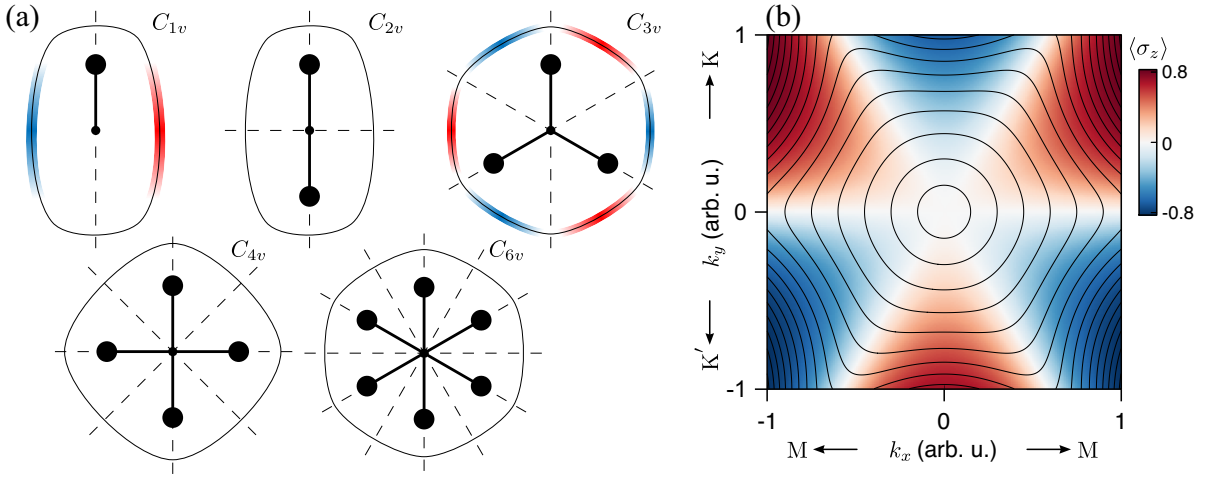

Figure 4.1: **(a)** Possible constant energy contours (solid lines) and out-of-plane spin polarization (color) for different surface symmetries with mirror planes (dashed lines). The time-reversal symmetry allows out-of-plane polarization only in odd-fold rotational symmetric surfaces. **(b)** Constant energy contours (solid lines) and out-of-plane spin polarization $\langle\sigma_z\rangle$ (color) of the spectrum of Hamiltonian Eq. (4.1) with C_{3v} symmetry.

orientation of the spin polarization is further constricted. Since the spin polarization vector transforms as a pseudovector under reflection, it has to be perpendicular to the mirror plane for a state with $\boldsymbol{k}$ within the plane.

Most of the topological insulators known to date have cleaving planes along surfaces with C_{3v} symmetry; in particular this is true for the compounds discussed within this Thesis, namely Bi_2Se_3 (Ch. 5) and Bi_2Te_3 (Sect. 4.2), and the Pb-based chalcogenides (Sect. 4.3). Further, the (0001) surfaces of BiTeX (X = Cl, Br, I) discussed in Ch. 7 have C_{3v} symmetry as well and host correspondingly warped, but topologically trivial surface states. The Hamiltonian of an electronic state on such a surface must be invariant with respect to the time-reversal operation and the members of the C_{3v} point group containing three mirror operations, and two rotations by $\pm 2\pi/3$. It can be shown [109] that the effective Hamiltonian Eq. (3.22) expanded up to third order in k, while respecting these symmetries, is of the form

$$\mathcal{H}_{\text{eff}} = \varepsilon_0(\boldsymbol{k}) + v_k\,(k_x\sigma_y - k_y\sigma_x) + \tfrac{\lambda}{2}\,(k_+^3 + k_-^3)\,\sigma_z, \tag{4.1}$$

where $k_\pm = k_x \pm i\,k_y$, and $v_k = v_{\text{eff}}\,(1 + \alpha k^2)$ includes an additional second-order correction. The cubic term yields a hexagonal warping of the constant energy contours which is small in the energetic vicinity of the Dirac point but changes the constant energy contours into star-like shapes further away from the Dirac point. The coupling of the cubic-in-k term to σ_z results in a three-fold oscillating out-of-plane component of the spin polarization (see

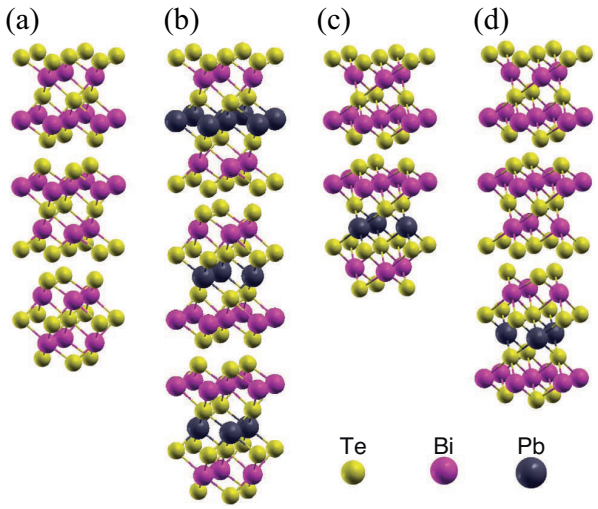

Figure 4.2: Atomic structure of Bi_2Te_3 and Pb-based ternary compounds $A^{IV}B^{VI}\,mA^{V}_{2}B^{VI}_{3}$. **(a)** Bi_2Te_3; **(b)** $PbBi_2Te_4$; **(c)** $PbBi_4Te_7$; **(d)** $PbBi_6Te_{10}$.

Fig. 4.1b, for $v_k = 1$ and $\lambda = 2$), while the absolute value of the in-plane polarization is reduced by the absolute value of the out-of-plane polarization. Up to third order in k, the in-plane spin polarization is strictly perpendicular to the momentum, and is therefore no longer tangential to the constant energy contours. Spin-resolved DFT calculations of rhombohedral topological insulators with warped surface states, however, predict in-plane polarizations that loosely follow the constant energy contour tangentially. This behavior can be effectively described by expanding the above Hamiltonian up to fifth order in k by introducing the term $i\zeta(k_+^5\sigma_+ - k_-^5\sigma_-)$, with $\varepsilon(\boldsymbol{k})$ and v_k including a forth-order-in-k term, and ζ being a constant parameter [139].

As a consequence of the warped Fermi surfaces, backscattering is less suppressed compared to the ideal helical Dirac gas. In general, this introduces changes in the properties of the surface conductivity [104, 140, 141]. The parallel sections of the Fermi surface of hexagonally warped surface state, lead to nesting which can be observed as Friedel oscillations in the LDOS in the vicinity of surface defects in STM experiments [110,142,143]. In the energy range of slight warping, backscattering is still suppressed and no oscillations can be observed. In the presence of nesting in principle allows for the existence of charge or spin density waves [144].

4.2 Effects of the elemental contribution to the topological surface state

In a real topological insulator, the surface states are derived from bulk states upon truncation of the crystal. The contribution to the near-gap bulk states is specific for the different atoms in the unit cell. Likewise, the surface state is a superposition of states localized around the atomic nuclei with specific contributions. Next to its dispersion, therefore, also the surface

state's localization depends on the chemical composition and configuration of the surface, and on the in-plane momentum.

Among the known topological insulators, the layered binary compounds Bi_2Te_3, Bi_2Se_3 and Sb_2Te_3 [106, 108, 145, 146] have been heavily investigated both experimentally and theoretically [94, 147–150]. The realization of many of the predicted topological phenomena requires tuning of the conduction properties of topological insulators, when they are in contact with magnetic semiconductors or superconductors [102, 124, 125, 128, 131, 151–155]. This tuning or modification of the topological state is usually achieved by doping or intercalation. A promising way to design new topological insulator materials with tunable surface electronic properties relies on the fact that pseudo-binary systems $A^{IV}B^{VI} - mA_2^{V}B_3^{VI}$ (A^{IV} = Ge, Sn, Pb; A^{V} = Bi, Sb; B^{VI} = Te, Se) form homologous series of ternary compounds. These include a wide variety of mixed-layer materials that have a more complex crystal structure than their parent Bi_2Te_3-type compounds. All these systems have tetradymitelike layered structures but with distinct many-layered slabs stacked along the c axis of the hexagonal unit cell. The bonding within the slabs is ionic–covalent, whereas the slabs are linked by weak van der Waals forces.

Most of these compounds are three-dimensional topological insulators (see Table 4.1 for their $\mathbb{Z}_2$ topological invariants determined by the method for inversion-symmetric crystals described in Sect. 3.4.1). Peculiarities of the bulk spectrum of these materials give rise to more complex surface band structures that depend on the surface termination, which can be quintuple layer (5L) or septuple layer (7L) terminated. Here we concentrate on the Pb-based compounds of Bi_2Te_3 type. The crystal structures of the parent compound and Pb-based systems are shown in Fig. 4.2. In contrast to Bi_2Te_3 (Fig. 4.2a), whose structure is formed by 5Ls, the structure of $PbBi_2Te_4$ contains 7L slabs (Fig. 4.2b), whereas $PbBi_4Te_7$ and $PbBi_6Te_{10}$ are formed by combining 5L and 7L building blocks (Figs. 4.2c,d).

4.2.1 Bulk electronic structures of Pb-based Bismuth tellurides

Parent compounds The binary chalcogenides Bi_2Te_3, Bi_2Se_3, and Sb_2Te_3 are three-dimensional topological insulators with the conducting topological surface state mostly localized in the outermost 5L block [94]. The surface electronic structure and spatial localization of the Dirac state of the parent compound Bi_2Te_3 are shown in Fig. 4.3a. The shapes of the ab-initio iso-energy contours in the vicinity of the $\overline{\Gamma}$ point are hexagonally warped in accordance with those predicted from the model calculation (Sect. 4.1, [109,139]) and show an out-of-plane spin component along $\overline{\Gamma}$–$\overline{K}$, which increases with increasing warping (Fig. 4.3b). Layer-resolved calculations of the spin structure (Fig. 4.3c) exhibit oscillatory contributions to the total spin, both in the helicity and the out-of-plane component, similar to the layer-dependent contri-

m	Bi_2Te_3	ν_0	Sb_2Te_3	ν_0	Bi_2Se_3	ν_0
1	$GeBi_2Te_4$	1	$GeSb_2Te_4$	1		
	$SnBi_2Te_4$	1	$SnSb_2Te_4$	1	$SnBi_2Se_4$	0
	$PbBi_2Te_4$	1	$PbSb_2Te_4$	1	$PbBi_2Se_4$	1
2	$GeBi_4Te_7$	1	$GeSb_4Te_7$	1		
	$SnBi_4Te_7$	1	$SnSb_4Te_7$	1	$PbBi_4Se_7$	1
	$PbBi_4Te_7$	1	$PbSb_4Te_7$	1		
3	$GeBi_6Te_{10}$	1	$GeSb_6Te_{10}$	0		
	$SnBi_6Te_{10}$	1				
	$PbBi_6Te_{10}$	1				

Table 4.1: The $\mathbb{Z}_2$ topological number ν_0 for $n\mathrm{A^{IV}B^{VI}} - m\mathrm{A_2^VB_3^{VI}}$ ($n = 1$; $m = 1$–3) compounds based on the Bi_2Te_3, Sb_2Te_3, and Bi_2Se_3 parent phases.

butions to the total spin splitting in Pb quantum-well states [156]. The Dirac cone in Bi_2Te_3 originates from the inversion of the bands forming the gap edges: the conventional sequence of the energy levels is inverted by strong spin–orbit interaction [95, 157]. The bottom of the conduction band in the vicinity of the Γ point is predominantly derived from the states localized at the outermost 5L Te atoms whereas the top of the valence band is formed by the Bi atoms.

Pb-based ternary compounds A similar band inversion is found in $PbBi_2Te_4$, with the only difference that the top of the valence band is constituted by both Bi and Pb states (Fig. 4.4a). In $PbBi_4Te_7$ (Fig. 4.4b) and $PbBi_6Te_{10}$ a more complicated spin–orbit-induced band structure is found with alternating 5L and 7L slabs. Here the gap edges are formed by the atoms of the 7L of the crystal structure. This leads to some peculiarities in the formation of the topological state in these compounds, as will be discussed below.

4.2.2 Surface electronic structure of $PbBi_4Te_7$

In the following we will focus on the surface spectrum of $PbBi_4Te_7$. Figure 4.5 shows DFT calculations of the surface band structure of $PbBi_4Te_7$. Because the crystal structure of $PbBi_4Te_7$ is constituted by alternating 5L and 7L building blocks (Fig. 4.2c), the surfaces formed after cleavage of this crystal have two possible terminations. For the 7L-terminated surface (Fig. 4.5a), the dispersion of the topological surface state is similar to the 5L termination except that the cone is more warped near the conduction band minimum and features a slight concave dispersion close to the Dirac point. While the spatial localization of the Dirac state is

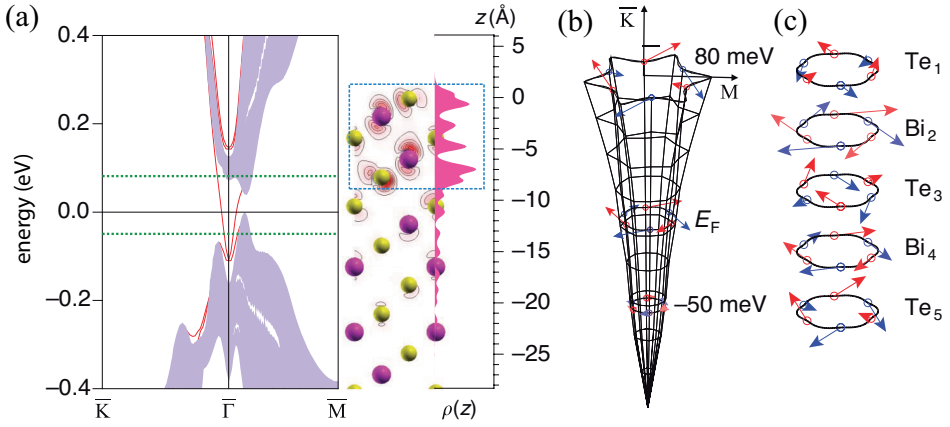

Figure 4.3: Surface electronic and spin structure of the parent Bi_2Te_3 compound. **(a)** Surface band structure of Bi_2Te_3 and spatial charge density distribution of the Dirac state (blue dashed rectangle marks the outermost 5L block). **(b)** Dirac cone with iso-energy contours at energies indicated in (a) by green dashed lines and at the Fermi energy; arrows indicate both the total spin magnitude and direction whereas red and blue represent positive and negative out-of-plane component of the spin, respectively. **(c)** Layer-resolved spin structure of the Dirac state in the topmost 5L of Bi_2Te_3 at the Fermi energy.

in the terminating 7L; for the 5L-terminated surface (Fig. 4.5b), the situation is more intriguing; the topological surface state is also localized in the outermost 7L block, which is now a subsurface block. Thus, in this system, the Dirac state at the $\overline{\Gamma}$ point is buried about 10–25 Å below the surface, which makes this state more protected against possible surface modifications. This localization of the Dirac state in the 7L block follows from the aforementioned peculiarity of the bulk band structure of $PbBi_4Te_7$; as one can see in Fig. 4.4b, the gap edges are formed by spin–orbit-interaction-inverted states, localized at atoms of the 7L block (in particular the Pb atoms), which form the Dirac cone on breaking the translational symmetry at the surface. Next to the topological Dirac state trivial surface state exist on both possible surfaces. Furthermore, the surface states at the 5L-terminated surface, are related to the surface states found on the parent compound Bi_2Te_3 (cf. Fig. 4.3a), namely the unoccupied Rashba-type spin-split state (red lines with roughly 0.2 eV energy at the $\overline{\Gamma}$ point in Fig. 4.5b) and the occupied state (blue lines with -0.2 eV at $\overline{\Gamma}$ Fig. 4.5b), which becomes the Dirac state in the parent compound. Accordingly, the charge distribution (blue line in the right panel of Fig. 4.5b) of this state is similar to the Dirac state in Bi_2Te_3.

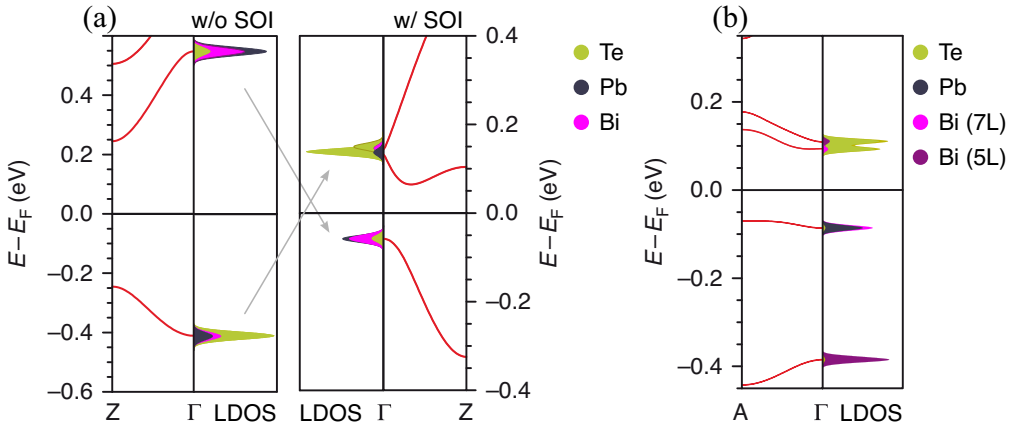

Figure 4.4: (a) Spin–orbit-induced band inversion scheme in $PbBi_2Te_4$. Band structure without spin–orbit interaction (*left panel*) and with spin–orbit interaction (*right panel*). **(b)** Calculated orbital composition including spin–orbit interaction of the near-gap bands in $PbBi_4Te_7$. The colors in the LDOS show the localization of the state on the different atomic sites; The conduction band is mainly Te derived while the valence band is mainly derived from Pb and Bi states in the 7L.

4.3 Fermi surface mapping of the $PbBi_4Te_7$ topological surface state

To study the depth dependence of the topological surface state, ARPES and STM experiments were performed on $PbBi_4Te_7$ single crystals, as shown in Figs. 4.6 and 4.7, respectively. The ARPES measurements were obtained at a sample temperature of 20 K (60 K for the spin-resolved scans). Compared with the *ab-initio* results from Figs. 4.5a,b, we observe a rigid band shift of about 500 meV, presumably because of bulk and surface defects. Between binding energies of about 0.3 eV and 0.5 eV, the spectra (Figs. 4.6a,b) and the constant energy contours (Fig. 4.6c) only show the topological surface state. At lower binding energies, one observes both the topological state and the bulk states, which can also be identified by their three-fold intensity symmetry. Along the $\overline{\Gamma}$–$\overline{M}$ direction, the bulk bands cross the topological state, whereas along the $\overline{\Gamma}$–$\overline{K}$ direction, the topological surface state remains clearly separated from the bulk bands. At binding energies higher than the Dirac point, the topological state and the bulk bands overlap for a small energy range and, for even higher binding energies (from 0.6 eV), one observes only the bulk bands. A detailed analysis of the band dispersion of the Dirac cone, as exemplified by the constant energy contours in Figs. 4.6d,e and the slightly convex energy dispersion, indicates that the photoemission signal primarily originates from a 5L-terminated surface.

On the other hand, the STM data in Figs. 4.7a,b indicate that both surface terminations are

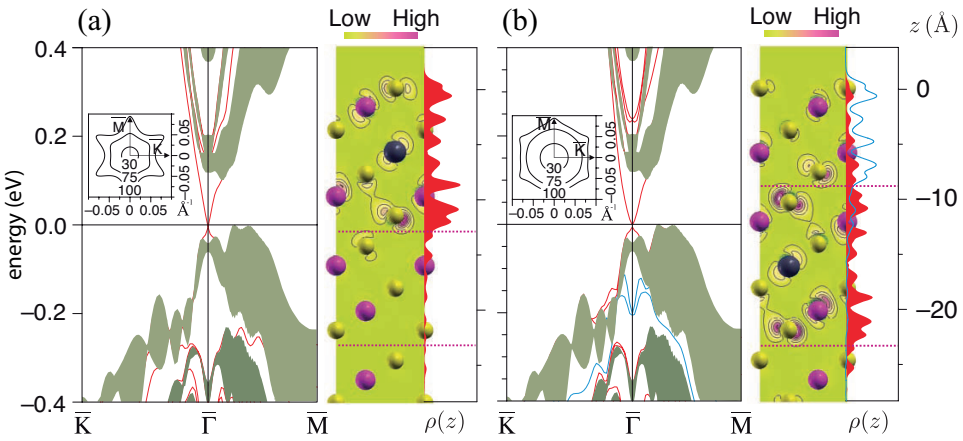

Figure 4.5: Surface electronic structure of $PbBi_4Te_7$ with **(a)** 7L and **(b)** 5L terminated surface. *Left panels*: Calculated surface band structure. The insets show the iso-energy contours of the Dirac cone at various energies. *Right panels*: Spatial distribution of the charge density of the Dirac state at the $\bar{\Gamma}$ point in the $(11\bar{2}0)$ plane and the charge density $\rho(z)$ (red) of this state integrated over the x–y plane; $z = 0$ corresponds to the surface atomic layer.

present. For the measurements, both tungsten tip and sample were cooled to $T = 30\,\mathrm{K}$. The images show alternating step heights of 10 Å and 14 Å that correspond to the predicted heights of the 5L and 7L in the $PbBi_4Te_7$ crystal, respectively. An analysis of the surface termination including 18 images with a total area of $212.7\,\mu\mathrm{m}^2$ reveals a coverage of about 53 % for 7L layers and 47 % for 5L layers. Atomically resolved images exhibit a clear hexagonal lattice. There is no discernible difference between the atomic resolution images of either the 5L or 7L indicating that, in each case, the STM is imaging the tellurium surface sublattice.

Self-burying model This apparent contradiction between the ARPES and STM results might be resolved by considering the defect density at the surface and the fact that the topological state lies beneath the surface for energies well below the conduction band (Fig. 4.5b) while on approaching the conduction band it shifts to the outermost 5L block (Fig. 4.7c). The latter fact leads to further increase of the intensity and the linewidth of the Dirac cone at energies at (and above) the conduction band minimum (Fig. 4.6a) with respect to the lower energies due to defect scattering. In the 5L-terminated areas of the surface, the topological state is located for small $k_{\|}$ in the 7L subsurface block, protecting this state against scattering at the surface. On the other hand, at the 7L terminated surface areas defects might push the topological state down to the next subsurface 7L block, as sketched in Fig. 4.7d, where it is no longer accessible by ARPES. This interpretation is corroborated by the absence of the occupied surface state (blue line in Fig. 4.5b) in the measurements; the topmost layers can not accommodate

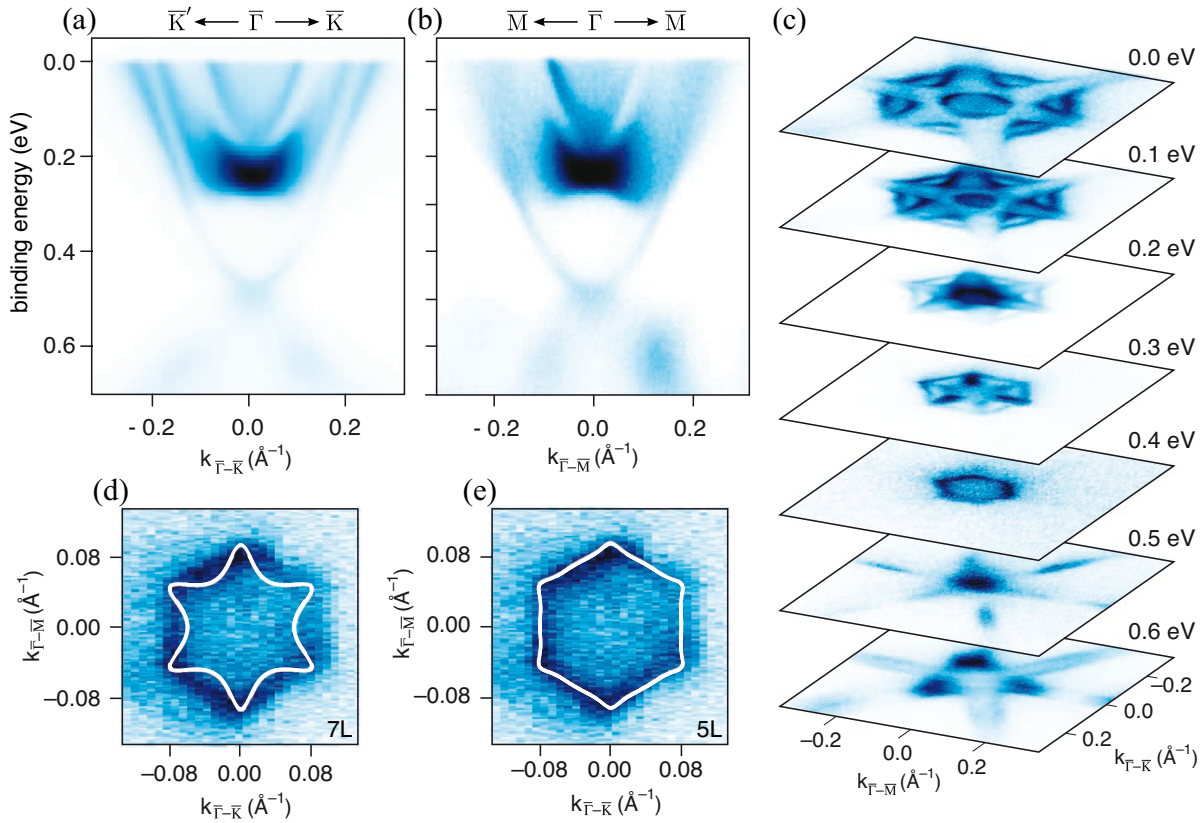

Figure 4.6: Spin-integrated band structure map of $PbBi_4Te_7$ measured at $h\nu = 20\,\text{eV}$ along the **(a)** $\overline{\text{K}}'$–$\overline{\Gamma}$–$\overline{\text{K}}$ and **(b)** $\overline{\text{M}}$–$\overline{\Gamma}$–$\overline{\text{M}}$ direction and **(c)** iso-energy contours at various binding energies. **(d)** and **(e)** comparison between measured and calculated iso-energy contours 100 meV above the Dirac point for the 7L and 5L surface terminations, respectively.

a surface state; however, because of its protected nature, the topological state shifts down further into the bulk. To date a direct experimental observation of the retraction of the surface state is missing. But in a theoretical tight-binding study it could be shown that upon introduction of randomly distributed non-magnetic surface disorder, the topological surface state is broadened for weak disorder and retracts to the subsurface layer in the case of strong disorder and restores its dispersion [158].

A more recent ARPES study [159] on the surface states of $PbBi_4Te_7$ presented band maps of the Dirac cone for a photon energy of 22 eV consistent with the here presented data. But in measurements with a Xe lamp as excitation source (8.6 eV) a superposition of two Dirac cones was observed. By comparing the dispersions of the cones, the authors attributed the surface state observable at both photon energies to the 7L-terminated surface, while the state on the 5L-terminated surface would be only probed in the more bulk-sensitive measurement

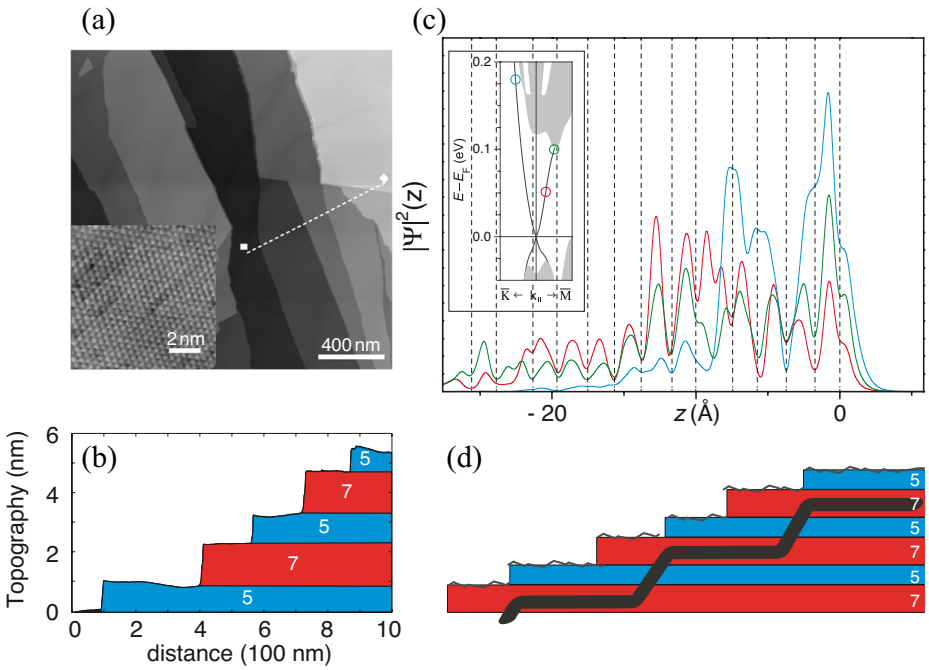

Figure 4.7: **(a)** STM topograph showing the mixture of 5L and 7L steps ($V_{\text{bias}} = 0.5\,\text{V}$, $I_t = 0.25\,\text{nA}$). The inset shows an atomic resolution image on a 5L-terminated surface ($V_{\text{bias}} = 0.5\,\text{V}$, $I_t = 10.5\,\text{nA}$). **(b)** Height profile along the dashed line. **(c)** Calculated energy-dependent charge density distribution of the surface state on a 5L-terminated surface, the vertical dashed lines indicate the position of the nuclei. **(d)** Proposed self-protecting behavior of the topological state

at lower photon energies. Triggered by this result, we performed additional measurements in the search for a spot on the sample surface where this second Dirac cone could be observed also for $h\nu = 20\,\text{eV}$. Figure 4.8 presents ARPES band maps where in the in-gap region spectral intensity from two superimposed Dirac cones is evident. It is concluded that the outer Dirac cone corresponds to the cone observed in the previous measurements (Fig. 4.6) based on the comparison of the Dirac point energies and the dispersions. In particular the outer cone is convex, consistent with Fig. 4.6, whereas the inner Dirac cone is slightly concave (Fig. 4.8a). Further, the homogeneous intensity distribution of the hexagonal constant energy contour of the outer Dirac cone (Fig. 4.6c) reflects what is observed in Fig. 4.6e, in constrast to the strong three-fold intensity variation of the inner cone. These arguments and the comparison with the *ab-initio* calculations, lead to the conclusion that the outer (inner) cone is the surface state of the 5L (7L) termination, consistent with the above interpretation but opposed to what is stated in Ref. [159]. In the light of these new results, the statement of a general quenching of the top-7L surface state must be put into perspective. An alternative explanation for the

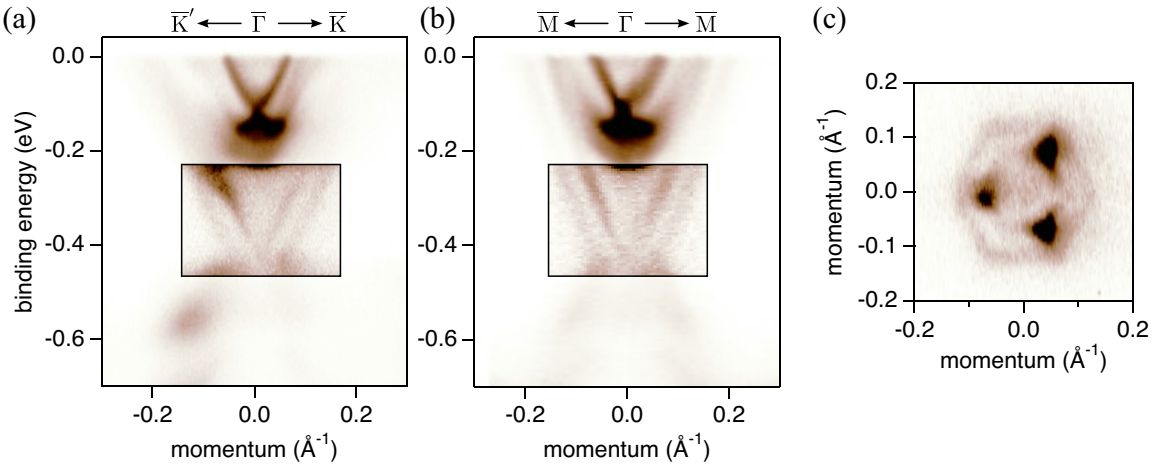

Figure 4.8: ARPES map for $h\nu = 20\,\text{eV}$ on a sample spot with both terminations present along the **(a)** $\overline{K}'$–$\overline{\Gamma}$–$\overline{K}$ and **(b)** $\overline{M}$–$\overline{\Gamma}$–$\overline{M}$ direction. The in-gap region is highlighted by an adjusted color scale. **(c)** Constant energy cut 200 meV above the Dirac point of the outer cone shows two concentric hexagons.

observed 7L spectrum could be crystal impurities in the form of $PbBi_2Te_4$ islands. In the case of a retraction, the surface state would then be only be covered by a 7L rather than by a 5L *and* a 7L, and possibly still accessible by ARPES. In either case, a systematic spatially resolved ARPES study is necessary to quantify the spatial abundance of the two possible electronic surface structures.

4.3.1 Spin structure of the $PbBi_4Te_7$ topological surface state

After having verified the electronic structure of the topological state, we address its spin structure, which is directly linked to the topological properties. In Fig. 4.9a, the calculated layer-resolved spin structure of the Dirac state is visualized at 50 meV and 100 meV above the Dirac point in the two topmost blocks. The magnitude of the local spin follows the charge density localization of the state shown in Fig. 4.7c. This behavior may allow for the possibility to tune the spatial localization of the spin transport channel by shifting the Fermi level. The spin structure of the Dirac state at the 5L-terminated surface of $PbBi_4Te_7$, as well as at the 7L-terminated surface of this compound and at the surfaces of the other Pb-Bi-Te compounds, agrees in all features with that of its parent binary compound. In particular, a counter-clockwise spin rotation in the topmost Te atom is found, regardless of the surface termination, whereas for all other atomic layers it is clockwise.

To determine the net helicity for the complete wave function of the Dirac state, we performed

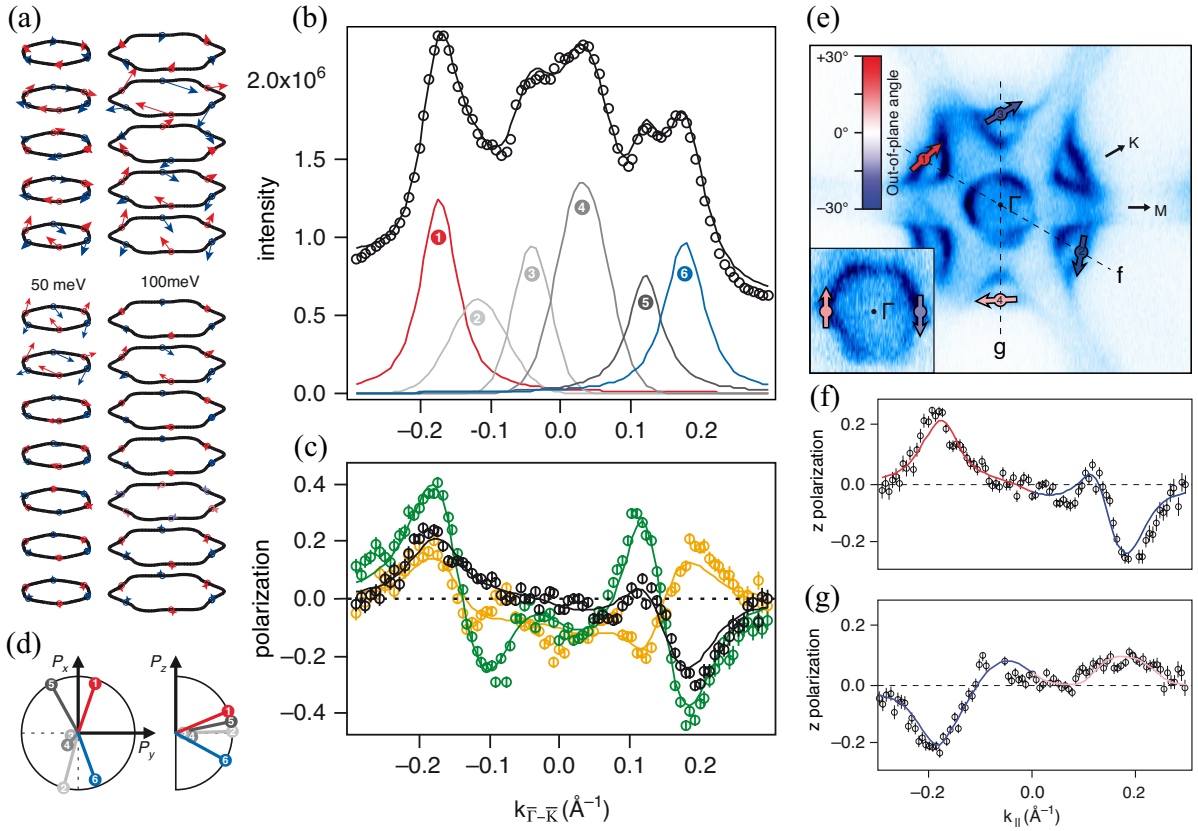

Figure 4.9: Measured and calculated spin texture of $PbBi_4Te_7$. **(a)** Calculated layer-resolved spin structure throughout a complete unit cell 50 meV and 100 meV above the Dirac point for the 5L-terminated surface. **(b)** Total intensity of a spin-resolved momentum cut 10 meV below the Fermi energy with fitted peaks. **(c)** Measured (symbols) and fitted (solid lines) spin polarization along the three spatial directions: P_x is orange, P_y green and P_z. black. **(d)** Peak-specific spin polarization vectors where the numbers refer to the fitted peaks of (b). **(e)** Summary of the spin texture for two different binding energies (10 meV and 350 meV (inset)), the arrows correspond to the obtained spin polarization vectors where the color reflects the out-of-plane angle (see color scale). **(f)** Measured out-of-plane spin polarization along $\overline{\mathrm{K}}$–$\overline{\Gamma}$–$\overline{\mathrm{K}}'$. **(g)** Corresponding measurement with sample azimuth rotated by $\varphi = 60\,^\circ$ along the neighbouring $\overline{\mathrm{K}}'$–$\overline{\Gamma}$–$\overline{\mathrm{K}}$ line showing an opposite out-of-plane spin polarization.

spin-resolved ARPES measurements. Figures 4.9b,c show a spin-resolved momentum cut along the $\overline{\mathrm{K}}'$–$\overline{\Gamma}$–$\overline{\mathrm{K}}$ direction at a binding energy of 10 meV, cutting both through the topological state and the bulk states. By using a vectorial analysis routine (Sect. 2.2.2, [44]), one can assign a three-dimensional spin-polarization vector to each band throughout the constant energy surface, as summarized in Fig. 4.9d. Note that the photoelectrons stemming from

the bulk states also show spin polarization due to photoemission transition matrix element effects. But upon changing the photon energy, the measured polarization from bulk states drastically changes while the surface state polarization is robust (see Ch. 6 for a more detailed discussion).

The out-of-plane spin polarization shows an even stronger difference in the contributions from each atomic layer, both in direction and magnitude compared to the in-plane polarization. Unfortunately, spin-resolved ARPES is not suited to link the absolute crystal orientation to the calculations, and it is thus not possible to discriminate which atomic contribution prevails. On the other hand, in the spin-resolved ARPES measurements in Figs. 4.9e–g, the three-fold symmetry of the out-of-plane polarization is reproduced including the smooth changes between $\overline{\Gamma}$–$\overline{\mathrm{K}}$ and $\overline{\Gamma}$–$\overline{\mathrm{M}}$. It should be noted that, although the out-of-plane spin polarization (P_z) is related to the warping [109] and disappears when the warping factor goes to zero (Fig. 4.1a), the atomic layer contributions show that warping does not directly determine the direction and magnitude of P_z.

4.4 Conclusion

In this Chapter was discussed, how the chemical composition of the surface and its symmetry affect the dispersion, spin texture and localization of the topological surface state. In particular it was shown, that in the homologous series of ternary compounds based on Bi_2Te_3, Bi_2Se_3 and Sb_2Te_3, most of the compounds $A^{IV}B^{IV}-mA_2^VB_3^{VI}$ (A^{IV} = Ge, Sn, Pb; A^V = Bi, Sb; B^{VI} = Te, Se; $m = 1$–3) are three-dimensional topological insulators. Part of these systems ($m = 2$, 3) represent naturally grown superlattices composed of 5L and 7L blocks, which demonstrate much richer physics than the parent topological insulators. Their more complex surface electronic and spin structures originate from peculiarities of the bulk spectrum of these materials.

The presented findings provide a promising pathway to tune both the electronic and spin properties of a topological insulator, by using the ordered ternary compounds on the basis of well-known binary topological insulators. These compounds exhibit a more complicated surface electronic structure and spin behavior than their binary parents, which provides an efficient way to manipulate both the spin structure and the spatial localization of the conducting state. This subsequently may allow for a variation of the depth of the spin transport channel below the surface. The spin-resolved measurements and atomic layer resolved theory provide a new pathway to the aimed design of spin structure properties in topological insulators.

Chapter 5

Topological transition in ultra-thin Bi_2Se_3 films

The classification of a material as a $\mathbb{Z}_2$ topological insulator with protected metallic states at its surfaces is a global property of the occupied bulk band structure (cf. Sect. 3.4.1). On the other side, the characteristics of a surface state such as its dispersion or the spin structure depend on the chemical composition (Sect. 4.2), structure and symmetry (Sect. 4.1) of the particular surface. Naturally, changing these surface parameters allow for tuning of the properties of the surface state [45,74,77,79]. A more indirect way to engineer the surface state is changing the bulk band structure, while retaining the non-trivial topology by for example iso-valent doping of the bulk crystal [160,161] or introducing ternary elements (Ch. 4). Even more intriguing is the fate of the surface state in the case where the bulk band structure is continuously driven across the topological transition ultimately becoming a normal insulator. Recent ARPES studies showed that the system $BiTl(S_{1-x}Se_x)_2$ undergoes a topological transition upon sulfur doping, while being a trivial semiconductor for large sulfur doping concentration, after having closed the bulk band gap at $x = 0.6$ it enters the topological insulator phase for low sulfur content [97, 123]. Interestingly, the materials of this system host spin-polarized precursor states even on the trivial side of the transition from which the topological surface states smoothly emerge at the phase transition [123].

When the dimensions of a crystal are reduced to a few units cells, the physical properties start to deviate from the bulk materials and thickness-dependent finite-size effects appear. Since also the band structure depends on the thickness of the material, it is expectable that topological transitions can occur when changing the film thickness. Indeed, such a topological transition was found e.g. in the electronic structure of HgTe films, which enter a two-dimensional QSH phase above a critical thickness [91,92]. It is then a natural question to ask, how many unit cell are needed to form a three-dimensional topological insulator. This is

the topic of the following Chapter.

We will discuss the electronic structure of the three-dimensional topological insulator Bi_2Se_3 in the limit of few quintuple layer (QL) thick films, in particular the evolution of the topological surface state and its spin texture. By means of spin-integrated and spin-resolved ARPES, the spin structure of thin films Bi_2Se_3 grown on InP(111)B are studied. For small thicknesses the spin-polarized metallic topological surface states on either sides of the film interact with each other via quantum tunneling and below 6 QL a gap is resolved [148,162,163]. The resulting surface states can be described by massive Dirac cones which are split in a Rashba-like manner due to the substrate-induced inversion asymmetry. The inner and the outer Rashba branches have distinct localization in the top and the bottom part of the film, whereas the band apices are delocalized throughout the entire film. Supported by *ab-initio* calculations, the observations help understand the evolution of the surface states at the topological phase transition and contribute to the groundwork for the realization of two-dimensional spintronic devices based on topological semiconductors.

5.1 Bulk properties of Bi_2Se_3

Bi_2Se_3 has a rhombohedral crystal structure with five atoms in the unit cell, which can also be represented as a hexagonal structure with 15 atoms in the unit cell [94, 147] (Fig. 5.1a).

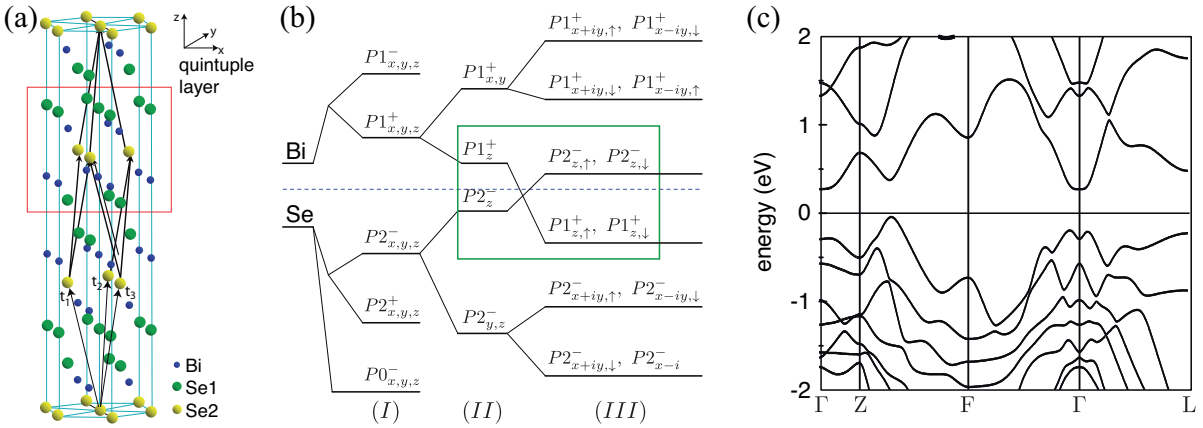

Figure 5.1: **(a)** Bi_2Se_3 crystal structure with a rhombohedral unit cell ($a = 4.076$ Å, $c = 29.830$ Å [94]) of space group $R\bar{3}m$ (black lines) and quintuple layer (red). **(b)** Illustration of the band inversion at the Γ point of the atomic Bi and Se p orbitals upon turning on (*I*) chemical bonding, (*II*) crystal field splitting, and (*III*) spin–orbit interaction. **(c)** DFT calculation of the Bi_2Se_3 bulk band structure. Figures taken from Ref. [94].

Along the trigonal axis, the compound is layered and built up out of QLs (Se1–Bi–Se2–Bi–Se1). Within the QLs the bonding is mainly ionic–covalent, whereas the bonding between the QLs is predominantely of van der Waals type. This weak bonding plane provides a natural cleaving plane such that cleaved Bi_2Se_3(111) surfaces are terminated by a single atomic Se layer [164]. Since the Se2 atoms are inversion centers of the crystal, the topology of the band structure can be determined from the product of the TRIM parity of the occupied bands (Eq. 3.21). The bands closest to the gap have opposite parity and their order is reversed at the Γ point by the spin–orbit interaction but retain their order at the other TRIM (Fig. 5.1b) [94]. A detailed analysis of the parities of all the occupied bands shows that this band inversion makes Bi_2Se_3 a three-dimensional topological insulator [94]. The reversal of the effective mass in the top valence band of the bulk structure around the Γ point and the indirect band gap is a result of the spin–orbit-interaction-induced avoided crossing (Fig. 5.1c).

Experimental indications for metallic two-dimensional states localized in the surface QL have been found already in an STS study before it was realized that Bi_2Se_3 is a topological insulator [165]. Later, high-resolution ARPES measurements confirmed the theoretical predictions based on DFT calculations of a single Dirac cone at the $\overline{\Gamma}$ point [106]. Spin-resolved ARPES measurements verified the spin polarization of the surface state and gave final proof of the non-trivial character of the surface states [43, 166]. The rest of this Chapter deals with thin films of Bi_2Se_3, especially the evolution of the topological surface state.

5.2 Bi_2Se_3 at the dimensional crossover

For $k_z = 0$, the Hamiltonian (3.19) for a three-dimensional topological insulator reduces to the model Hamiltonian by Bernevig, Hughes, and Zhang [91] describing a two-dimensional QSH insulator [162]. It is therefore not surprising that under certain circumstances a three-dimensional topological insulator may enter the QSH phase when its dimensions are reduced to a thin film. In fact, the quantum well states in a thin-film topological insulator shows a thickness-dependent gap inversion similar to the HgTe films [91, 92] if $\nu_z = 0$ in Eq. (3.19) (cf. Fig. 5.2a). For the general case where $\nu_z \neq 0$, hole- and electron-like states with the same parity hybridize (while retaining the parity at $k = 0$), and a gap opens and closes with thickness. Due to the opposite parity of the gap-defining states S_1^+, S_2^- (cf. Fig. 5.2b), the system oscillates between a trivial insulator and a two-dimensional QSH phase (Fig. 5.2b) with metallic one-dimensional edge states [162]. For larger thicknesses the gap decreases and eventually closes, then S_1^+, S_2^- become the bonding and anti-bonding surface states of a three-dimensional topological insulator [162]. This oscillatory change of topology results from the effective Hamiltonian (3.19) and is reproduced in *ab-initio* calculations of the electronic structure of Bi_2Se_3 which predict a QSH phase with a sizeable gap for film thicknesses of

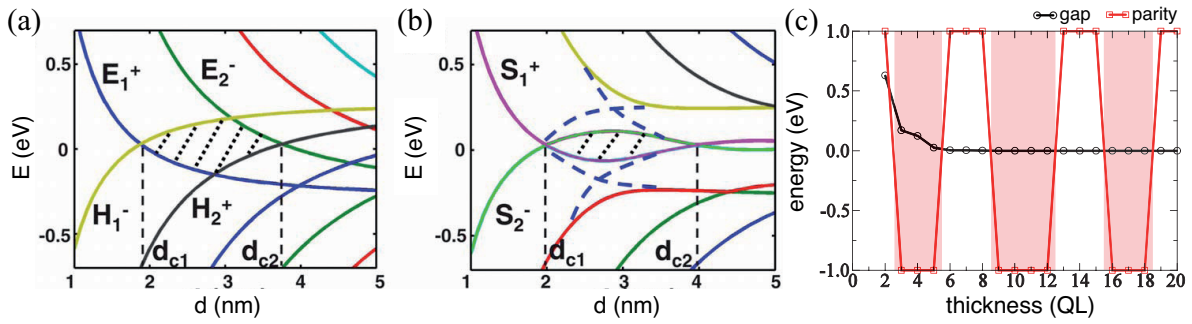

Figure 5.2: (a) Quantum well energies of Hamiltonian (3.19) at $k_{\parallel} = 0$ for $v_z = 0$ and **(b)** $v_z = 1.1\,\text{eV Å}$ as a function of well thickness. d_{c1} and d_{c2} indicate the lower and upper limit of the lowest-thickness QSH phase. **(c)** Band gap and total parity as a function of the Bi_2Se_3 thickness. Figures adopted from Ref. [162].

3–5 QL (Fig. 5.2c) [99, 162, 163]. A direct observation of the edge states is to date still missing, due to difficulties of discerning the surface from the strong bulk conductivity which occurs due to the tendency of Bi_2Se_3 to be strongly n-doped by growth defects. On the other hand, a spectroscopic study claims to have found indirect evidence for 2 QL thick Bi_2Se_3/Si(111) to be in the QSH state, based on the top valence band dispersion [167].

Films of Bi_2Se_3 have been grown by molecular beam epitaxy on various substrates [148, 167–171]. In addition to the gap opening, Zhang *et al.* observed by ARPES measurements on Bi_2Se_3 films grown on a graphene double-layer that the massive Dirac state for films with thicknesses below 6 QL appears to show a Rashba-like spin splitting [148], in accordance with a theoretical study [99]. It remained unclear how the topological surface states exactly emerge from these Rashba-split states at the topological phase transition.

Given the inherent difference between the chemical potential in the bulk and at the surface of such small band gap semiconductors [160], any technological application of the unique properties of topological insulators will most likely be based on thin films. However, the strong coupling between the surface states on both sides of the film is expected to significantly influence their spin structure. Therefore an experimental verification of the spin structure of the surface states in the ultrathin limit is essential.

In this Chapter, systematic spin-resolved ARPES measurements of the surface states of Bi_2Se_3 films on InP(111)B with thicknesses ranging from 2 QL to 6 QL are presented. Evidence of a Rashba-like spin-splitting of the hybridized surface states is found and DFT calculations model the observations and clarify the evolution of the dispersion and the localization of the surface states upon the transition from the two-dimensional limit to the three-dimensional topological insulator.

5.3 Bi_2Se_3 growth on InP(111)B

The films were grown by molecular beam epitaxy in a vertical CreaTec system, equipped with standard effusions cells for Se and Bi (99.9999 % purity each) at a base pressure below 10^{-10} mbar. Undoped InP(111) wafers were used as substrate, and their natural oxide layer was removed by a dip in 50 % hydrofluoric acid. The substrate temperature during the growth was 300 °C for all films. The fluxes of Bi and Se were constant, with a growth speed of 1 nm per minute, under Se rich conditions. The film thicknesses were determined by the growth time, which was calibrated by X-ray diffraction thickness fringes on a reference bulk film. After growth, the samples were cooled *in-situ* to a temperature below 15 °C, and were then capped with an amorphous Se layer to protect the films during *ex-situ* transport. In the ARPES chamber the films were decapped by heating the sample to a temperature of about 120 °C.

Scanning transmission electron microscopy studies on the microstructure of Bi_2Se_3 films on InP(111)B showed the existence of an interface layer with poor crystalline quality. The thickness of this amorphous interface layer varies across the sample ranging from zero, with a sharp interface between the substrate and Bi_2Se_3, up to 1 nm (corresponding roughly to the height of one QL). The subsequent layers show crystalline structure though with lamellar and rotational twinning, the latter occurs because of the two possible layer stacking orders in the Bi_2Se_3 unit cell. By atomic force microscopy, it could be shown that the film surface consists of pyramid-shaped twin domains of a size which increases with layer thickness. [168, 172, 173] A recent study showed that on rough Fe-doped InP(111)B the twinning in Bi_2Se_3 is suppressed [174].

The effects of the imperfect crystallinity on the ARPES measurements are two-fold. First, the 60 ° rotational twinning of Bi_2Se_3/InP(111)B cancel out any out-of-plane spin polarization induced by warping (cf. Ch. 4). And secondly, the film thicknesses are not homogeneous throughout the sample. In the following, the thickness declarations correspond to the spatial thickness average over the sample as determined by the X-ray diffraction measurements.

5.4 Topological transition of ultra-thin Bi_2Se_3 films

Figure 5.3a shows spin-integrated ARPES band maps of Bi_2Se_3/InP(111)B films with thicknesses ranging from 2 QL to 6 QL. The data are taken along the $\overline{\Gamma}$–$\overline{\mathrm{M}}$ direction with *p*-polarized light of 20 eV photon energy, which placed the perpendicular momentum of the initial state around the Brillouin zone center for bulk crystals. In the band map for the 5 QL film, dashed lines indicate the different bands contributing to the spectra. The Dirac cones (orange, red) are separated by a band gap accompanied by a non-linear dispersion around

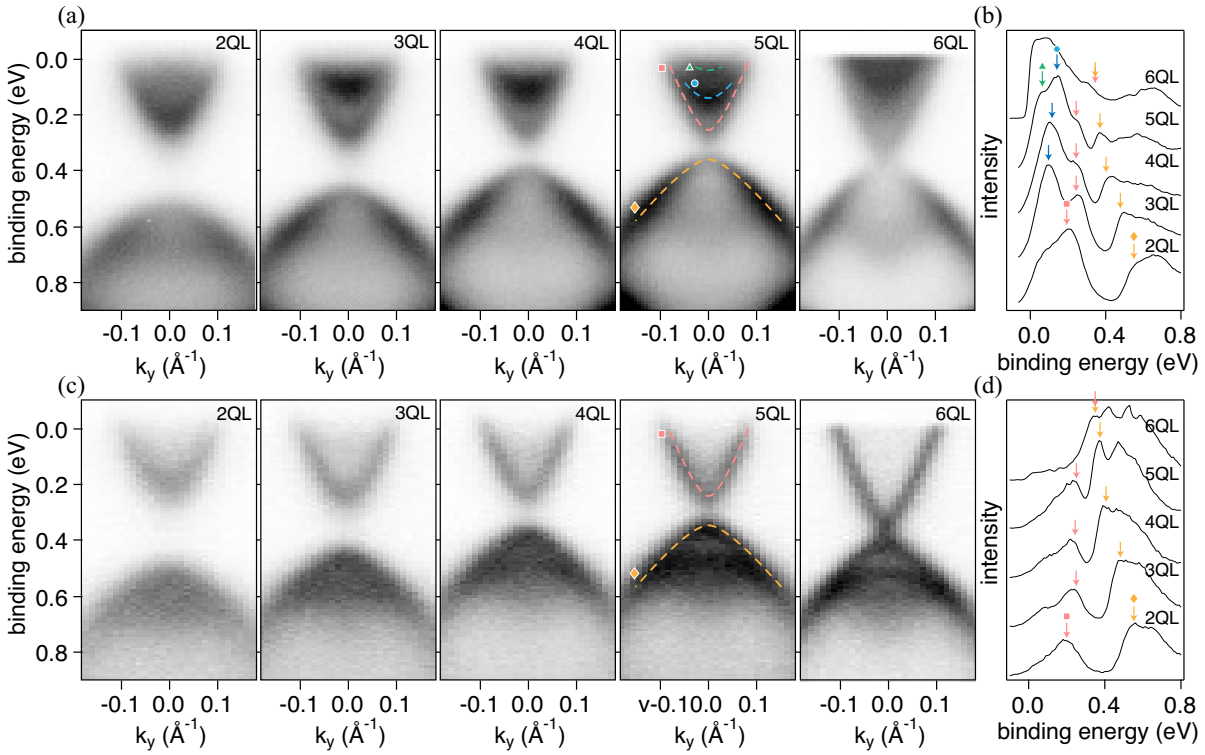

Figure 5.3: **(a)** Band dispersion for 2 QL–6 QL Bi_2Se_3/InP(111)B measured with 20 eV and **(b)** corresponding EDCs at $\overline{\Gamma}$. **(c,d)** Analogous measurements at 50 eV photon energy. The measurements were performed at room temperature, except for the 6 QL band map which was taken at 20 K.

$\overline{\Gamma}$. Both, the bulk conduction band (blue, green) and the valence band are split into quantum well states, due to the confinement of the states between the substrate band gap and the vacuum barrier. Their energy separation increases towards lower film thicknesses and the number of occupied quantum well states decreases. The energy distribution curves (EDCs) in Fig. 5.3b at $\overline{\Gamma}$ clarify the evolution of the band dispersion with film thickness. The red (orange) arrows indicate the minima (maxima) of the massive electron-like (hole-like) Dirac states, the blue and green arrows mark the conduction band quantum well states.

Figures 5.3c,d show the band maps and EDCs measured on the same samples at a photon energy of 50 eV. The spectral intensity of the quantum well states is strongly reduced with respect to the surface states for all of the shown film thicknesses. This allows to easily discern the spin polarization of the Dirac cones from the spin signal of the quantum well states as will be discussed below. Previous studies suggest that the gap closes around 6 QL [148, 167]. Our measurements confirm a gap that is smaller than the experimental resolution at this thickness. The 6 QL band map was taken at a temperature of 20 K, the observed shift

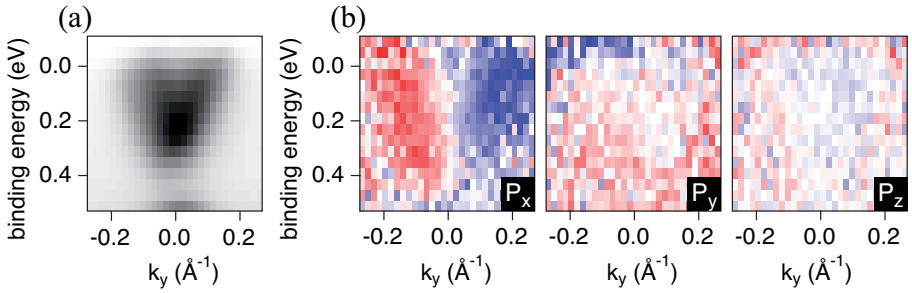

Figure 5.4: **(a)** Mott detector band map and **(b)** spin polarization along the three spatial directions for 2 QL Bi_2Se_3/InP(111).

of the bands towards higher binding energies by about 100 meV with respect to the room temperature measurements is consistently observed on all film thicknesses when measured at low temperature.

5.5 Evolution of the surface state spin texture

In Figs. 5.4 and 5.6 we present our spin-resolved ARPES data measured with p-polarized 50 eV photons. The measurement direction is along the y coordinate as sketched in Fig. 2.5a. The orbital character of the surface states in Bi_2Se_3 films is mostly of p_z type, whereas the in-plane p orbitals are mostly oriented tangentially to a constant energy contour [28]. As described in Ch. 6, in the COPHEE measurement geometry the photoemission transition matrix elements imply that mostly p_z and p_x orbitals are probed [29, 30]. The spin–orbit interaction couples the spin of the electrons in these orbitals in a helical spin structure with the same rotation direction [28]. Therefore the measured spin polarization of the photoelectrons represents mostly the spin texture of the p_z orbitals.

Systematic spin-resolved measurements with circularly polarized light and circular dichroism (CD) maps are summarized in Fig. 5.5. For in-plane momenta within the scattering plane (k_x) no CD contrast in the Dirac states is observed, while for perpendicular in-plane momenta (k_y), the CD contrast increases with film thickness. As shown for the surface state of bulk Bi_2Te_3 by Scholz *et al.* [175], the CD contrast strongly oscillates with photon energy and is thus not a suitable probe of the spin structure. On the contrary, the shown spin-resolved MDCs are robust and do not show a significant difference for $C+$ and $C-$ light polarization; apart from the out-of-plane component in Figs. 5.5j–l, which is induced by light with $C+$ polarization but not by $C-$-polarized light (see Ch. 6 for the discussion of photoemission induced spin reorientation).

Fig. 5.4a shows the total intensity and Fig. 5.4b the spin polarization components of a 2 QL

film along the three spatial directions (P_x, P_y, P_z) measured with the Mott detectors at a sam-

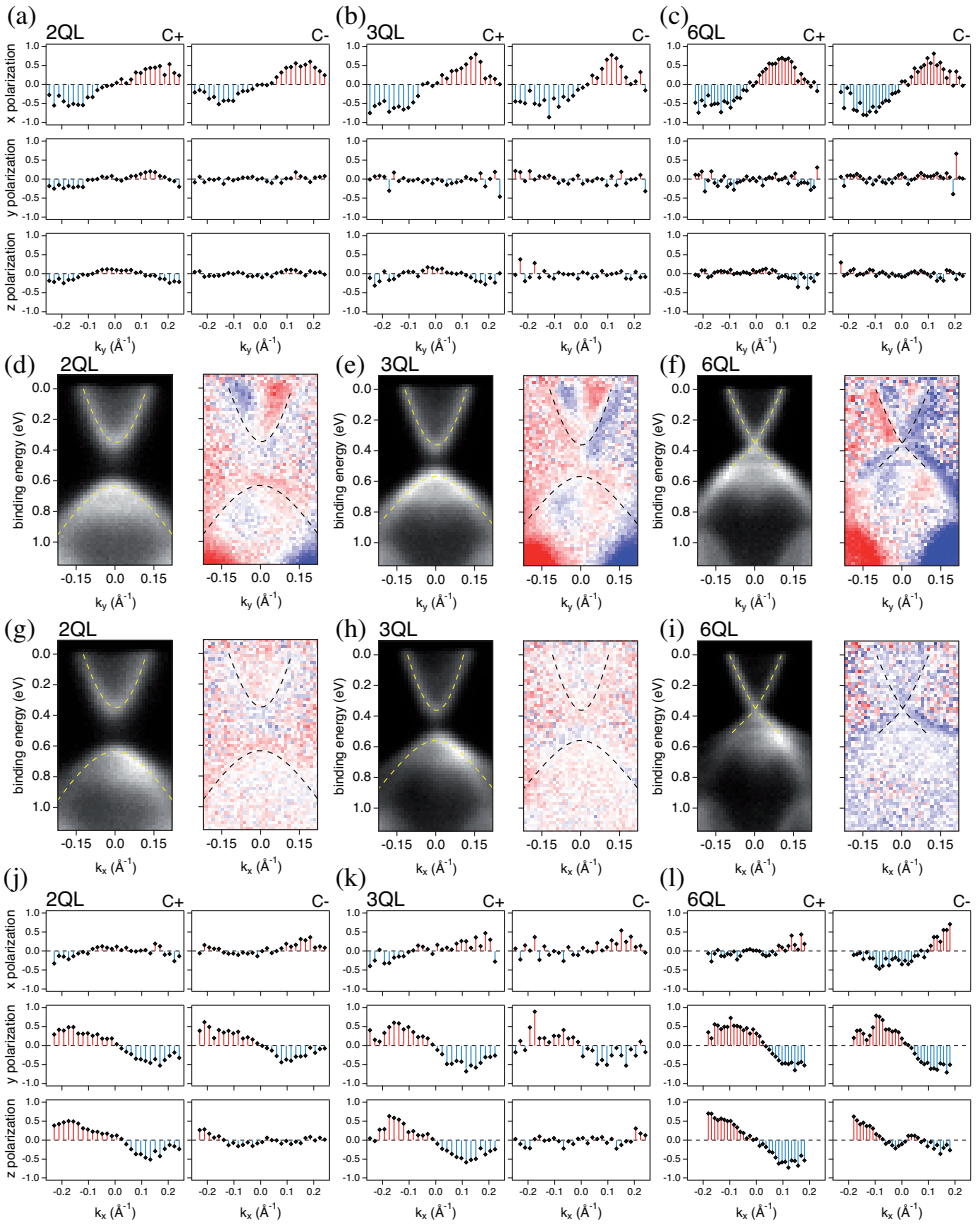

Figure 5.5: (a–c) Components of the spin polarization measured with $C+$ and $C-$ polarized light for film thicknesses 2 QL, 3 QL and 6 QL whith a measurement direction perpendicular to the photoemission scattering plane (k_y). **(d–f)** CD for the different film thicknesses along k_y. **(g–i)** CD within the scattering plane, along k_x. **(j–l)** Spin polarization measured along k_y. All measurements were performed at 50 eV photon energy and a sample temperature of 20 K; the spin-resolved measurements were taken at the Fermi level.

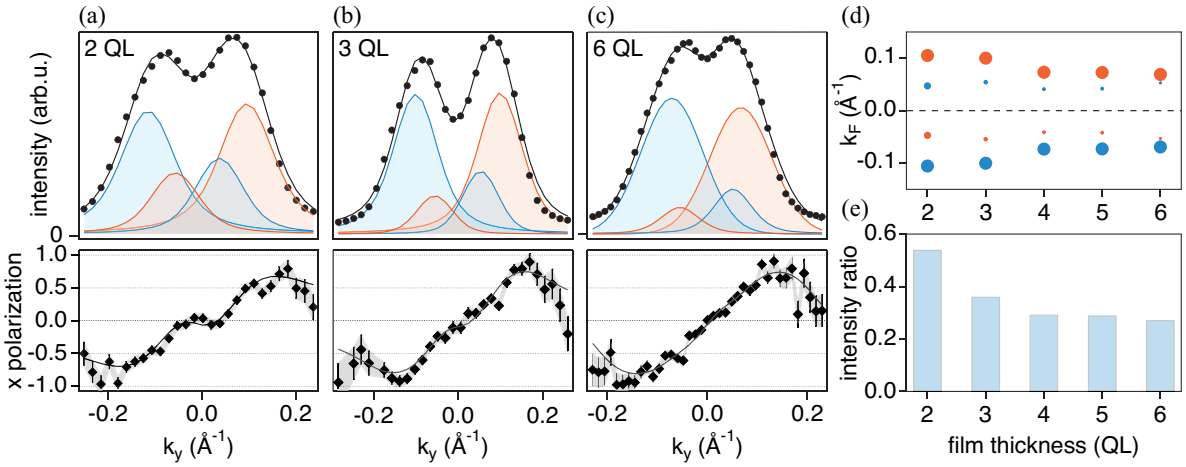

Figure 5.6: **(a)** Spin-resolved momentum cut at the Fermi level for a 2 QL film, **(b)** 3 QL film and **(c)** 6 QL film. **(d)** Thickness-dependent Fermi momenta obtained from fitting the spin-resolved measurements. The color indicates the spin polarization and the size of the markers is proportional to the relative intensity as in (e). **(e)** Ratio of the average intensities of the inner and the outer Rashba bands.

ple temperature of 20 K. The spin polarization is in-plane and orthogonal to the crystal momentum (i.e. along x). The spin expectation vector circles counter-clockwise on a constant energy contour, in qualitative accordance to the topological surface state of bulk Bi_2Se_3. An out-of-plane polarization is in principle allowed by the crystal symmetry for momenta along $\overline{\Gamma}$–$\overline{K}$ [109], but is not observed.

Higher statistics spin-resolved MDCs on the same 2 QL sample reveal the existence of an inner pair of bands with opposite spin polarization, as shown in Fig. 5.6a. These inner bands lead to a plateau in the x polarization around the $\overline{\Gamma}$ point, as seen in the bottom panel. The upper panel shows the total Mott detector intensity (black dots) and the individual peaks of the bands obtained by simultaneously fitting the total intensity and the spin polarization (Sect. 2.2.2, [44]). The momentum splitting at the Fermi level gradually decreases from about 0.058 $Å^{-1}$ at 2 QL to 0.016 $Å^{-1}$ at 6 QL. The intensity of the inner bands is suppressed with respect to the outer band and consequently the plateau in the vicinity of the $\overline{\Gamma}$ point is less pronounced and the peaks in the spin-resolved intensity have lower amplitudes (Figs. 5.6b,c). Figure 5.6d summarizes the shrinking spin splitting at the Fermi level and the intensity reduction of the inner bands is evident from Fig. 5.6e. Additional spin-resolved measurements at other photon energies (not shown) feature an anticipated energy dependence of the absolute value of the measured spin polarization but confirm the reported spin structure.

Furthermore, we compare spin-resolved measurements at different binding energies for var-

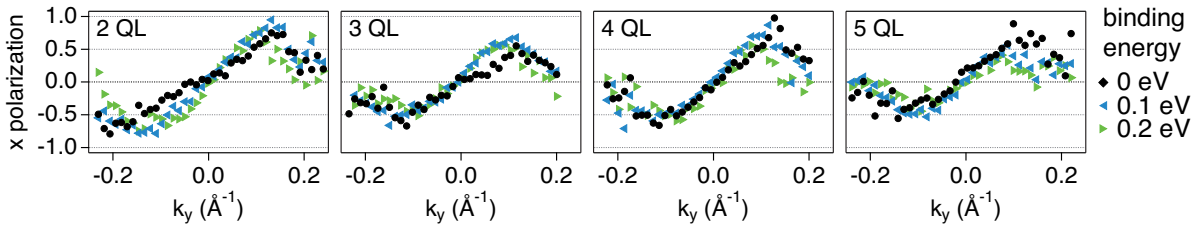

Figure 5.7: Binding-energy-dependent tangential (P_x) spin polarization for 2 QL–5 QL thick Bi_2Se_3 films on InP(111)B.

ious thicknesses in Fig. 5.7. There is a small decrease of the spin signal amplitude when comparing the measurements closer to the band apex to the data taken at the Fermi level. This behavior is in principle expected due to the larger delocalization throughout the film along the out-of-plane direction for the state towards the band apex (see discussion below). Most of the observed reduction, however, must be attributed to the increasing angular overlap of the experimentally broadened bands.

At the Fermi level the Dirac states are spin-polarized with an intrinsic degree of polarization that is almost independent of the film thickness also when compared to the gapless case in the bulk limit. The experimentally measured polarization amplitudes do not significantly decrease towards smaller film thicknesses despite the larger spectral weight of the oppositely polarized inner branches. This is also in contrast to previous theoretical predictions for symmetric films [176] and shows the importance of the choice of substrate for the utilization of ultra thin topological insulators.

5.6 Ab-initio calculation of a model system

In order to mimic the substrate-induced symmetry breaking in our DFT calculations, the Se surface layer of the freestanding Bi_2Se_3 films is artificially displaced along the surface normal, either towards the crystal bulk ($-dz$) or towards the vacuum ($+dz$). Figure 5.8 shows the results for a 2 QL thick film. The spatial overlap leads to a hybridization of the two surface states and a gap opens around the Dirac point. Due to the missing structural inversion symmetry the two massive Dirac states are split in a Rashba-like manner but with distinct localization of the inner and outer branches depending on the direction of displacement of the Se surface layer. The spatial localization is indicated by the size of the colored data points; the color indicates the sign of the net spin polarization. For a $+dz$ displacement the outer (inner) branches are mainly localized at the ideal (distorted) surface as shown in Fig. 5.8a (Fig. 5.8c), and *vice versa* for a $-dz$ displacement, Figs. 5.8d,e. Towards the band apex below

the Kramers point, however, the states become delocalized throughout both QLs due to the hybridization, as shown in Figs. 5.8c,f. With increasing film thickness but keeping the surface layer displacement constant, the wave function overlap and the gap diminish and the splitting decreases (Fig. 5.9). Finally, the gapless topological surface states emerge.

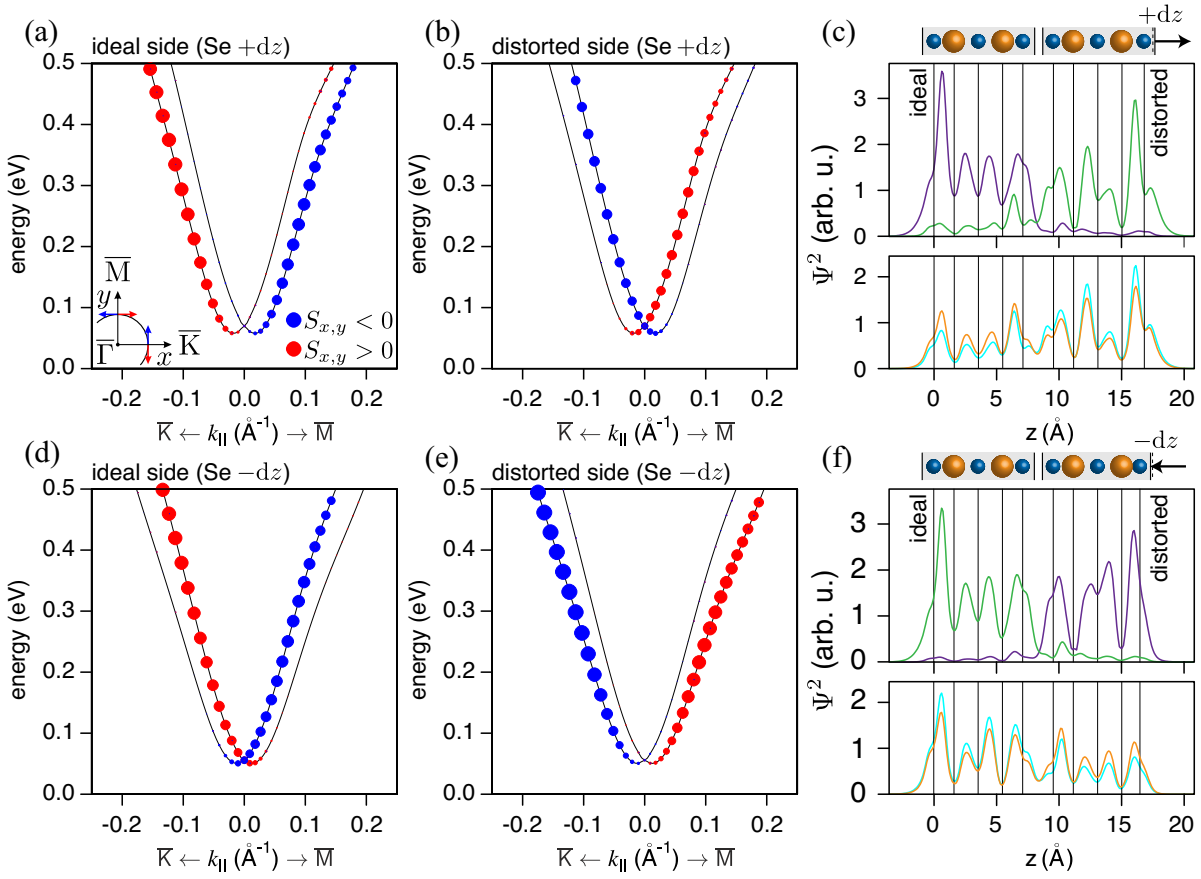

Figure 5.8: DFT calculations of a freestanding 2 QL Bi_2Se_3 film where one of the Se surface layers is artificially displaced towards the vacuum (+dz) or towards the crystal (−dz). **(a)** Dispersion of the electron-like spin-split massive Dirac state (black); the size of the colored data points indicate the weight of the wave function in the ideal surface QL (+dz). **(b)** Weight of the wave function in the QL with the displaced surface layer (+dz). **(c)** Charge density distribution along the stacking axis z for different energies: at $E = 0.3$ eV for the inner (green) and outer (violet) Rashba branch, at the Kramers point (cyan) and at the band apex (orange). **(d–f)** Corresponding calculations for a $-\mathrm{d}z$ displacement of the interfacial Se layer.

5.7 Discussion

Our measurements suggest that the effect of the InP(111)B substrate is mimicked in this model by a +dz displacement of the Se layer which is equivalent to a small charge transfer from the film to the substrate. The smaller spectral intensity of the inner branches and its continuous reduction towards thicker films (Fig. 5.6) indicate that the outer (inner) branches are localized in the QL at the surface (film/substrate interface). This contrasts with the situation of Bi_2Se_3 films grown on a double layer graphene on top of a 6H-SiC substrate where the inner branches are localized at the film surface, considering the spectral intensity distribution and the evolution of dispersion with film thickness [148]. On the other hand for Bi_2Se_3 films

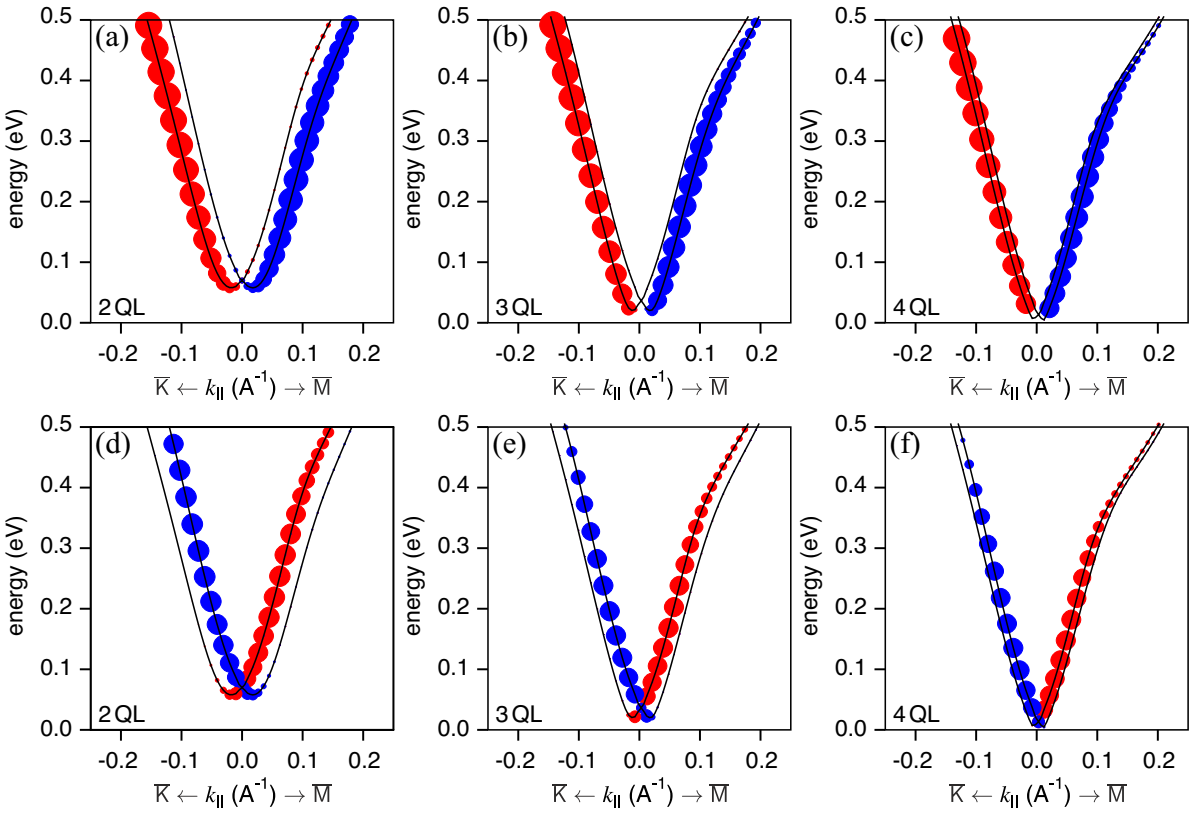

Figure 5.9: DFT calculations of the surface states in freestanding Bi_2Se_3 slab where one of the Se surface layers is artificially displaced towards the vacuum (+dz) for **(a)** 2 QL, **(b)** 3 QL, **(c)** 4 QL. The size of the data points indicates the contribution of p_z orbitals localized the ideal QL and the color indicates the sign of the spin polarization. **(d–f)** Corresponding calculations where the size of the data points indicates the contribution from p_z orbital in the distorted QL.

grown on Si(111) no such splitting could be resolved up to now [167]. These observations are in line with other Rashba systems where the splitting is known to be determined by the relative spatial shift of the wave function with respect to the atomic cores and therefore strongly depends on the coupling to the substrate [77, 177].

While at higher energies the dispersions of the two surface states are mostly spatially decoupled, towards the band apex the states are mixed and the net spin polarization decreases. The energy range in which a significant change can be observed is confined close to the band apex. An experimental determination of this reduction (cf. Fig. 5.6) is intricate as the measured spin polarization amplitude is depending on the measurement geometry, photon energy and probing depth but in any case it is mostly overshadowed by the larger experimental overlap due to the smaller k separation of the branches.

The main difference between Bi_2Se_3 films and other Rashba systems is that in the latter case the spatial distribution of both spin branches is very similar, whereas here they are localized on different sides of the film (Fig. 5.10). This opens the possibility to create a spintronic device where the states on either side of the film can be manipulated independently of each other.

The continuous spatial separation of the surface states upon increasing the film thickness and the accompanying reduction of the gap, shows that the topological surface states and their spin polarization do not emerge abruptly at the topological phase transition but develop smoothly from pre-existing states. A similar mechanism is discussed in the topological transition of $BiTl(S_{1-x}Se_x)_2$ upon sulfur doping [97, 123], where spin-polarized precursor states are observed already on the trivial side of the transition.

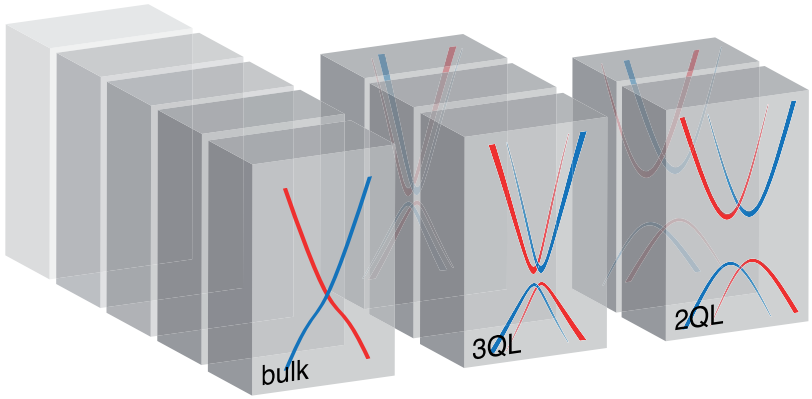

Figure 5.10: Schematic illustration of the dimensional crossover in Bi_2Se_3 films.

5.8 Conclusion

In summary, this this Chapter presented systematic spin-resolved ARPES measurements on Bi_2Se_3/InP(111)B films with thicknesses ranging from 2 QL to 6 QL. The measurements show that towards lower thicknesses the two surface states hybridize and a gap opens. Due to the substrate-induced structural inversion asymmetry the resultant massive Dirac state is split in a Rashba-like manner with distinct localization of the outer and inner branches at the top and at the bottom boundary of the film, respectively.

Chapter 6

Photoemission effects in spin-resolved ARPES on Bi_2Se_3

In the light of the discovery of three-dimensional topological insulators and the experimental studies on the spin structure of their topological surface states, the question about the reliability of spin-resolved ARPES as a probe for the intrinsic spin polarization was raised. Recent theoretical and experimental studies on the surface state of Bi_2Se_3 found a strong influence of the photoemission geometry, the light polarization, and the photon energy on the measured spin polarization. In this Chapter, systematic photon-energy-dependent spin-resolved ARPES measurements are presented. While small deviations from the initial state spin texture are indeed observed, the presented theoretical models systematically overestimate the size of the effects and fail to describe the details of the variation with photon energy.

6.1 Spin–orbital texture

Zhang *et al.* [28] pointed out that besides the usual locking between the electron spin and the crystal momentum in the surface state of Bi_2Se_3 (and other topological insulators), the spin texture is also locked to the atomic orbital, which is dubbed as the *spin–orbital texture*. The reason for this is that, in contrast to the near-gap bulk states which are of pure p_z character due to a strong crystal field splitting (Fig. 5.1b), the surface states are a mixture of the different p orbitals [150,178]. The latter couple differently to the momentum and the spin via spin–orbit interaction depending on their orbital angular momentum [30].

When neglecting warping effects, the surface spectrum is described by the effective Hamiltonian (3.22) yielding the dispersion of massless helical Dirac fermions. The crucial point is to notice that σ_x and σ_y in the Hamiltonian are not the operators of the real spin but rather

of the total angular momentum with $j = \frac{1}{2}$. So, instead of expressing the eigenstates $|\Phi_\pm\rangle$ of the Hamiltonian (3.22) as a superposition of the spin states (as in Eq. 3.15), they should be expressed with the eigenstates of the total angular momentum $|\Psi_{\pm 1/2}\rangle$

$$|\Phi_\pm\rangle = \tfrac{1}{\sqrt{2}}[\pm i\, e^{-i\vartheta_k}|\Psi_{1/2}\rangle + |\Psi_{-1/2}\rangle], \tag{6.1}$$

where ϑ_k is the polar angle of the in-plane momentum $\boldsymbol{k} = k\,(\cos\vartheta_k, \sin\vartheta_k, 0)$. By expressing $|\Psi_{\pm 1/2}\rangle$ as a superposition of the different p orbitals such that the individual terms have conserved total angular momentum along the z direction, i.e. $j_z = \pm\frac{1}{2}$, follows for the energy eigenstates of the upper $(+)$ and lower $(-)$ Dirac cone

$$\begin{aligned} |\Phi_+\rangle &= \sum_i [\alpha_+ |i, p_z, \uparrow_\vartheta\rangle + \beta_+ |i, p_r, \uparrow_\vartheta\rangle + \gamma_+ |i, p_t, \downarrow_\vartheta\rangle] \\ |\Phi_-\rangle &= \sum_i [\alpha_- |i, p_z, \downarrow_\vartheta\rangle + \beta_- |i, p_r, \downarrow_\vartheta\rangle + \gamma_- |i, p_t, \uparrow_\vartheta\rangle], \end{aligned} \tag{6.2}$$

where i denotes the atomic indices, $|\uparrow_\vartheta\ (\downarrow_\vartheta)\rangle = 1/\sqrt{2}\,[\pm i\, e^{-i\vartheta_k}|\uparrow\rangle + |\downarrow\rangle]$ stand for the left(right)-handed helical spin texture, and $|p_r\rangle = \cos\vartheta_k|p_x\rangle + \sin\vartheta_k|p_y\rangle$, $|p_t\rangle = -\sin\vartheta_k|p_x\rangle + \cos\vartheta_k|p_y\rangle$ are the radial and tangential orbital textures, respectively (see Fig. 6.1a). From Eqs. 6.2, it is evident that for the upper Dirac cone the p_z and p_r orbitals couple to the left-handed spin texture, while p_t couples to the right-handed spin texture (*vice versa* for the lower cone). A comparison with *ab-initio* calculations of the surface band structure of Bi_2Se_3, shows that the surface states are mainly of p_z character dominating over the in-plane orbitals. As for the latter, the tangential (radial) orbital orientation has slightly higher contribution to the upper (lower) cone. The orbital selectivity of an ARPES measurement allows to experimentally verify this spin–orbital texture. [28]

6.2 Orbital selectivity of ARPES

As shown in Sect. 2.1, the photoelectron intensity depends on the geometry of the scattering process and the symmetry of the involved initial and final state orbitals via the one-particle transition matrix elements $I \sim |M^{\boldsymbol{k}}_{f,i}|^2 \sim |\langle\phi^{\boldsymbol{k}}_f|\boldsymbol{A}\cdot\boldsymbol{p}|\phi^{\boldsymbol{k}}_i\rangle|^2 \sim |\langle\phi^{\boldsymbol{k}}_f|\hat{\varepsilon}\cdot\boldsymbol{x}|\phi^{\boldsymbol{k}}_i\rangle|^2$ in the dipole approximation, where $\hat{\varepsilon}$ is a unit vector along the polarization vector of the vector potential $\boldsymbol{A}$ [16]. For simplicity, the photoemission scattering plane is assumed to be along a mirror plane of the crystal surface, as sketched in Fig. 6.1b. The initial states shall be p states that are even or odd with respect to the mirror plane, respectively. For the photoelectron intensity to be finite in the mirror plane, the matrix element integrand must be even with respect to the plane. In addition, because odd wavefunctions have nodes in the mirror plane, the final state $|\phi^{\boldsymbol{k}}_f\rangle$ must be even as well. As the detector is assumed to lie in the mirror plane, $\boldsymbol{x}$ is always

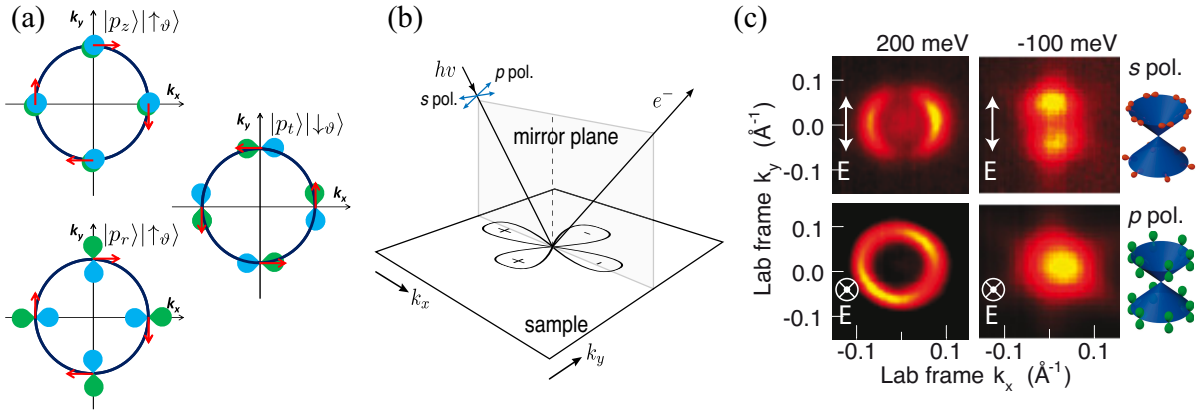

Figure 6.1: (a) Spin–orbital locking for the p orbitals. Figure adapted from Ref. [28] **(b)** Orbital selectivity of ARPES; p orbitals with the long axis perpendicular to the polarization vector are suppressed. **(c)** Constant energy ARPES maps of the Bi_2Se_3 topological surface state with different polarizations, reveal a dominant p_z contribution and a weaker in-plane p_t (p_r) contribution above (below) the Dirac point. Figure taken from Ref. [30].

even. In summary, a finite photoelectron intensity is measured if [16, 179]

$$\langle +|+|+\rangle : \quad |\phi_i^k\rangle \text{ even, and } \hat{\varepsilon} \text{ even } (p \text{ polarization}) \tag{6.3}$$

$$\langle +|-|-\rangle : \quad |\phi_i^k\rangle \text{ odd, and } \hat{\varepsilon} \text{ odd } (s \text{ polarization}). \tag{6.4}$$

In the case of the surface state of Bi_2Se_3 this means that in a setup with gracing light incidence and the photoelectron detection along the crystal surface normal, the photoemission intensity predominately originates from the even p_z orbitals in the case of p-polarized light. This is because the photon electric field points along the surface normal and enhances the cross-section for the out-of-plane orbitals. In turn, s-polarized light probes mostly odd p_y orbitals. In accordance with the above mentioned DFT calculations Cao *et al.* [30] measured in the described ARPES geometry strong signal from the p_z orbital for p-polarized light, and a main contribution from tangentially (radially) orientated in-plane orbitals above (below) the Dirac point for s polarization. The latter is expressed in a suppression of the photoemission intensity, whenever the polarization vector is orthogonal to the long axis of the in-plane orbitals, see Fig. 6.1c. [30]

6.3 Polarization-dependent spin-resolved ARPES

This orbital selectivity allows for measuring the spin texture of the involved orbitals independently. Figure 6.2 displays band maps and spin-resolved MDCs across the upper Dirac

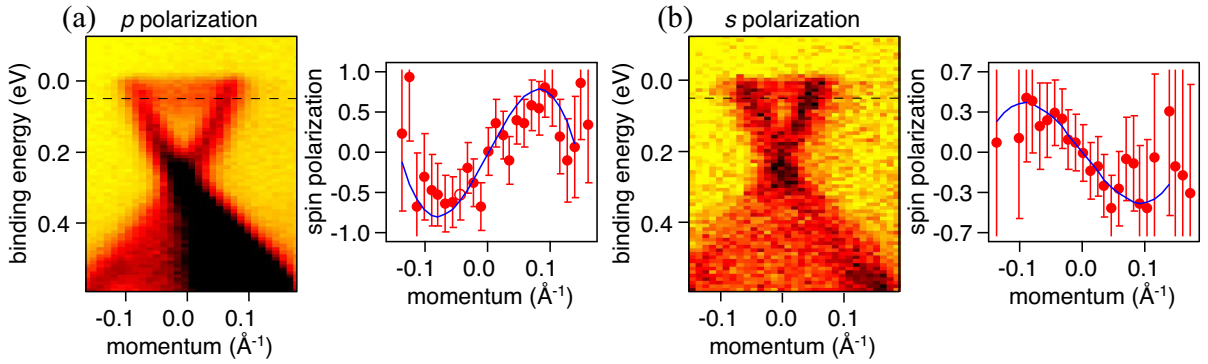

Figure 6.2: Bi_2Se_3 surface state ARPES spectra (*left panels*) and spin-resolved MDCs at the Fermi level (*right panels*) for **(a)** *p*-polarized light **(b)** *s*-polarized light, selecting out the $|p_z\rangle$ and the in-plane $|p_t\rangle$ orbitals, respectively. Taken from Ref. [180].

cone of Bi_2S_3 close to the Fermi level along the k_x direction (along this line p_x (p_y) orbitals correspond to p_r (p_t)). Due to experimental constraints of the spin-resolved ARPES setup, the incidence angle was around 45 ° with the result that *p*-polarized light probes p_z and p_x orbitals equally. However, as in the upper cone the radial orbital contribution is weak, the measured spin polarization is mainly originating from the p_z orbitals with left-handed helicity and a spin polarization close to 1 (right panel of Fig. 6.2a). On the other hand, *s*-polarized light is sensitive to the tangentially oriented p_t orbitals which are expected to couple to a right-handed spin texture. Indeed, the spin-resolved MDC in Fig. 6.2b shows a spin polarization opposite to the one in Fig. 6.2a. The count rate of the experiments with *s*-polarized light is highly reduced with respect to the *p* polarization measurements due to the order of magnitude lower photon flux of the SIS beamline at this polarization. The maximal degree of polarization is slightly reduced due to the worsened signal to noise ratio, partly related to the lower degree of light polarization (*p* polarization $\sim$ 95 % *LHQ*, *s* polarization $\sim$ 85 % *LVlE*).

6.4 Photon-energy-dependent spin-resolved ARPES

In the above model, the final state is characterized only by the constraint that it is assumed to be even with respect to the measurement plane. Therefore, from the model the photoelectron intensity and spin polarization are independent of the photon energy, only the light polarization is incorporated. Zhu *et al.* [29] extended the model in the attempt to describe the influence of the photon energy on measured spin polarizations. The starting point of their considerations is that the topological surface state of Bi_2Se_3 not only features a spin–orbital texture but that the orbital contribution to the energy eigenstate is layer-dependent (Fig. 6.3a).

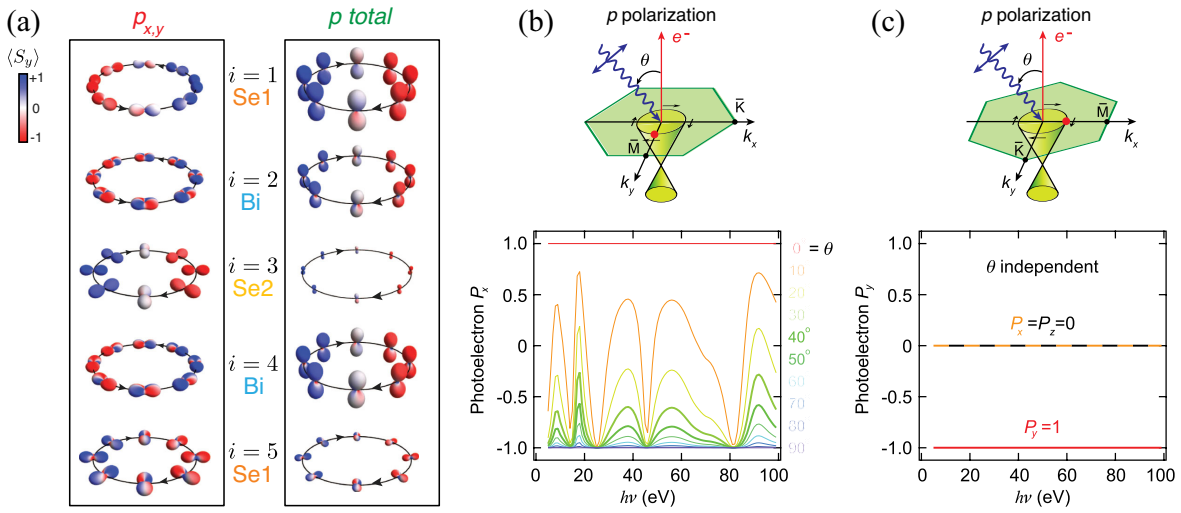

Figure 6.3: (a) *Left panel:* Layer-dependent in-plane orbital texture with the color indicating the spin expectation value along y. *Right panel:* Total layer-dependent orbital texture, i.e. including the dominating p_z orbitals. **(b)** Predicted photoelectron polarization for different incidence angles as a function of the photon energy with the initial state being 0.13 eV above the Dirac point and k along x. **(c)** Predicted photoelectron polarization for k in the scattering plane. Figure adopted from Ref. [29].

The topological surface state, being the initial state of the photoemission process, should be written as $|\phi_i^k\rangle = \sum_{i,\sigma} \alpha_i |\psi_{i,\tau}^\sigma\rangle$, where i, τ, and σ are the layer, the orbital and spin indices, respectively. Assuming a free-electron final state the ARPES intensity according to Eq. (2.3) can be written as

$$I \sim \sum_\sigma |\sum_i e^{-i k_z z_i} e^{-z_i/(2\lambda)} \alpha_i \langle e^{i \boldsymbol{k}_\parallel \cdot \boldsymbol{r}_\parallel} | \boldsymbol{A} \cdot \boldsymbol{p} | \psi_{i,\tau}^\sigma \rangle|^2. \tag{6.5}$$

The phase term $e^{-i k_z z_i}$ stems from the free-electron final state and accounts for the photoelectron path of length z_i, and the term $e^{-z_i/(2\lambda)}$ is introduced to incorporate the finite probing depth[1]. In words, the photoemission intensity is constituted out of the initial states $\psi_{i,\tau}^\sigma$ located in a certain layer i, and interfering with each other with phases $e^{-i k_z z_i}$. In this respect, the photoemission intensity can be regarded as the Fourier transform of the initial states along the surface normal. [29]

Since the spin polarization is measured as an asymmetry of photoelectron intensities, it becomes dependent on the geometry and photon energy. Along the spatial direction η one finds

[1]The authors of Ref. [29] note that the results of the calculation are nearly insensitive to variations of λ from 5 to 10 Å.

for the photoelectron spin polarization

$$P_\eta = \frac{1}{I}\sum_{i,\tau}\langle S_\eta^{i,\tau}\rangle |M_{i,\tau}|^2 + \frac{1}{I}\sum_{i\neq i',\tau\neq\tau'}\langle S_\eta^{i,\tau;i',\tau'}\rangle M_{i,\tau}^* M_{i',\tau'}, \tag{6.6}$$

where I is the total intensity, and $S_\eta^{i,\tau;i',\tau'} = |\psi_{i,\tau}\rangle\langle\psi_{i',\tau'}|\,\sigma_\eta$ is the spin operator with σ_η being the Pauli matrices. The matrix element $M_{i,\tau}$ and the interference in the second term can make the measured photoelectron spin polarization deviate from the ground state spin polarization. In fact, the authors found by plugging in the surface spectrum of a DFT slab calculation as initial states, that the expected photoelectron polarization measured with p-polarized light is strongly dependent on the photon incidence angle and the photon energy, if measured along the y direction (cf. upper panel of Fig. 6.3b). In this case, the spin expectation vector of the dominantly probed p_z and p_t orbitals are opposite and interfere (Fig. 6.3b). On the other hand, for a measurement along the x direction, the p_z and p_r orbitals are probed which have parallel oriented spin expectation vectors such that according to the model no interference-induced reorientation of the final state spin polarization occurs. In the latter case, the photoelectron spin polarization is independent of the light incidence angle and the photon energy, and should allow for a measurement of the intrinsic spin polarization (Fig. 6.3c). [29]

To verify the model, we performed systematic spin-resolved measursements Bi_2Se_3 topological surface state. Figures 6.4a–c show the three components of the measured spin polarization

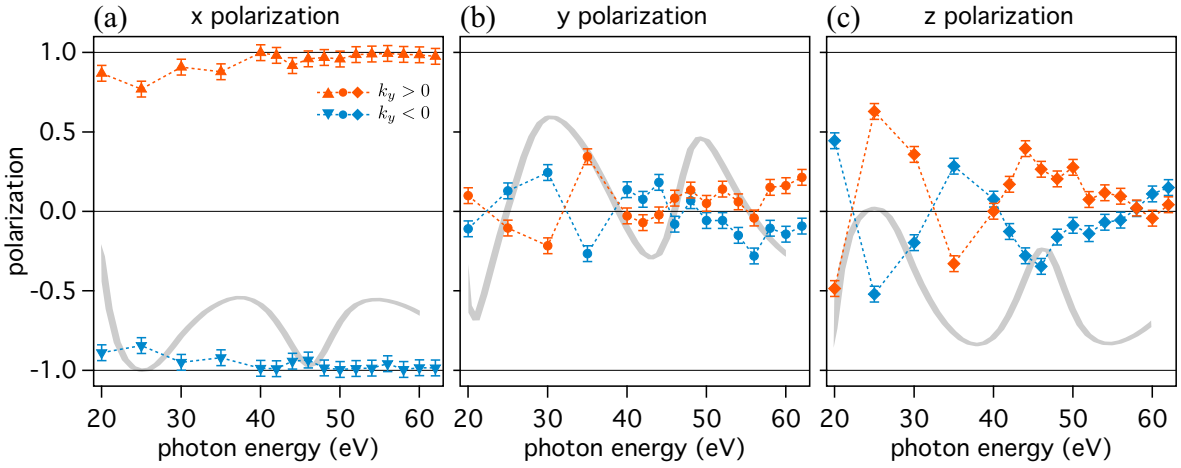

Figure 6.4: Measured photoelectron spin polarization of the Bi_2Se_3 topological surface state on either side of $\overline{\Gamma}$ at 150–200 meV above the Dirac point with p-polarized light at an incidence angle of 45 ° along **(a)** x, **(b)** y, and **(c)** z in the geometry depicted in Fig. 6.3b. The grey lines indicate the calculated results for an incidence angle of $\vartheta = 45\,°$, taken from Ref. [181]. The data points for 20–40 eV were taken in collaboration with the group of A. Damascelli.

150–200 meV above the Dirac point along the $\overline{\Gamma}$–$\overline{\mathrm{M}}$ crystal direction. The measurement geometry is approximately the same as depicted in Fig. 6.3b for a light incidence angle of $\vartheta = 45\,^\circ$, with the difference that the x axis at COPHEE is reversed and for the momentum scan the tilt angle ψ about the x axis (Fig. 2.5a) needs to varied. This slightly off-normal setup ($|\psi| < 4\,^\circ$), however, is not expected to fundamentally change the outcome of the experiment. The tangential x spin polarization is the largest component and its absolute value is close to unity for higher photon energies, while at lower photon energies the spin polarization vector deviates slightly from its tangential orientation. The radial (y) and out-of-plane (z) polarization components oscillate around the zero line, the latter being large in particular for photon energies around 25 eV. In comparison with these experimental data, the theoretical calculations fail to describe the main features. On the one hand, the deviation from the tangential orientation is significantly overestimated and on the other hand, no clear match with the phase of the oscillations can be observed; with the exception of the out-of-plane component, for which however no sign reversal is predicted contrary to the measurements. In Ref. [181], the number the published spin-resolved ARPES data points at different photon energies given in is much lower than shown in Fig. 6.4 and are only partly consistent with the theoretical model.

For p-polarized light in the above mentioned geometry (Fig. 6.3b), the predicted oscillation amplitude of the spin polarization components are larger for smaller incidence angles ϑ. Due to the fixed relative angle of 45 ° between the analyzer and the beamline at the COPHEE endstation, changing the incidence angle simultaneously alters the emission angle of the measured photoelectrons, thus making it necessary to measure in a higher order Brillouin zone. In comparison to the previously described setup with detection close to normal emission, the photoelectrons pick up a different in-plane and out-of-plane phase and such measurements can not directly be compared to the described calculations. In Fig. 6.5, the photoelectron spin polarization of the Bi_2Se_3 topological surface state measured in the second Brillouin zone along x is presented for three different photon energies. Since the emission angles of higher order Brillouin zones depend on the photon energy as indicated in the Figure, the measurements were performed at different emission and incidence angles. Here, the spin polarization is almost strictly tangential and in-plane, irrespective of the change of photon energy and incidence angle. It is important to mention that the measurements in Fig. 6.5 were performed not on a bulk Bi_2Se_3 sample but on a 6 QL thick Bi_2Se_3 film. Since the layer-dependent orbital and spin texture of the surface state is almost the same as for the surface state on bulk Bi_2Se_3, the model is not expected to produce a different result for thin films, as in both cases the final states are approximated by free-electron final states.

Figure 6.5d shows again a spin-resolved MDC along $\overline{\Gamma}$–$\overline{\mathrm{M}}$ on a 6 QL thick Bi_2Se_3 film but this time measured along x within the scattering plane of the light as illustrated in Fig. 6.3c. As predicted by the model, p_z and p_r orbitals with parallel orientation of the spin expectation

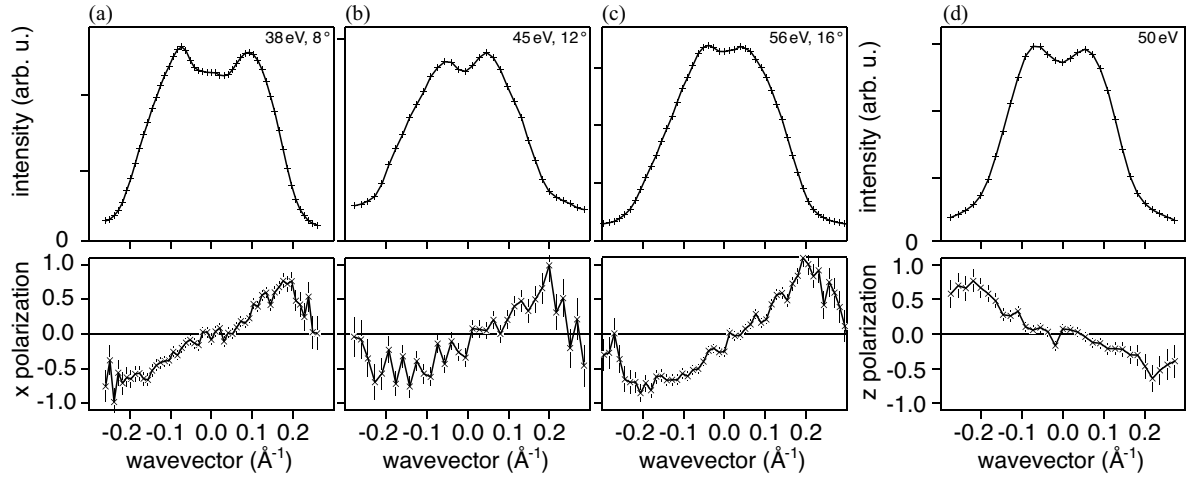

Figure 6.5: Spin-resolved ARPES MDCs at the Fermi level of a 6 QL thick Bi_2Se_3 film for different photon energies ($h\nu$) at low photon beam incidence angles (ϑ), which are chosen such that the measured photoelectron emission angle ($45^\circ - \vartheta$) corresponds to the second zone $\overline{\Gamma}$ point. The measurement geometry is as indicated in Fig. 6.3b. The upper panels show the total intensity and the lower panels the tangential x polarization measured for **(a)** $h\nu = 38\,\text{eV}$, $\vartheta = 8^\circ$, **(b)** $h\nu = 45\,\text{eV}$, $\vartheta = 12^\circ$, **(c)** $h\nu = 56\,\text{eV}$, $\vartheta = 16^\circ$. **(d)** Out-of-plane polarization measured along $\overline{\Gamma}$–$\overline{\text{M}}$ in the geometry as sketched in Fig. 6.3c.

vector are probed and no spin interference should occur. However, next to the in-plane tangential spin polarization, a sizeable out-of-plane component is observed in this geometry, although the measurement is performed in a mirror plane of the crystal, where no other than in-plane tangential spin polarization is allowed in the initial state by symmetry.

6.5 Discussion

The results shown if Figs. 6.4 and 6.5a–c are in accordance with a study by Sánchez-Barriga *et al.* [32] performed on the surface state of Bi_2Se_3 for photon energies in the range of 50–70 eV. The authors found no significant spin reorienation of the photoelectrons with photon energy or light polarization (p, $C+$, $C-$) neither in their spin-resolved ARPES measurements nor in the photoemission *one-step* calculations. On the other hand, in accordance with a previous spin-resolved laser-ARPES study [34] and a theoretical paper based on free-electron final states [33], for a photon energy of 6 eV the photoelectron spin polarization rotates from being in-plane to become fully out-of-plane for C-polarized light with opposite signs of the out-of-plane spin component for $C+$ and $C-$ polarization and with the same sign on either

side of normal emission. This different behavior of light-induced spin reorientation in the two photon energy regimes must be related to the different final states reached by the light excitation. In particular, it is known that in photoemission the spin-degenerate free-electron description of the final states is only a coarse approximation [21]. In Ref. [32], the authors claim that the strong deviation from the initial state spin texture measured with 6 eV photons arises because at this excitation energy following the dipole selection rules spin-degenerate *s*-type final states are populated. In earlier studies it was found that if the final states are fully symmetric, the photoelectron spin polarization is determined by the quantization axis defined by *C* polarized light [32, 182].

In the photon energy range 20–70 eV as in the measurements shown in Figs. 6.4, 6.5a–c and in Ref. [32], the experimental spin polarization is only weakly depending on the photon energy, light polarization, and incidence angle, mostly reflecting the initial state spin polarization. Whereas deviations from the initial state spin structure are found in the geometry of Fig. 6.5d. The mentioned theoretical models of Refs. [29, 183] fail to describe the photoelectron spin polarization in this energy range. Both models assume a free-electron final state. Due to the sensitivity of the predicted photoelectron spin orientation on relative phases originating from the transition matrix elements of initial and final states, an accurate description not only of the initial but also of the final state must be incorporated in a successful description. The *one-step* photoemission calculations given in Ref. [32] are capable of describing the correct photoelectron spin polarization for distinct experimental parameters, however due to the their complexity and computational effort, systematic calculations as a function of photon energy, light polarization and experimental geometry are hitherto unpublished.

Chapter 7

Bulk Rashba effect in non-centrosymmetric crystals

As shown in Sect. 3.2, the Kramers degeneracy can be only lifted by spin–orbit interaction in systems lacking inversion symmetry. The systems so far discussed in this Thesis, dealt with situations where structural inversion asymmetry due to a surface (Ch. 4) or asymmetric films (Ch. 5) induced spin splittings in two-dimensional states. The only way that the spin–orbit interaction can lift the spin degeneracy of three-dimensional states is when the crystal structure itself lacks inversion symmetry [184]. Depending on the symmetry of the crystal and thus the orientation of the spin polarization and its k dependence, the spin splitting is called Rashba-type [11] or Dresselhaus-type [62] and is known to occur for e.g. in wurtzite [185] or zincblende crystal structures [186], respectively. Recently, very large Rashba-type splittings were discovered both in the surface spectrum and the bulk bands of the materials belonging to the class of noncentrosymmetric bismuth tellurohalides BiTeX with X = I, Cl, Br. Ishizhaka *et al.* provided *ab-initio* calculations on the bulk band structure of BiTeI which showed large spin splittings of all the bulk bands (Fig. 7.2a, [187]). Further, the authors presented spin-integrated and spin-resolved ARPES data of a two-dimensional state at the surface of BiTeI with large Rashba-type spin splitting. In a subsequent perturbative $k \cdot p$ study Bahramy *et al.* related the large splitting of the top valence and bottom conduction bands of the bulk to the large atomic spin-orbit splitting, to the noncentrosymmetric crystal structure and to the fact that the symmetry characters of these bands, separated by a relatively narrow energy gap, are the same [188]. A bulk-sensitive optical transition study was in accordance with the bulk conduction band dispersion obtained by DFT calculations [189].

Direct spectroscopic evidence of the bulk Rashba splitting was missing up to this point. In this Chapter, the properties of the electronic states BiTeI and BiTeCl are discussed on the basis of ARPES measurements in the ultra-violet (UV-ARPES) and soft X-ray photon energy

regime (SX-ARPES). By photon-energy-dependent mapping, the bulk electronic structure is discerned from the surface contributions and the peculiar toroidal Fermi surfaces are mapped out. It will be shown that because of the lacking inversion symmetry, the surfaces of these compounds have two distinct surfaces, which was not considered in previous publications. The surfaces host distinct sets of surface states which are split-off from the bulk states in the staircase-like surface potential.

The text and figures of Sect. 7.1 are published in Ref. [190], Sect. 7.2 in Ref. [191].

7.1 Fermi surface mapping of BiTeI

BiTeI has a hexagonal crystal structure and is built up of alternating layers of bismuth, tellurium and iodine atoms stacked along the hexagonal axis (Fig. 7.1a). The continuous stacking order of the layers of the three atomic species breaks the inversion symmetry. DFT calculations show that the absence of inversion symmetry allows the strong spin–orbit interaction to lift the spin degeneracy of every band away from the time reversal invariant momenta (Γ, A, M, L, cf. Fig. 7.1b) [187]. In particular, the bulk conduction band minimum and the valence band maximum are shifted away from the A point at the Brillouin zone boundary towards the H and L points (Fig. 7.2a).

The ARPES study by Ishizhaka *et al.* in the ultra-violet photon energy regime observed two overlapping two-dimensional electron-like states with large Rashba-type spin splitting on the BiTeI(0001) surface without specified surface termination (Fig. 7.2b, [187]). The authors presented spin-resolved ARPES data indicating a large degree of spin polarization. Based on

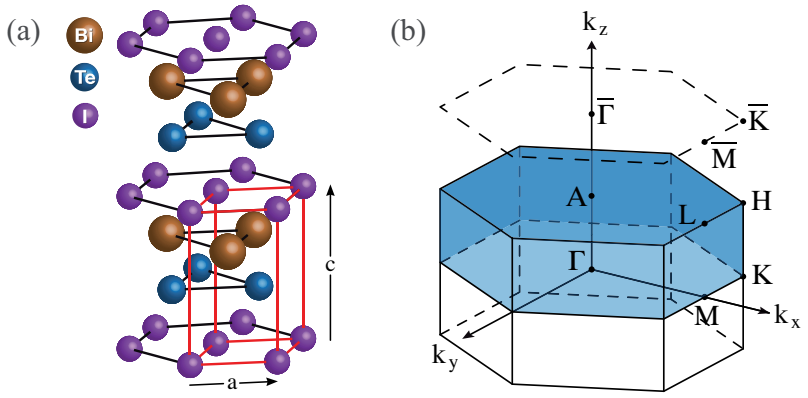

Figure 7.1: (a) Hexagonal crystal structure of BiTeI with the unit cell marked in red (space group $P3m1$, $a = 4.3392(1)$ Å, $c = 6.854(1)$ Å [192]). **(b)** Bulk and surface Brillouin zone of BiTeI.

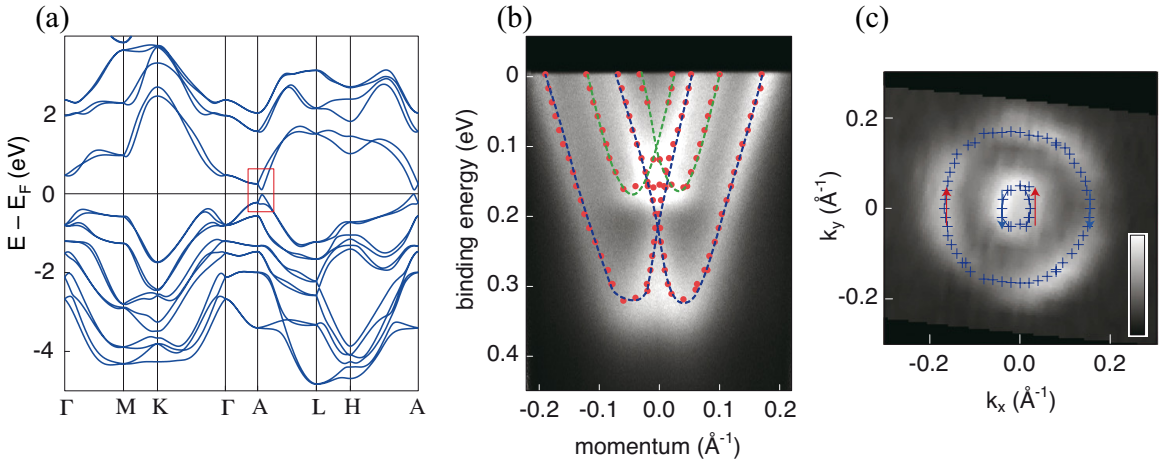

Figure 7.2: (a) *Ab-initio* calculation of the BiTeI bulk band structure. **(b)** Laser-ARPES map of two-dimensional Rashba-split bands close to the Fermi level of BiTeI(0001), mistakenly interpreted as quantum well subbands in Ref. [187]. **(c)** Fermi surface map measured with UV-ARPES. Figures taken from Ref. [187].

the two states' lacking k_z dispersion, their similar in-plane dispersion and the staggering in binding energy, the authors claimed that these states are the first and second order quantum well subbands derived from the bulk conduction band and confined at the surface due to downward surface band bending. In this Section it is shown that the observed states are rather surface states based on i) the direct observation of the k_z dispersing bulk bands measured with SX-ARPES, ii) comparison with termination-dependent *ab-initio* calculations, and iii) the observed constant spin structure of the surface state upon inversion of the crystal out-of-plane axis. A clear distinction from the bulk band structure and the understanding of the origin and the properties of the surface state are indispensable for future spintronic applications and tuning of the transport properties.

7.1.1 Bulk Fermi surface

Due to the broken inversion symmetry an untwinned BiTeI crystal has two different terminations. The weak bonding between the Te and I layers provides a natural cleaving plane, therefore the termination layer is either purely formed of iodine or tellurium atoms depending on the stacking order of the underlying layers. Despite the lacking inversion symmetry in the crystal structure the bulk band structure (neglecting spin) is inversion symmetric with respect to the TRIM due to the time reversal symmetry (cf. Sect. 3.2). Thus for the mapping of the bulk band structure the termination is only important insofar as it affects the position of the chemical potential.

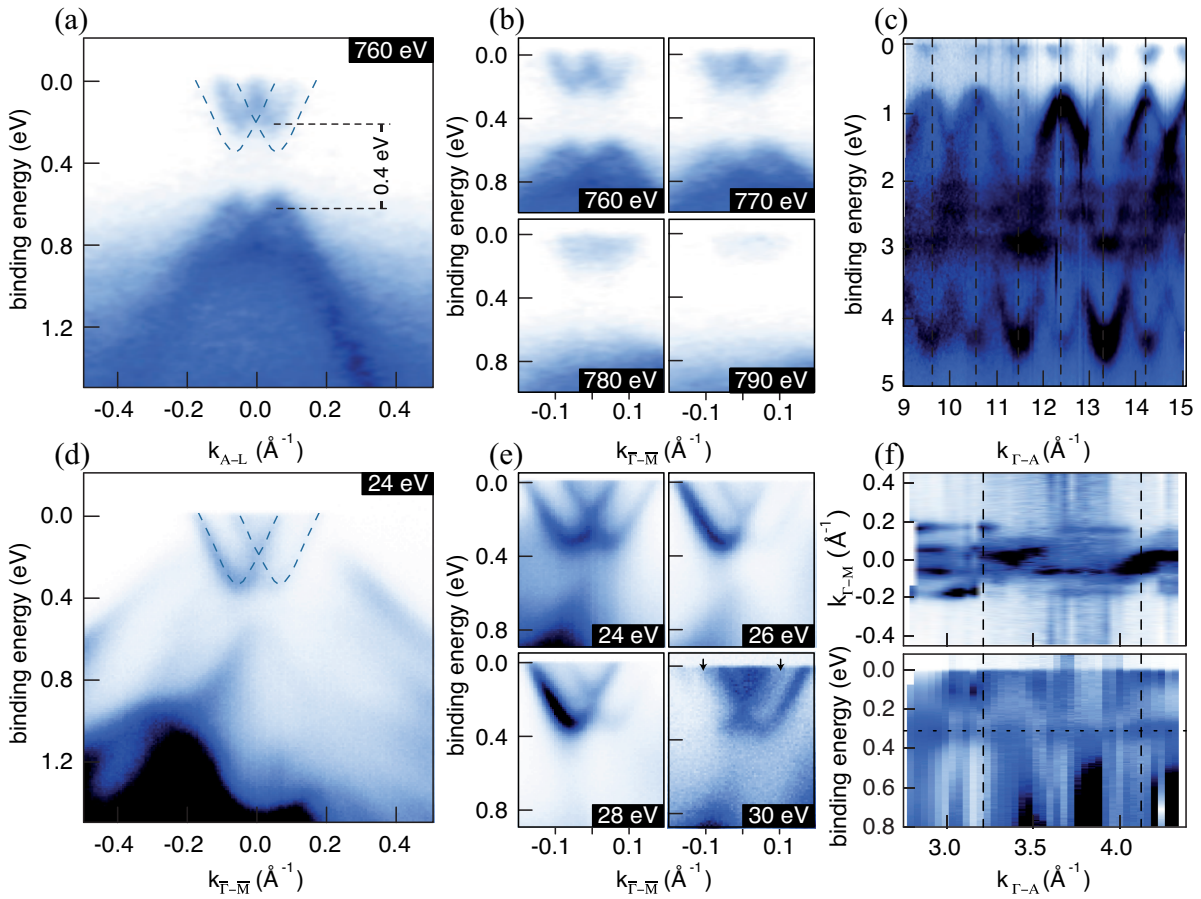

Figure 7.3: **(a)** SX-ARPES band map of the bulk states at 760 eV photon energy (16^{th} zone boundary). The dashed lines indicate the surface state dispersion shown in (d). **(b)** Band maps at 760 eV–790 eV photon energy. **(c)** Band map along Γ–A (i.e. $k_{||} = 0$), the dashed lines indicate the Brillouin zone boundaries.
(d) UV-ARPES band map of the surface state at 24 eV photon energy. **(e)** Band maps at 24–30 eV photon energy. **(f)** *Upper panel:* Fermi surface map along $\overline{\Gamma}$–$\overline{\text{M}}$ as a function of photon energy (20 eV–63 eV). *Lower panel:* Map of the band apex at $k_{||} = 0.06\,\text{Å}^{-1}$ as a function of photon energy. Indicated are the Brillouin zone boundaries (dashed lines) and the band apex (dotted line).

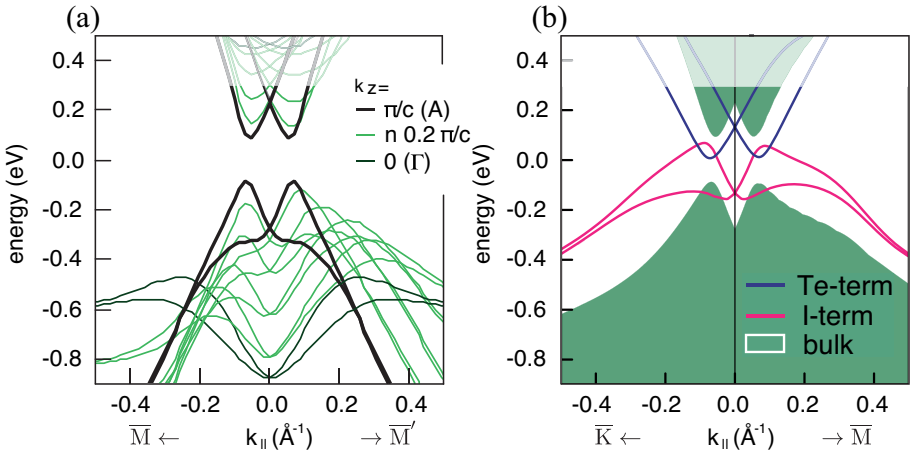

Figure 7.4: (a) DFT bulk spectra for a set of k_z values along $\overline{\mathrm{M}}$–$\overline{\Gamma}$–$\overline{\mathrm{M}}'$. The measured Fermi level is indicated by a lower intensity of the unoccupied states. **(b)** Slab calculations for iodine and tellurium termination. For both terminations a surface state appears in the bulk band gap.

The bulk band structure of BiTeI as observed with SX-ARPES is presented in Figs. 7.3a–c. At these high photon energies, photoemission from the bulk states is dominant over surface state emission, while the latter is emphasized in the more surface sensitive UV-ARPES (Figs. 7.3d–e). Figure 7.3a shows a band map along the A–L direction in the Brillouin zone measured at 760 eV photon energy. In agreement with previous optical measurements [189] the bulk band gap is determined to be 400 meV. The three-dimensional nature of these bands is evident from their dispersion behavior shown in Fig. 7.3b. Both for the valence band and the conduction band, a clear k_z dispersion is observed. At 760 eV photon energy, corresponding to the 16$^{\mathrm{th}}$ A point in the reciprocal space along the out-of-plane momentum, the binding energy of the conduction band minimum is largest and decreases away from the A point and eventually disperses above the Fermi level at around 800 eV photon energy.

Figure 7.3c shows the dispersion along the Γ–A direction, i.e. for $k_{\|} = 0$, measured by sweeping photon energies from 310 eV to 850 eV. Because of the non-negligible photon momentum transferred to the photoelectrons at the used photon energies, the measured electron momenta have been corrected for the photon momentum projected on the particular electron momentum axis (Sect. 2.1.2). The k_z dispersion of the conduction band follows the periodicity of the valence bands, so the highest conduction band binding energies occur periodically at the A points ($k_z = (2n+1)\pi/c$, where c is the out-of-plane lattice constant), indicated by the vertical dashed lines. The calculated k_z dependence of the lowest conduction band and highest valence band along $\overline{\mathrm{M}}$–$\overline{\Gamma}$–$\overline{\mathrm{M}}'$ reproduce these observations (Fig. 7.4a). At the A point

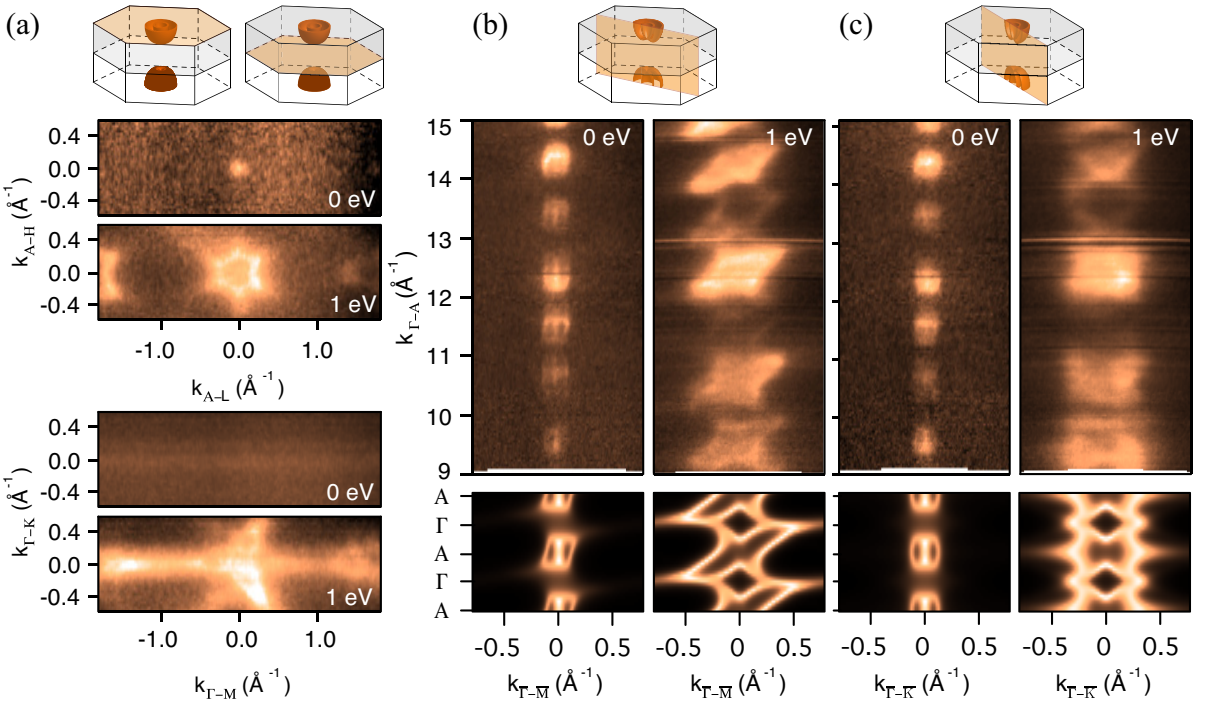

Figure 7.5: (a,b) In-plane BiTeI constant energy contours at the Fermi level and at 1 eV binding energy around the A point (310 eV photon energy) and the Γ point (385 eV photon energy), respectively. **(b,c)** *Upper panels*: SX-ARPES photon-energy dependent constant binding energy maps of the lowest bulk conduction band at the Fermi level and of the highest valence band at 1 eV binding energy in the (c) Γ–M–A–L and (d) Γ–K–A–H plane. *Lower panels*: DFT calculations corresponding to the directions and energies in (c) and (d).

the calculation perfectly matches the measured spectrum at 760 eV in Fig. 7.3a, apart from a smaller calculated band gap, which is a typical problem of DFT calculations.

Our SX-ARPES data clearly indicate that the bulk states do disperse at the surface and are thus not quantized into quantum well states. This statement is reinforced by realizing that despite the probing depth of SX-ARPES being slightly larger than in the ultra-violet regime (6–8 Å at 600 eV photon energy), it is distinctly smaller than the typical length scale for surface band bending. Thus, simultaneous observation of the bulk states and of the thereof derived quantum well states would be impossible, due to the limited probing depth. Figure 7.5 shows the three-dimensional bulk Fermi surface of BiTeI which is typical for an entire class of non-centrosymmetric materials with strong spin–orbit interaction. In the in-plane direction the Fermi surface around the A point is described by two concentric hexagonally distorted rings while it disappears around the Γ point (Fig. 7.5a). In the out-of-plane direction the Fermi surface takes the form of two loops, intersecting at the Γ–A line. The left panels of Figs. 7.5b,c

show the measured Fermi surface in the Γ–M–L–A and Γ–K–H–A plane, respectively. The right panels display constant energy cuts in the same momentum planes at a binding energy of 1 eV cutting through the valence band close to the lower gap edge.

The measured constant energy cuts are well reproduced by DFT calculations: the lower panels of Figs. 7.5b,c show sections through the calculated Fermi surface in the momentum planes corresponding to the measurements in the upper panels of Figs. 7.5b,c, about 275 meV above the conduction band minimum (left panels), and constant energy cuts through the valence band 485 meV below the valence band maximum (right panels). The band broadening has been manually added. These data complete the picture of the three-dimensional Rashba-type Fermi surface taking the form of a spindle torus distorted according to the crystal symmetry and, as will be shown below, coexisting with a two-dimensional Rashba-split surface state (Fig. 7.6a).

An other SX-ARPES study confirmed the reported bulk valence band structure [193]. Truly bulk sensitive measurements of the Fermi surface based on the Shubnikov–de Haas and de Haas–van Alphen effects [183,194–196], as well as optical [189] and magneto-optical [197,198] transition measurements are in accordance with the dispersion of the bulk conduction band as presented above. Related to the linear in-plane dispersion close to the A point, a large diamagnetic susceptibility is found if the chemical potential is close to the degeneracy point [199].

7.1.2 Fermi surface of the surface spectrum

The UV-ARPES data (Figs. 7.3d–f, 7.7a) show a state with an in-plane dispersion similar to that of the bulk conduction band state measured near the A point (Fig. 7.3a), but shifted by 100 meV to higher binding energies and exhibiting a 20 % larger momentum splitting. In contrast to Ref. [187] here this state is interpreted as a surface state and not a bulk-derived quantum well states, based on the following arguments. First, the absence of dispersion of the surface state in the out-of-plane momentum (k_z) direction is shown through photon-energy-dependent dispersion maps as presented in Figs. 7.3d,e. Aside from strong intensity variations due to matrix element effects the bands do not change as a function of photon energy. Taking into account that at these low photon energies half a Brillouin zone is swept by changing the photon energy by roughly 10 eV, the states can be said to not disperse in k_z at all. There is neither a significant photon energy dependence in the Fermi momenta nor in the parabola apex around 0.33 eV, as can be seen in the upper and lower panel in Fig. 7.3f.

The origin of this state can be understood from DFT calculations for both Te- and I-terminated surfaces. To calculate the spectrum of the Te terminated surface, a 24 layer slab was used with a free tellurium surface on one slab side and a hydrogen-passivated iodine termination on the

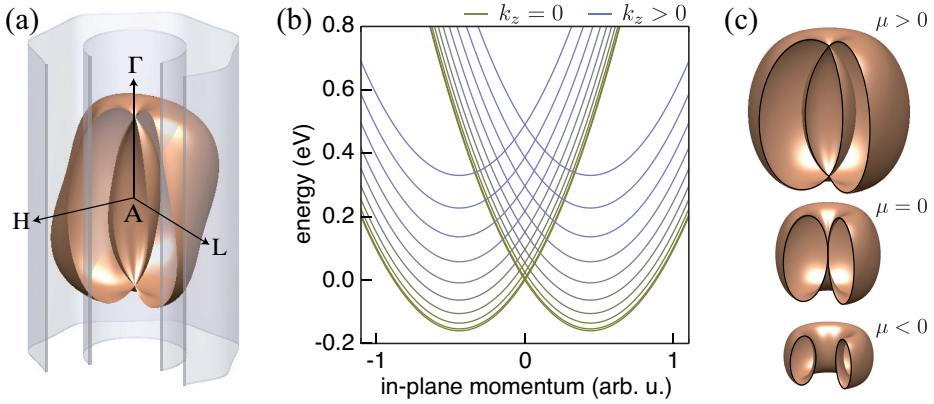

Figure 7.6: **(a)** Schematic illustration of the bulk Fermi surface (orange) and the surface state Fermi surface (gray). **(b)** Three-dimensional Rashba spectrum Eq. (7.1) for $\mu = 0$. **(c)** Topological transition of the bulk Fermi surface as function of the chemical potential.

other side. The tellurium surface hosts the Rashba-split electron-like surface state within the bulk band gap, and with a dispersion that is in excellent agreement with the photoemission data. On the other hand, a hole-like surface state appears at the I-terminated surface (in this case the Te-terminated side of the slab is passivated). In Fig. 7.4b both in-gap spin-split surface states at the Te- and I-terminated surfaces are shown. In the photoemission data in Fig. 7.3d, a hole-like state indeed crosses the gap and overlaps with the electron-like surface state in agreement with the theoretical predictions. Since on all measured samples both surface states were observed, it is concluded that both surface terminations are present in domains of sizes smaller than the synchrotron light spot. This is only possible if both stacking orders are equally present in the sample, due to a large number of stacking faults.

Now the spin structure is invoked as a further argument for the surface state interpretation. In the bulk the stacking order breaks the inversion symmetry in the unit cell, creating the potential gradient responsible for the Rashba field. The spin structures of crystals with opposite stacking order are therefore related to each other by a reversal of the spin helicity. In a sample with both stacking orders equally present, Rashba fields of opposite directions will be balanced and no spin polarization can be measured in a spatially averaging spin-resolved ARPES experiment. The same would be true for quantum well states formed from bulk states due to surface band bending. Figures 7.7b–d show the spin polarization measured at 24 eV photon energy along $\overline{\Gamma}$–$\overline{\mathrm{M}}$ close to the Fermi energy on a sample pair with macroscopically oppositely mounted out-of-plane axis. The data reflect the structure of a large Rashba-type spin splitting with a high in-plane tangential polarization and in both cases clockwise helicity of the outer bands. The inner bands overlap strongly with the adjacent bands resulting in a vanishing polarization amplitude near normal emission (see Sect. 2.2.2 for details on

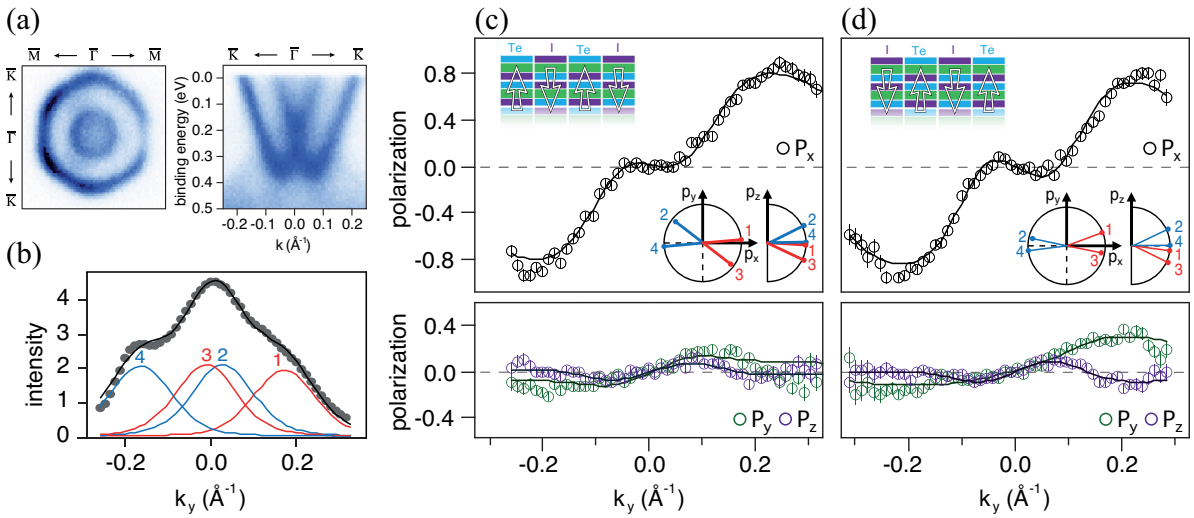

Figure 7.7: (a) *Left panel*: UV-ARPES Fermi surface map. *Right panel*: Conduction band map. **(b)** Momentum distribution curve of the spin-resolved ARPES measurement in (c) with fitted peaks. **(c)** Spin polarizations of the conduction band at the Fermi level along $\overline{\Gamma}$–$\overline{\mathrm{M}}$. The top-left inset illustrates the mixed stacking orders resulting in mixed surface terminations. The bottom-right insets shows the fitted spin polarization vectors of the individual bands as defined in (b). **(d)** Corresponding measurement to (c) with macroscopically inverted out-of-plane axis but with the same mixing of surface terminations.

the data analysis). The high degree of spin polarization confirms the surface state character of the observed conduction band where the surface potential gradient of one of the surface terminations produces the Rashba effect.

The equal appearance of both surface states (Te and I termination) has been taken as an indication for the presence of roughly equal amounts of both terminations on our samples (insets of Figs. 7.7c,d). In order to corroborate this fact, a spin-resolved measurement is performed on the same crystal as was used for the data in Fig. 7.7c, but mounted with inverted out-of-plane axis. Indeed, both surface states are found with the same degree of spin polarization and the same spin helicity near the Fermi energy (Fig. 7.7d).

Additional evidence is given in Ref. [200] where the authors present X-ray photoelectron spectroscopy (XPS) measurements and ARPES maps from small areas with pure Te- and I-terminated surfaces and opposite band bending (beam spot 10 μm). They observe in the bulk band gap, Rashba-split electron-like (hole-like) surface states on the surfaces with Te (I) termination, in agreement with DFT calculations of BiTeI slabs [201] and to our measurements (Fig. 7.8). By increasing the band bending via K doping of the surface, no significant increase of the Rashba splitting could be observed which again contradicts the quantum well state

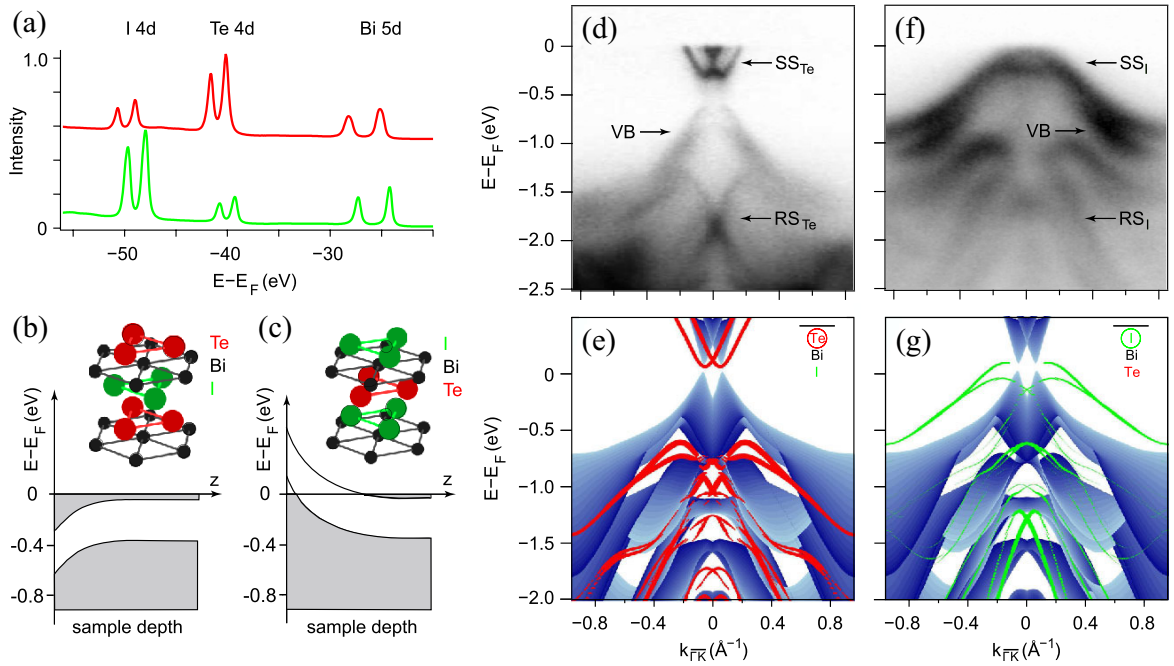

Figure 7.8: (a) I 4d, Te 4d, and Bi 5d core level spectra measured at a photon energy of 120 eV on Te- (red) and I-terminated (green) surfaces. **(b,c)** Schemes of the surface band bending for the two surface terminations. **(d)** ARPES dispersion along the $\overline{\Gamma}$–$\overline{\mathrm{K}}$ direction measured at $h\nu = 93\,\mathrm{eV}$ and $T = 40\,\mathrm{K}$, for a Te-terminated surface, compared to **(e)** the projected slab band structure calculated from first principles. The continuum of bulk states is shown in blue and the surface spectrum is colored red. **(f,g)** Corresponding plots for the I-terminated surface with the surface spectrum in green color. Figures taken from Ref. [200].

scenario [200]. Later STM studies confirmed the mixing of surface terminations and the opposite surface band bending with p–n junction at the interfaces of areas with different termination [202, 203].

7.1.3 Discussion

Having disentangled the surface states from the bulk states, now the special bulk Fermi surface and its physical implications are discussed. This peculiar Fermi surface is approximated around the A point by the Hamiltonian of free electrons with effective mass m and subject to a Rashba spin–orbit interaction of strength α

$$\mathcal{H} = \frac{\hbar^2 \boldsymbol{k}^2}{2m} + \alpha\left(k_x\sigma_y - k_y\sigma_x\right) - \mu, \tag{7.1}$$

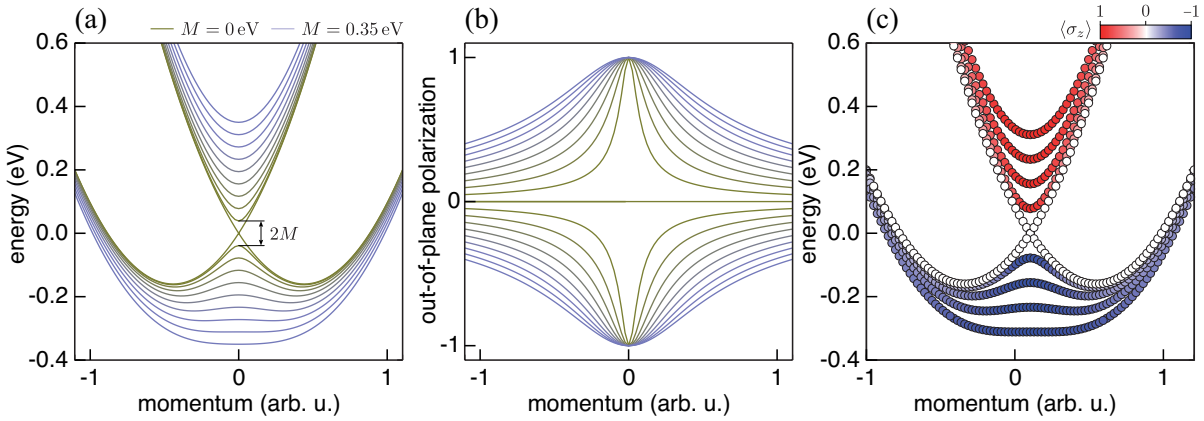

Figure 7.9: **(a)** In-plane Rashba spectrum ($k_z = 0$) including a magnetic order term $M\sigma_z$, with $\mu = 0$ for different M. **(b)** Out-of-plane spin polarization of the inner ($\langle\sigma_z\rangle > 0$) and outer ($\langle\sigma_z\rangle < 0$) Rashba branches. **(c)** Same as (a) with color indicating the out-of-plane spin polarization.

which is analogous to Eq. (3.13) except that $\boldsymbol{k}$ is a three-dimensional vector (see Fig. 7.6b for the energy spectrum). Depending on the chemical potential μ, the Fermi surface undergoes a topological transition, a so-called *Liftshitz* transition [73]. For $-\alpha^2/(2m) < \mu < 0$ it is a ring torus, at $\mu = 0$ the hole in the torus closes, and for $\mu > 0$ it becomes a spindle torus (Fig. 7.6b). At the transition, both the number of Fermi surfaces and the genus of the remaining Fermi surface changes by one. The toroidal ($\mu < 0$) Fermi surface encloses none of the TRIM and, due to spin-momentum locking, the electronic states acquire a Berry phase of π when transported once around the non-contractible toroidal loop that encloses the Γ–A line. Even though this picture does not include any lattice effects, it serves as a lowest order approximation to illustrate our results for BiTeI. Remarkably, BiTeI not only shows a giant Rashba splitting in absolute terms, but also its chemical potential is found to be small compared to the spin–orbit energy scale and thus the measured spindle-torus Fermi surface is close to the topological transition described above. Upon hole-doping the BiTeI crystal, its Fermi surface can in fact be driven through the topological transition from the observed spindle torus to a ring torus. As shown in Ref. [204] reducing the carrier density can also be achieved by employing different growth techniques. The resulting competition between the kinetic energy and the energy scale of the non-Abelian Rashba gauge field would render BiTeI a suitable platform for spintronics applications and an ideal playground to address questions of fundamental research. In particular, the interplay of the Fermi surface topology with symmetry-breaking phenomena by the examples of superconductivity and ferromagnetism shall be illustrated.

First, if a material with a similar bulk Fermi surface would show a superconducting instability, the topological change in the Fermi surface is predicted to drive a crossover from a Bardeen-Cooper-Schrieffer superconductor to a Bose-Einstein condensate of Cooper pairs (BCS-BEC crossover) [205]. Another interesting aspect is the expected superconducting pairing symmetry, where noncentrosymmetricity generically implies a mixture of singlet and triplet pairing: If the p wave component is dominant, as is the case in $CePt_3Si$ [206], the toroidal Fermi surface has the potential to realize a *fully gapped* $p_x + i\,p_y$ superconductor in three dimensions. The reason is that the ring torus has no intersection with the Γ–A or H–K lines, at which the superconducting $p_x + i\,p_y$ gap function vanishes.

As a second example, the effect of a dopant that orders ferromagnetically is considered. This amounts to supplementing Hamiltonian Eq. (7.1) by a Zeeman term $M\sigma_z$ (where $2M$ is the Zeeman gap. See App. B for general orientations of the magnetic field). In this case, if the chemical potential satisfies $\mu < M$, there arises a *single* three-dimensional Fermi surface without spin degeneracy, but with a non-trivial spin texture (Fig. 7.9). This situation of a single, non-degenerate Fermi surface is responsible for the potential of one-dimensional semiconductor nano-wires [127] and the two-dimensional Dirac surface states of $\mathbb{Z}_2$ topological insulators [9] to host exotic physical phenomena. It would be interesting to study what effects arise from such a single, non-degenerate Fermi surface in three dimensional, besides its relevance for spin transport due to the reduced phase space for scattering.

In addition it was shown in a theoretical work that BiTeI can become a topological insulator under action of hydrostatic pressure [207] which was subsequently tempted to observe experimentally by means of structural and optical measurements; though with controversial results for the transition pressure [208, 209]. In a recent publication the idea was portrayed that the Te surface of BiTeCl undergoes a topological transition due to "electric pressure" induced by surface charges, forming a Dirac cone at this surface [210]. However, the questionable physical explanation, the similarity of the published ARPES data of the Dirac cone with the one known from Bi_2Te_2Cl, and the fact that earlier published experimental reports on this compound show a trivial band structure (Sect. 7.2, [191, 211]), suggest a mixture of crystalline phases. More promising in engineering topological non-trivial phases are the $(BiTeI)_m(Bi_2Te_3)_n$ heterostructures which allow for tuning the bulk spin splitting and the $\mathbb{Z}_2$ topological invariant by changing the parameters n and m. It has for example been shown by *ab-initio* calculations that the compound with $n = m = 1$ is a strong topological insulator without inversion symmetry, hosting termination-dependent Dirac states at the surfaces and featuring Rashba splitting in the bulk [212]. In this context, the structurally similar but inversion-symmetric Bi_2TeI should also be mentioned, which is predicted to be an intrinsic topological insulator [213].

7.1.4 Conclusion

To conclude, direct measurements of the bulk band dispersion of noncentrosymmetric BiTeI have been presented that confirm its giant three-dimensional Rashba-type spin splitting, leading to the unusual spindle torus shaped Fermi surface. Further, the surface state character of the two-dimensional Rashba-split conduction band state at the Te-terminated surface was clarified and the relation between the two- and three-dimensional Fermi surfaces was established. The toroidal Fermi surface has unique properties and may open a pathway for the realization of exotic physical systems.

7.2 Bulk band mapping of BiTeCl

In the previous Section it was shown that BiTeI features not only spin-split bulk bands which result in toroidal Fermi surfaces but also two-dimensional surface states with large spin splitting that are hosted on the crystal's two inequivalent (0001) surfaces. In this section, ARPES measurements on the related compound BiTeCl are presented. This material features a bulk Rashba splitting slightly smaller than BiTeI and possesses a significantly larger bulk band gap. In contrast to previously studied BiTeI, which has been reported to suffer from stacking faults [190, 200] leading to mixed surface terminations, the here examined BiTeCl samples are single-crystalline on a macroscopic scale (several mm) with well defined surface terminations. On the one hand, single-terminated surfaces allows for the independent examination of the two distinct BiTeCl(0001) surfaces which host quantized sets of two-dimensional states localized in the near-surface triple layers [201,211,214]. And on the other hand, the preserved stacking order along the polar axis is indispensable for transport measurements since spin effects would cancel out in systems with a mixed orientation of quantization axes.

7.2.1 BiTeCl crystal structure

BiTeCl has a hexagonal crystal structure (space group $P6_3mc$) of alternating layers of chlorine, bismuth and tellurium atoms as illustrated in Fig. 7.10a [192]. The crystal has no inversion symmetry due to the continuous stacking order of the three atomic layers. In contrast to BiTeI and BiTeBr, the unit cell of BiTeCl is doubled in the c direction in such a way that the crystal is

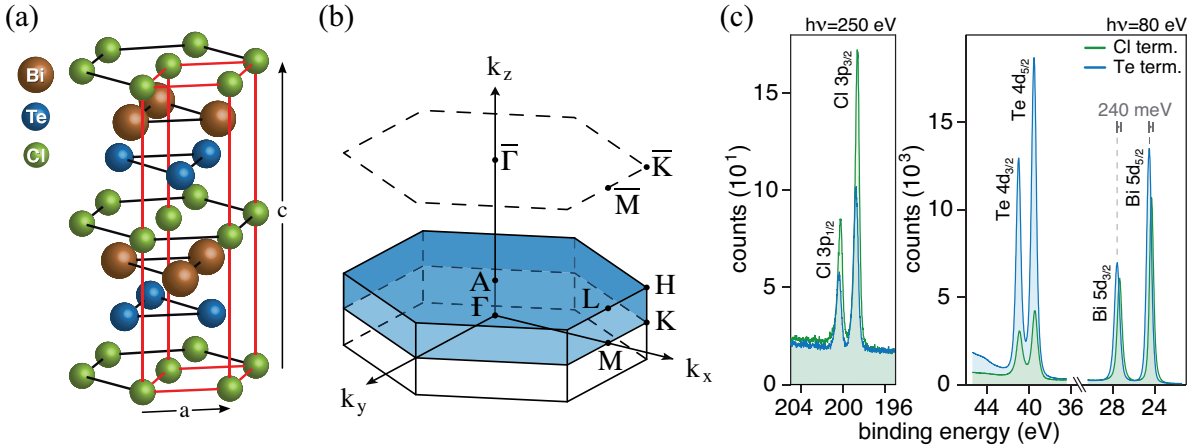

Figure 7.10: (a) BiTeCl crystal structure (space group $P6_3mc$, $a = 4.2426(1)$ Å, $c = 12.397(1)$ Å [192]). **(b)** Brillouin zone of the bulk (solid lines) and the surface (dashed lines). **(c)** X-ray photoelectron spectroscopy of shallow core levels comparing Cl- and Te-terminated BiTeCl(0001).

symmetric under the screw operation composed of a non-primitive translation by $c/2$ along the hexagonal axis and a rotation of $\pi/3$ around the same axis. In other words, $P6_3mc$ is a nonsymmorphic space group with the consequence that additional selection rules for the final state in the photoemission process are introduced, which makes the band structure observed with ARPES depend on the Brillouin zone number [215], as will be discussed below.

Analogously to BiTeI, the weak bonding between the Te and Cl layer provides a natural cleaving plane in the (0001) plane. Due to the lack of inversion symmetry, an ideal crystal can have two nonequivalent surfaces, with either Te or Cl termination, determined by the underlying crystal stacking order. For the measurements presented here, care was taken to produce chemically pure terminations.

7.2.2 Crystal growth

The BiTeCl crystal was grown based on $BiCl_3$–Bi_2Te_3. The telluride compound was obtained by fusing stoichiometric amounts of elemental Bi and Te at 600°C. $BiCl_3$ was prepared by evaporation of a saturated solution of Bi_2O_3 in HCl acid. The binary compounds were weighed in proportions of 11 mol.% Bi_2Te_3 and 89 mol.% $BiCl_3$ which corresponds to the peritectic melting composition of BiTeCl [216]. The charge was then sealed in a growth quartz ampoule under a pressure of 10^{-3} torr. After heating to 430°C at a rate of 20°C/hour followed by 1 day of soaking at this temperature the melt was crystallized by a modified Bridgman method [217]. The top part of the resultant ingot contained eutectic, while the bottom part presented an aggregate of layered crystals. According to an X-ray diffraction analysis a major part of the aggregate consisted of the BiTeCl phase, which was selected for the ARPES measurements.

7.2.3 Energy spectrum of the two terminations of BiTeCl(0001)

Time-reversal symmetry ensures the electronic bulk band structure of the two possible stacking orders to be equal for the two terminations, when neglecting the spin structure. Figures 7.11a,b show ARPES band maps along the Γ–K direction measured with p-polarized light of 20 eV photon energy on a pair of samples with Cl and Te termination, respectively. The spectra show sharp band dispersions significantly different for the two samples, without any indication of mixed terminations, in contrast to what was observed for BiTeI [190, 200]. The bulk bands at the Te-terminated surface are rigidly shifted by 140 meV towards higher binding energies when compared to the situation at the Cl termination due to a different surface band bending.

Tellurium termination

In this section the ARPES signature of the Te-terminated BiTeCl(0001) surface will be discussed in more detail. The ARPES band map in Fig. 7.11b shows several states located on the Te-terminated surface. A set of hole-like surface states with unusually narrow line widths are energetically located on top of the bulk valence band, better resolved in the off-normal

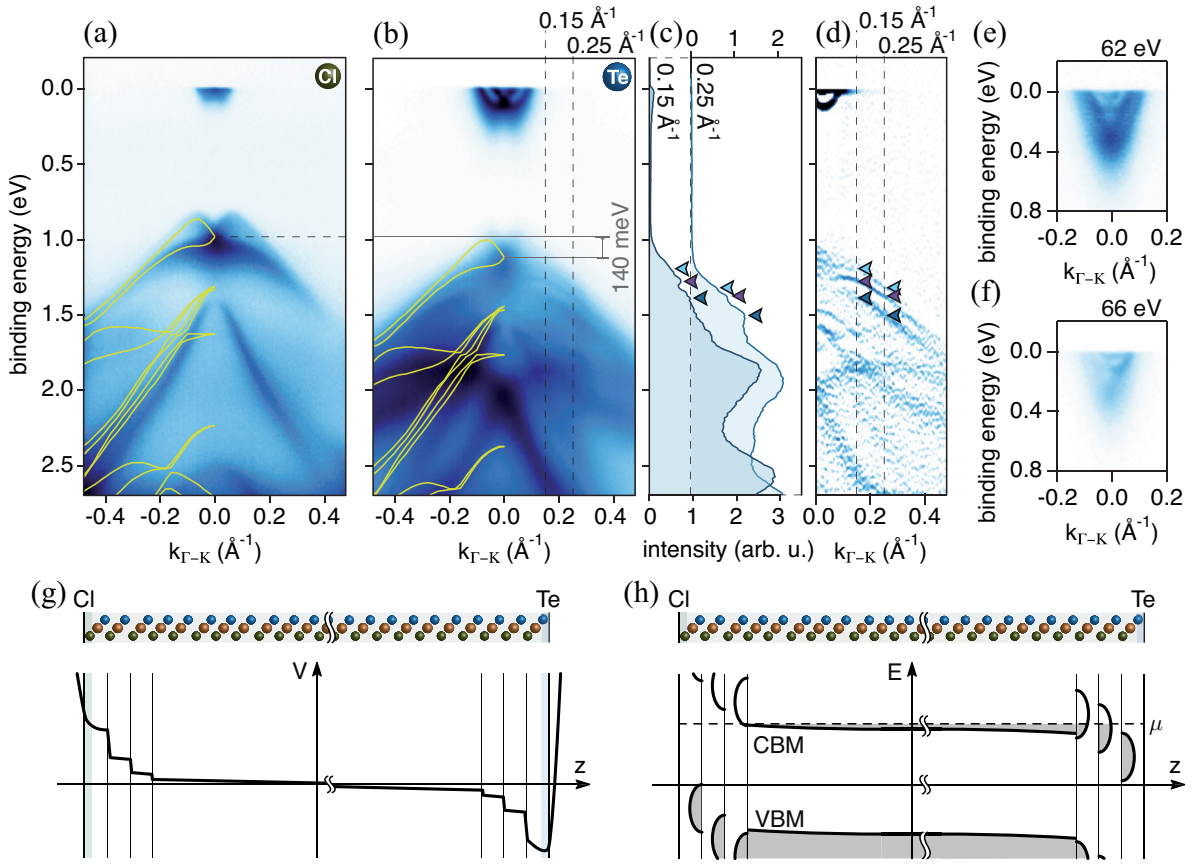

Figure 7.11: **(a)** ARPES measurement at 20 eV photon energy on Cl-terminated BiTeCl(0001) with overlaid bulk band structure obtained from DFT calculations. **(b)** Same as (a) but measured on inversely stacked, Te-terminated BiTeCl(0001). **(c)** EDCs from the band map in (b) at $k_{\parallel} = 0.15\,\text{Å}^{-1}$ and $0.25\,\text{Å}^{-1}$, the arrows indicate sharp two-dimensional states. **(d)** Second derivative of the ARPES map (b) for $k_{\parallel} > 0$, the arrows correspond to the peaks highlighted in (c). **(e)** Band maps of Te-terminated BiTeCl(0001) at 62 eV and **(f)** 66 eV photon energy exhibit an additional broader two-dimensional electron-like state in the conduction band. **(g)** Schematic illustration of the staircase-like potential at the two *pristine* (0001) surfaces of a BiTeCl crystal. **(h)** Schematic band diagram with split-off surface states located in the first three surface triple layers.

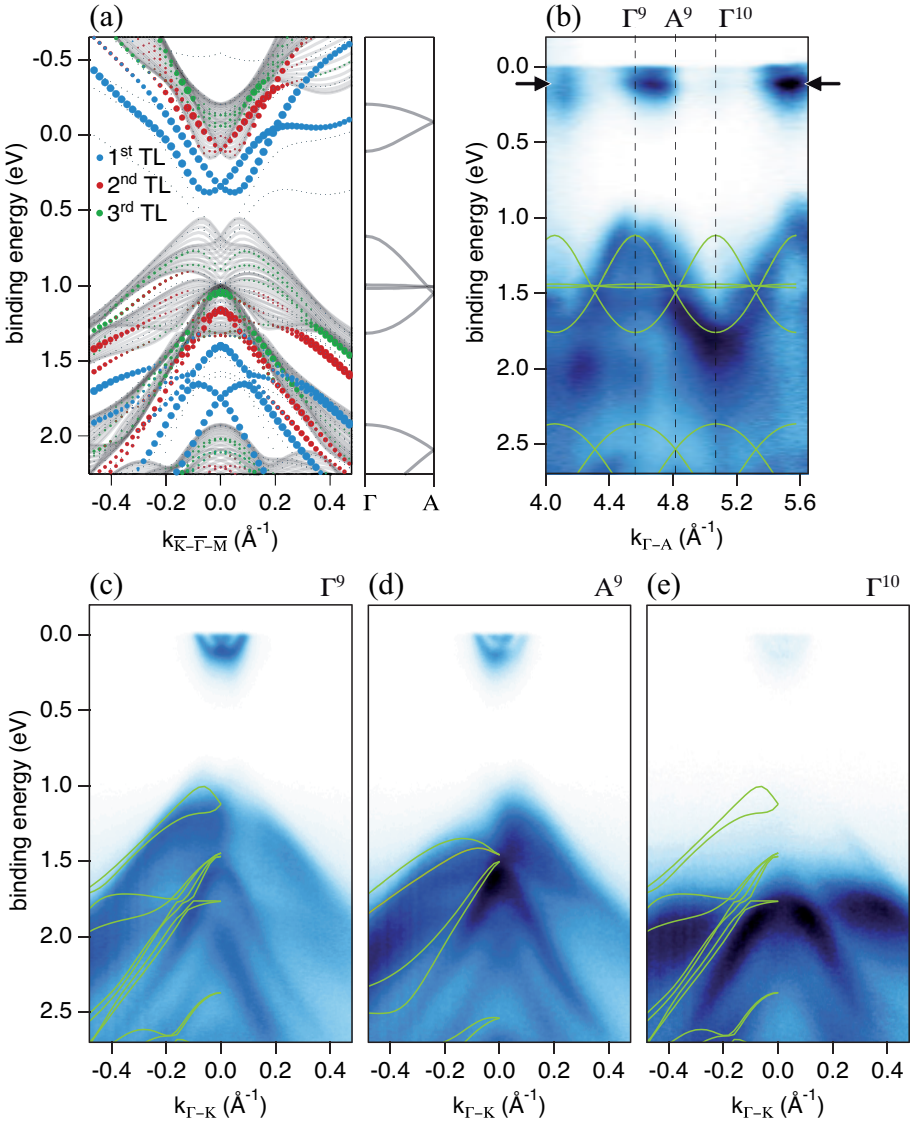

Figure 7.12: UV-ARPES and DFT spectra of Te-terminated BiTeCl(0001). **(a)** *Left panel:* DFT calculations of a Te-terminated BiTeCl(0001) slab with bulk bands for different k_z (gray) exhibit two-dimensional states in the first (blue), second (red), and third (green) triple layer beneath the surface. *Right panel:* bulk dispersion along Γ–A. **(b)** Photon energy scan showing the k_z dispersion at normal emission, overlaid with the bulk band dispersion obtained by DFT. **(c–e)** Spectra at selected k_z values corresponding to Γ^9 ($h\nu \simeq 74\,\text{eV}$), A^9 ($h\nu \simeq 83\,\text{eV}$), Γ^{10} ($h\nu \simeq 93\,\text{eV}$). The differences in spectra observed at Γ^9 and Γ^{10} are related to special matrix element effects, see text.

EDCs in Figs. 7.11c,d showing the second derivative of the ARPES spectrum for positive wave vectors. The electron-like state at the Fermi level is also part of a set of surface states; an additional state with weaker intensity and larger line width can be observed on freshly cleaved samples (Figs. 7.11e,f).

These findings are supported by DFT calculations. To simulate the semi-infinite BiTeCl(0001) system, a slab was composed of 24 atomic layers separated by roughly 20 Å vacuum space with the chlorine side (for the Te-terminated surface) or the tellurium side (for the Cl-terminated surface) passivated by a hydrogen monolayer. The calculations predict surface states to be present at both possible terminations. The crystal potential at the surface is found to show a downward (upward) band bending for the Te-(I)-terminated surfaces. Because of the polar crystal structure, the potential is staircase-like with increasing potential steps towards the surface and step lengths corresponding to a crystal triple layer (Fig. 7.11g). In the first few triple layers two-dimensional states split-off from the bulk states, and are localized in the particular triple layer (Fig. 7.11f). Figure 7.12a shows the surface spectrum of a Te-terminated surface where the localization in the first three surface triple layers is represented by the size of the DFT data points. Consistent with the staircase-like downward band bending the bands are increasingly shifted towards lower energies for localizations closer to the crystal surface.

With ARPES, the dispersion of the bulk bands along the out-of-plane momentum k_z can be studied by varying the photon energy. Figure 7.12b shows the photoemission spectra along the Γ–A direction (i.e. $k_{\parallel} = 0\,\text{Å}^{-1}$) for a continuous range of photon energies (56–117 eV) measured on Te-terminated BiTeCl(0001). The out-of-plane momentum is obtained by inferring a parabolic dispersion of the photoemission final states in the crystal and neglecting the photon momentum transfer (cf. Sect. 2.1). For the inner potential a value of $V_0 = 5\,\text{eV}$ with respect to the Fermi level was obtained.

The two-dimensional state close to the Fermi level (indicated by the arrows) oscillates in spectral intensity but no dispersion in k_z direction can be observed. On the other hand, the k_z dispersion of the bulk states in the valence band is evident. The overlaid lines represent the bulk band dispersion as shown in the right panel of Fig. 7.12a. As a striking difference, the spectral features show a periodicity that is twice the size of the Brillouin zone, i.e. compared to what is expected from the hexagonal lattice parameter $c = 12.397(1)$ Å [192]. The photoemission intensity of each band is suppressed in every other Brillouin zone as a consequence of a special photoemission selection rule in crystals belonging to the nonsymmorphic space group, as it is observed in graphite [215] and other materials [218–220]. Experimentally, this results in non-equivalent photoemission spectra around the Γ points. Figures 7.12c–e show the in-plane dispersion along the $\overline{\Gamma}$–$\overline{\text{K}}$ at three neighboring high symmetry points Γ^9, A^9 and Γ^{10}. On each spectrum, the DFT bulk band structure around the particular high symmetry k

point is overlaid.

As a result of the screw symmetry in the $P6_3mc$ space group the bulk band structure at the A points features band sticking; at these points all bands are at least two-fold degenerate [63]. The underlying physics is that the structure factor at the A point vanishes $\sum_i e^{i\boldsymbol{k}_A \cdot \boldsymbol{r}_i} = 0$ ($\boldsymbol{r}_i$: positions of basis atoms) since each atom in the unit cell has a partner of the same atomic species that is shifted by a $c/2$ translation. Consequently, the Bragg reflection for $\boldsymbol{k}$ around the A point is suppressed and no band gap opens. The group velocity at the Brillouin zone boundary is non-zero and has the same absolute value for the touching bands due to time-reversal symmetry. This leads to a braid-like band structure in the Γ–A direction which can experimentally not be observed due to the above mentioned photoemission selection rule.

Chlorine termination

When the BiTeCl crystal c axis is reversed, the stacking order of the atomic layers inverts and the surface termination changes from a tellurium to a chlorine layer. Time-reversal symmetry, however, ensures that the electronic bulk band structure remains unchanged and only its spin polarization changes sign. Any spectroscopic difference observed in the electronic structure of BiTeCl crystals of opposite stacking orders therefore arises from the different surface terminations.

The k_z dispersion of the bands in Fig. 7.11a is examined in Figs. 7.13b–e which show ARPES data of Cl-terminated BiTeCl(0001) taken in the soft X-ray photon energy regime. The k_z dispersion map in Fig. 7.13b was measured with photon energies in the range from 432 eV to 825 eV and the band maps in Figs. 7.13b–d were measured at three neighboring high-symmetry points Γ^{23}, A^{23} and Γ^{24}. Because of the non-negligible photon momentum transferred to the photoelectrons at these high photon energies, the measured electron momenta have been corrected for the photon momentum projected on the particular electron momentum axis. The inner potential was determined to be $V_0 = 0$ eV (with respect to the Fermi level) which is smaller than the value in the ultra-violet regime but consistent with the weakening of the electron exchange-correlation potential for the final states at high photoelectron energies.

The measured bulk band structure is in good agreement with what was found for the Te-terminated crystal and the bulk DFT calculations (Fig. 7.13a), apart from offsets of the band binding energies. The band gap of about 0.8 eV is in good agreement with *ab-initio GW* calculations [221]. In contrast to the electronic structure of the Te-terminated samples, no two-dimensional state is present neither in the presented photon energy range nor in measurements done in the ultra-violet range, cf. Figs. 7.13b–e and Fig. 7.14. This is clear from the fact that on the one hand every observed band can be related to a band in the bulk DFT

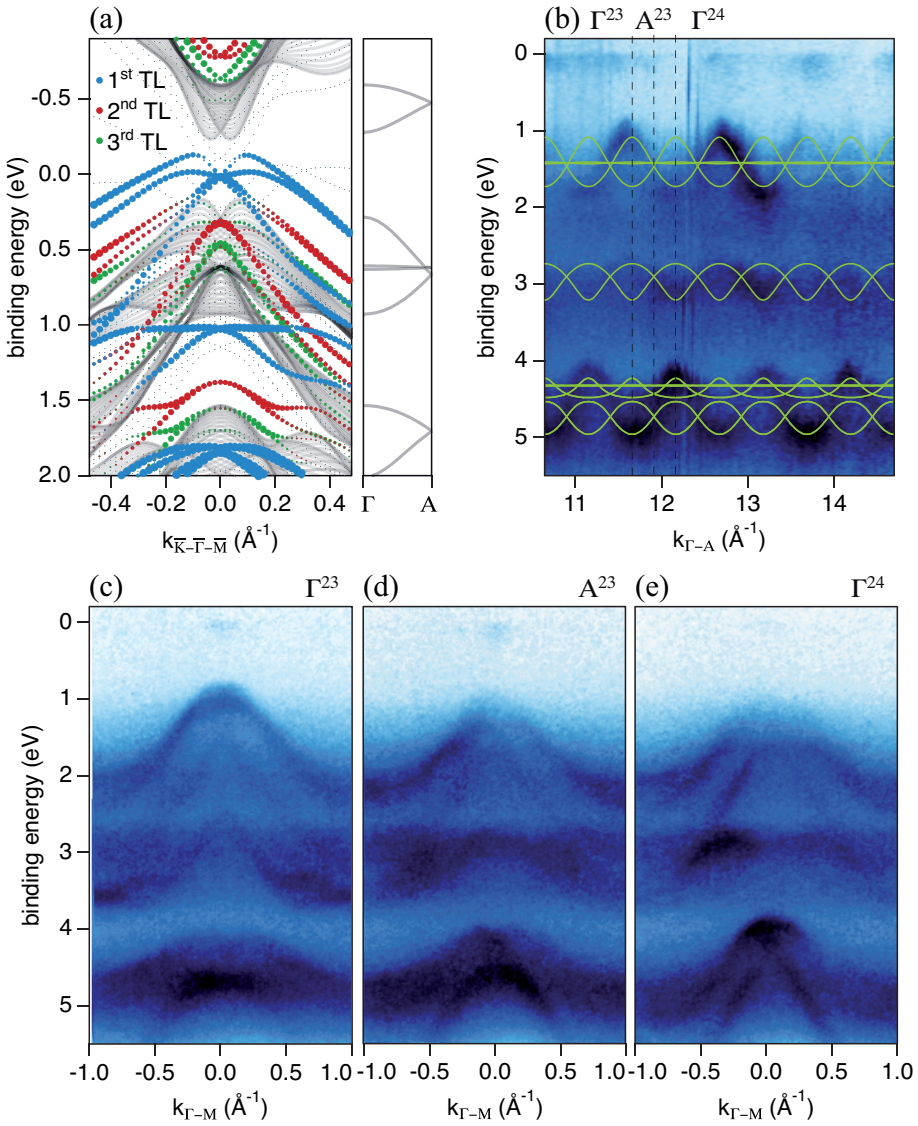

Figure 7.13: ARPES and DFT spectra of Cl-terminated BiTeCl(0001). **(a)** DFT calculations of a Cl-terminated BiTeCl slab with bulk bands (gray) and the two-dimensional states in the first (blue), second (red), and third triple layer (green). **(b)** SX-ARPES photon energy scan, showing the k_z dispersion along Γ–A. **(c–e)** Spectra at selected k_z values corresponding to Γ^{23} ($h\nu \simeq 513\,\text{eV}$), A^{23} ($h\nu \simeq 535\,\text{eV}$), Γ^{24} ($h\nu \simeq 559\,\text{eV}$).

calculations and on the other hand that the photon energy scans in Figs. 7.13b and Fig. 7.14 do not feature any sign of a k_z-independent state. The DFT calculations in Fig. 7.13a predict the existence of a set of two-dimensional hole-like surface (blue) and subsurface states (red, green) for Cl-terminated BiTeCl(0001). Here, the surface states energies are step-wise

increased for localizations in triple layers closer to the surface. Equivalent states have been observed on the iodine termination of the related BiTeI compound [190, 200].

In addition, the observed difference in band bending at the Te- and Cl-terminated surfaces is about 140 meV and thus much smaller than the 400 meV predicted by DFT. The Cl-terminated surface is even slightly *n*-doped. The relative band bending is obtained by fitting the highest energy bulk valence band to the ARPES data of both terminations and comparing the binding energies. It is argued here that a chemical process at the chlorine surface induced by the intense synchrotron photon beam or the consequently occurring lifting of the surface band bending are the reason for the reduced size of the band bending and the absence of surface states on the Cl termination. Figure 7.15a shows the photoemission spectrum of the Bi 4f state measured with a photon energy of 500 eV. After having positioned the beam spot to a previously unexposed sample area, the 4f levels appear to be split by 800 meV. Under the influence of the photon beam the peak intensity is redistributed to the higher binding energy levels within a few minutes (right panel in Fig. 7.15a). A similar behavior is observed for the Cl 2p core levels measured with 250 eV photon energy, where the energy difference is about 700 meV (Fig. 7.15b). The figure shows that the redistribution time scales with the photon flux impinging on the sample, confirming that the core level intensity redistribution at the Cl-terminated surface is photon beam induced. The Te core levels (not shown) show a similar intensity redistribution due to a changing chemical environment. Figure 7.15c shows a low-statistics ARPES band map promptly after cleaving the sample and without prior light exposure. In agreement with the measurements on BiTeI, the surface band bending is upwards such that the Fermi level is located in the top of the valence band. Spectral features of surface states are not observed, either due to their absence or the low quality of the band map.

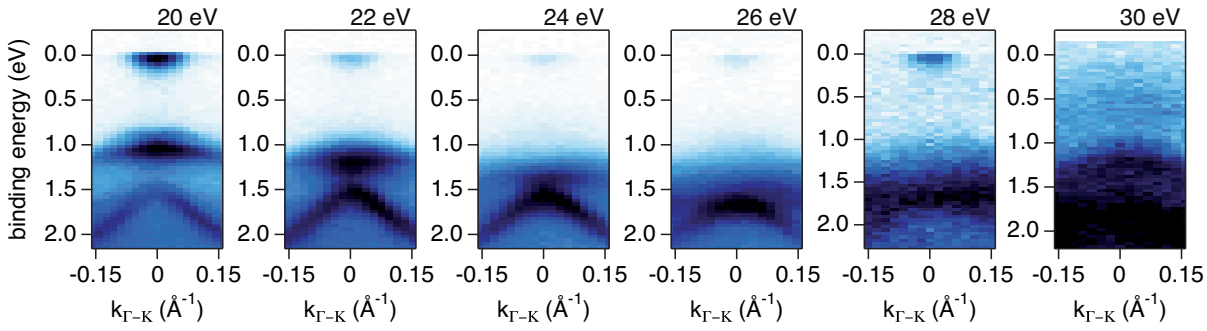

Figure 7.14: UV-ARPES maps of Cl-terminated BiTeCl(0001) at photon energies 20 eV (Γ point) to 30 eV (A point).

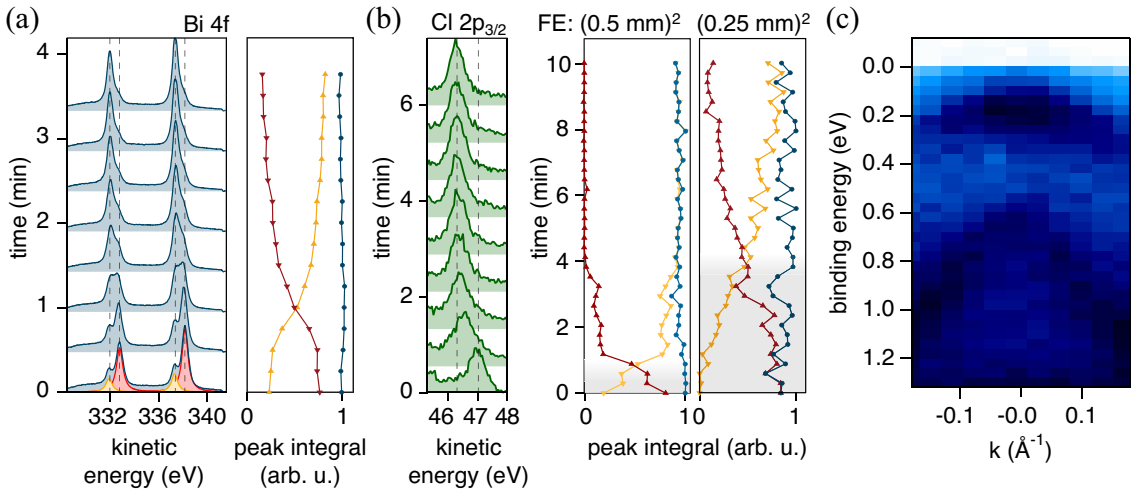

Figure 7.15: Photon beam induced core levels shifts. **(a)** *Left panel:* Bi 4f core levels shifts. *Right panel:* background subtracted pristine (red), shifted (yellow) and overall (blue) core level peak integral. **(b)** *Left panel:* Cl $2p_{2/3}$ core level shift. *Right panel:* core level peak integrals for two photon fluxes differing by a factor of 8. **(c)** Band map of freshly cleaved Cl-terminated BiTeCl(0001).

Surface work function

The surface work functions of the two terminations significantly differ, due the polar nature of the material and the opposing surface band bending [191]. By measuring the kinetic energies

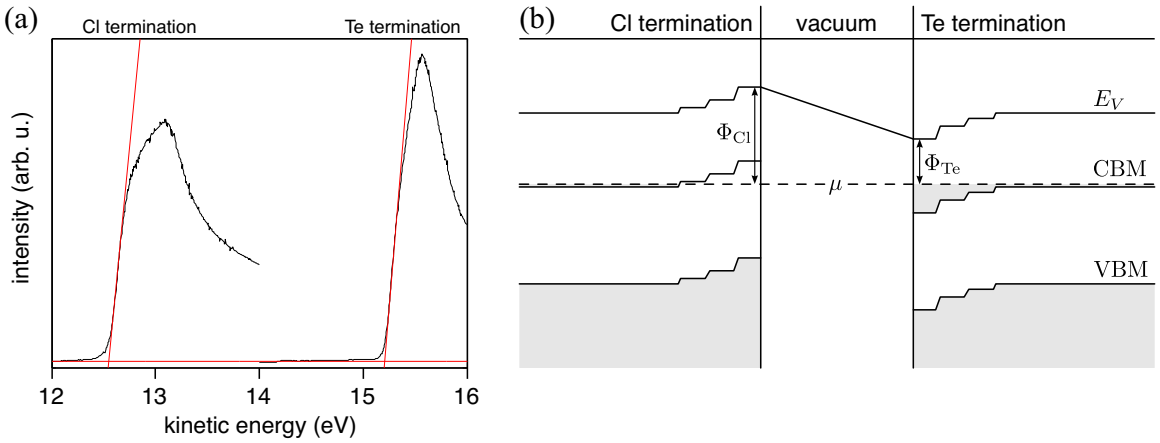

Figure 7.16: Photon beam induced core levels shifts. **(a)** Secondary cutoff of Cl- and Te-terminated BiTeCl(0001) (−10.04 V bias). **(b)** Surface band bending of pristine BiTeCl(0001) and qualitatively expected termination-dependent workfunctions.

of the secondary cutoff (Fig. 7.16a) and the Fermi level of negatively biased samples, the surface work functions were determined to be $\Phi^{\mathrm{Cl}} = (6.85 \pm 0.03)$ eV and $\Phi^{\mathrm{Te}} = (9.58 \pm 0.03)$ eV for the Cl- and the Te-terminated surface, respectively. The values are unusually large; for comparison, Pt has the largest work function of the elements (5.65 eV for polycrystalline Pt) [222]. Further, based on the predicted band bending at the pristine BiTeCl(0001) surfaces (Fig. 7.16b), the Cl-terminated surface is expected to have a larger work function than the Te surface, since the surface work function differs from the bulk work function by the surface band bending. Judging from the nearly equal band bending in the experiment (Fig. 7.11a,b), the work functions should deviate from each other only by 140 meV. The interpretation of these large values for the work function remain an open question and needs further investigation and theoretical support.

7.2.4 Discussion

In contrast to Te-terminated BiTeCl(0001), which shows spectroscopic signals of the three-dimensional bulk states and the two-dimensional surface states, all bands observed on a Cl-terminated sample disperse in the out-of-plane direction. The absence of the predicted surface states on the Cl-terminated samples indicates either that the surface states do not form at all or they die out before or during the measurements. Here, it is suggested that the states are destroyed by the photon beam which significantly changes the surface chemistry and the surface band bending. In this case, the absence of the surface states in the ARPES maps recorded just after the start of the light exposure could be related to the higher photon flux used as compared to the XPS measurements, which increases the speed of the chemical reaction. Given the fact that the core level shifts are only observed on Cl-terminated BiTeCl and that they are largest for Cl and Bi indicates that the chemical reaction takes place in the chlorine layer. A decrease of the spectral intensity of the Cl core level can not be observed, ruling out beam-induced desorption, etching or segregation of the surface. A possible scenario could be the interplay of the photon beam with residual gases of the vacuum, such as beam-enhanced hydrogen adsorption or other photochemical effects of adsorbed molecules on the surface [223].

In the ARPES measurements on the Te-terminated BiTeCl(0001) samples, no indication for beam-induced aging is found and the predicted surface states are observed. A remarkable feature of especially the hole-like surface states in the valence band is their small line width down to 40 meV at binding energies of around 1 eV. The small line widths at these binding energies indicate small electron-defect and electron-phonon scattering. Considering that these hole-like surface states are energetically overlapping the bulk states, electron-electron interaction can only be small if the surface states are spatially decoupled from the bulk states. The

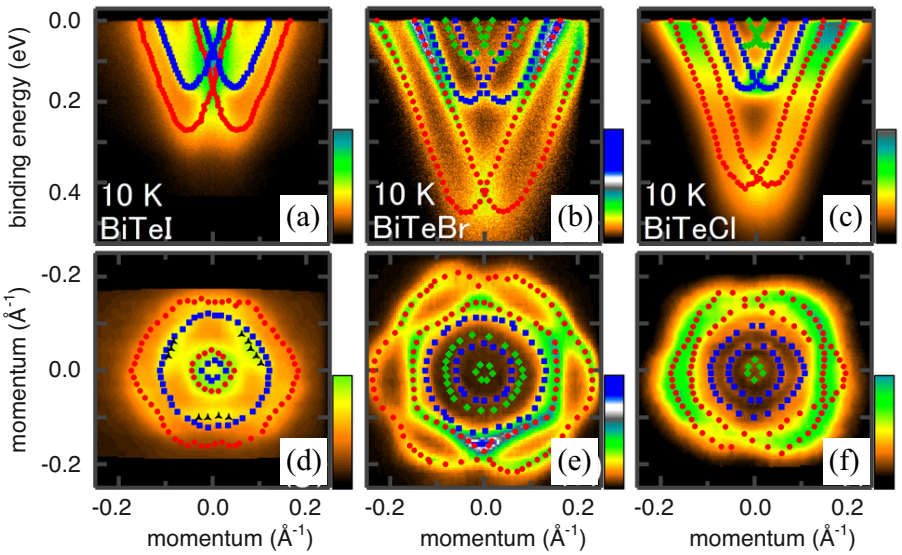

Figure 7.17: Comparative ARPES maps of the (0001) surface states of **(a)** BiTeI, **(b)** BiTeBr, **(c)** BiTeCl, and **(d–f)** the corresponding Fermi surfaces. The size of the spin splitting scales inversely with the atomic number of the halogen. The surface termination is not specified in Ref. [211], but most likely all three sample surfaces were Te-terminated. Figure taken from Ref. [211].

trapping of the surface states in the first surface triple layers supports such a decoupling but can not explain why the line width generally decreases for states being hosted in triple layers further away from the surface. Such sharp states have also been observed near the Fermi levels of BiTeI(0001) and BiTeBr(0001) (see Sect. 7.1 and Fig. 7.17, [190,211]). Additional theoretical and experimental effort will be needed to explain this behavior.

7.2.5 Conclusion

In conclusion, ARPES measurements on BiTeCl(0001) were performed in the ultra-violet and soft X-ray regime. The large Rashba splitting of the bulk bands of this noncentrosymmetric and nonsymmorphic material is observed. A BiTeCl(0001) single crystal is either terminated by a chlorine or a tellurium layer, depending on the underlying stacking order. While the Te-terminated surface hosts a set of surface states localized in the distinct steps of the potential landscape at the surface, the theoretically predicted surface states on the Cl-terminated surface could not be observed with ARPES due to a photon induced change of the surface chemistry. This absence of the surface states makes Cl-terminated BiTeCl(0001) an ideal candidate to study the spin structure of the bulk bands as will be discussed in the next Section.

7.3 Spin structure of BiTeCl

In this Section, the spin polarization of the bulk valence band of BiTeCl is studied by means of spin-resolved ARPES. While the spin structures of two-dimensional surface or quantum well states have been extensively studied in the past [224], to date spin-resolved ARPES measurements of spin-split bulk bands do not exist to the best of the authors knowledge. As described in the previous Section at Te-terminated (0001) BiTeCl surfaces several sets of surface states both in the valence band and conduction band can be spectroscopically observed, but their theoretically anticipated counterparts on Cl-terminated surfaces are absent. This can be exploited to perform spin-resolved ARPES measurements of the spin splitting of the bulk bands without any interfering signal from surface states as shown in the following.

7.3.1 Spin structure of the valence band of Cl-terminated BiTeCl(0001)

The experimental setup and definition of the sample coordinate system for the following measurements are given in Figs. 2.5a,b. All the experiments shown in the following were performed with p-polarized light. The band map in the left panel of Fig. 7.18a shows the top of the valence band and bottom of the bottom band of the bulk measured at a Cl-terminated surface with 20 eV photon energy, roughly corresponding to the bulk Γ–K direction. The Rashba-type splitting of the top of the valence band has its maximum at $k_+ = -k_- \approx 0.07\,\text{Å}^{-1}$ and is around 170 meV as shown in the EDC in the right panel.

The spin-resolved ARPES experiments were performed at these momenta on either side of normal emission. Figures 7.19a,b show spin-resolved EDCs at 20 eV photon energy across the top of the valence band at k_- and k_+ along the bulk Γ–K crystal direction, in this case, the y direction of the manipulator. While the top panels show the sum of the intensity profiles measured by each Mott channel, the bottom panels contain the measured photoelectron spin polarization in the direction tangential (S_x) to the constant energy contour of the initial state. The radial and out-of-plane component of the spin polarization are small compared to the tangential component. By simultaneously fitting the measured total intensity and the three measured spin polarization curves, a spin polarization vector is assigned to each band (see Sect. 2.2.2 for details of the fitting procedure, [44]). The numbered pseudo Voigt profiles in the top panels are the result of the fitting procedure. Their splitting is determined to be (130±10) meV and matches reasonably well with the spin-integrated measurement, considering the larger angular integration range of a spin-resolved measurement. A representation of the spin polarization vectors of the individual bands can be found in the inset of the bottom panel.

For measurements with momenta along the x direction of the manipulator, the spin polar-

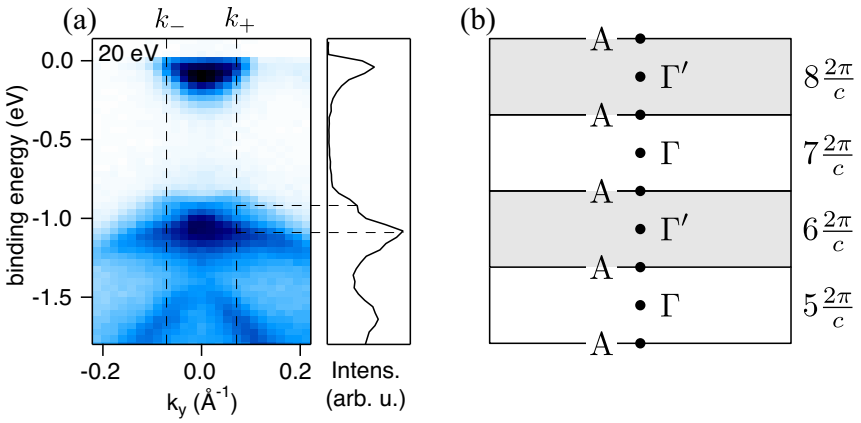

Figure 7.18: (a) *Left panel:* ARPES band map around the bulk Γ point ($h\nu = 20\,\text{eV}$) of Cl-terminated BiTeCl. *Right panel:* EDC at the momentum of the valence band maximum ($k_+ \approx 0.07\,\text{Å}^{-1}$). **(b)** Illustration of the Brillouin zone along the out-of-plane momentum.

ization retains its mostly tangential (S_y) orientation. Figures 7.19c,d show the tangential component of the spin polarization for $k_x = k_-$ and k_+, respectively, measured along the bulk Γ–M crystal direction. The insets show the result of the fitting procedure; within experimental resolution no out-of-plane polarization is measured and the radial polarization is small.

The absence of surface states of the Cl-terminated BiTeCl (0001) surface and the large spin–orbit interaction of BiTeCl give the opportunity to examine the evolution of the photoelectron polarization of a k_z dispersing bulk state. The measured spin polarization is significantly reduced at higher photon energies of 22 eV and 24 eV, which roughly correspond to k_z momenta halfway along the Γ–A line (Figs. 7.20a,b), and at the A point (Figs. 7.20c,d). Further, no reorientation away from its tangential orientation can be observed. At these low photon energies the k_z broadening is large due to the low probing depth [20] and half of the relatively small Brillouin zone is swept over roughly within an only 4 eV wide photon energy range. Generally, the k_z resolution in ARPES is enhanced by increasing the photon energy, therefore additionally photon energy dependent spin-resolved EDCs were measured in the Brillouin zone around the 9th bulk Γ point at roughly 77 eV photon energy. The spin-integrated band maps in Fig. 7.21a measured along the projected $\overline{\Gamma}$–$\overline{\text{K}}$ direction depict the dispersion between the A^8 point (68 eV) and the Γ^9 point (77 eV).

The spin-resolved EDCs in Fig. 7.21b were performed at two momenta $k_y \approx \pm 0.11\,\text{Å}^{-1}$ located on either side of normal emission along the $\overline{\Gamma}$–$\overline{\text{K}}$ crystal direction. The measurements were recorded starting with low photon energies with a total acquisition time of 14 h. A progressive degradation of the sample surface is reflected in the diminishing intensity (solid

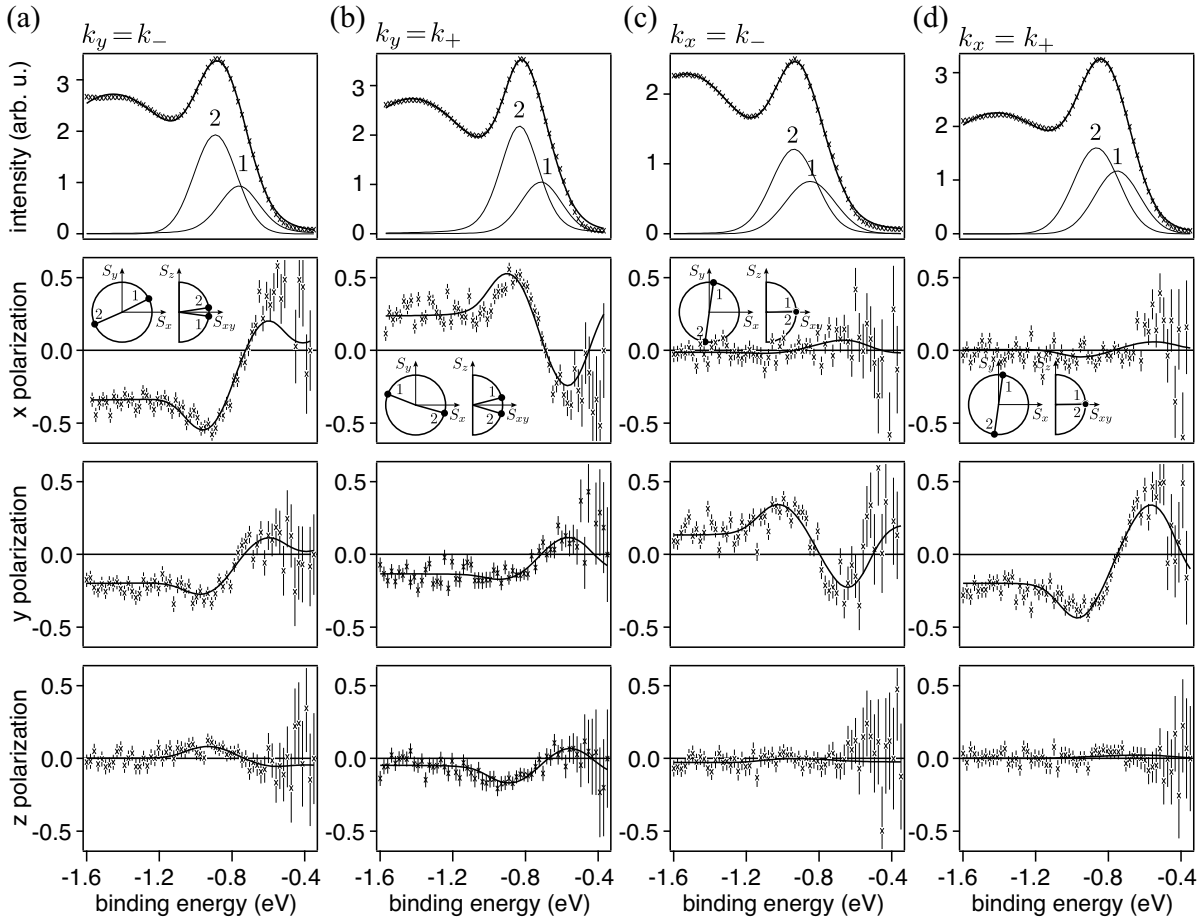

Figure 7.19: **(a)** Spin-resolved EDC at $k_y = k_- = -k_+$. *Top panel:* Total intensity measured with the Mott detectors (+). The lines represent the fitted total intensity and the energy-split top valence band, respectively. *Bottom panels:* In-plane tangential (x), radial (y), and out-of-plane (z) polarization ($\times$) with fitted curve (line). The inset shows a vectorial representation of the spin polarization of the individual bands **(b)** Same as (a), but measured at k_+ along k_y. **(c)** and **(d)** show the in-plane radial (x), tangential (y), and out-of-plane (z) polarization measured at $k_x = k_-$ and k_+, respectively, confirming the helical spin texture.

lines) towards higher photon energies. The in-plane spin polarization ($\times$) of the top valence band at 77 eV is compatible with the corresponding measurement at 20 eV photon energy, in the sense that the helicity is the same, while the maximal measured spin polarization is reduced by roughly 50 %. The mainly in-plane polarization is again accompanied by a small out-of-plane component (not shown). Towards lower photon energies, i.e. closer towards the bulk A point, the spin polarization amplitude gradually decreases. This increase towards the bulk Γ point is observed contrary to the trend of decreasing sample quality with time and is

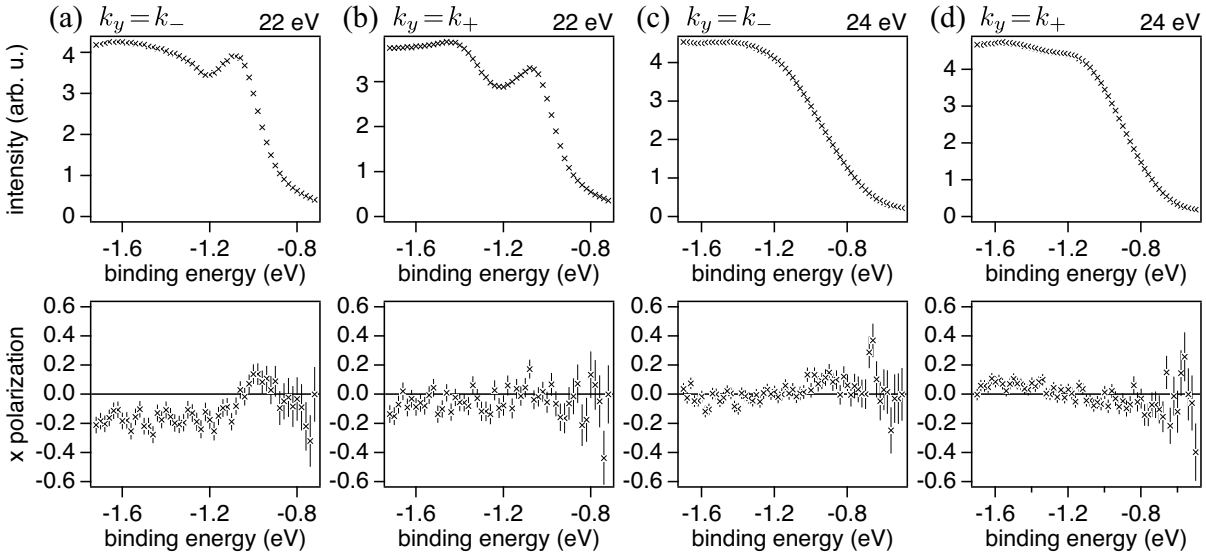

Figure 7.20: Spin-resolved ARPES EDCs analogous to Fig. 7.19a,b on either sides of the $\overline{\Gamma}$ point at different photon energies corresponding to different out-of-plane momenta: **(a,b)** halfway between the Γ and the A point (22 eV) and **(c,d)** at the A point (24 eV).

compatible to the measurements at lower photon energies.

In order to understand the link between the measured photoelectron spin polarizations and the spin structure of the initial state, fully relativistic DFT calculations were performed as shown in Figs. 7.22a–d. The color of the data points (defined in the inset of Fig. 7.22a) reflects the degree of spin polarization, projected in-plane and tangentially to the momentum vector. Figures 7.22a–c show the in-plane dispersion and spin polarization of the valence bands close to the band gap at $k_z = 0$ (along K–Γ–M), $\frac{1}{2}\pi/c$ (along $\overline{\text{K}}$–$\overline{\Gamma}$–$\overline{\text{M}}$) and π/c (along H–A–L), respectively. The vertical dashed lines indicate the momentum of the valence band maximum.

Generally, the mirror symmetry of the crystal demands the spin polarization to be fully in-plane and tangential along $\overline{\Gamma}$–$\overline{\text{M}}$ for any k_z. While out-of-plane spin polarization is allowed for e.g. the related compound BiTeI along and around the $\overline{\Gamma}$–$\overline{\text{K}}$ crystal direction [187], in the case of BiTeCl the screw operation symmetry inhibits out-of-plane spin polarization of any band in the entire Brillouin zone. Figure 7.22d shows the k_z dispersion of the same bands at fixed in-plane momenta $k = k_+$ ($\overline{\Gamma}$–$\overline{\text{M}}$), 0 ($\overline{\Gamma}$) and k_- ($\overline{\Gamma}$–$\overline{\text{K}}$), corresponding to the momenta of the valence band maximum on either side of the $\overline{\Gamma}$ point and the zone center, respectively. Along the entire Γ–A line all the bands are doubly spin degenerate. Due to the screw axis symmetry, the bands are at least doubly degenerate in the H–A–L plane, while retaining a finite spin polarization. In order for two bands with the same spin polarization to meet in the H–A–L plane, the band order is interchanged at a k_z close to the zone boundary: in the

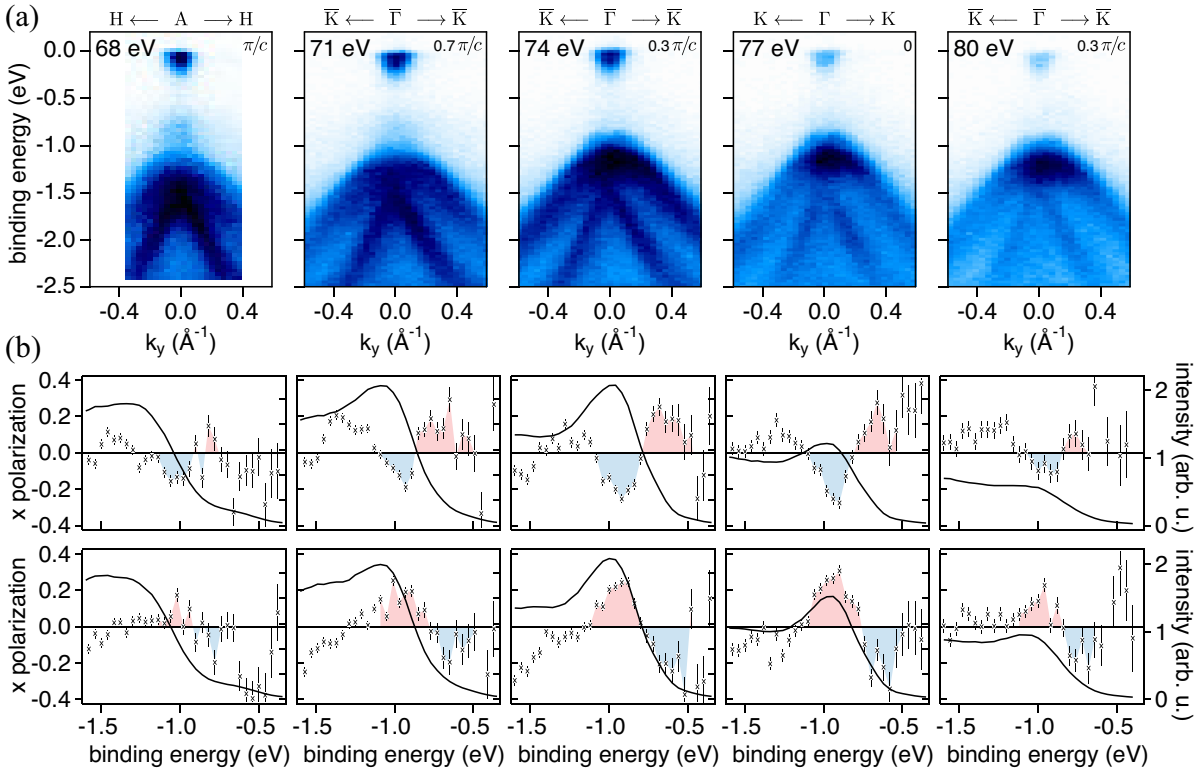

Figure 7.21: **(a)** Band maps at different photon energies; 68 eV and 77 eV photon energy roughly correspond to the k_z of the A and the Γ point, respectively. **(b)** Spin-resolved EDCs at $k_y \approx \pm 0.11$ Å^{-1} at the same photon energies as in (a). **(c)** DFT calculations showing the in-plane valence band dispersion at k_z values roughly corresponding to the photon energy.

$\overline{\Gamma}$–$\overline{\mathrm{K}}$ direction, two bands of opposite spin polarization hybridize and swap the sign of their polarization (left panel of Fig. 7.22d), whereas in the $\overline{\Gamma}$–$\overline{\mathrm{M}}$ direction they cross each other (right panel of Fig. 7.22d).

Apart from the momentum region where the mentioned hybridization takes place, the spin polarization is gradually reduced towards the H–A–L zone boundary plane, as depicted in Fig. 7.22e. The graph on the one hand shows the k_z dependence of the tangential spin polarization of the energy-split top band (α and β, cf. Fig. 7.22a) at the in-plane momenta of the valence band maximum along $\overline{\Gamma}$–$\overline{\mathrm{K}}$ ($S^{\alpha}(k_1)$ and $S^{\beta}(k_1)$ and along $\overline{\Gamma}$–$\overline{\mathrm{M}}$ ($S^{\alpha}(k_2)$ and $S^{\beta}(k_2)$). In addition, the energy splitting of the top valence band steadily decreases towards the A point ($\Delta(k_1)$ and $\Delta(k_2)$). Based on the theoretical calculations, a schematic illustration of the initial state Fermi surface of BiTeCl and its spin structure is given in Fig. 7.22f. The strictly in-plane helical spin structure is reflected in the measured spin polarization as will be discussed below.

7.3.2 Discussion

It has been shown that CD measurements of the surface states of BiTeCl and the related compounds are strongly photon energy dependent and thus CD is not a suitable probe for the spin polarization [175, 225]. It is under debate how and whether the photoelectron spin polarization measured in spin-resolved ARPES portray the spin structure of the initial state. The role of orbital selectivity of the photoemission process seems crucial, since the different orbitals forming an initial state, couple to distinct spin structures [28, 30]. As described in

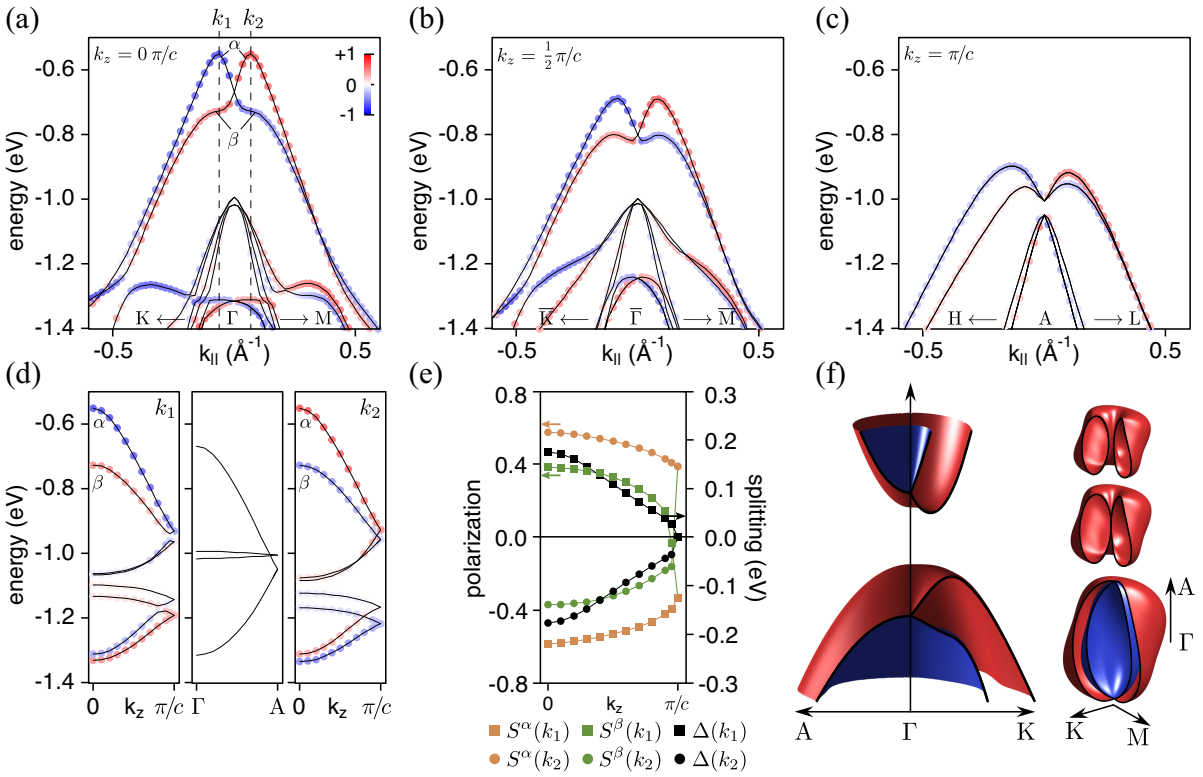

Figure 7.22: Relativistic DFT calculations of the BiTeCl valence band dispersion and spin structure close to the bulk band gap along $\overline{\text{K}}$–$\overline{\Gamma}$–$\overline{\text{M}}$ at **(a)** $k_z = 0$, **(b)** $k_z = \frac{1}{2}\pi/c$, and **(c)** $k_z = \pi/c$. The color of the data points indicates the degree of polarization, which is purely in-plane and perpendicular to the in-plane momentum. The dashed lines indicate the valence band maxima at $k_{\parallel} = k_1$ and k_2 along $\overline{\Gamma}$–$\overline{\text{K}}$ and $\overline{\Gamma}$–$\overline{\text{M}}$, respectively. **(d)** k_z dispersion and spin structure for $k_{\parallel} = k_1$ (left panel), 0 (center panel) and k_2 (right panel). **(e)** k_z dependence of the spin polarization for the topmost valence bands α and β $S_{\alpha,\beta}(k)$. Also shown is the energy splitting between α and β (Δ(k)). **(f)** *Left:* Schematic illustration of the dispersion. *Right:* Transition of the Fermi surface topology depending on the chemical potential. The colors indicate the helicity of the spin structure.

greater detail in Ch. 6, several mechanisms that additionally introduce photon energy dependence into the spin signal are also under investigation for either certain energy ranges [32] or generally [29].

All the above mentioned studies refer to two-dimensional states. To date, no spin-resolved data on truly three-dimensional spin split bands have been published, to the best of our knowledge. The main features of the measured spin polarization of the photoelectrons are consistent with the DFT calculation of the initial state; most importantly the helical rotation tangentially to the in-plane constant energy contour which is independent of the experimental geometry (cf. Fig. 7.19c–f). The photon energy dependent reduction of the maximally measured degree of spin polarization towards the zone boundary can be explained with the reducing energy splitting and the band crossing on either side of the H–A–L plane. In addition, the steeper k_z dispersion of the photoemission, initial state around the H–A–L zone boundary leads to a decreased resolution due to the intrinsic energy and k_z broadening, respectively [20]. The k_z broadening at the used photon energies is in the order of 20% of the Brillouin zone ($2\pi/c \approx 0.51\,\text{Å}^{-1}$ [192]). Spin-resolved ARPES measurements in the soft x-ray photon energy regime which would significantly increase the k_z resolution are not feasible to date.

7.3.3 Conclusion

In summary, systematic spin-resolved measurements on the bulk valence band of BiTeCl at various photon energies corresponding to different k_z in the bulk Brillouin zone were presented. The spin polarization of the photoelectrons is consistent with the theoretically calculated spin polarization of the initial state. In particular, no reorientation of the spin polarization vector as a function of the excitation energy was found. However, a significant reduction of the degree of spin polarization was observed in the k_z direction towards the Brillouin zone boundary, where the bands are doubly degenerate but still spin-polarized. The reduction of the measured spin polarization can be explained by an increased band overlap and limited k_z resolution.

7.4 Summary

In this Chapter, it has been shown that the electric field due to the polar layers of the bismuth thellurohalides BiTeI and BiTeCl (and in analogy also BiTeBr) together with the strong atomic spin–orbit interaction of especially the Bi atoms lead to a sizeable spin splitting of the bulk bands. In particular, the top bulk valence and the bottom bulk conduction band show an exceptionally large Rashba-type of splitting, rendering the Fermi surface to take the shape of a torus. In fact, the Fermi surface undergoes a topological transition with the energetic location of the chemical potential, with consequences for derived physical properties such as the transport properties, the density of states, the magnetic susceptibility, and possible effects in structurally similar materials with more complex electronic transitions.

On the example of BiTeCl it was demonstrated that the spin–orbit interaction induces a spin texture in the Fermi surface, that in lowest-order-approximation is perpendicular to the in-plane momentum, i.e. tangential to the Fermi surface and perpendicular to the polar axis. Together with the Fermi surface, the spin texture changes with the band filling. For weak n or p doping the Fermi surface consists of states with a single helicity, while for strong doping with the chemical potential beyond the degeneracy point at the particular TRIM, additional states with an opposite helicity are occupied. Like in the two-dimensional analogon, the spin structure of the Fermi surface therefore is determined by the chemical doping of the system, and by the crystal-field-induced warping of the dispersion. Further, it can be extrinsically tuned e.g. by introducing magnetic order, but the main in-plane helical spin texture is determined by the polar fields inherent in the system due to the stacking order of the atomic layers. More advantageous in this respect are ferroelectric materials which by definition have an inversion-asymmetric crystal potential that — in contrast to BiTeX — is switchable by an external electric field. Recently, it has been shown that the ferroelectric semiconductor GeTe shows a sizeable Rasbha-like bulk spin splitting with a helicity that in principle can be reversed by switching the electric polarization [226].

Further we have found, that BiTeI and BiTeCl have two distinct surfaces with either Te or I/Cl termination with opposite surface band bending. Because of the polar layered structure, the crystal potential is staircase-like at the surface, with the effect that two-dimensional states are split-off from the bulk states. These states show a large Rashba splitting that is governed by the polar electric field of the crystal rather by the particular surface band bending and thus resemble the bulk state dispersion. In further contrast to usual quantum well states induced by surface band bending, these states are localized only in the first few relatively narrow steps of the potential staircase, making the three-dimensionally dispersing bulk states localized deeper in the bulk still accessible by ARPES. This interpretation of the origin of the surface states and the disentangling of the surface and bulk spectra are important amendments to

the claims of a previous study [187] and are crucial for the understanding of the electronic structure of these materials. In particular, the presented ARPES data of the Rashba-split surface states on Te-terminated BiTeCl(0001) contradict Ref. [210] where the authors claim to have observed a Dirac-cone-like topological surface state.

Chapter 8

Conclusions and outlook

The main subject of this Thesis was to examine the spin texture of electronic bands in novel materials and to investigate how this can be tuned. In systems with a simple uniaxial asymmetry the spin–orbit interaction causes a linear-in-k splitting of the electronic bands and induces a spin polarization that is locked orthogonal to the momentum and to the asymmetry axis. Deviations from this spin structure can only be obtained by further reducing the symmetry of the system or by introducing interaction between the spin magnetic moments. The results presented in this Thesis show that any changes in the crystal structure or symmetry of a material is directly reflected in the spin texture. Such findings can help to taylor materials for applications or further in-depth studies of exotic physical phenomena.

In the first part of this Thesis the topological insulator $PbBi_4Te_7$ was examined. By means of high-resolution and spin-resolved ARPES mapping of the Fermi surface a strongly hexagonally warped Dirac-like surface states according to the C_{3v} surface symmetry was found. The states feature a three-fold oscillating out-of-plane spin polarization along the $\overline{\Gamma}$–$\overline{\mathrm{K}}$ crystallographic directions. DFT calculations have shown that for ideal surfaces the Dirac state is always mainly localized in the topmost 7L, irrespective of the surface termination. Contrary to an analysis of the surface step heights by STM, which indicated an equal distribution of both possible surface terminations, ARPES measurements showed preferentially a surface state dispersion similar the one predicted for the 5L termination. To confirm the suggested retraction mechanism of the surface state due to surface defects, systematic spatially resolved ARPES measurements, ideally combined with a XPS chemical analysis of the surface composition, are necessary to quantify the abundance of the two possible electronic surface structures.

Most of the known topological insulators based on Bi_2Se_3 or Bi_2Te_3 have a layered crystal structure with a preferred cleaving plane. While the published ARPES maps of topological surface states have been performed on these easy accessible C_{3v} surfaces, from a theoretical point of view all arbitrary surfaces of the crystal should host protected surface states. As

a consequence of the different chemical composition, structure and symmetry, the physical properties of the surface states, such as their dispersion, spin texture and localization is expected to differ significantly from the simple helical Dirac model or its six-fold warped variation.

As an alternative approach to alter the spin texture of the surface state of a topological insulator, it has been suggested to introduce magnetic order in the system. Externally applied magnetic fields in a strength that could open an resolvable Zeeman gap would need to be in the energy scale of the spin–orbit interaction and are in any case undesirable in ARPES experiments. Further, the ferromagnetic ordering of dilute magnetic dopants in the bulk or at the surface of topological insulators has been lately put into question by several studies [119–121]. A more promising possibility could be to grow films of topological insulators on top of ferromagnetic thin films. The thickness-dependent reorientation of the magnetic directional anisotropy of certain ferromagnetic materials [227] would allow to subject Dirac state in the topological insulator film to the either in-plane or out-of-plane magnetic stray field of the underlying film. Additional magnetic doping of the topological insulator could be used to further enhance the effect.

Another approach for changing the spin texture was pursued in the second part of the Thesis. Due to the relatively extended localization of the surface states of the topological insulators, they start to hybridize below certain film thicknesses and change their dispersion and spin texture. For Bi_2Se_3 films with thicknesses below ~ 6 QL, a gap is opened around the former Dirac point and the state loses its topological protection. By spin-resolved ARPES is could be shown that the surface states on either sides of the films are split in a Rashba-like manner because of the substrate-induced structural asymmetry. In contrast to a typical Rashba system, the two branches are separately localized in the surface and the interface QL, respectively. Future experiments on the electronic structure of these thin films could further examine the localization of the surface states. Considering the size of the momentum splitting, direct observation should be possible with high-resolution ARPES. The probing depth of the ARPES experiment could be tuned by changing the light incidence angle or the photon energy, and map out the retraction of the interfacial Dirac state upon increase of the film thickness. Furthermore, there is evidence that the localization of the branches of the spin-split states depend on the substrate: the presented data of Bi_2Se_3 suggest the outer branches to be localized in the top layer and the inner branches in the interfacial QL, while previously published results on graphene as substrate indicate the opposite behavior [148]. As Bi_2Se_3 films have been successfully grown on a variety of different substrates, a comparative study of the splitting and the localization of the Dirac states would be insightful.

In the context of the gap induced in the Dirac states of topological insulator thin films, theoretical studies found that these systems oscillate between the trivial insulator and the

QSH phase. Definite experimental confirmation of these transitions and the existence of one-dimensional boundary state is pending to date. Conceivably, such states could be observable by ARPES when their density is artificially increased, e.g. by growth of topological insulator thin films on vicinal substrates where the surface steps induce the necessary lateral confinement of the states.

In the third part of this Thesis, the method of spin-resolved ARPES was put into focus and in particular its application to measure the spin texture of topological surface states. Previous experiments with different light polarizations showed a dependence of the spin texture on the probed orbitals contributing to the surface state [30]. The surface states of the topological insulator Bi_2Se_3 are p-derived with a predominant p_z component and a relatively simple spin–orbital texture [28]. Other spin-polarized states such as the Rashba-split surface state of Au(111) are mainly of d character [76] which results in a different orbital selectivity in the photoemission process and a presumably more complicated spin–orbital texture.

In addition to these polarization-induced effects, slight variations of the measured spin polarization of the Bi_2Se_3 surface state with photon energy were found. A theoretical model based on free-electron final states and a layer-dependent orbital texture of the surface state, predicted photon-energy-dependent interference effects in certain ARPES geometries [29]. The anticipated oscillatory behavior of the spin polarization components, however, could not be reproduced in this Thesis and the obtained results show a different ampliude and periodicity. In the future, additional measurements systematically covering smoothly the parameter space are necessary, including a wide photon energy range, various light polarizations, different experimental geometries and other compounds of topological insulators. Of particular interest would be spin-resolved ARPES measurements in the soft X-ray regime, where the model's assumption of free-electron final states is nearly fulfilled. It is in principle straightforward to apply the model to other systems with spin-polarized electronic states, such as the bulk states of spin–orbit-coupled noncentrosymmetric materials.

In the last part of this Thesis, the electronic structure of the noncentrosymmetric materials BiTeI and BiTeCl was discussed. By means of SX-ARPES their spin-split bulk bands and the Fermi surfaces were mapped out for a wide range of photon energies. In the energetic vicinity of the band gap the bulk valence and conduction band or these materials are described by a three-dimensional Rashba Hamiltonian with toroidal Fermi surfaces and an in-plane helical spin texture. The latter was confirmed by photon-energy-dependent spin-resolved ARPES measurements of the top of the BiTeCl valence band over a significant region of the three-dimensional Brillouin zone. Future measurements should address the spin texture of the hardly occupied conduction band which by theory should have the same helicity as the valence band. It could be made accessible for ARPES by doping the surface with alkali metals. Especially the mapping of the spin structure of bulk bands would profit from currently

not available spin-resolved ARPES facilities in the soft X-ray photon energy regime. The presented results were measured with a fixed order of the atomic layers, in principle the measured polarization of the bulk states should be opposite when the hexagonal axis of the crystal is reversed. While for these materials the electric polarization is inherent to the crystal structure, other materials such as ferroelectrica allow for switching the electric polarization by externally applied fields and in consequence reverse also the spin polarizations. A promising canditate for the realization of this idea is the ferroelectric semiconductor GeTe that has a sizeable Rasbha-like bulk spin splitting [226].

Spin-resolved measurements on the bulk states of BiTeI and BiTeCl are impeded because sets of two-dimensional spin-split states are localized in their staircase-like surface potentials. A remarkable feature of these surface states is their small linewidth which shrinks for states localized farther away from the crystal surface. The mechanism of this effect is yet unknown and further theoretical and experimental work is necessary. Both compounds, BiTeI and BiTeCl, have two possible surfaces with either a Te termination or an I and Cl termination, respectively. In the case of BiTeI the surfaces were found to have an opposite band bending and both hosting the mentioned surface states. On the Cl-terminated surface of BiTeCl on the other hand, a light-induced chemical process at the surface reverses the surface band bending and no surface states could be experimentally observed, in contrast to the Te-terminated surface. The microscopic process is unkown, but presumably it could by suppressed making the pristine surface spectrum accessible by applying different measurement conditions, like a reduced photon flux density, a different sample temperature or a different surface preparation procedure.

A suitable method to directly determine the surface band bending would be the determination of the work function locally on the different surface terminations e.g. by means of Kelvin probes. The preliminary results based on photoelectron spectroscopy indicate a counterintuitively large work function for the Te-terminated BiTeCl surface. Further measurements could not be included in this Thesis due to time limitations.

Appendices

Appendix A

Tight binding model of a spin–orbit coupled system

The goal of this chapter is to examine a two-dimensional, spin–orbit coupled electronic system with a tight binding model. It shall be shown that even if L_z and S_z, the z component of the angular momentum and the spin operator, no longer commute with the Hamiltonian, the eigenstates of examined system have high degrees of spin polarization.

The discussion is oriented on the paper by Hamiltonian of Petersen and Hedegard [75], though correcting several errors. All of the surface states studied in this thesis are derived from orbitals with mainly p symmetry. We therefore restrict our model to a hexagonal lattice of $p_\alpha = p_x$, p_y and p_z orbitals, interacting with nearest neighbours and being located at $\boldsymbol{R}_i, \boldsymbol{R}_j$ The tight binding Hamiltonian without spin–orbit interaction [Czycholl, Kittel2]

$$H = \sum t_{\alpha\beta}(\boldsymbol{R}_i - \boldsymbol{R}_j)|p_\alpha(\boldsymbol{R}_i, \sigma\rangle\langle p_\beta(\boldsymbol{R}_j), \sigma'|. \tag{A.1}$$

The overlap matrices are given as [1]

$$t_{x,x} = \ell^2 V_{pp\sigma} + (1 - \ell^2) V_{pp\pi} \tag{A.2}$$

$$t_{y,y} = m^2 V_{pp\sigma} + (1 - m^2) V_{pp\pi} \tag{A.3}$$

$$t_{z,z} = V_{pp\pi} \tag{A.4}$$

$$t_{x,y} = \ell m V_{pp\sigma} - \ell m V_{pp\pi} \tag{A.5}$$

$$t_{x,z} = \ell n V_{pp\sigma} - \ell n V_{pp\pi} \tag{A.6}$$

using the standard notation of Slater for the direction cosines to the neighboring atom $\boldsymbol{R}_i - \boldsymbol{R}_j = R(\ell, m, n)$ and the $V_{pp\sigma,\pi}$ are the bond integrals [Slater (siehe wikipedia]. In order to

[1] The matrix elements given in Ref. [75] are erroneous.

mimic the broken inversion symmetry at the surface, the p_z orbitals are artificially made asymmetric by introducing non-zero overlaps between p_z and the in-plane orbitals

$$t_{x,z} = \ell V_{pp\sigma\pi} \tag{A.7}$$

$$t_{y,z} = m V_{pp\sigma\pi}. \tag{A.8}$$

We now introduce the atomic spin–orbit interaction (see sec. 3.1) to the above Hamiltonian such that

$$H = \sum t_{\alpha\beta} \left(\boldsymbol{R}_i - \boldsymbol{R}_j\right)(\delta_{\sigma,\sigma'} + H_{SOC}) \, |p_\alpha(\boldsymbol{R}_i), \sigma\rangle\langle p_\beta(\boldsymbol{R}_j), \sigma'|, \tag{A.9}$$

with the atomic spin–orbit coupling term

$$H_{SOC} = \alpha \boldsymbol{L} \cdot \boldsymbol{S} = \frac{\alpha}{2}\boldsymbol{J}^2 - \boldsymbol{L}^2 - \boldsymbol{S}^2. \tag{A.10}$$

The eigenvalues of $\boldsymbol{L} \cdot \boldsymbol{S}$ of an electronic state in an atom are well known [Schwabl], in the case of a $l = 1$ state they are

$$\frac{\hbar^2}{2}[j(j+1) - l(l+1) - s(s+1)] \tag{A.11}$$

$$= \frac{\hbar^2}{2}[j(j+1) - \tfrac{11}{4}] = \begin{cases} 1 & \text{for } j = \frac{3}{2} \\ -2 & \text{for } j = \frac{1}{2} \end{cases} \tag{A.12}$$

The eigenfunctions are characterized by the quantum numbers of the total angular momentum $|j, m_j\rangle$. In this basis H_{SOC} is diagonal

$$H_{SOC} = \frac{\alpha}{2}\frac{\hbar^2}{2} \begin{pmatrix} 1 & 0 & 0 & 0 & 0 & 0 \\ 0 & 1 & 0 & 0 & 0 & 0 \\ 0 & 0 & 1 & 0 & 0 & 0 \\ 0 & 0 & 0 & 1 & 0 & 0 \\ 0 & 0 & 0 & 0 & -2 & 0 \\ 0 & 0 & 0 & 0 & 0 & -2 \end{pmatrix}. \tag{A.13}$$

The Hamiltonian needs to be transformed into the same basis of as the hopping matrix, namely the parity eigenfunctions

$$|p_x, \uparrow\rangle, |p_x, \downarrow\rangle, |p_y, \uparrow\rangle, |p_y, \downarrow\rangle, |p_z, \uparrow\rangle, |p_z, \downarrow\rangle. \tag{A.14}$$

To do this, the eigenstates of $\boldsymbol{L} \cdot \boldsymbol{S}$ are written as superposition of the eigenstates of the angular momentum and spin operator with Clebsch-Gordan coefficiants as pre-factors [Schwabl, S. 199]

$$|j = l \pm \tfrac{1}{2}, m_j\rangle = \pm \sqrt{\frac{l \pm m_j + \frac{1}{2}}{2l+1}} |l, m_l = m_j - \tfrac{1}{2}\rangle|\tfrac{1}{2}, \tfrac{1}{2}\rangle \tag{A.15}$$

$$+ \sqrt{\frac{l \mp m_j + \frac{1}{2}}{2l+1}} |l, m_l = m_j + \tfrac{1}{2}\rangle|\tfrac{1}{2}, -\tfrac{1}{2}\rangle, \tag{A.16}$$

or explicitely:

$$
\begin{array}{lcll}
|j,m_j\rangle & = & |l,m_l\rangle|s,m_s\rangle & \\
\hline
|\frac{3}{2},\frac{3}{2}\rangle & = & |1,1\rangle|\frac{1}{2},\frac{1}{2}\rangle & =: \quad |p_+,\uparrow\rangle \\
|\frac{3}{2},\frac{1}{2}\rangle & = & \sqrt{\frac{2}{3}}|1,0\rangle|\frac{1}{2},\frac{1}{2}\rangle + \sqrt{\frac{1}{3}}|1,1\rangle|\frac{1}{2},-\frac{1}{2}\rangle & =: \quad \sqrt{\frac{2}{3}}|p_z,\uparrow\rangle + \sqrt{\frac{1}{3}}|p_+,\downarrow\rangle \\
|\frac{3}{2},-\frac{1}{2}\rangle & = & \sqrt{\frac{1}{3}}|1,-1\rangle|\frac{1}{2},\frac{1}{2}\rangle + \sqrt{\frac{2}{3}}|1,0\rangle|\frac{1}{2},-\frac{1}{2}\rangle & =: \quad \sqrt{\frac{1}{3}}|p_-,\uparrow\rangle + \sqrt{\frac{2}{3}}|p_z,\downarrow\rangle \\
|\frac{3}{2},-\frac{3}{2}\rangle & = & |1,-1\rangle|\frac{1}{2},-\frac{1}{2}\rangle & =: \quad |p_-,\downarrow\rangle \\
|\frac{3}{2},\frac{1}{2}\rangle & = & -\sqrt{\frac{1}{3}}|1,0\rangle|\frac{1}{2},\frac{1}{2}\rangle + \sqrt{\frac{2}{3}}|1,1\rangle|\frac{1}{2},-\frac{1}{2}\rangle & =: \quad -\sqrt{\frac{1}{3}}|p_z,\uparrow\rangle + \sqrt{\frac{2}{3}}|p_+,\downarrow\rangle \\
|\frac{3}{2},-\frac{1}{2}\rangle & = & -\sqrt{\frac{2}{3}}|1,-1\rangle|\frac{1}{2},\frac{1}{2}\rangle + \sqrt{\frac{1}{3}}|1,0\rangle|\frac{1}{2},-\frac{1}{2}\rangle & =: \quad -\sqrt{\frac{2}{3}}|p_-,\uparrow\rangle + \sqrt{\frac{1}{3}}|p_z,\downarrow\rangle
\end{array}
\tag{A.17}
$$

Finally, the relations of the parity orbitals and the angular momentum orbitals are given for both spin species by

$$|p_\pm\rangle = \tfrac{1}{\sqrt{2}}\left(|p_x\rangle \pm i|p_y\rangle\right) \tag{A.18}$$

$$|p_z\rangle = |p_z\rangle. \tag{A.19}$$

Therefore, the transform matrix S takes the basis $\{|j,m_j\rangle\}$ to the basis $\{|p_{x,y,z}\rangle\}$ with

$$S = \begin{pmatrix}
\frac{1}{\sqrt{2}} & 0 & \frac{1}{\sqrt{6}} & 0 & 0 & -\frac{1}{\sqrt{3}} \\
0 & \frac{1}{\sqrt{6}} & 0 & \frac{1}{\sqrt{2}} & \frac{1}{\sqrt{2}} & 0 \\
-\frac{i}{\sqrt{2}} & \frac{i}{\sqrt{6}} & 0 & 0 & 0 & -\frac{i}{\sqrt{3}} \\
0 & -\frac{i}{\sqrt{6}} & 0 & \frac{i}{\sqrt{2}} & -\frac{i}{\sqrt{3}} & 0 \\
0 & \sqrt{\frac{2}{3}} & 0 & 0 & -\sqrt{\frac{1}{3}} & 0 \\
0 & 0 & \sqrt{\frac{2}{3}} & 0 & 0 & \sqrt{\frac{1}{3}}
\end{pmatrix}. \tag{A.20}$$

such that the Hamiltonian with respect to the parity orbital basis reads

$$H'_{SOC} = S\,H_{SOC}\,S^{-1} = \frac{\alpha}{2}\frac{\hbar^2}{2}\begin{pmatrix}
0 & 0 & i & 0 & 0 & 1 \\
0 & 0 & 0 & -i & 1 & 0 \\
-i & 0 & 0 & 0 & 0 & i \\
0 & i & 0 & 0 & -i & 0 \\
0 & 1 & 0 & i & 0 & 0 \\
1 & 0 & -i & 0 & 0 & 0
\end{pmatrix}, \tag{A.21}$$

$$\text{basis: } \{|p_x,\uparrow\rangle, |p_x,\downarrow\rangle, |p_y,\uparrow\rangle, |p_y,\downarrow\rangle, |p_z,\uparrow\rangle, |p_z,\downarrow\rangle\}. \tag{A.22}$$

In contrast to the spin–orbit Hamiltonian listed in ref. [75] this operator is self-adjunct and therefore has real energy eigenvalues.

The eigenstates of the Hamiltonian (A.9) are found by forming Bloch states out of the atomic orbitals $|\psi_{\alpha,\boldsymbol{k}},\sigma\rangle(\boldsymbol{r}) \sim \sum_{\boldsymbol{R}_i} e^{i\boldsymbol{k}\boldsymbol{R}_i}|p_\alpha,\sigma\rangle(\boldsymbol{r}-\boldsymbol{R}_i)$ and subsequent diagonalization of the matrix

$$H_{\alpha\sigma,\beta\sigma'} = \langle\psi_{\alpha,\boldsymbol{k}},\sigma|H|\psi_{\beta,\boldsymbol{k}},\sigma'\rangle. \tag{A.23}$$

In order to obtain the full dispersion numerically, first the sum in Eq. (A.9) needs to be calculated at least over the nearest neighbours for a certain $\boldsymbol{k}$ value, subsequent diagonalization of the final matrix gives the different energy eigenvalues ε_i at the particular $\boldsymbol{k}$ point. The eigenvectors $|\boldsymbol{\lambda}_i\rangle$ related to the eigenvalue ε_i contain as components the mixing factors with respect to the parity orbital basis. The orbital composition of the eigenstate can thus be calculated by projection

$$\langle \boldsymbol{\lambda}_i | p_\alpha, \sigma \rangle \langle p_\alpha, \sigma | \boldsymbol{\lambda}_i \rangle, \tag{A.24}$$

where for example

$$|p_x, \uparrow\rangle\langle p_x, \uparrow| = \begin{pmatrix} 1 & 0 & 0 & 0 & 0 & 0 \\ 0 & 0 & 0 & 0 & 0 & 0 \\ 0 & 0 & 0 & 0 & 0 & 0 \\ 0 & 0 & 0 & 0 & 0 & 0 \\ 0 & 0 & 0 & 0 & 0 & 0 \\ 0 & 0 & 0 & 0 & 0 & 0 \end{pmatrix} \tag{A.25}$$

gives the contribution of the p_x orbital with up spin.

Similarly, the spin expectation value along the spatial direction $\alpha = x, y, z$ can be calculated by evaluating

$$\langle \boldsymbol{\lambda}_i | S_\alpha | \boldsymbol{\lambda}_i \rangle, \quad \text{with } S = \frac{\hbar}{2} \begin{pmatrix} \sigma_\alpha & 0 & 0 \\ 0 & \sigma_\alpha & 0 \\ 0 & 0 & \sigma_\alpha \end{pmatrix}, \tag{A.26}$$

where σ_α are the Pauli matrices in standard definition.

Appendix B

Effects of magnetism on a Rashba gas

The Hamiltonian of a two-dimensional free-electron gas with Rashba-type spin splitting in a magnetic field is given by

$$\mathcal{H} = \frac{\hbar^2 \boldsymbol{k}^2}{2m} + \alpha \left(k_x \sigma_y - k_y \sigma_x\right) + M\, \hat{m} \cdot \boldsymbol{\sigma} - \mu, \tag{B.1}$$

where m is the electron mass, α the Rashba parameter, $2M$ the Zeeman gap, $\hat{m} = (m_x, m_y, m_z)$ the unit vector along the magnetization, the components of $\boldsymbol{\sigma}$ the Pauli matrices, and μ the chemical potential. The energy eigenvalues are given by

$$\varepsilon_{\pm} = \frac{\hbar^2 \boldsymbol{k}^2}{2m} \pm \sqrt{\alpha^2 \left(k_x^2 + k_y^2\right) + 2\alpha M \left(k_x m_y + k_y m_x\right) + M^2}. \tag{B.2}$$

Fig. B.1 summarizes the dispersion and the in-plane spin polarization for different combinations of magnetic fields and Rashba-like spin–orbit interaction. Any orientation of the magnetic field opens a gap $2M$ at $k = 0$. For purely in-plane magnetic fields, the degeneracy point is not lifted shifted towards finite $k \neq 0$ perpendicular to the applied field. In the this case, the spin polarization of the energy eigenstates is strictly in-plane, while in the presence of out-of-plane magnetic order the spin of the Rashba electron reorient along the magnetic field for small absolute values of k.

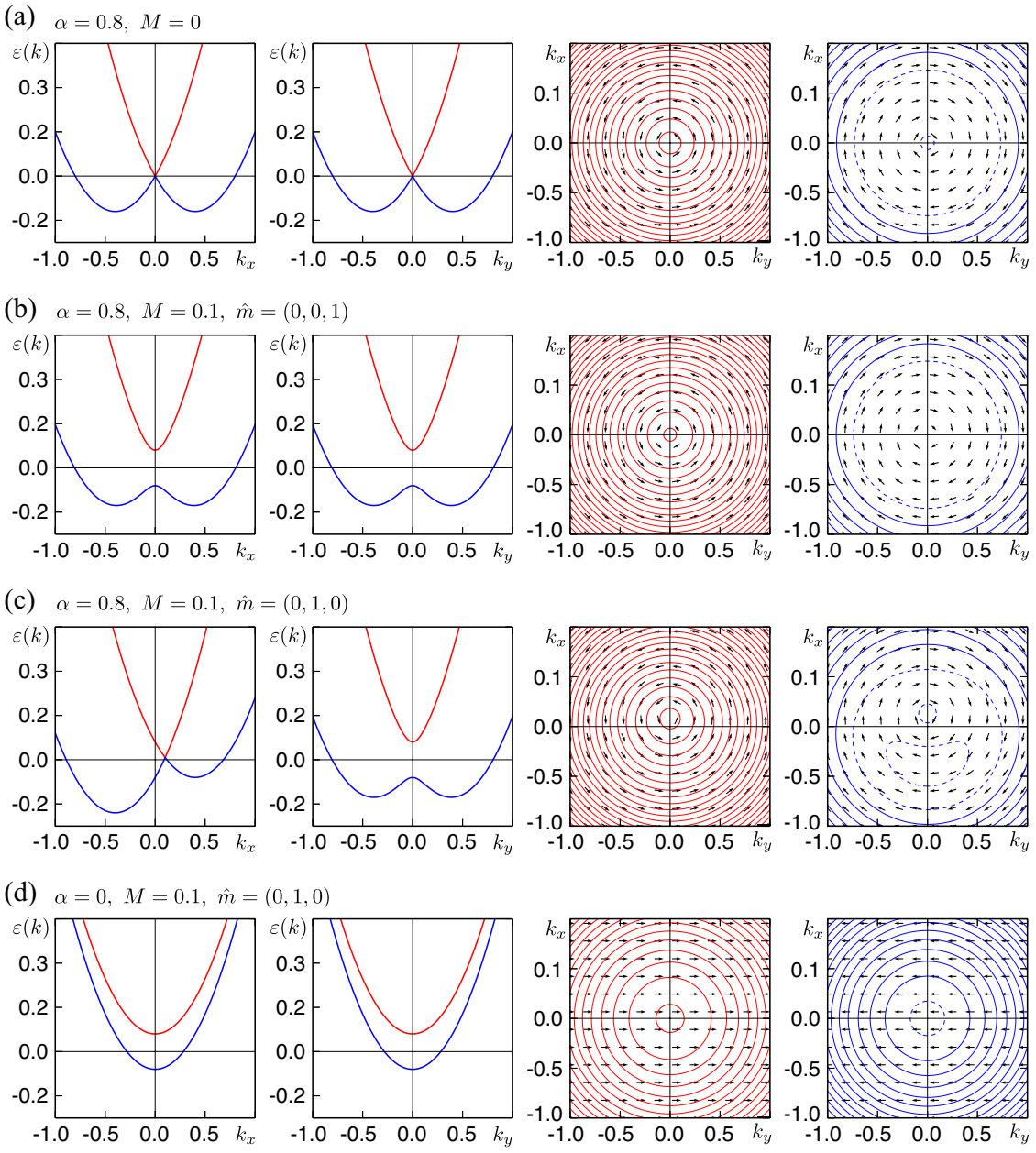

Figure B.1: Spectrum of a Rashba gas described by the Hamiltonian (B.1) **(a)** without Zeeman splitting, **(b)** with out-of-plane magnetic field, **(c)** with magnetic field along y, and **(d)** without spin orbit interaction. The two left panels show the in-plane dispersion of ε_+ (red) and ε_- (blue) along k_x and k_y. The two right panels show the constant energy contours of ε_+ and ε_-, respectively, with arrows indicating the in-plane spin polarization.

Bibliography

[1] W. Gerlach and O. Stern
Das magnetische Moment des Silberatoms.
Zeitschrift für Physik A Hadrons and Nuclei **9**, 353–355 (1922), 10.1007/BF01326984.

[2] B. Friedrich and D. Herschbach
Stern and Gerlach: How a bad cigar helped reorient atomic physics.
Physics Today **56**, 53 (2003).

[3] Johan Å kerman
Toward a Universal Memory.
Science **308**, 508–510 (2005).

[4] Stuart S. P. Parkin, Masamitsu Hayashi and Luc Thomas
Magnetic Domain-Wall Racetrack Memory.
Science **320**, 190–194 (2008).

[5] Supriyo Datta and Biswajit Das
Electronic analog of the electro-optic modulator.
Applied Physics Letters **56**, 665–667 (1990).

[6] M. N. Baibich, J. M. Broto, A. Fert, F. Nguyen Van Dau, F. Petroff, P. Etienne, G. Creuzet, A. Friederich and J. Chazelas
Giant Magnetoresistance of (001)Fe/(001)Cr Magnetic Superlattices.
Phys. Rev. Lett. **61**, 2472–2475 (1988).

[7] M. Julliere
Tunneling between ferromagnetic films.
Physics Letters A **54**, 225–226 (1975).

[8] D.C. Ralph and M.D. Stiles
Spin transfer torques.
Journal of Magnetism and Magnetic Materials **320**, 1190 – 1216 (2008).

[9] M. Z. Hasan and C. L. Kane
Colloquium: Topological insulators.
Reviews of Modern Physics **82** (2010).

[10] X.-L. Qi and S.-C. Zhang
Topological insulators and superconductors.
Rev. Mod. Phys. **83**, 1057–1110 (2011).

[11] Y. A. Bychkov and E. I. Rashba
Oscillatory effects and the magnetic susceptibility of carriers in inversion layers.
Journal of Physics C: Solid State Physics **17**, 6039–6045 (1984).

[12] C. L. Kane and E. J. Mele
Z2 Topological Order and the Quantum Spin Hall Effect.
Phys. Rev. Lett. **95**, 146802 (2005).

[13] L. Fu, C. L. Kane and E. J. Mele
Topological Insulators in Three Dimensions.
Phys. Rev. Lett. **98**, 106803 (2007).

[14] H. Hertz
Über den Einfluss des ultravioletten Lichtes auf die elektrische Entladung.
Ann. Phys **31** (1887).

[15] A. Einstein
Ueber einen die Erzeugung und Verwandlung des Lichtes betreffenden heuristischen Gesichtspunkt.
Annalen der Physik **14**, 164–181 (1905).

[16] A. Damascelli
Probing the Electronic Structure of Complex Systems by ARPES.
Physica Scripta **2004**, 61 (2004).

[17] A. X. Gray, C. Papp, S. Ueda, B. Balke, Y. Yamashita, L. Plucinski, J. Minár, J. Braun, E. R. Ylvisaker, C. M. Schneider, W. E. Pickett, H. Ebert, K. Kobayashi and C. S. Fadley
Probing bulk electronic structure with hard X-ray angle-resolved photoemission.
Nat Mater **10**, 759–764 (2011).

[18] S. Huefner. *Photoelectron Spectroscopy - Principles and Applications*. Springer, 2010.

[19] J. Osterwalder
Spin-Polarized Photoemission.
Lecture Notes in Physics **697**, 95–120 (2006).

[20] V. N. Strocov
Intrinsic accuracy in 3-dimensional photoemission band mapping.
Journal of Electron Spectroscopy and Related Phenomena **130**, 65–78 (2003).

[21] Ph. Hofmann, Ch. Søndergaard, S. Agergaard, S. V. Hoffmann, J. E. Gayone, G. Zampieri, S. Lizzit and A. Baraldi
Unexpected surface sensitivity at high energies in angle-resolved photoemission.
Phys. Rev. B **66**, 245422 (2002).

[22] V. N. Strocov, X. Wang, M. Shi, M. Kobayashi, J. Krempasky, C. Hess, T. Schmitt and L. Patthey
Soft-X-ray ARPES facility at the ADRESS beamline of the SLS: concepts, technical realisation and scientific applications.
Journal of Synchrotron Radiation **21**, 32–44 (2014).

[23] V. N. Strocov, T. Schmitt, U. Flechsig, T. Schmidt, A. Imhof, Q. Chen, J. Raabe, R. Betemps, D. Zimoch, J. Krempasky, X. Wang, M. Grioni, A. Piazzalungaa and L. Patthey
High-resolution soft X-ray beamline ADRESS at the Swiss Light Source for resonant inelastic X-ray scattering and angle-resolved photoelectron spectroscopies.
Journal of Synchrotron Radiation **17**, 631 (2010).

[24] C. C. Chusuei and D. W. Goodman
X-Ray Photoelectron Spectroscopy.
Encyclopedia of Physical Science and Technology **17**, 921–938 (2002).

[25] C. Solterbeck, W. Schattke, J.-W. Zahlmann-Nowitzki, K.-U. Gawlik, L. Kipp, M. Skibowski, C. S. Fadley and M. A. Van Hove
Energetic and Spatial Bonding Properties from Angular Distributions of Ultraviolet Photoelectrons: Application to the GaAs(110) Surface.
Phys. Rev. Lett. **79**, 4681–4684 (1997).

[26] J. Osterwalder
Can spin-polarized photoemission measure spin properties in condensed matter?.
Journal of Physics: Condensed Matter **24**, 171001 (2012).

[27] U. Heinzmann and J. H. Dil
Spin–orbit-induced photoelectron spin polarization in angle-resolved photoemission from both atomic and condensed matter targets.
Journal of Physics: Condensed Matter **24**, 173001 (2012).

[28] H. Zhang, Ch.-X. L. and Sh.-Ch.. Zhang
Spin-Orbital Texture in Topological Insulators.
Phys. Rev. Lett. **111**, 066801– (2013).

[29] Z. H. Zhu, C. N. Veenstra, G. Levy, A. Ubaldini, P. Syers, N. P. Butch, J. Paglione, M. W. Haverkort, I. S. Elfimov and A. Damascelli
Layer-By-Layer Entangled Spin-Orbital Texture of the Topological Surface State in Bi_2Se_3.
Phys. Rev. Lett. **110**, 216401– (2013).

[30] Y. Cao, J. A. Waugh, X-W. Zhang, J-W. Luo, Q. Wang, T. J. Reber, S. K. Mo, Z. Xu, A. Yang, J. Schneeloch, G. D. Gu, M. Brahlek, N. Bansal, S. Oh, A. Zunger and D. S. Dessau
Mapping the orbital wavefunction of the surface states in three-dimensional topological insulators.
Nat. Phys. **9**, 499–504 (2013).

[31] Z. Xie, S. He, C. Chen, Y. Feng, H. Yi, A. Liang, L. Zhao, D. Mou, J. He, Yi. Peng, X. Liu, Y. Liu, G. Liu, X. Dong, L. Yu, J. Zhang, S. Zhang, Z. Wang, F. Zhang, F. Yang, Q. Peng, X. Wang, C. Chen, Z. Xu and X. J. Zhou
Orbital-selective spin texture and its manipulation in a topological insulator.
Nat Commun **5** (2014).

[32] J. Sánchez-Barriga, A. Varykhalov, J. Braun, S.-Y. Xu, N. Alidoust, O. Kornilov, J. Minár, K. Hummer, G. Springholz, G. Bauer, R. Schumann, V. Yashina, L. H. Ebert, Z. Hasan, M. and O. Rader
Photoemission of Bi_2Se_3 with Circularly Polarized Light: Probe of Spin Polarization or Means for Spin Manipulation?.
Phys. Rev. X **4**, 011046 (2014).

[33] C.-H. Park and S. G. Louie
Spin Polarization of Photoelectrons from Topological Insulators.
Phys. Rev. Lett. **109**, 097601 (2012).

[34] C. Jozwiak, C.-H. Park, K. Gotlieb, C. Hwang, D.-H. Lee, S. G. Louie, J. D. Denlinger, C. R. Rotundu, R. J. Birgeneau, Z. Hussain and A. Lanzara
Photoelectron spin-flipping and texture manipulation in a topological insulator.
Nat. Phys. **9**, 293–298 (2013).

[35] U. Fano
Spin Orientation of Photoelectrons Ejected by Circularly Polarized Light.
Phys. Rev. **178**, 131–136 (1969).

[36] D. T. Pierce, R. J. Celotta, G. C. Wang, W. N. Unertl, A. Galejs, C. E. Kuyatt and S. R. Mielczarek
The GaAs spin polarized electron source.
Review of Scientific Instruments **51**, 478–499 (1980).

[37] A. Kimura, E. E. Krasovskii, R. Nishimura, K. Miyamoto, T. Kadono, K. Kanomaru, E. V. Chulkov, G. Bihlmayer, K. Shimada, H. Namatame and M. Taniguchi
Strong Rashba-Type Spin Polarization of the Photocurrent from Bulk Continuum States: Experiment and Theory for Bi(111).
Phys. Rev. Lett. **105**, 076804 (2010).

[38] M. Hoesch. *Spin-resolved Fermi surface mapping*. PhD thesis, Universität Zürich, 2002.

[39] M. Hoesch, T. Greber, V. N. Petrov, M. Muntwiler, M. Hengsberger, W. Auwaerter and J. Osterwalder
Spin-polarized Fermi surface mapping.
Journal of Electron Spectroscopy and Related Phenomena **124**, 263–279 (2002).

[40] H. Batelaan, T. J. Gay and J. J. Schwendiman
Stern-Gerlach Effect for Electron Beams.
Phys. Rev. Lett. **79**, 4517–4521 (1997).

[41] G. H. Rutherford and R. Grobe
Comment on "Stern-Gerlach Effect for Electron Beams".
Phys. Rev. Lett. **81**, 4772–4772 (1998).

[42] C. Amsler. *Kern- und Teilchenphysik*. vdf Hochschulverlag AG der ETH Zürich, 2007.

[43] P. D. C. King, R. C. Hatch, M. Bianchi, R. Ovsyannikov, C. Lupulescu, G. Landolt, B. Slomski, J. H. Dil, D. Guan, J. L. Mi, E. D. L. Rienks, J. Fink, A. Lindblad, S. Svensson, S. Bao, G. Balakrishnan, B. B. Iversen, J. Osterwalder, W. Eberhardt, F. Baumberger and Ph. Hofmann
Large Tunable Rashba Spin Splitting of a Two-Dimensional Electron Gas in Bi_2Se_3.
Phys. Rev. Lett. **107**, 096802 (2011).

[44] F. Meier, H. Dil, J. Lobo-Checa, L. Patthey and J. Osterwalder
Quantitative vectorial spin analysis in angle-resolved photoemission: Bi/Ag(111) and Pb/Ag(111).
Phys. Rev. B **77**, 165431 (2008).

[45] F. Meier. *Rashba-Type Spin-Orbit Coupling in the Surface Alloys on Ag(111) Probed by Spin- and Angle-Resolved Photoemission Spectroscopy*. PhD thesis, Universität Zürich, 2011.

[46] B. Slomski. *A Spin- and Angle-Resolved Photoemission Study of the Rashba-Bychkov Effect in Lead Quantum Well States*. PhD thesis, Universität Zürich, 2013.

[47] P. Hohenberg and W. Kohn
Inhomogeneous Electron Gas.
Phys. Rev. **136**, B864–B871 (1964).

[48] W. Kohn and L. J. Sham
Self-Consistent Equations Including Exchange and Correlation Effects.
Phys. Rev. **140**, A1133–A1138 (1965).

[49] P. A. M. Dirac
Note on Exchange Phenomena in the Thomas Atom.
Mathematical Proceedings of the Cambridge Philosophical Society **26**, 376–385 (1930).

[50] J. P. Perdew, K. Burke and M. Ernzerhof
Generalized Gradient Approximation Made Simple.
Phys. Rev. Lett. **77**, 3865–3868 (1996).

[51] G. Kresse and J. Furthmüller
Efficiency of ab-initio total energy calculations for metals and semiconductors using a plane-wave basis set.
Comput. Mater. Sci. **6**, 15 (1996).

[52] P. B. Blöchl
Projector augmented-wave method.
Phys. Rev. B **50**, 17953 (1994).

[53] G. Kresse and D. Joubert
From ultrasoft pseudopotentials to the projector augmented-wave method.
Phys. Rev. B **59**, 1758 (1999).

[54] D. D. Koelling and B. N. Harmon
A technique for relativistic spin-polarised calculations.
J. Phys. C **10**, 3107 (1977).

[55] W. Kohn and N. Rostoker
Solution of the Schrödinger Equation in Periodic Lattices with an Application to Metallic Lithium.
Phys. Rev. **94**, 1111–1120 (1954).

[56] J. Korringa
On the calculation of the energy of a Bloch wave in a metal.
Physica **13**, 392–400 (1947).

[57] L. I. Schiff. *Quantum Mechanics*. McGraw-Hill book company, Third Edition, 1968.

[58] F. Schwabl. *Quantenmechanik*. Springer, 7. Auflage, 2007.

[59] J. J. Sakurai. *Modern Quantum Mechanics*. Addison Wesly Longman, Revised Version, 1994.

[60] V. B. Berestetskii, E. M. Lifshitz and L. P. Pitaevskii. *Quantum electrodynamics*. Butterworth-Heinemann, 1982.

[61] C. Kittel. *Quantum Theory of Solids*. John Wiley & Sons, Second Revised Printing, 1987.

[62] G. Dresselhaus
Spin-Orbit Coupling Effects in Zinc Blende Structures.
Phys. Rev. **100**, 580–586 (1955).

[63] M. S. Dresselhaus, G. Dresselhaus and A. Jorio. *Group Theory*. Springer, 2008.

[64] R. Winkler. *Spin-Orbit Coupling Effects in Two-Dimensional Electron and Hole Systems*. Springer Tracts in Modern Physics, Springer, Berlin, 2003.

[65] L. Meier, G. Salis, I. Shorubalko, E. Gini, S. Schon and K. Ensslin
Measurement of Rashba and Dresselhaus spin-orbit magnetic fields.
Nat. Phys. **3**, 650–654 (2007).

[66] S. LaShell, B. A. McDougall and E. Jensen
Spin Splitting of an Au(111) Surface State Band Observed with Angle Resolved Photoelectron Spectroscopy.
Phys. Rev. Lett. **77**, 3419–3422 (1996).

[67] M. Hoesch, M. Muntwiler, V. N. Petrov, M. Hengsberger, L. Patthey, M. Shi, M. Falub, T. Greber and J. Osterwalder
Spin structure of the Shockley surface state on $Au(111)$.
Phys. Rev. B **69**, 241401 (2004).

[68] N. W. Ashcroft and D. N. Mermin. *Solid State Physics*. Harcourt College Publisher, 1976.

[69] Christian R. Ast, Gero Wittich, Peter Wahl, Ralf Vogelgesang, Daniela Pacilé, Mihaela C. Falub, Luca Moreschini, Marco Papagno, Marco Grioni and Klaus Kern

Local detection of spin-orbit splitting by scanning tunneling spectroscopy.
Phys. Rev. B **75**, 201401 (2007).

[70] D. S. Saraga and D. Loss
Fermi liquid parameters in two dimensions with spin-orbit interaction.
Phys. Rev. B **72**, 195319 (2005).

[71] E. Cappelluti, C. Grimaldi and F. Marsiglio
Electron-phonon effects on spin-orbit split bands of two-dimensional systems.
Phys. Rev. B **76**, 085334 (2007).

[72] D. Guan, M. Bianchi, S. Bao, E. Perkins, F. Meier, J. H. Dil, J. Osterwalder and P. Hofmann
Strongly enhanced electron-phonon coupling in the Rashba-split state of the Bi/Ag(111) surface alloy.
Phys. Rev. B **83**, 155451 (2011).

[73] E. Cappelluti, C. Grimaldi and F. Marsiglio
Topological Change of the Fermi Surface in Low-Density Rashba Gases: Application to Superconductivity.
Phys. Rev. Lett. **98**, 167002 (2007).

[74] C. R. Ast, D. Pacilé, L. Moreschini, M. C. Falub, M. Papagno, K. Kern, M. Grioni, J. Henk, S. Ernst, A.and Ostanin and P. Bruno
Spin-orbit split two-dimensional electron gas with tunable Rashba and Fermi energy.
Phys. Rev. B **77**, 081407 (2008).

[75] L. Petersen and P. Hedegård
A simple tight-binding model of spin-orbit splitting of sp-derived surface states.
Surface Science **459**, 49–56 (2000).

[76] G. Bihlmayer, Y. M. Koroteev, P.M. Echenique, E.V. Chulkov and S. Blgel
The Rashba-effect at metallic surfaces.
Surface Science **600**, 3888 – 3891 (2006).

[77] B. Slomski, G. Landolt, Fa. Meier, L. Patthey, G. Bihlmayer, J. Osterwalder and J. H. Dil
Manipulating the Rashba-type spin splitting and spin texture of Pb quantum well states.
Phys. Rev. B **84**, 193406 (2011).

[78] M. Nagano, A. Kodama, T. Shishidou and T. Oguchi
A first-principles study on the Rashba effect in surface systems.
Journal of Physics: Condensed Matter **21** (2009).

[79] Bartosz Slomski, Gabriel Landolt, Gustav Bihlmayer, Jürg Osterwalder and J. Hugo Dil
Tuning of the Rashba effect in Pb quantum well states via a variable Schottky barrier.
Sci. Rep. **3** (2013).

[80] J. Nitta, T. Akazaki, Hi Takayanagi and T. Enoki
Gate Control of Spin-Orbit Interaction in an Inverted $In_{0.53}Ga_{0.47}As/In_{0.52}Al_{0.48}As$ Heterostructure.
Phys. Rev. Lett. **78**, 1335–1338 (1997).

[81] M. Studer, G. Salis, K. Ensslin, D. C. Driscoll and A. C. Gossard
Gate-Controlled Spin-Orbit Interaction in a Parabolic GaAs/AlGaAs Quantum Well.
Phys. Rev. Lett. **103**, 027201 (2009).

[82] Hyun Cheol Koo, Jae Hyun Kwon, Jonghwa Eom, Joonyeon Chang, Suk Hee Han and Mark Johnson
Control of Spin Precession in a Spin-Injected Field Effect Transistor.
Science **325**, 1515–1518 (2009).

[83] Christian R. Ast, Jürgen Henk, Arthur Ernst, Luca Moreschini, Mihaela C. Falub, Daniela Pacilé, Patrick Bruno, Klaus Kern and Marco Grioni
Giant Spin Splitting through Surface Alloying.
Phys. Rev. Lett. **98**, 186807 (2007).

[84] D. Pacilé, C. R. Ast, M. Papagno, C. Da Silva, L. Moreschini, M. Falub, Ari P. Seitsonen and M. Grioni
Electronic structure of an ordered Pb/Ag(111) surface alloy: Theory and experiment.
Phys. Rev. B **73**, 245429 (2006).

[85] Fabian Meier, Vladimir Petrov, Hossein Mirhosseini, Luc Patthey, Jürgen Henk, Jürg Osterwalder and J. Hugo Dil
Interference of spin states in photoemission from Sb/Ag(111) surface alloys.
Journal of Physics: Condensed Matter **23** (2011).

[86] F. Meier, V. Petrov, S. Guerrero, C. Mudry, L. Patthey, J. Osterwalder and J. H. Dil
Unconventional Fermi surface spin textures in the Bi_xPb_{1-x}/Ag(111) surface alloy.
Phys. Rev. B **79**, 241408 (2009).

[87] D. J. Thouless, M. Kohmoto, M. P. Nightingale and M. den Nijs
Quantized Hall Conductance in a Two-Dimensional Periodic Potential.
Phys. Rev. Lett. **49**, 405–408 (1982).

[88] K. von Klitzing
The quantized Hall effect.
Rev. Mod. Phys. **58**, 519–531 (1986).

[89] A. P. Schnyder, S. Ryu, A. Furusaki and A. W. W. Ludwig
Classification of topological insulators and superconductors in three spatial dimensions.
Phys. Rev. B **78**, 195125 (2008).

[90] C. L. Kane and E. J. Mele
Quantum Spin Hall Effect in Graphene.
Phys. Rev. Lett. **95**, 226801 (2005).

[91] B. A. Bernevig, T. L. Hughes and Sh.-Ch. Zhang
Quantum Spin Hall Effect and Topological Phase Transition in HgTe Quantum Wells.
Science **314**, 1757–1761 (2006).

[92] M. König, S. Wiedmann, Ch. Brüne, A. Roth, H. Buhmann, L. W. Molenkamp, X.-L. Qi and Sh.-Ch. Zhang
Quantum Spin Hall Insulator State in HgTe Quantum Wells.
Science **318**, 766–770 (2007).

[93] S.-Q. Shen. *Topological insulators*. Springer-Verlag Berlin Heidelberg, 2012.

[94] H. Zhang, C.-X. Liu, X.-L. Qi, X. Dai, Zh. Fang and Sh.-Ch. Zhang
Topological insulators in Bi_2Se_3, Bi_2Te_3 and Sb_2Te_3 with a single Dirac cone on the surface.
Nature Physics **5**, 438 (2009).

[95] L. Fu and C. L. Kane
Topological insulators with inversion symmetry.
Phys. Rev. B **76**, 045302 (2007).

[96] S.-Y. Xu, Y. Xia, L. A. Wray, S. Jia, F. Meier, J. H. Dil, J. Osterwalder, B. Slomski, A. Bansil, H. Lin, R. J. Cava and M. Z. Hasan
Topological Phase Transition and Texture Inversion in a Tunable Topological Insulator.
Science **332**, 560 (2011).

[97] S. Souma, M. Komatsu, M. Nomura, T. Sato, A. Takayama, T. Takahashi, K. Eto, K. Segawa and Y. Ando
Spin Polarization of Gapped Dirac Surface States Near the Topological Phase Transition in $TlBi(S_{1-x}Se_x)_2$.
Phys. Rev. Lett. **109**, 186804 (2012).

[98] R. B. Laughlin
Quantized Hall conductivity in two dimensions.
Phys. Rev. B **23**, 5632–5633 (1981).

[99] W.-Y. Shan, H.-Zh. Lu and Sh.-Q. Shen
Effective continuous model for surface states and thin films of three-dimensional topological insulators.
New Journal of Physics **12**, 043048 (2010).

[100] D. Hsieh, D. Qian, L. Wray, Y. Xia, Y. S. Hor, R. J. Cava and M. Z. Hasan
A topological Dirac insulator in a quantum spin Hall phase.
Nature **452**, 970–974 (2008).

[101] D. Hsieh, L. Wray, D. Qian, Y. Xia, J. H. Dil, F. Meier, L. Patthey, J. Osterwalder, G. Bihlmayer, Y. S. Hor, R. J. Cava and M. Z. Hasan
Direct observation of spin-polarized surface states in the parent compound of a topological insulator using spin- and angle-resolved photoemission spectroscopy in a Mott-polarimetry mode.
New Journal of Physics **12**, 125001 (2010).

[102] D. Hsieh, Y. Xia, L. Wray, D. Qian, A. Pal, J. H. Dil, J. Osterwalder, F. Meier, G. Bihlmayer, C. L. Kane, Y. S. Hor, R. J. Cava and M. Z. Hasan
Observation of Unconventional Quantum Spin Textures in Topological Insulators.
Science **323**, 919–922 (2009).

[103] D. Hsieh, Y. Xia, D. Qian, L. Wray, J.H. Dil, F. Meier, J. Osterwalder, L. Patthey, J.G. Checkelsky, N.P. Ong, A.V. Fedorov, H. Lin, A. Bansil, D. Grauer, Y.S. Hor, R.J. Cava and M.Z. Hasan
A tuneable topological insulator in the spin helical Dirac transport regime.
Nature **460**, 1101 (2009).

[104] P. Roushan, J. Seo, C. V. Parker, Y. S. Hor, D. Hsieh, D. Qian, A. Richardella, M. Z. Hasan, R. J. Cava and A. Yazdani
Topological surface states protected from backscattering by chiral spin texture.
Nature **460**, 1106–1109 (2009).

[105] J. I. Pascual, G. Bihlmayer, Yu. M. Koroteev, H.-P. Rust, G. Ceballos, M. Hansmann, K. Horn, E. V. Chulkov, S. Blügel, P. M. Echenique and Ph. Hofmann
Role of Spin in Quasiparticle Interference.
Phys. Rev. Lett. **93**, 196802 (2004).

[106] Y. Xia, D. Qian, D. Hsieh, L. Wray, A. Pal, H. Lin, A. Bansil, D. Grauer, Y. S. Hor, R. J. Cava and M. Z. Hasan

Observation of a large-gap topological-insulator class with a single Dirac cone on the surface.
Nature Physics **5**, 398 (2009).

[107] D. Hsieh, Y. Xia, D. Qian, L. Wray, F. Meier, J. H. Dil, J. Osterwalder, L. Patthey, A. V. Fedorov, H. Lin, A. Bansil, D. Grauer, Y. S. Hor, R. J. Cava and M. Z. Hasan
Observation of Time-Reversal-Protected Single-Dirac-Cone Topological-Insulator States in Bi_2Se_3 and Sb_2Te_3.
Phys. Rev. Lett. **103**, 146401 (2009).

[108] Y. L. Chen, J. G. Analytis, J.-H. Chu, Z. K. Liu, S.-K. Mo, X. L. Qi, H. J. Zhang, D. H. Lu, X. Dai, Z. Fang, S. C. Zhang, I. R. Fisher, Z. Hussain and Z.-X. Shen
Experimental Realization of a Three-Dimensional Topological Insulator, Bi_2Te_3.
Science **325**, 178–181 (2009).

[109] L. Fu
Hexagonal Warping Effects in the Surface States of the Topological Insulator Bi_2Te_3.
Phys. Rev. Lett. **103** (2009).

[110] Z. Alpichshev, J. G. Analytis, J.-H. Chu, I. R. Fisher, Y. L. Chen, Z. X. Shen, A. Fang and A. Kapitulnik
STM Imaging of Electronic Waves on the Surface of Bi_2Te_3: Topologically Protected Surface States and Hexagonal Warping Effects.
Phys. Rev. Lett. **104**, 016401 (2010).

[111] Y. Ando
Topological Insulator Materials.
Journal of the Physical Society of Japan **82**, 102001 (2013).

[112] M. Bianchi, D. Guan, S. Bao, J. Mi, B. B. Iversen, P. D. C. King and P. Hofmann
Coexistence of the topological state and a two-dimensional electron gas on the surface of Bi2Se3.
Nat Commun **1**, 128 (2010).

[113] M. Bianchi, R. C. Hatch, J. Mi, B. B. Iversen and P. Hofmann
Simultaneous Quantization of Bulk Conduction and Valence States through Adsorption of Nonmagnetic Impurities on Bi_2Se_3.
Phys. Rev. Lett. **107**, 086802 (2011).

[114] Hadj M. Benia, Chengtian Lin, Klaus Kern and Christian R. Ast
Reactive Chemical Doping of the Bi_2Se_3 Topological Insulator.
Phys. Rev. Lett. **107**, 177602 (2011).

[115] S. V. Eremeev, M. G. Vergniory, T. V. Menshchikova, A. A. Shaposhnikov and E. V. Chulkov
The effect of van der Waal's gap expansions on the surface electronic structure of layered topological insulators.
New Journal of Physics **14**, 113030 (2012).

[116] K. Kuroda M. Nakatake S. Kim Y. Yamada E. E. Krasovskii E. V. Chulkov M. Arita H. Miyahara T. Maegawa K. Okamoto K. Miyamoto T. Okuda K. Shimada H. Namatame M. Taniguchi Y. Ueda A. Kimura M. Ye, S. V. Eremeev
Relocation of the topological surface state of Bi_2Se_3 beneath the surface by Ag intercalation.
arXive, Condensed Matter, Materials Science (2011).

[117] Y. L. Chen, J.-H. Chu, J. G. Analytis, Z. K. Liu, K. Igarashi, H.-H. Kuo, X. L. Qi, S. K. Mo, R. G. Moore, D. H. Lu, M. Hashimoto, T. Sasagawa, S. C. Zhang, I. R. Fisher, Z. Hussain and Z. X. Shen
Massive Dirac Fermion on the Surface of a Magnetically Doped Topological Insulator.
Science **329**, 659–662 (2010).

[118] S.-Y. Xu, M. Neupane, C. Liu, D. Zhang, A. Richardella, L. A. Wray, N. Alidoust, M. Leandersson, T. Balasubramanian, J. Sanchez-Barriga, O. Rader, G. Landolt, B. Slomski, J. H. Dil, J. Osterwalder, T.-R. Chang, H.-T. Jeng, H. Lin, A. Bansil, N. Samarth and M. Z. Hasan
Hedgehog spin texture and Berry/'s phase tuning in a magnetic topological insulator.
Nat Phys **8**, 616–622 (2012).

[119] M. R. Scholz, J. Sánchez-Barriga, D. Marchenko, A. Varykhalov, A. Volykhov, L. V. Yashina and O. Rader
Tolerance of Topological Surface States towards Magnetic Moments: Fe on Bi_2Se_3.
Phys. Rev. Lett. **108**, 256810 (2012).

[120] T. Valla, Z.-H. Pan, D. Gardner, Y. S. Lee and S. Chu
Photoemission Spectroscopy of Magnetic and Nonmagnetic Impurities on the Surface of the Bi_2Se_3 Topological Insulator.
Phys. Rev. Lett. **108**, 117601 (2012).

[121] J. Honolka, A. A. Khajetoorians, V. Sessi, T. O. Wehling, S. Stepanow, J.-L. Mi, B. B. Iversen, T. Schlenk, J. Wiebe, N. B. Brookes, A. I. Lichtenstein, Ph. Hofmann, K. Kern and R. Wiesendanger
In-Plane Magnetic Anisotropy of Fe Atoms on $Bi_2Se_3(111)$.
Phys. Rev. Lett. **108**, 256811 (2012).

[122] T. Sato, Kouji Segawa, K. Kosaka, S. Souma, K. Nakayama, K. Eto, T. Minami, Yoichi Ando and T. Takahashi
Unexpected mass acquisition of Dirac fermions at the quantum phase transition of a topological insulator.
Nat Phys **7**, 840–844 (2011).

[123] S.-Y. Xu, M. Neupane, C. Liu, S. Jia, L. A. Wray, G. Landolt, B. Slomski, J. H. Dil, N. Alidoust, S. Basak, H. Lin, J. Osterwalder, A. Bansil, R. J. Cava and M. Z. Hasan
Anomalous spin-momentum locked two-dimensional states in the vicinity of a topological phase transition.
ArXiv e-prints , 1204.6518 (2012).

[124] X.-L. Qi, R. Li, J. Zang and Sh.-Ch. Zhang
Inducing a Magnetic Monopole with Topological Surface States.
Science **323**, 1184–1187 (2009).

[125] L. Fu and C. L. Kane
Probing Neutral Majorana Fermion Edge Modes with Charge Transport.
Phys. Rev. Lett. **102**, 216403 (2009).

[126] L. Fu and C. L. Kane
Superconducting Proximity Effect and Majorana Fermions at the Surface of a Topological Insulator.
Phys. Rev. Lett. **100**, 096407 (2008).

[127] V. Mourik, K. Zuo, S. M. Frolov, S. R. Plissard, E. P. A. M. Bakkers and L. P. Kouwenhoven
Signatures of Majorana Fermions in Hybrid Superconductor-Semiconductor Nanowire Devices.
Science **336**, 1003–1007 (2012).

[128] J. Linder, Y. Tanaka, T. Yokoyama, A. Sudbø and N. Nagaosa
Unconventional Superconductivity on a Topological Insulator.
Phys. Rev. Lett. **104**, 067001 (2010).

[129] L. Fu
Topological Crystalline Insulators.
Phys. Rev. Lett. **106**, 106802 (2011).

[130] S.-Y. Xu, C. Liu, N. Alidoust, M. Neupane, D. Qian, I. Belopolski, J. D. Denlinger, Y. J. Wang, H. Lin, L. A. Wray, G. Landolt, B. Slomski, J. H. Dil, A. Marcinkova, E. Morosan, Q. Gibson, R. Sankar, F. C. Chou, R. J. Cava, A. Bansil and M. Z. Hasan

Observation of a topological crystalline insulator phase and topological phase transition in Pb1,àíxSnxTe.
Nat Commun **3**, 1192 (2012).

[131] M. Dzero, K. Sun, V. Galitski and P. Coleman
Topological Kondo Insulators.
Phys. Rev. Lett. **104**, 106408 (2010).

[132] F. Lu, J. Z. Zhao, H. Weng, Z. Fang and X. Dai
Correlated Topological Insulators with Mixed Valence.
Phys. Rev. Lett. **110**, 096401 (2013).

[133] N. Xu, X. Shi, P. K. Biswas, C. E. Matt, R. S. Dhaka, Y. Huang, N. C. Plumb, M. Radović, J. H. Dil, E. Pomjakushina, K. Conder, A. Amato, Z. Salman, D. McK. Paul, J. Mesot, H. Ding and M. Shi
Surface and bulk electronic structure of the strongly correlated system SmB_6 and implications for a topological Kondo insulator.
Phys. Rev. B **88**, 121102 (2013).

[134] N. Xu, P. K. Biswas, J. H. Dil, R. S. Dhaka, G. Landolt, S. Muff, C. E. Matt, X. Shi, N. C. Plumb, M. Radović, E. Pomjakushina, K. Conder, A. Amato, S. V. Borisenko, R. Yu, H. M. Weng, Z. Fang, X. Dai, J. Mesot, H. Ding and M. Shi
Direct observation of the spin texture in SmB6 as evidence of the topological Kondo insulator.
Nat Commun **5** (2014).

[135] X. Wan, A. M. Turner, A. Vishwanath and S. Y. Savrasov
Topological semimetal and Fermi-arc surface states in the electronic structure of pyrochlore iridates.
Phys. Rev. B **83**, 205101 (2011).

[136] Z. Wang, Y. Sun, X.-Q. Chen, C. Franchini, G. Xu, H. Weng, X. Dai and Z. Fang
Dirac semimetal and topological phase transitions in A_3Bi ($A = Na, K, Rb$).
Phys. Rev. B **85**, 195320 (2012).

[137] Z. K. Liu, B. Zhou, Y. Zhang, Z. J. Wang, H. M. Weng, D. Prabhakaran, S.-K. Mo, Z. X. Shen, Z. Fang, X. Dai, Z. Hussain and Y. L. Chen
Discovery of a Three-Dimensional Topological Dirac Semimetal, Na_3Bi.
Science **343**, 864–867 (2014).

[138] S. V. Eremeev, G. Landolt, T. V. Menshchikova, B. Slomski, Y. M. Koroteev, Z. S. Aliev, M. B. Babanly, J. Henk, A. Ernst, L. Patthey, A. Eich, A. A. Khajetoorians, J. Hagemeister,

O. Pietzsch, J. Wiebe, R. Wiesendanger, P. M. Echenique, St. S. Tsirkin, I. R. Amiraslanov, J. H. Dil and E. V. Chulkov
Atom-specific spin mapping and buried topological states in a homologous series of topological insulators.
Nat Commun **3**, 635 (2012).

[139] Susmita Basak, Hsin Lin, L. A. Wray, S.-Y. Xu, L. Fu, M. Z. Hasan and A. Bansil
Spin texture on the warped Dirac-cone surface states in topological insulators.
Phys. Rev. B **84**, 121401 (2011).

[140] C. M. Wang and F. J. Yu
Effects of hexagonal warping on surface transport in topological insulators.
Phys. Rev. B **84**, 155440 (2011).

[141] H. K. Pal, V. I. Yudson and D. L. Maslov
Effect of electron-electron interaction on surface transport in the Bi2Te3 family of three-dimensional topological insulators.
Phys. Rev. B **85**, 085439 (2012).

[142] P. Rakyta, A. Pályi and J. Cserti
Electronic standing waves on the surface of the topological insulator Bi2Te3.
Phys. Rev. B **86**, 085456 (2012).

[143] Jin An and C. S. Ting
Surface states scattering from a step defect in the topological insulator Bi2Te3.
Phys. Rev. B **86**, 165313 (2012).

[144] M. Z. Hasan, H. Lin and A. Bansil
Warping the cone on a Topological Insulator.
Physics **2**, 108 (2009).

[145] T. Zhang, P. Cheng, X. Chen, J.-F. Jia, X. Ma, K. He, L. Wang, H. Zhang, X. Dai, Zh. Fang, X. Xie and Q.-K. Xue
Experimental Demonstration of Topological Surface States Protected by Time-Reversal Symmetry.
Phys. Rev. Lett. **103**, 266803 (2009).

[146] K. Kuroda, M. Arita, K. Miyamoto, M. Ye, J. Jiang, A. Kimura, E. E. Krasovskii, E. V. Chulkov, H. Iwasawa, T. Okuda, K. Shimada, Y. Ueda, H. Namatame and M. Taniguchi
Hexagonally Deformed Fermi Surface of the 3D Topological Insulator Bi_2Se_3.
Phys. Rev. Lett. **105**, 076802 (2010).

[147] S. Eremeev, Y. Koroteev and E. Chulkov
Effect of the atomic composition of the surface on the electron surface states in topological insulators $A_2^V B_3^{VI}$.
JETP Letters **91**, 387–391 (2010), 10.1134/S0021364010080059.

[148] Y. Zhang, K. He, C.-Z. Chang, C.-L. Song, L.-L. Wang, X. Chen, J.-F. Jia, Zh. Fang, X. Dai, W.-Y. Shan, Sh.-Q. Shen, Q. Niu, X.-L. Qi, Sh.-Ch. Zhang, X.-. Ma and Q.-K. Xue
Crossover of the three-dimensional topological insulator Bi_2Se_3 to the two-dimensional limit.
Nat. Phys. **6**, 584–588 (2010).

[149] J.-H. Song, H. Jin and A. J. Freeman
Interfacial Dirac Cones from Alternating Topological Invariant Superlattice Structures of Bi_2Se_3.
Phys. Rev. Lett. **105**, 096403 (2010).

[150] W. Zhang, R. Yu, H.-J. Zhang, X. D. and Z. Fang
First-principles studies of the three-dimensional strong topological insulators Bi_2Te_3 , Bi_2Se_3 and Sb_2Te_3.
New Journal of Physics **12**, 065013 (2010).

[151] L. A. Wray, S.-Y. Xu, Y. Xia, D. Hsieh, A. V. Fedorov, Y. San Hor, R. J. Cava, A. Bansil, H. Lin and M. Z. Hasan
A topological insulator surface under strong Coulomb, magnetic and disorder perturbations.
Nat. Phys. **7**, 32–37 (2011).

[152] Y. S. Hor, P. Roushan, H. Beidenkopf, J. Seo, D. Qu, J. G. Checkelsky, L. A. Wray, D. Hsieh, Y. Xia, S.-Y. Xu, D. Qian, M. Z. Hasan, N. P. Ong, A. Yazdani and R. J. Cava
Development of ferromagnetism in the doped topological insulator $Bi_{2-x}Mn_xTe_3$.
Phys. Rev. B **81**, 195203 (2010).

[153] R. Roy
Topological phases and the quantum spin Hall effect in three dimensions.
Phys. Rev. B **79**, 195322 (2009).

[154] A. M. Essin, J. E. Moore and D. Vanderbilt
Magnetoelectric Polarizability and Axion Electrodynamics in Crystalline Insulators.
Phys. Rev. Lett. **102**, 146805 (2009).

[155] M. Franz
Topological insulators: Starting a new family.
Nat Mater **9**, 536–537 (2010).

[156] J. Hugo Dil, Fabian Meier, Jorge Lobo-Checa, Luc Patthey, Gustav Bihlmayer and Jürg Osterwalder
Rashba-Type Spin-Orbit Splitting of Quantum Well States in Ultrathin Pb Films.
Phys. Rev. Lett. **101**, 266802 (2008).

[157] C. L. Kane
Condensed matter: An insulator with a twist.
Nat. Phys. **4**, 348–349 (2008).

[158] G. Schubert, H. Fehske, L. Fritz and M. Vojta
Fate of topological-insulator surface states under strong disorder.
Phys. Rev. B **85**, 201105 (2012).

[159] T. Okuda, T. Maegawa, M. Ye, K. Shirai, T. Warashina, K. Miyamoto, K. Kuroda, M. Arita, Z. S. Aliev, I. R. Amiraslanov, M. B. Babanly, E. V. Chulkov, S. V. Eremeev, A. Kimura, H. Namatame and M. Taniguchi
Experimental Evidence of Hidden Topological Surface States in $PbBi_4Te_7$.
Phys. Rev. Lett. **111**, 206803 (2013).

[160] S. Muff, F. von Rohr, G. Landolt, B. Slomski, A. Schilling, R. J. Cava, J. Osterwalder and J. H. Dil
Separating the bulk and surface n- to p-type transition in the topological insulator $GeBi_{4-x}Sb_xTe_7$.
Phys. Rev. B **88**, 035407 (2013).

[161] C. Niu, Y. Dai, Y. Zhu, Y. Ma, L. Yu, S. Han and B. Huang
Realization of tunable Dirac cone and insulating bulk states in topological insulators $(Bi_{1-x}Sb_x)_2Te_3$.
Sci. Rep. **2** (2012).

[162] C.-X. Liu, H.J. Zhang, B. Yan, X.-L. Qi, T. Frauenheim, X. Dai, Z. Fang and Sh.-Ch. Zhang
Oscillatory crossover from two-dimensional to three-dimensional topological insulators.
Phys. Rev. B **81**, 041307 (2010).

[163] H.-Z. Lu, W.-Y. Shan, W. Yao, Q. Niu and S.-Q. Shen
Massive Dirac fermions and spin physics in an ultrathin film of topological insulator.
Phys. Rev. B **81**, 115407 (2010).

[164] D. D. dos Reis, L. Barreto, M. Bianchi, G. A. S. Ribeiro, E. A. Soares, W. S. Silva, V. E. de Carvalho, J. Rawle, M. Hoesch, C. Nicklin, W. P. Fernandes, J. Mi, B. B. Iversen and

P. Hofmann
Surface structure of Bi2Se3(111) determined by low-energy electron diffraction and surface x-ray diffraction.
Phys. Rev. B **88**, 041404 (2013).

[165] S. Urazhdin, D. Bilc, S. D. Mahanti, S. H. Tessmer, Theodora Kyratsi and M. G. Kanatzidis
Surface effects in layered semiconductors Bi_2Se_3 and Bi_2Te_3.
Phys. Rev. B **69**, 085313 (2004).

[166] Z.-H. Pan, E. Vescovo, A. V. Fedorov, D. Gardner, Y. S. Lee, S. Chu, G. D. Gu and T. Valla
Electronic Structure of the Topological Insulator Bi_2Se_3 Using Angle-Resolved Photoemission Spectroscopy: Evidence for a Nearly Full Surface Spin Polarization.
Phys. Rev. Lett. **106**, 257004 (2011).

[167] Y. Sakamoto, T. Hirahara, H. Miyazaki, S.-I. Kimura and S. Hasegawa
Spectroscopic evidence of a topological quantum phase transition in ultrathin Bi_2Se_3 films.
Phys. Rev. B **81**, 165432 (2010).

[168] S. Schreyeck, N. V. Tarakina, G. Karczewski, C. Schumacher, T. Borzenko, C. Brune, H. Buhmann, C. Gould, K. Brunner and L. W. Molenkamp
Molecular beam epitaxy of high structural quality Bi_2Se_3 on lattice matched InP(111) substrates.
Applied Physics Letters **102**, 041914 (2013).

[169] A. Richardella, D. M. Zhang, J. S. Lee, A. Koser, D. W. Rench, A. L. Yeats, B. B. Buckley, D. D. Awschalom and N. Samarth
Coherent heteroepitaxy of Bi_2Se_3 on GaAs (111)B.
Applied Physics Letters **97**, 262104 (2010).

[170] X. F. Kou, L. He, F. X. Xiu, M. R. Lang, Z. M. Liao, Y. Wang, A. V. Fedorov, X. X. Yu, J. S. Tang, G. Huang, X. W. Jiang, J. F. Zhu, J. Zou and K. L. Wang
Epitaxial growth of high mobility Bi_2Se_3 thin films on CdS.
Applied Physics Letters **98**, 242102 (2011).

[171] P. Tabor, C. Keenan, S. Urazdhin and D. Lederman
Molecular beam epitaxy and characterization of thin Bi_2Se_3 films on Al_2O_3 (110).
Applied Physics Letters **99**, 013111 (2011).

[172] N. V. Tarakina, S. Schreyeck, T. Borzenko, C. Schumacher, G. Karczewski, K. Brunner, C. Gould, H. Buhmann and L. W. Molenkamp
Comparative Study of the Microstructure of Bi2Se3 Thin Films Grown on Si(111) and InP(111)

Substrates.
Crystal Growth & Design **12**, 1913–1918 (2012).

[173] N. V. Tarakina, S. Schreyeck, T. Borzenko, S. Grauer, C. Schumacher, G. Karczewski, C. Gould, K. Brunner, H. Buhmann and L. W. Molenkamp
Microstructural characterisation of Bi 2 Se 3 thin films.
Journal of Physics: Conference Series **471**, 012043 (2013).

[174] N. V. Tarakina, S. Schreyeck, M. Luysberg, S. Grauer, C. Schumacher, G. Karczewski, K. Brunner, C. Gould, H. Buhmann, R. E. Dunin-Borkowski and L. W. Molenkamp
Suppressing Twin Formation in Bi_2Se_3 Thin Films.
Advanced Materials Interfaces , n/a–n/a (2014).

[175] M. R. Scholz, J. Sánchez-Barriga, J. Braun, D. Marchenko, A. Varykhalov, M. Lindroos, Yung Jui Wang, Hsin Lin, A. Bansil, J. Minár, H. Ebert, A. Volykhov, L. V. Yashina and O. Rader
Reversal of the Circular Dichroism in Angle-Resolved Photoemission from Bi_2Te_3.
Phys. Rev. Lett. **110**, 216801 (2013).

[176] M. Neupane, A. Richardella, J. Sanchez-Barriga, S.-Y. Xu, N. Alidoust, I. Belopolski, C. Liu, G. Bian, D. M. Zhang, D. Marchenko, A. Varykhalov, O. Rader, M. Leandersson, T. Balasubramanian, T.-R. Chang, H.-T. Jeng, S. Basak, H. Lin, A. Bansil, N. Samarth and M. Z. Hasan
Tunneling Tuned Spin Modulations in Ultrathin Topological Insulator Films.
ArXiv e-prints (2013).

[177] A. Varykhalov, J. Sánchez-Barriga, A. M. Shikin, W. Gudat, W. Eberhardt and O. Rader
Quantum Cavity for Spin due to Spin-Orbit Interaction at a Metal Boundary.
Phys. Rev. Lett. **101**, 256601 (2008).

[178] C.-X. Liu, X.-L. Qi, H.J. Zhang, X. Dai, Z. Fang and Sh.-Ch. Zhang
Model Hamiltonian for topological insulators.
Phys. Rev. B **82**, 045122 (2010).

[179] G. W. Gobeli, F. G. Allen and E. O. Kane
Polarization Evidence for Momentum Conservation in Photoelectric Emission from Germanium and Silicon.
Phys. Rev. Lett. **12**, 94–97 (1964).

[180] Y. Cao, J. A. Waugh, N. C. Plumb, T. J. Reber, S. Parham, G. Landolt, Z. Xu, A. Yang, J. Schneeloch, G. Gu, J. H. Dil and D. S. Dessau

Coupled Spin-Orbital Texture in a Prototypical Topological Insulator.
ArXiv e-prints (2012).

[181] Z.-H. Zhu, N. Veenstra, C. S. Zhdanovich, P. Schneider, M. T. Okuda, K. Miyamoto, S.-Y. Zhu, H. Namatame, M. Taniguchi, W. Haverkort, M. S. Elfimov, I. and A. Damascelli
Photoelectron Spin-Polarization Control in the Topological Insulator Bi_2Se_3.
Phys. Rev. Lett. **112**, 076802 (2014).

[182] C. M. Schneider and J. Kirschner
Spin- and angle-resolved photoelectron spectroscopy from solid surfaces with circularly polarized light.
Critical Reviews in Solid State and Materials Sciences **20**, 179–283 (1995).

[183] J. Park, E. Kampert, K.-H. Jin, M. J. Eom, J. Ok, E. S. Choi, F. Wolff-Fabris, K. D. Lee, N. Hur, J.-S Rhyee, Y. J. Jo, S.-H. Jhi and J. S. Kim
Spin-Chiral Bulk Fermi Surfaces of BiTeI Proven by Quantum Oscillations.
ArXiv e-prints (2013).

[184] P. D. Dresselhaus, C. M. A. Papavassiliou, R. G. Wheeler and R. N. Sacks
Observation of spin precession in GaAs inversion layers using antilocalization.
Phys. Rev. Lett. **68**, 106–109 (1992).

[185] L. C. Lew Yan Voon, M. Willatzen, M. Cardona and N. E. Christensen
Terms linear in k in the band structure of wurtzite-type semiconductors.
Phys. Rev. B **53**, 10703–10714 (1996).

[186] J.-W. Luo, G. Bester and A. Zunger
Full-Zone Spin Splitting for Electrons and Holes in Bulk GaAs and GaSb.
Phys. Rev. Lett. **102**, 056405 (2009).

[187] K. Ishizaka, M. S. Bahramy, H. Murakawa, M. Sakano, T. Shimojima, T. Sonobe, K. Koizumi, S. Shin, H. Miyahara, A. Kimura, K. Miyamoto, T. Okuda, H. Namatame, M. Taniguchi, R. Arita, N. Nagaosa, K. Kobayashi, Y. Murakami, R. Kumai, Y. Kaneko, Y. Onose and Y. Tokura
Giant Rashba-type spin splitting in bulk BiTeI.
Nat Mater **10**, 521–526 (2011).

[188] M. S. Bahramy, R. Arita and N. Nagaosa
Origin of giant bulk Rashba splitting: Application to BiTeI.
Phys. Rev. B **84**, 041202 (2011).

[189] J. S. Lee, G. A. H. Schober, M. S. Bahramy, H. Murakawa, Y. Onose, R. Arita, N. Nagaosa and Y. Tokura
Optical Response of Relativistic Electrons in the Polar BiTeI Semiconductor.
Phys. Rev. Lett. **107**, 117401 (2011).

[190] G. Landolt, S. V. Eremeev, Y. M. Koroteev, B. Slomski, S. Muff, T. Neupert, M. Kobayashi, V. N. Strocov, T. Schmitt, Z. S. Aliev, M. B. Babanly, I. R. Amiraslanov, E. V. Chulkov, J. Osterwalder and J. H. Dil
Disentanglement of Surface and Bulk Rashba Spin Splittings in Noncentrosymmetric BiTeI.
Phys. Rev. Lett. **109**, 116403 (2012).

[191] G. Landolt, S. V. Eremeev, O. E. Tereshchenko, S. Muff, B. Slomski, K. A. K., M. Kobayashi, T. Schmitt, V. N. Strocov, J. Osterwalder, E. V. Chulkov and J. H. Dil
Bulk and surface Rashba splitting in single termination BiTeCl.
New Journal of Physics **15**, 085022 (2013).

[192] A.V. Shevelkov, E.V. Dikarev, R.V. Shpanchenko and B.A. Popovkin
Crystal Structures of Bismuth Tellurohalides BiTeX (X = Cl, Br, I) from X-Ray Powder Diffraction Data.
Journal of Solid State Chemistry **114**, 379–384 (1995).

[193] M. Sakano, J. Miyawaki, A. Chainani, Y. Takata, T. Sonobe, T. Shimojima, M. Oura, S. Shin, M. S. Bahramy, R. Arita, N. Nagaosa, H. Murakawa, Y. Kaneko, Y. Tokura and K. Ishizaka
Three-dimensional bulk band dispersion in polar BiTeI with giant Rashba-type spin splitting.
Phys. Rev. B **86**, 085204 (2012).

[194] C. Martin, E. D. Mun, H. Berger, V. S. Zapf and D. B. Tanner
Quantum oscillations and optical conductivity in Rashba spin-splitting BiTeI.
Phys. Rev. B **87**, 041104 (2013).

[195] Chang-Ran Wang, Jen-Chuan Tung, R. Sankar, Chia-Tso Hsieh, Yung-Yu Chien, Guang-Yu Guo, F. C. Chou and Wei-Li Lee
Magnetotransport in copper-doped noncentrosymmetric BiTeI.
Phys. Rev. B **88**, 081104 (2013).

[196] C. Bell, M. S. Bahramy, H. Murakawa, J. G. Checkelsky, R. Arita, Y. Kaneko, Y. Onose, M. Tokunaga, Y. Kohama, N. Nagaosa, Y. Tokura and H. Y. Hwang
Shubnikov–de Haas oscillations in the bulk Rashba semiconductor BiTeI.
Phys. Rev. B **87**, 081109 (2013).

[197] L. Demkó, G. A. H. Schober, V. Kocsis, M. S. Bahramy, H. Murakawa, J. S. Lee, I. Kézsmárki, R. Arita, N. Nagaosa and Y. Tokura
Enhanced Infrared Magneto-Optical Response of the Nonmagnetic Semiconductor BiTeI Driven by Bulk Rashba Splitting.
Phys. Rev. Lett. **109**, 167401 (2012).

[198] Sándor Bordács, Joseph G. Checkelsky, Hiroshi Murakawa, Harold Y. Hwang and Yoshinori Tokura
Landau Level Spectroscopy of Dirac Electrons in a Polar Semiconductor with Giant Rashba Spin Splitting.
Phys. Rev. Lett. **111**, 166403 (2013).

[199] G. A. H. Schober, H. Murakawa, M. S. Bahramy, R. Arita, Y. Kaneko, Y. Tokura and N. Nagaosa
Mechanisms of Enhanced Orbital Dia- and Paramagnetism: Application to the Rashba Semiconductor BiTeI.
Phys. Rev. Lett. **108**, 247208 (2012).

[200] A. Crepaldi, L. Moreschini, G. Autès, C. Tournier-Colletta, S. Moser, N. Virk, H. Berger, Ph. Bugnon, Y. J. Chang, K. Kern, A. Bostwick, E. Rotenberg, O. V. Yazyev and M. Grioni
Giant Ambipolar Rashba Effect in the Semiconductor BiTeI.
Phys. Rev. Lett. **109**, 096803 (2012).

[201] S. V. Eremeev, I. A. Nechaev, Y. M. Koroteev, P. M. Echenique and E. V. Chulkov
Ideal Two-Dimensional Electron Systems with a Giant Rashba-Type Spin Splitting in Real Materials: Surfaces of Bismuth Tellurohalides.
Phys. Rev. Lett. **108**, 246802 (2012).

[202] C. Tournier-Colletta, G. Autès, B. Kierren, Ph. Bugnon, H. Berger, Y. Fagot-Revurat, O. V. Yazyev, M. Grioni and D. Malterre
Atomic and electronic structure of a Rashba p–n junction at the BiTeI surface.
Phys. Rev. B **89**, 085402 (2014).

[203] C. J. Butler, H.-H. Yang, J.-Y. Hong, S.-H. Hsu, R. Sankar, C.-I. Lu, H.-Y. Lu, K.-H. O. Yang, H.-W. Shiu, C.-H. Chen, C.-C. Kaun, G.-J. Shu, F.-C. Chou and M.-T. Lin
Mapping polarization induced surface band bending on the Rashba semiconductor BiTeI.
Nat Commun **5** (2014).

[204] M. Kanou and T. Sasagawa
Crystal growth and electronic properties of a 3D Rashba material, BiTeI, with adjusted carrier

concentrations.
Journal of Physics: Condensed Matter **25**, 135801 (2013).

[205] J. P. Vyasanakere and V. B. Shenoy
Bound states of two spin-12 fermions in a synthetic non-Abelian gauge field.
Phys. Rev. B **83**, 094515 (2011).

[206] E. Bauer, G. Hilscher, H. Michor, C. Paul, E. W. Scheidt, A. Gribanov, Y. Seropegin, H. Noël, M. Sigrist and P. Rogl
Heavy Fermion Superconductivity and Magnetic Order in Noncentrosymmetric CePt3Si.
Phys. Rev. Lett. **92**, 027003 (2004).

[207] M. S. Bahramy, B. J. Yang, R. Arita and N. Nagaosa
Emergence of non-centrosymmetric topological insulating phase in BiTeI under pressure.
Nat Commun **3**, 679 (2012).

[208] X. Xi, C. Ma, Z. Liu, Z. Chen, W. Ku, H. Berger, C. Martin, D. B. Tanner and G. L. Carr
Signatures of a Pressure-Induced Topological Quantum Phase Transition in BiTeI.
Phys. Rev. Lett. **111**, 155701 (2013).

[209] M. K. Tran, J. Levallois, P. Lerch, J. Teyssier, A. B. Kuzmenko, G. Autes, O. V. Yazyev, A. Ubaldini, E. Giannini, D. van der Marel and A. Akrap
Infrared- and Raman-Spectroscopy Measurements of a Transition in the Crystal Structure and a Closing of the Energy Gap of BiTeI under Pressure.
Phys. Rev. Lett. **112**, 047402 (2014).

[210] Y. L. Chen, M. Kanou, Z. K. Liu, H. J. Zhang, J. A. Sobota, D. Leuenberger, S. K. Mo, B. Zhou, S. L. Yang, P. S. Kirchmann, D. H. Lu, R. G. Moore, Z. Hussain, Z. X. Shen, X. L. Qi and Sasagawa T.
Discovery of a single topological Dirac fermion in the strong inversion asymmetric compound BiTeCl.
Nature Physics **9** (.

[211] M. Sakano, M. S. Bahramy, A. Katayama, T. Shimojima, H. Murakawa, Y. Kaneko, W. Malaeb, S. Shin, K. Ono, H. Kumigashira, R. Arita, N. Nagaosa, H. Y. Hwang, Y. Tokura and K. Ishizaka
Strongly Spin-Orbit Coupled Two-Dimensional Electron Gas Emerging near the Surface of Polar Semiconductors.
Phys. Rev. Lett. **110**, 107204 (2013).

[212] J. J. Zhou, W. Feng, Y. Zhang, S. A. Yang and Y. Yao
Engineering Topological Surface States and Giant Rashba Spin Splitting in BiTeI/Bi_2Te_3 Heterostructures.
Sci. Rep. **4** (2014).

[213] P. Tang, Bi. Yan, W. Cao, S.-C. Wu, C. Felser and W. Duan
Weak topological insulators induced by the interlayer coupling: A first-principles study of stacked Bi_2TeI.
Phys. Rev. B **89**, 041409 (2014).

[214] S. V. Eremeev, I. P. Rusinov, I. A. Nechaev and E. V. Chulkov
Rashba split surface states in BiTeBr.
New Journal of Physics **15**, 075015 (2013).

[215] D. Pescia, A.R. Law, M.T. Johnson and H.P. Hughes
Determination of observable conduction band symmetry in angle-resolved electron spectroscopies: non-symmorphic space groups.
Solid State Communications **56**, 809–812 (1985).

[216] U. Petasch, C. Hennig and H. Oppermann
Investigation on the pseudibinary system Bi_2Te_3/$BiCl_3$.
Z. Naturforsch **54b**, 234 (1999).

[217] K. A. Kokh, B. G. Nenashev, A. E. Kokh and G. Y. Shvedenkov
Application of a rotating heat field in Bridgman-Stockbarger crystal growth.
J. Crystal Growth **275** (2005).

[218] R. Coehoorn, C. Haas and R. A. de Groot
Electronic structure of $MoSe_2$, MoS_2, *and* WSe_2. *II. The nature of the optical band gaps*.
Phys. Rev. B **35**, 6203–6206 (1987).

[219] Th. Finteis, M. Hengsberger, Th. Straub, K. Fauth, R. Claessen, P. Auer, P. Steiner, S. Hüfner, P. Blaha, M. Vögt, M. Lux-Steiner and E. Bucher
Occupied and unoccupied electronic band structure of WSe_2.
Phys. Rev. B **55**, 10400–10411 (1997).

[220] S. W. Yu, T. Lischke, N. Müller, U. Heinzmann, C. Pettenkofer, A. Klein, P. Blaha and J. Braun
Spin resolved photoemission spectroscopy from InSe(0001) using circularly polarized radiation.
Journal of Physics-Condensed Matter **35**, 6715–6723 (1999).

[221] I. P. Rusinov, I. A. Nechaev, S. V. Eremeev, C. Friedrich, S. Blügel and E. V. Chulkov
Many-body effects on the Rashba-type spin splitting in bulk bismuth tellurohalides.
Phys. Rev. B **87**, 205103 (2013).

[222] H. B. Michaelson
The work function of the elements and its periodicity.
Journal of Applied Physics **48** (1977).

[223] H. L. Dai and W. Ho. *Laser spectroscopy and photo-chemistry on metal surfaces, Part II*.
Wolrd Scientific Publisher Co. Pte. Ltd., 2008.

[224] J Hugo Dil
Spin and angle resolved photoemission on non-magnetic low-dimensional systems.
Journal of Physics: Condensed Matter **21**, 403001 (22pp) (2009).

[225] A. Crepaldi, F. Cilento, M. Zacchigna, M. Zonno, J. C. Johannsen, C. Tournier-Colletta, L. Moreschini, I. Vobornik, F. Bondino, E. Magnano, H. Berger, A. Magrez, Ph. Bugnon, G. Autès, O. V. Yazyev, M. Grioni and F. Parmigiani
Momentum and photon energy dependence of the circular dichroic photoemission in the bulk Rashba semiconductors BiTeX (X =I, Br, Cl).
Phys. Rev. B **89**, 125408 (2014).

[226] D. Di Sante, P. Barone, R. Bertacco and S. Picozzi
Electric Control of the Giant Rashba Effect in Bulk GeTe.
Advanced Materials **25**, 509–513 (2013).

[227] B. F. Miao, Y. T. Millev, L. Sun, B. You, W. Zhang and H. F. Ding
Thickness-driven spin reorientation transition in ultrathin films.
Science China Physics, Mechanics and Astronomy **56**, 70–84 (2013).

List of publications

- **G. Landolt**, S. V. Eremeev, O. E. Tereshchenko, S. Muff, K. A. Kokh, E. V. Chulkov, J. H. Dil
  Spin-polarized photocurrents from BiTeCl bulk states.
  to be published.

- C. Liu, S.-Y. Xu, N. Alidoust, T.-R. Chang, H. Lin, C. Dhital, S. Khadka, M. Neupane, I. Belopolski, **G. Landolt**, H.-T. Jeng, R. S. Markiewicz, J. H. Dil, A. Bansil, S. D. Wilson, and M. Z. Hasan
  Spin-correlated electronic state on the surface of a spin-orbit Mott system.
  Phys. Rev. B **90**, 045127 (2014).

- N. Xu, P. K. Biswas, J. H. Dil, R. S. Dhaka, **G. Landolt**, S. Muff, C. E. Matt, X. Shi, N. C. Plumb, M. Radović, E. Pomjakushina K. Conder A. Amato S. V. Borisenko, R. Yu, H. M. Weng, Z. Fang, X. Dai, J. Mesot, H. Ding, and M. Shi
  Direct observation of the spin texture in SmB6 as evidence of the topological Kondo insulator.
  Nature Communications **5**, 4566 (2014).

- N. Oncel, D. Çakır, J. H. Dil, B. Slomski, and **G. Landolt**
  Angle-resolved synchrotron photoemission and density functional theory on the iridium modified Si(111) surface.
  Journal of Physics: Condensed Matter **26**, 285501 (2014).

- C. N. Veenstra, Z. H. Zhu, M. Raichle, B. M. Ludbrook, A. Nicolaou, B. Slomski, **G. Landolt**, S. Kittaka, Y. Maeno, J. H. Dil, I. S. Elfimov, M. W. Haverkort, and A. Damascelli,
  Spin-Orbital Entanglement and the Breakdown of Singlets and Triplets in Sr_2RuO_4 Revealed by Spin- and Angle-Resolved Photoemission Spectroscopy.
  Physical Review Letters **112**, 127002 (2014).

- **G. Landolt**, S. Schreyeck, S. V. Eremeev, B. Slomski, S. Muff, J. Osterwalder, E. V. Chulkov, C. Gould, G. Karczewski, K. Brunner, H. Buhmann, L. W. Molenkamp, and J. H. Dil
  Spin Texture of Bi_2Se_3 Thin Films in the Quantum Tunneling Limit.
  Physical Review Letters **112**, 057601 (2014).

- B. Slomski, **G. Landolt**, S. Muff, F. Meier, J. Osterwalder and J. H. Dil
  Interband spin–orbit coupling between anti-parallel spin states in Pb quantum well states.
  New Journal of Physics **15**, 125031 (2013).

- A. Barfuss, L. Dudy, M. R. Scholz, H. Roth, P. Höpfner, C. Blumenstein, **G. Landolt**, J. H. Dil, N. C. Plumb, M. Radovic, A. Bostwick, E. Rotenberg, A. Fleszar, G. Bihlmayer, D. Wortmann, G. Li, W. Hanke, R. Claessen, and J. Schäfer
Elemental Topological Insulator with Tunable Fermi Level: Strained α-Sn on InSb(001).
Physical Review Letters **111**, 157205 (2013).

- **G. Landolt**, S. V. Eremeev, O. E. Tereshchenko, S. Muff, B. Slomski, K. A. Kokh, M. Kobayashi, T. Schmitt, V. N. Strocov, J. Osterwalder, E. V. Chulkov and J. H. Dil
Bulk and surface Rashba splitting in single termination BiTeCl.
New Journal of Physics **15**, 085022 (2013).

- S. Muff, F. von Rohr, **G. Landolt**, B. Slomski, A. Schilling, R. J. Cava, J. Osterwalder, and J. H. Dil
Separating the bulk and surface n- to p-type transition in the topological insulator $GeBi4_xSb_xTe_7$.
Physical Review B **88**, 035407 (2013).

- B. Slomski, **G. Landolt**, G. Bihlmayer, J. Osterwalder and J. H. Dil
Tuning of the Rashba effect in Pb quantum well states via a variable Schottky barrier.
Nature Scientific Reports **3**, 1963 (2013).

- S. Y. Xu, C. Liu, N. Alidoust, M. Neupane, D. Qian, I. Belopolski, J. D. Denlinger, Y. J. Wang, H. Lin, L. A. Wray, **G. Landolt**, B. Slomski, J.H. Dil, A. Marcinkova, E. Morosan, Q. Gibson, R. Sankar, F. C. Chou, R. J. Cava, A. Bansil, and M. Z. Hasan
Observation of a topological crystalline insulator phase and topological phase transition in $Pb_{1-x}Sn_xTe$.
Nature Communications **3**, 1192 (2012)

- C. Tegenkamp, D. Lükermann, H. Pfnür, B. Slomski, **G. Landolt**, and J. H. Dil
Fermi Nesting between Atomic Wires with Strong Spin-Orbit Coupling.
Physical Review Letters **109**, 266401 (2012).

- **G. Landolt**, S. V. Eremeev, Y. M. Koroteev, B. Slomski, S. Muff, T. Neupert, M. Kobayashi, V. N. Strocov, T. Schmitt, Z. S. Aliev, M. B. Babanly, I. R. Amiraslanov, E. V. Chulkov, J. Osterwalder, and J. H. Dil
Disentanglement of Surface and Bulk Rashba Spin Splittings in Noncentrosymmetric BiTeI.
Physical Review Letters **109**, 116403 (2012).

- S. Y. Xu, M. Neupane, C. Liu, D. Zhang, A. Richardella, L. A. Wray, N. Alidoust, M. Leandersson, T. Balasubramanian, J. Sanchez-Barriga, O. Rader, **G. Landolt**, B. Slomski, J. H. Dil, J. Osterwalder, TR. Chang, HT. Jeng, H. Lin, A. Bansil, N. Samarth, and M. Z. Hasan

Hedgehog spin texture and Berry's phase tuning in a magnetic topological insulator.
Nature Physics **8**, 616 (2012).

- S. V. Eremeev, **G. Landolt**, T. V. Menshchikova, B. Slomski, Y. M. Koroteev, Z. S. Aliev, M. B. Babanly, J. Henk, A. Ernst, L. Patthey, A. Eich, A. A. Khajetoorians, J. Hagemeister, O. Pietzsch, J. Wiebe, R. Wiesendanger, P. M. Echenique, S. S. Tsirkin, I. R. Amiraslanov, J. H. Dil, and E. V. Chulkov
  Atom-specific spin mapping and buried topological states in a homologous series of topological insulators
  Nature Communications **3**, 635 (2012).

- B. Slomski, **G. Landolt**, F. Meier, J. Osterwalder, and J. H. Dil
  Manipulating the Rashba-type spin splitting and spin texture of Pb quantum well states.
  Physical Review B **84**, 193406(B) (2011).

- P. D. C. King, R. C. Hatch, M. Bianchi, R. Ovsyannikov, C. Lupulescu, **G. Landolt**, B. Slomski, J. H. Dil, D. Guan, J. L. Mi, E. D. L. Rienks, J. Fink, A. Lindblad, S. Svensson, S. Bao, G. Balakrishnan, B. B. Iversen, J. Osterwalder, W. Eberhardt, F. Baumberger, and P. Hofmann
  Large Tunable Rashba Spin Splitting of a Two-Dimensional Electron Gas in Bi_2Se_3.
  Physical Review Letters **107**, 096802 (2011).

Acknowledgements

In the course of the last four years at the Swiss Light Source, I could count on the willing help and contribution from many people. First of all, I want to thank my supervisor Hugo Dil for his support and guidance. He has been an inexhaustible source of ideas and a pragmatic doer. Further, I want to express my gratitude to Jürg Osterwalder for giving me the opportunity to work in his group. I have always appreciated his critical appraisal of my manuscripts and his constructive input. Special thanks go to my fellow students at the COPHEE endstation, Bartosz «Barti» Slomski and Stefan «Müffi» Muff, for their effort during the uncountable user beamtimes and the hours of refurbishing the old lady. They made the troublesome times easier and the rest more fun.

An important part of the measurements were performed at the SX-ARPES endstation of the Swiss Light Source. For the kind support, I thank Vladimir N. Strocov, the builder of this great machine, and his postdocs Masaki Kobayashi, Federico Bisti, Victor Rogalev, and Leonid Lev. Further, I would like to thank Ming Shi, Nick Plumb, Milan Radovic, Elia Razzoli, Christian Matt, Luc Patthey, and Nan Xu from the SIS beamline for helping me during beamtimes at the HRPES endstation and for keeping the beamline in shape. Special thanks go to the highly competent triumvirate of the technicians Fritz Dubi, Markus Kropf, Christoph Hess, who were always willing to offer help and share their knowledge.

Throughout the years, many people contributed to the building and the maintenance of the COPHEE endstation. During my time at PSI especially Matthias Muntwiler, Vladimir Petrov, and Juraj Krempasky spent a lot of their valuable time on the many idiosyncrasies of the machine.

For the theoretical contribution to our work, I thank Sergey V. Eremeev, Konstantin A. Kokh, Yury M. Koroteev, and Evgueni V. Chulkov. Their DFT calculations and the discussion with them helped understand our data and enrichend our papers. Without good crystals, ARPES would not be possible, therefore I want to acknowledge the crystal growers Ziya S. Aliev, Mahammad B. Babanly, Imamaddin R. Amiraslanov and Oleg E. Tereshchenko. In particular, I give thanks for the Bi_2Se_3 thin films to Steffen Schreyeck and his group colleagues including Hartmut Buhmann, Charles Gould, Grzegorz Karczewski, Karl Brunner, Laurens W. Molenkamp. I have appreciated the discussions with Hartmut Buhmann and thank him for being the second assessor of this Thesis.

Further, I want to thank everyone who contributed in any way to my Thesis, including Titus Neupert, Christopher Mudry, Matthias Hengsberger, Thomas Greber, Adrian Hemmi, Michael Greif, Thomas Kälin, and many others.

Finally, I thank my parents for all their support throughout my studies.